Experimental investigations of turbulent heat transfer at corroded surface under supercritical pressure conditions

Zur Erlangung des akademischen Grades eines
Doktors der Ingenieurwissenschaften (Dr.-Ing.)

von der KIT-Fakultät für Maschinenbau des
Karlsruher Instituts für Technologie (KIT)
genehmigte

DISSERTATION

von

M. Sc. Fabian Alexander Wiltschko

Tag der mündlichen Prüfung: 21.10.2025

Hauptreferent: Prof. Dr.-Ing. Xu Cheng

Korreferent: Prof. Dr.-Ing. Thomas Schulenberg

Eidesstattliche Erklärung

Ich versichere wahrheitsgemäß, die Arbeit selbstständig angefertigt, alle benutzten Hilfsmittel vollständig und genau angegeben und alles kenntlich gemacht zu haben, was aus Arbeiten anderer unverändert oder mit Abänderungen entnommen wurde.

Karlsruhe, 22.10.2025

. . . .
(Fabian Alexander Wiltschko)

Danksagung

Diese Arbeit wurde während meiner Zeit als wissenschaftlicher Mitarbeiter am Institut für Angewandte Thermofluidik (IATF) des Karlsruher Instituts für Technologie (KIT) durchgeführt.

Mein besonderer Dank gilt dem Leiter des Instituts, Professor Xu Cheng, für seine stetige Unterstützung, die anregenden fachlichen Diskussionen und die wertvollen Anregungen, die wesentlich zum Gelingen dieser Arbeit beigetragen haben. Ich danke ihm insbesondere für die zahlreichen offenen und konstruktiven Gespräche, die neue Perspektiven eröffnet und entscheidend zur Weiterentwicklung dieser Arbeit beigetragen haben. Sein kontinuierlicher Support und das positive Klima am Institut haben maßgeblich dazu beigetragen, dass ich meine Forschung mit großem Engagement und Freude durchführen konnte.

Ebenso möchte ich mich bei Professor Thomas Schulenberg herzlich bedanken, der als Korreferent durch seine fundierten Anmerkungen und konstruktiven Hinweise wichtige Impulse für diese Arbeit gegeben hat. Die Diskussionen mit ihm waren auch über den Rahmen dieser Dissertation hinaus bereichernd und lehrreich.

Mein Dank gilt außerdem allen Kolleginnen und Kollegen am IATF, die durch ihre Unterstützung, den kollegialen Zusammenhalt und die angenehme Arbeitsatmosphäre zum Gelingen dieser Arbeit beigetragen haben. Die vielen fachlichen Gespräche und wertvollen Diskussionen im Kollegium haben mir neue Perspektiven eröffnet. Besonders hervorheben möchte ich die anregenden Diskussionen mit Nikolai Rensch und Ludwig Köckert, insbesondere im Zusammenhang mit den Laborarbeiten, die sowohl fachlich als auch persönlich bereichernd waren. Ein besonderer Dank gilt außerdem Denis Klingel, der mir die Versuchsanlage eingehend erläutert und damit den Einstieg in die experimentelle Arbeit erleichtert hat. Ebenso danke ich Marvin Day, der mich während der Laborarbeiten tatkräftig unterstützt hat. Mein herzlicher Dank gilt auch dem Sekretariat, insbesondere Isolde Stamm, für die Unterstützung bei der organisatorischen Abwicklung, insbesondere bei den Bestellungen für das Labor, sowie für die freundlichen Gespräche und das angenehme Arbeitsklima.

Abschließend möchte ich meiner Partnerin, Jessica de Pede, von Herzen danken, die mich während der gesamten Promotionszeit mit Geduld, Verständnis und emotionaler Unterstützung begleitet hat. Ihr Rückhalt hat mir die nötige Stärke gegeben, auch herausfordernde Phasen zu meistern. Meinen Eltern danke ich für ihre langjährige Unterstützung, ihre Ermutigung und das Vertrauen, das sie mir während meines Studiums und auf meinem Lebensweg entgegengebracht haben.

Kurzfassung

Diese Dissertation widmet sich der experimentellen Untersuchung des turbulenten Wärmeübergangs an korrodierten, rauen Oberflächen unter überkritischen Druckbedingungen, wie sie in Wassergekühlten Reaktoren mit überkritischem Betriebsdruck auftreten. Ein Zentrales Ziel der Arbeit ist die Generierung von experimentellen Daten für raue Oberflächen, deren Rauigkeit präzise charakterisiert wurde. Durch Gegenüberstellung von Ergebnissen aus einem rauen und einem glatten Testrohr, kann der Einfluss der Oberflächenrauigkeit auf den turbulenten Wärmeübergang ermittelt werden. Die Experimente decken einen breiten und technisch relevanten Parameterbereich ab, darunter Variationen des Druckes, des Massenstromes, des Wärmestromes, sowie der Eintrittstemperatur. Die gewonnenen experimentelle Daten stellen eine Grundlage für die Analyse der komplexen Phänomene dar, die den Wärmeübergang unter überkritischen Druckbedingungen beeinflussen.

Die erzeugten experimentellen Daten ermöglichen eine umfassende systematische Analyse der Wärmeübergangsmechanismen und dienen als Referenz zur Modellentwicklung und -validierung. Aufbauend auf den Ergebnissen wurde eine neue empirische Korrelation entwickelt, die den Einfluss der Oberflächenrauigkeit auf den Wärmeübergang unter Berücksichtigung der Dicke der viskosen Unterschicht modelliert. Diese Korrelation verbessert die Vorhersagegenauigkeit für den Wärmeübergang an rauen Wänden unter überkritischen Druckbedingungen und bietet eine Grundlage für technische Anwendungen.

Abschließend wurde basierend auf den gewonnenen experimentellen Daten ein Neuronales Netz zur Modellierung des Wärmeübergangs trainiert. Dieses Modell bildet eine alternative Herangehensweise zu den typischerweise verwendeten empirischen Korrelationen und liefert selbst unter den Bedingungen des verschlechterten Wärmeübergangs brauchbare Ergebnisse.

Abstract

This dissertation focuses on the experimental investigation of turbulent heat transfer at corroded, rough surfaces under supercritical pressure conditions, as encountered in supercritical water-cooled reactors. A central objective of this work is the generation of experimental data for rough surfaces with precisely characterized roughness. By comparing results from a rough and a smooth test tube, the influence of surface roughness on turbulent heat transfer can be determined. The experiments cover a wide and technically relevant parameter range, including variations in pressure, mass flux, heat flux, and inlet temperature. The experimental data obtained form a basis for analyzing the complex phenomena influencing heat transfer under supercritical pressure conditions.

The generated experimental data enable a comprehensive systematic analysis of heat transfer mechanisms and serve as a reference for model development and validation. Based on the results, a new empirical correlation was developed that models the influence of surface roughness on heat transfer, taking into account the thickness of the viscous sublayer. This correlation improves the predictive accuracy for heat transfer at rough surfaces under supercritical pressure conditions and provides a foundation for technical applications.

Finally, a neural network for modeling heat transfer was trained based on the experimental data obtained. This model offers an alternative approach to the typically used empirical correlations and delivers usable results even under conditions of deteriorated heat transfer.

Contents

List of Figures

List of Tables

Abbreviations

ABWR Advanced Boiling Water Reactor

ANN artificial neural network

BWR Boiling Water Reactor

CFD Computational Fluid Dynamics

CHF critical heat flux

DC direct current

DNN Deep Neural Network

DHT deteriorated heat transfer

DNS direct numerical simulation

EPR European Pressurized Reactor

GIF Generation IV International Forum

HPLWR High Performance Light Water Reactor

HTC heat transfer coefficient

IATF Institute for Applied Thermofluidics

IHT improved heat transfer

KIMOF KIT Model Fluid Facility

KIT Karlsruhe Institute of Technlogy

LWR Light Water Reactor

MAE mean absolute error

ME mean error

MSE mean squared error

MSLE mean squared logarithmic error

NHT normal heat transfer

NIST National Institute of Standards and Technology

PWR Pressurized Water Reactor

ReLU rectified linear unit

R&D Research and Development

RMS root mean squared

sCO2 supercritical pressure CO2

SCWR Supercritical-Water-Cooled Reactor

SJTU Shanghai Jiao Tong University

STD standard deviation

TBC thermal barrier coating

TC thermocouple

Nomenclature

Latin Letters

Symbol	Description	Dimension
A	area	m^2
Ac	bulk flow acceleration parameter	-
Bu	buoyancy parameter	-
C	coefficient	-
Ec	Eckert number	-
F	force	N
G	mass flux	$\frac{kg}{m^2 s}$
Ga	Galilei number	-
Gr	Grashof number	-
L	length	m
Nu	Nusselt number	-
Pr	Prandtl number	-
$\dot{Q}$	heat	W
R_a	mean roughness height	μm
Re	Reynolds number	-
R_q	root mean squared roughness height	μm
Ri	Richardson number	-
R_z	maximum peak to valley roughness height	μm
St	Stanton number	-
T	temperature	$^\circ C$

Symbol	**Description**	**Dimension**
a	thermal diffusivity	$\frac{m^2}{s}$
c_f	Darcy friction factor ($c_f = 4f$)	-
c_p	isobaric specific heat	$\frac{J}{kg \cdot K}$
d	diameter	m
f	Fanning friction factor ($f = c_f/4$)	-
g	gravitational constant	$\frac{m}{s^2}$
h	enthalpy	$\frac{J}{kgK}$
k	roughness	m
$\dot{m}$	mass flow rate	$\frac{kg}{s}$
p	pressure	MPa
$\dot{q}$	heat flux	$\frac{W}{m^2}$
r	radius	m
u	velocity	$\frac{m}{s}$
x	streamwise coordinate	x
y	wall normal coordinate	m

Greek Letters

Symbol	Description	Dimension
α	heat transfer coefficient	$\frac{W}{m \cdot K}$
β	thermal expansion coefficient (isobaric)	$\frac{1}{K}$
Δ	difference	-
δ	sublayer thickness	m
κ	von Kármán constant	-
λ	thermal conductivity	$\frac{W}{m \cdot K}$
μ	dynamic viscosity	$\frac{kg}{m \cdot s}$
ν	kinematic viscosity	$\frac{m^2}{s}$
ρ	density	$\frac{kg}{m^3}$
σ	standard deviation	-
τ	shear stress	$\frac{N}{mm^2}$

Subscripts

Symbol	Description
ac	acceleration
amb	ambient
b	bulk
bu	buoyancy
c	critical
cs	conductive sublayer
DHT	deteriorated heat transfer
$heat$	heated
i	inside/ inner
m	mean
NHT	normal heat transfer
pc	pseudo-critical
s	equivalent to Nikuradse sand-grain
t	turbulent
VP	variable properties
vs	viscous sublayer
w	wall

1 Introduction

The worldwide growing population and economic growth of mankind are leading to an increase in the consumption of primary energy, while at the same time, global warming is considered as one of the main challenges of the present time. According to (International Atomic Energy Agency (IAEA), 2019), the world energy consumption is expected to increase annually by 1%. A way to decrease carbon dioxide emissions (CO_2) is the electrification of industrial processes, traffic, and building heating. Hence, electricity consumption will increase even by a larger growth rate. The IAEA expects a growth rate for electricity consumption of about 2.2% per year up to 2030 and another 2% per year thereafter. The growing demand for electrical power will ideally be covered by renewable energy, such as wind, solar, and hydro power. Since the first two mentioned are daytime and weather dependent, in addition, assured power is required, which can be provided CO_2 neutral by nuclear power plants. Nuclear power faces the challenge of having to gain acceptance in society. In the first place, inherent safety of nuclear power plants, but also efficiency in terms of erection costs, or fuel utilization, the recyclability of spent fuel and the proliferation resistance have to be addressed to convince people around the world. In the context of the Generation IV International Forum (GIF) (U.S. DOE & GIF, 2002), six promising concepts for future Research and Development (R&D) have been identified, namely the Gas-Cooled Fast Reactor System, the Lead-Cooled Fast Reactor System, the Molten Salt Reactor System, the Sodium-Cooled Fast Reactor System, the Very-High-Temperature System and the Supercritical-Water-Cooled Reactor (SCWR) System. This work contributes to the understanding of heat transfer process in the core of a SCWR.

1.1 Supercritical Water Cooled Reactors

The basic concept of a SCWR is schematically shown in Figure 1.1 (U.S. DOE & GIF, 2002) and is summarized here. The operation conditions of a SCWR are above the thermodynamic critical point of water, which is 374 ° C and 22.1 MPa. Depending on the core design, both a thermal spectrum and a fast spectrum may be realized. From an economical point of view, the SCWR has several advantages, compared to the state-of-the-art Light Water Reactor (LWR) systems. The thermal efficiency of up to 44% is increased, compared to about 35% of LWRs. Because the specific heat of the supercritical water is larger compared to that at single phase sub-critical conditions, a lower coolant mass flow rate is required per unit of core power, leading to smaller reactor coolant pumps and piping. In addition, no steam dryers, steam separators, recirculation pumps, and steam generators are required (Rowinski et al., 2018). Hence, the erection costs of such a power plant may be reduced, but this is not yet practically proven. In addition, SCWRs avoid classical boiling and

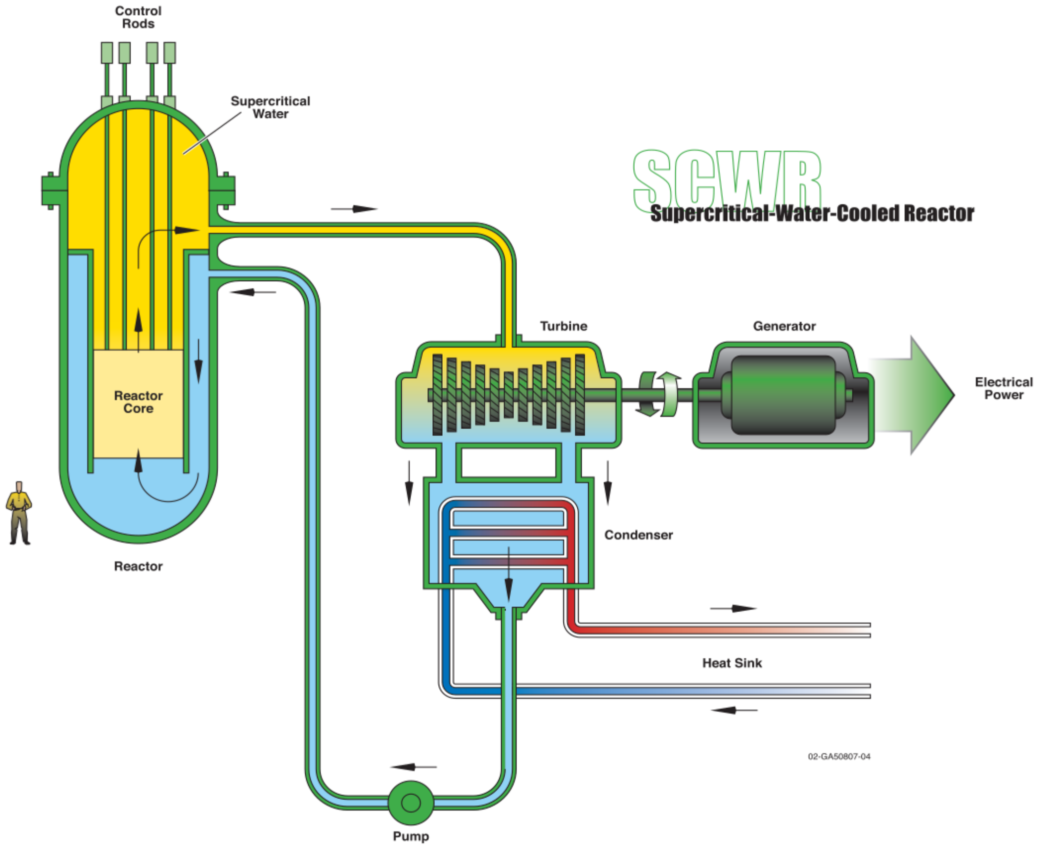

Figure 1.1: SCWR concept from Generation IV International Forum (U.S. DOE & GIF, 2002)

CHF phenomena under normal operating conditions, since water remains in a single supercritical phase. However, this benefit depends on maintaining pressure above the critical point, as CHF can re-emerge during depressurization events.

Meanwhile, many concepts of SCWRs have been developed all over the world, which are summa-

Table 1.1: Overview of SCWR designs all around the world (U.S. DOE & GIF, 2002)

	Canada	China	EU	Russian Federation		Japan	
	SCWR	CSR1000	HPLWR	VVER-SKD	VVER-SCP-600	Super LWR	Super FR
Spectrum	Thermal	Thermal	Thermal	Mixed	Fast-Resonant	Thermal	Fast
Pressure (MPa)	25	25	25	25.5	27.5	25	25
Inlet Temp. (°C)	350	280	280	290	400	280	280
Outlet Temp. (°C)	625	500	500	540	522	500	501
Thermal Pow.(MW)	2540	2300	2300	3830	1250	3492	2337

rized in (PRPPWG & GIF, 2022) and shown in Table 1.1. The Canadian SCWR design (Pencer & Colton, 2013) consists of pressure tubes, instead of a pressure vessel. The Chinese CSR1000 concept is described in (International Atomic Energy Agency (IAEA), 2015). Details about the High Performance Light Water Reactor (HPLWR), which was developed in a project of the EU can be found in (Schulenberg & Starflinger, 2012). The VVER-SKD, which has a mixed spectrum and was developed in the Russian Federation, is described in (Ryzhov et al., 2011), while the Russian VVER-SCP600 has a fast spectrum, and details are found in (Alekseev et al., 2018). The Japanese Super LWR is described in (Qu & Oka, 2014). In the book of (Oka & Mori, 2014), among others, the Japanese Super LWR as well as the Super FR, which is a fast reactor, are described.

1.2 Importance of heat transfer

One of the main technical challenges for SCWRs is the high requirements for the materials due to the high temperatures and the high pressure within the reactor core, especially for the fuel rod cladding material. It must be ensured, with some margin of safety, that the maximum bearable temperatures of the cladding material are not exceeded. Unfortunately, the heat transfer to fluids at supercritical pressure is an overly complex phenomenon, which is not fully understood at the current state-of-the-art. In the vicinity of the pseudocritical temperature, the heat transfer may deteriorate, and predictions of wall temperatures may not be accurate under such conditions. However, accurate prediction of heat transfer in the reactor core is indispensable to guarantee safe operation of the nuclear power plant. Furthermore, supercritical pressure water at high temperatures appears to be different from low temperature water in terms of ion-ion interactions, ion-solvent reactions, ionic mobilities, and other chemical processes (Cohen, 1979). This results in high requirements for the reactor materials in terms of corrosion resistivity. During the reactor operating time, an oxide layer is formed on the cladding of the fuel rod. The heat transfer surface is therefore changed and appears to have a larger roughness, compared to the cladding surface at the beginning of the refueling cycle. The increased surface roughness has an impact on the heat transfer from the fuel rods to the coolant. Hence, it is of great importance to understand the effect of the changed surface roughness on the heat transfer to supercritical pressure water, to guarantee the safe operation of SCWRs.

1.3 Objective

Experimental investigations are the key to understanding the complex phenomenon of heat transfer to supercritical pressure fluids. Upon analysis of the generated experimental data, different heat transfer mechanisms can be identified and described. In addition, the data can be used to assess and improve existing models, or new models can be developed. The aim of this work is to generate an experimental reference database for heat transfer to fluids under supercritical pressure conditions at rough heat transfer surfaces, to study the effect of the surface roughness on the heat transfer and to improve the state-of-the-art modeling of heat transfer under such conditions. The work is structured as follows:

In the 2nd chapter of the thesis, the peculiarity of fluids under supercritical pressure conditions is shown, and an overview of heat transfer experiments is presented. The state of the art of modeling heat transfer under supercritical pressure conditions is summarized. In addition, the effect of surface roughness on flows and heat transfer is explained on the basis of the state-of-the-art literature. Finally, knowledge gaps and the need for research are worked out. The experimental facility is explained in Chapter 3. In order to reduce the required operating pressure and temperature, the refrigerant R134a is used as a surrogate fluid, which has a lower critical pressure and a lower critical temperature compared to water. In Chapter 4, the experimental methodology is shown. By comparison of the experimental results of a reference tube with a smooth inner surface with that of the rough tubes, representing corroded surfaces, the effect of the roughness on the heat transfer to supercritical pressured fluids is investigated. The results are presented in Chapter 5, first for the smooth reference tube, pointing out the different features of the heat transfer to fluids at supercritical pressure conditions. Then, the effect of the surface roughness on the heat transfer is worked out, using the results obtained in the rough tube. In the 6th chapter, a new Nusselt correlation is derived and assessed, considering surface roughness, with the experimental data generated. In addition, existing models for heat transfer under supercritical pressure conditions are evaluated, with a focus on correlations that are applicable to rough heat transfer surfaces. In Chapter 7, a neural network for the prediction of heat transfer is established and trained with the experimental data. The newly proposed empirical correlation and the established machine learning model are compared with each other. Finally, in the last chapter, conclusions of the experimental campaign and the modeling work are drawn and needs for future research in the field of heat transfer to supercritical pressure fluids are shown.

2 Literature Review

In this chapter, the particularities in the thermodynamic properties of fluids at supercritical pressure conditions are shown and their impact on the heat transfer is pointed out. An overview of past experimental investigations is given and the state of the art of modeling of heat transfer under supercritical pressure conditions is shown. Further, the effect of roughness on flows under adiabatic conditions and on heat transfer is shown. Based on this literature review, knowledge gaps are identified and the necessity of research is worked out.

2.1 Fluids at supercritical pressure conditions

The thermodynamic state of aggregation of a fluid, referred to as phase, is determined by the pressure and temperature of the fluid. The phase diagram of water is shown in Figure 2.1, including the temperatures ranges from core inlet- to core outlet temperature of a BWR (Advanced Boiling Water Reactor (ABWR) (International Atomic Energy Agency (IAEA), 2011)), a PWR (European Pressurized Reactor (EPR) (TVO, 2010)) and of the HPLWR (Schulenberg & Starflinger, 2012). Water is liquid at room temperature and atmospheric pressure. When the temperature increases at constant pressure, the saturation line is reached. The energy supplied to the fluid at this point

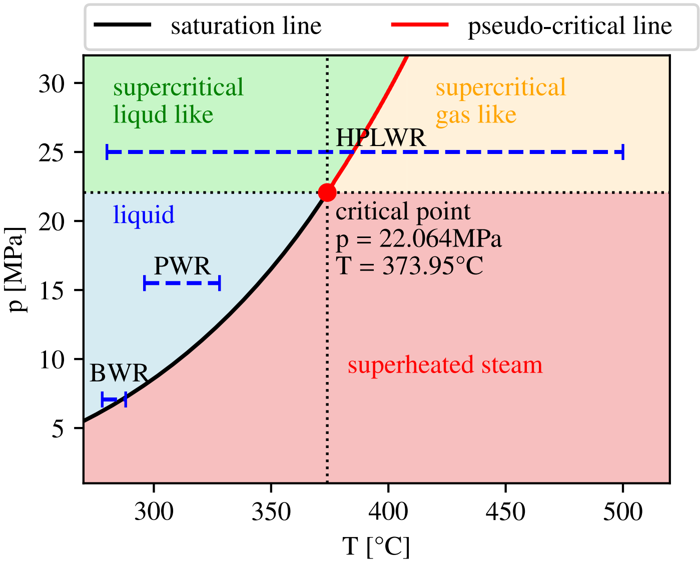

Figure 2.1: Phase diagram of water and operating conditions of light water reactors

will be used for the phase change, from liquid to steam. When a fluid evaporates, the thermophysical properties are changing abruptly, e.g. the density reduces significantly. Once the phase change is completed, the additional energy supplied to the steam will increase the temperature and the steam will be superheated. For higher pressures, the saturation temperature increases, up to $T_c = 373.95\ °C$, at a pressure of $p_c = 22.064\ MPa$. This is the critical point. For pressures above the critical value, the fluid is no longer subject to a phase change when the temperature is increased beyond the critical temperature, but the thermophysical properties are still changing significantly, but the change is continuously. This is shown exemplarily in Figure 2.2, for the density ρ, the isobaric specific heat c_p, the dynamic viscosity μ and the thermal conductivity λ of water, at the supercritical pressure of $p = 25\ MPa$ in a temperature range that includes the critical temperature. It is noticeable that the specific heat c_p shows a sharp peak. The temperature for which c_p shows

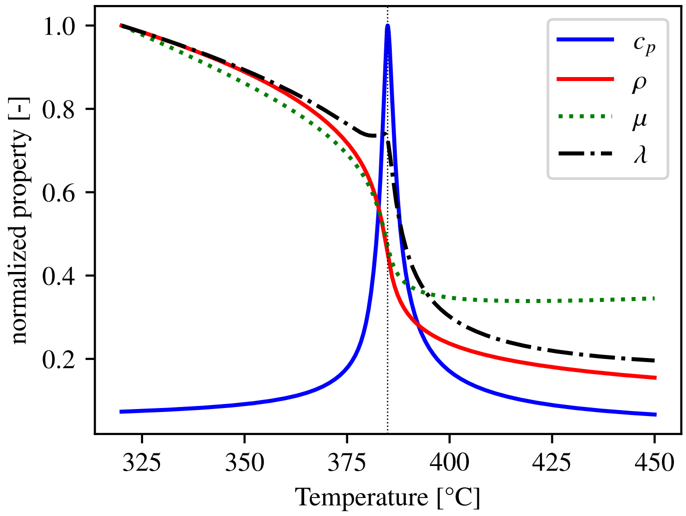

Figure 2.2: Variation of the thermophysical properties of water at 25 MPa

a maximum is called the pseudocritical temperature. For increasing pressure, the pseudocritical temperature is shifted to higher values, as indicated by the pseudocritical line in Figure 2.1. In the vicinity of the pseudocritical temperature, the density ρ and the viscosity μ are decreasing, with the largest gradient in a narrow temperature range around the pseudocritical value. The thermal conductivity λ also decreases, but shows a small peak at the pseudocritical temperature. The drastic variations of the thermophysical properties have a significant influence on the heat transfer, as will be shown later in this chapter. Here, a distinction can be made between effects which are directly caused by the variation of the thermophysical property itself, e.g. it stands to reason that the heat transfer is reduced when the thermal conductivity of the fluid decreases. Other effects are just indirectly caused by the variation of the thermophysical property; e.g. bulk flow velocity is increased when the density is decreased or buoyancy effects appear, which have an impact on the heat transfer. Around the pseudocritical temperature, all properties vary with large gradients, and many different effects are present, influencing each other and partially acting in opposite directions, and the heat transfer to fluids under supercritical pressure conditions has a high level of complexity. In Figure 2.3, the density variation ρ (2.3 (a)) and the specific heat variation c_p (2.3 (b)) are shown for water at different pressures. For comparison, the properties are shown at $p = 20\ MPa$, which is

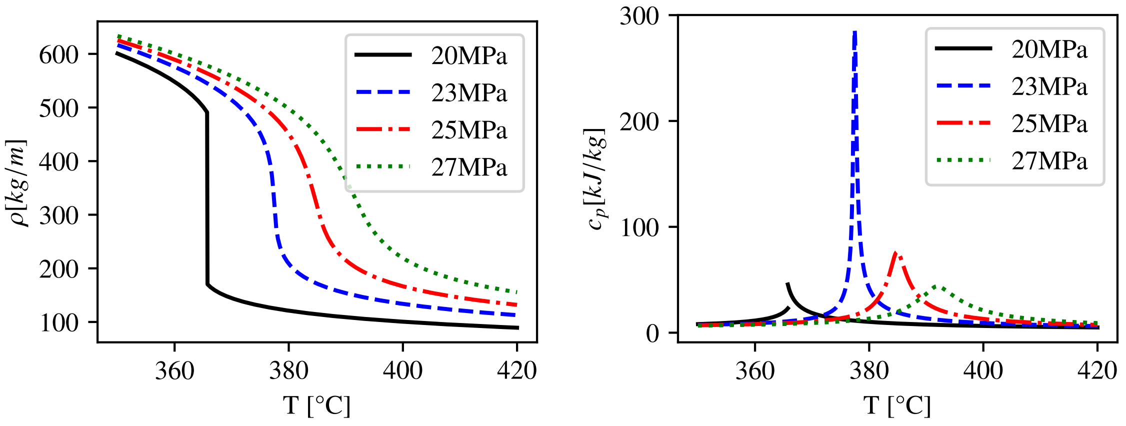

(a) (b)

Figure 2.3: Variation of density (a) and specific heat (b) of water at different pressures

a large subcritical pressure. When the saturation temperature is reached, the density suddenly jumps to a smaller value. At sub-critical pressure, the phase change causes a discontinuity in specific heat — with separate curves for the liquid and vapor phases, and a visible gap between them in the graph. At supercritical pressure, the properties change continuously, while the variation is sharper when the pressure is closer to the critical value.

There are many technical applications for supercritical fluids in heat transfer processes, mainly focusing on the enhancement of the thermal efficiency of such systems. In addition to the development of an SCWR, the following fields are in focus of the research.

- supercritical steam generators in fossil power plants (Paul, 1999)
- Supercritical Organic Rankine Cycle and Supercritical Brayton Cycle (Chowdhurry & Ehsan, 2023)
- supercritical pressure CO2 (sCO2) in pumped thermal energy storage, e.g. for concentrating solar power plants (McTigue et al., 2020)
- sCO2 in refrigeration and air-conditioning systems (Doerffel et al., 2021)
- access geothermal resources at supercritical pressure and temperature (Shnell et al., 2019)
- supercritical pressure methane in cooling channels of rocket engines (Negishi et al., 2012)
- cooling of superconducting magnet systems in fusion reactors with supercritical helium (Tanna, 2006)
- supercritical hydrocarbon fuels in high-speed aircraft (Edwards, 1993)

2.2 Heat transfer at supercritical pressure conditions

On the following pages, the first general definitions which are important for the understanding of heat transfer in general are given. Further, the main features of heat transfer to supercritical pressure fluids are shown, then experimental works and modeling approaches are summarized.

2.2.1 Main features

When the ability of a technical system to transfer heat from a solid surface to a flow needs to be evaluated, it makes sense to put the transferred heat $\dot{Q}_w$ per heat transfer surface area A_{heat}, the heat flux $\dot{q}_w$, in relation to the temperature difference from the heat transfer surface T_w to the bulk temperature T_b of the working fluid. This leads to the definition of the heat transfer coefficient α:

$$\dot{q}_w = \frac{\dot{Q}_w}{A_{heat}} = \frac{\dot{Q}_w}{\pi \cdot d_i \cdot L_{heat}} \tag{2.1}$$

$$\alpha = \frac{\dot{q}_w}{T_w - T_b} \tag{2.2}$$

The heat flux $\dot{q}_w$ in equation 2.1 is written for a tube with circular cross-section, as it is used in this experimental work, with an inner tube diameter d_i and a heated length L_{heat} For an optimum system with a large heat transfer coefficient α, the transferred heat is large, and the temperature difference from the wall to the bulk is small, and hence, wall temperature limits justified by the technical design and the material properties are not exceeded. The heat transfer coefficient is therefore the key parameter for the design and evaluation of a technical heat transfer system. The convective heat transfer in relation to the heat conduction of the fluid is described by the dimensionless Nusselt number Nu.

$$Nu = \frac{\alpha \cdot d_i}{\lambda_b} \tag{2.3}$$

Using dimensionless numbers, the conditions in different flow geometries or different working fluids can be compared. The inner diameter d_i of the round tube is the characteristic length. There are multiple empirical correlations, which can be used to predict the heat transfer in any technical system, which will be shown for the case of heat transfer to fluids under supercritical pressure conditions later. In general, those correlations are taking the Reynolds number Re and the Prandtl number Pr into account.

$$Re = \frac{F_{inertia}}{F_{viscous}} = \frac{\rho u d_i}{\mu} = \frac{G d_i}{\mu} \tag{2.4}$$

$$Pr = \frac{c_p \mu}{\lambda} \tag{2.5}$$

The Reynolds number is a dimensionless number, which is defined as the ratio of inertia forces to viscous forces and is therefore a measure for the turbulence of a flow. Generally, convective heat transfer increases with stronger turbulence. The Prandtl number is a dimensionless parameter, which characterizes the relative thickness of the momentum boundary layer to the thermal boundary layer in a flowing fluid. It is defined as the ratio of momentum diffusivity to thermal diffusivity. In equation 2.4, G is the mass flux, which is defined as the mass flow rate $\dot{m}$ per cross-flow area A_{flow} of the tube, which is often used for a better comparability in between different experimental setups or systems:

$$G = \frac{\dot{m}}{A_{flow}} = \frac{4 \cdot \dot{m}}{\pi \cdot d_i^2} \tag{2.6}$$

Convective heat transfer can be distinguished in between forced convection, in which the flow is driven by external forces like wind over a plate or a flow driven by a coolant pump, and natural convection, which is driven by local density differences in a fluid, which is caused by local temperature differences. In general, the density of a fluid decreases, when the temperature increases, resulting in a motion of the fluid caused by the buoyancy force. On the other hand, the viscous force in the fluid damps that motion. The relation of those two forces, multiplied by the ratio of the inertia force to the viscous force is expressed by the non-dimensional Grasshof number Gr:

$$Gr = \frac{F_{buoyancy}}{F_{viscous}} \cdot \frac{F_{inertia}}{F_{viscous}} = \frac{(\rho_b - \rho_w) \cdot g \cdot d_i^3}{\rho_b \cdot \nu_b^2} \tag{2.7}$$

For given flow conditions, it can be estimated if forced convection or natural convection is present, or in other words, if buoyancy effect on the flow can be neglected or not, using the non-dimensional Richardson number Ri. It is defined as the ratio of buoyancy force to the inertia force and can be calculated based on the Reynolds number Re and the Grasshof number Gr:

$$Ri = \frac{F_{buoyancy}}{F_{inertia}} = \frac{Gr}{Re^2} \tag{2.8}$$

For $Ri << 1$, buoyancy can be neglected, for $Ri >> 1$, the flow is clearly affected by buoyancy and for $Ri \approx 1$, mixed convection is present, which means some effect of buoyancy on the flow is present.

2.2.1.1 Heat transfer improvement and deterioration

Heat transfer to fluids at supercritical pressure is a complex phenomenon due to the variation of thermophysical properties. In the open literature, for example, in (Pioro et al., 2004), the heat transfer under supercritical pressure conditions is divided into 3 different modes, the normal heat transfer (NHT), the deteriorated heat transfer (DHT) and the improved heat transfer (IHT). However, there is still no clear definition of the terms DHT and especially IHT. Generally, it is distinguished in between the different heat transfer regimes by comparison with the normal heat transfer conditions. For a turbulent flow in a circular tube, the Dittus-Boelter equation is well accepted as a reference for NHT (Dittus & Boelter, 1930), (Winterton, 1998):

$$Nu = 0.023 \cdot Re^{0.8} \cdot Pr^{0.4} \tag{2.9}$$

According to the explanations given in (Cheng & Schulenberg, 2001), in Figure 2.4 (a), the heat transfer coefficient (HTC), obtained by the Dittus-Boelter equation 2.9 for water flowing in a circular tube with an inner diameter of 4 mm, mass flux of 1100 kg/m²s and heat flux of 800 kW/m², at a pressure of 25 Mpa, is shown. It can be seen that the heat transfer coefficient increases drastically close to the pseudocritical temperature, because of the variation of the thermophysical properties, and drops down again when the pseudocritical temperature is exceeded. However, it is common knowledge that the heat transfer coefficient under supercritical pressure conditions deviates from that predicted by the Dittus-Boelter equation, particularly at high heat fluxes and low mass fluxes. In Figure 2.4 (b) the ratio from the heat transfer coefficient to the HTC predicted by the Dittus-Boelter equation is shown schematically for a small and for a large heat flux. At supercritical pressure conditions, the HTC can deviate significantly from classical correlations, such as the Dittus-Boelter equation. For low heat fluxes (not approaching to zero), the HTC is often higher than predicted - a phenomenon commonly referred as *improved heat transfer*. In contrast, at high heat flux, a reduction in HTC to significantly lower values as predicted by the Dittus-Boelter equation can occur, known as *deteriorated heat transfer*. These terms describe observed deviations in heat transfer performance, but they do not correspond to distinct physical mechanisms such as boiling under subcritical conditions. Rather, they reflect the complex interplay of fluid property variations, buoyancy and flow acceleration near the pseudo-critical point.

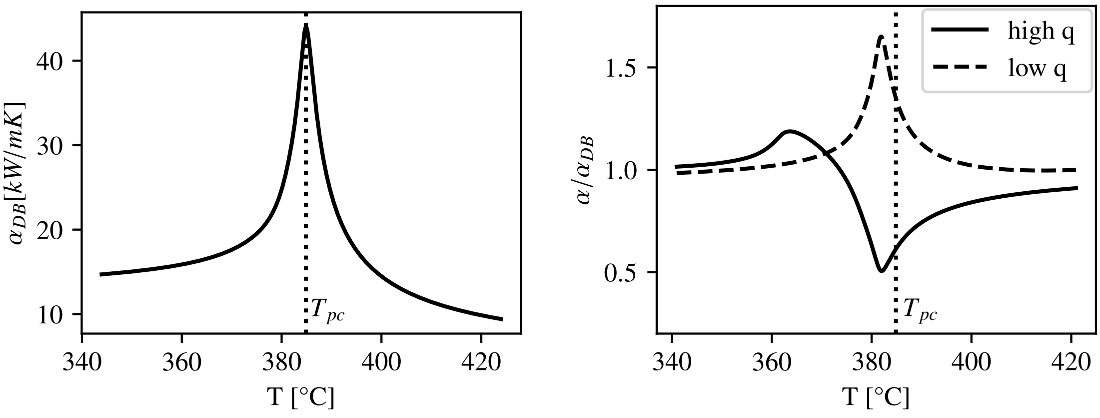

(a)

(b)

Figure 2.4: Heat transfer coefficient obtained by (a) Dittus Boelter equation and (b) deviation of heat transfer

An example is given by the experimental results of (Yamagata et al., 1972), presented in Figure

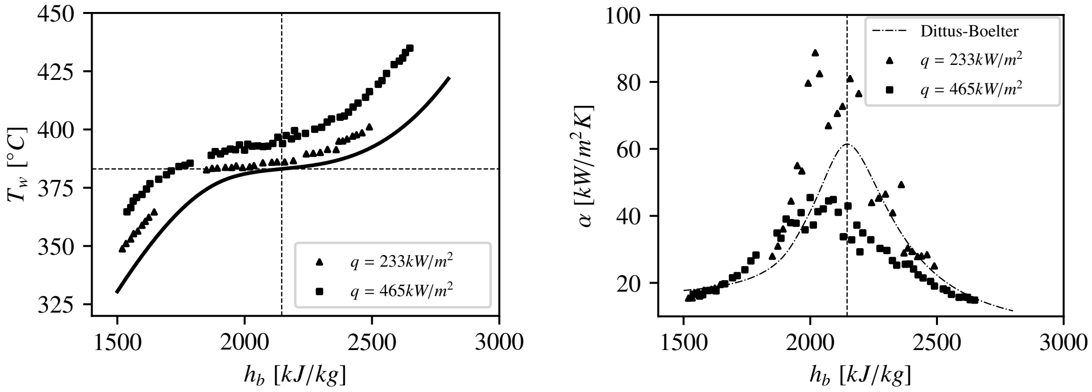

(a)

(b)

Figure 2.5: Trends of (a) wall temperature and (b) heat transfer coefficient for p=24.5 MPa, G=1260 kg/m²s and d=7.5 mm (Yamagata et al., 1972)

2.5. Yamagata referred to these cases as experiments with low heat flux. Towards the pseudocritical point, which is marked by the dashed line, for both of the cases presented in the figure, the heat transfer coefficient increases. In the case of the lower heat flux, the measured heat transfer coefficients are also clearly larger than the prediction of the Dittus-Boelter equation. This is what is called IHT in the literature. For the larger heat flux, the heat transfer coefficient also increases significantly towards the pseudocritical point but is well below the prediction of the Dittus-Boelter equation. One could still argue that heat transfer is improved here, as it is increasing.

In the open literature, the focus is clearly on the heat transfer deterioration, since DHT is critical for the design of technical systems. This phenomenon is more relevant for technical applications, since sharp temperature peaks may appear on heat transfer surfaces, which is a challenge in the design of heat transfer systems under supercritical pressure conditions. Figure 2.6 shows the wall temperature distribution schematically for large and small heat flux, where for the large heat flux the typical wall temperature peak due to heat transfer deterioration can be observed. However, there is no clear definition of heat transfer deterioration as well. Generally accepted is that a lower heat transfer coefficient compared to the one predicted by equation 2.9 means that the heat transfer is deteriorated. A very widely used criterion was proposed by (Koshizuka et al., 1995):

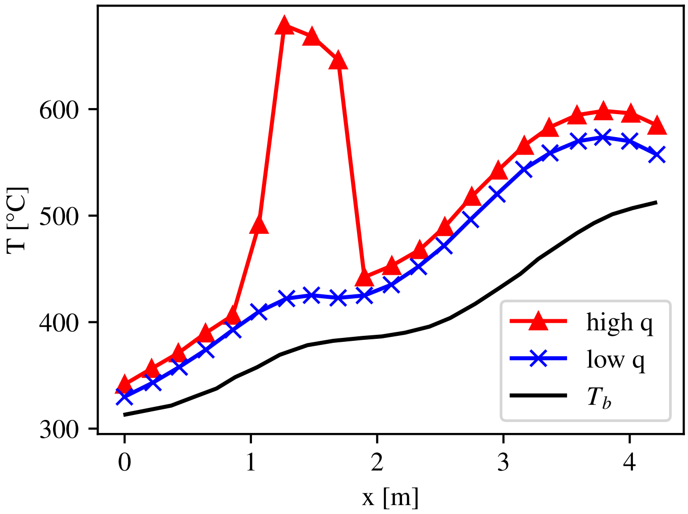

Figure 2.6: Schematically distribution of wall temperature for NHT and DHT (Cheng & Schulenberg, 2001)

$$\frac{\alpha}{\alpha_{NHT}} < 0.3 \tag{2.10}$$

This criterion was used, e.g., by (W. Chen & Fang, 2014), (M. F. Löwenberg, 2007), (Kunik, 2012), (Cheng et al., 2009b), (Cheng & Schulenberg, 2001) and many more. On the other hand, many authors are detecting peaks in the wall temperature of the test section to identify DHT. (Ackerman, 1970) defines "unusual performance" as a sudden decrease in the heat transfer coefficient and calls the phenomenon *pseudo boiling*. However, the term pseudo-boiling should be viewed critically as, unlike boiling, it is not an abrupt, clearly distinguishable phenomenon. In addition (Lee & K.H.Haller, 1974), (B. Zhu et al., 2020), (Licht et al., 2008) and (J. Chen et al., 2022) detect wall temperature peaks to detect DHT. At the current state of the art, there is generally no agreement on a certain definition of a wall temperature peak, but at least there is some common basis: (B. Zhu et al., 2020) define a peak as an overshoot of the temperature line over an imaginary normal heat transfer reference line, and the overshoot must be $\Delta T > 8K$. In (J. Chen et al., 2022), the criterion is also $\Delta T > 8K$. (Licht et al., 2008) handled it more strict and defined any small localized increase in wall temperature as DHT. In addition, Kurganov et al. (V. Kurganov et al., 2012), (V. Kurganov et al., 2013a), (V. Kurganov et al., 2013b), (V. Kurganov et al., 2014), (V. A. Kurganov et al., 2016) classified heat transfer deterioration into six different groups, according to the trends of wall temperature and the acting forces of buoyancy and acceleration.

In the present work, heat transfer is considered as deteriorated, if a temperature peak of $\Delta T >= 5K$ is detected, or, if the following criterion is fulfilled:

$$\frac{\alpha}{\alpha_G} = 0.7 \tag{2.11}$$

In equation 2.11, the normal heat transfer is represented by α_G, which is the prediction of the also well accepted Gnielinski correlation (Gnielinski, 1975). This correlation is chosen as a reference, since it considers the wall friction and therefore can be applied to tubes with rough inner surface as well.

In general, as already mentioned, DHT is more likely to occur when, at a given mass flux, the heat flux is large. As an example, the experimental results of (Shitsman, 1963), obtained for the mass flux of 430 kg/m²s are shown in Figure 2.7. For the smallest heat flux of 232 kW/m², NHT can be observed. Once the heat flux exceeds a certain limit, sharp wall temperature peaks are observed due to DHT. Many authors proposed correlations for the minimum heat flux $\dot{q}_{DHT}$, for which deterioration of the heat transfer occurs. Generally, the mass flux G is considered in those correlations, like in the early work of (Vikhref et al., 1967), which found the heat flux for with DHT

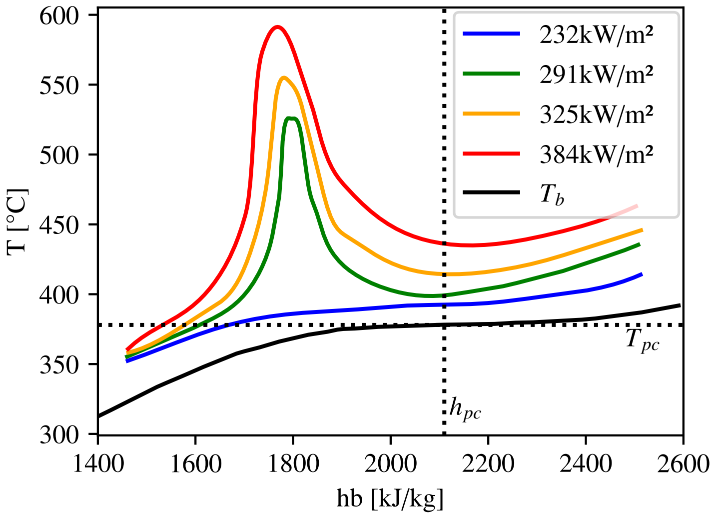

Figure 2.7: Experimental results from (Shitsman, 1963) using water at pressure of 23.3 MPa and mass flux of 430 kg/m²s

appears to be proportional to the mass flux:

$$\dot{q}_{DHT} = 0.4 \cdot G \tag{2.12}$$

In the experiments of (Vikhref et al., 1967), water was used as a working fluid. For other fluids, $\dot{q}_{DHT}$ may be significantly different. Even for the same fluid, (Styrikovich et al., 1967) found the heat flux for the onset of DHT to be:

$$\dot{q}_{DHT} = 0.58 \cdot G \tag{2.13}$$

All the other following equations for the onset of DHT are also for water. A linear dependency was found by (Mokry et al., 2011):

$$\dot{q}_{DHT} = -58.97 + 0.745 \cdot G \tag{2.14}$$

Other authors found the relationship between the mass flux G and the minimum heat flux q_{DHT} for which heat transfer deterioration occurs to be exponential, such as (Yamagata et al., 1972):

$$\dot{q}_{DHT} = 0.2 \cdot G^{1.2} \tag{2.15}$$

The correlation proposed by (Cheng et al., 2009b) additionally includes the effect of the pressure, using the ratio of the specific heat $c_{p,pc}$ and the thermal expansion coefficient β_{pc} in the pseudocritical point:

$$\dot{q}_{DHT} = 1.354 \cdot 10^{-3} \cdot \frac{c_{p,pc}}{\beta_{pc}} G \tag{2.16}$$

The more recently developed correlation of (Schatte et al., 2016) additionally takes the inner tube diameter d_i into account:

$$\dot{q}_{DHT} = 1.942 \cdot G^{-6} \cdot G^{0.795} \cdot (30 - d_i)^{0.339} \cdot \left(\frac{c_{p,pc}}{\beta_{pc}} \right)^{2.065} \tag{2.17}$$

Another correlation, taking pressure and, included in the Reynolds number, the viscosity and hydraulic diameter into account, was proposed by (Kondrat'ev, 1969):

$$\dot{q}_{DHT} = 5.815 \cdot 10^{-17} \cdot Re^{1.7} \cdot \left(\frac{p}{1.01325} \right)^{4.5} \tag{2.18}$$

In the paper of (Schatte et al., 2016), further correlations are given, which implicitly depend on the heat flux. In addition to correlations which can be applied directly to calculate the minimum heat flux for which DHT occurs, some authors proposed non-dimensional numbers for the evaluation of the heat transfer mode. For instance (Protopopov et al., 1973):

$$K = \frac{C\,(\rho_b - \rho_w)^4 \rho_b Pr_b}{\mu_b G \sqrt{c_f} \left(\frac{Gr}{Re^3} \right)^{0.23}} \tag{2.19}$$

For $K > 1.35 \cdot 10^4$, DHT occurs. The coefficient C was determined for water as $C = 8 \cdot 10^{-14}$ and for carbon dioxide as $C = 1 \cdot 10^{-14}$. Another non-dimensional parameter was proposed by (Kirillov et al., 1990) (from (Q. Zhang et al., 2018)):

$$k^* = \left(1 - \frac{\rho_w}{\rho_b}\right) \frac{Gr}{Re} \tag{2.20}$$

For $0.01 < k^* < 0.4$, DHT occurs.

2.2.1.2 The effect of buoyancy

J.D. Jackson significantly contributed to the theoretical description of the effect of buoyancy on heat transfer to supercritical pressure fluids, publishing many different papers on this phenomenon. The effect of buoyancy on heat transfer can be detected when the results of upward and downward flows in vertical or inclined tubes are compared (J. Jackson & Hall, 1979). Figure 2.8 exemplary shows the results of (J. D. Jackson et al., 1989), for supercritical pressure carbon dioxide at $p = 7.58\ MPa$, $\dot{q}_w = 56.9\ kW/m^2$ and inlet Reynolds number $Re_0 = 1.13 \cdot 10^5$ in a vertical tube with $d_i = 19\ mm$. While for the downward flow, NHT is present, for the upward flow, clearly DHT is present. In (W. Hall & Jackson, 1969), partial laminarisation of the flow is mentioned as the reason for the DHT in upward flow in a vertical tube. In (J. D. Jackson et al., 1989), several similar experimental works are listed, which have been carried out in the USSR, in which the results of upward and downward flows have been compared, as well as the work of (Bourke et al., 1970), in all of which the effect of buoyancy became apparent. In (J. Jackson & Hall, 1979), the following criteria for negligible buoyancy is given:

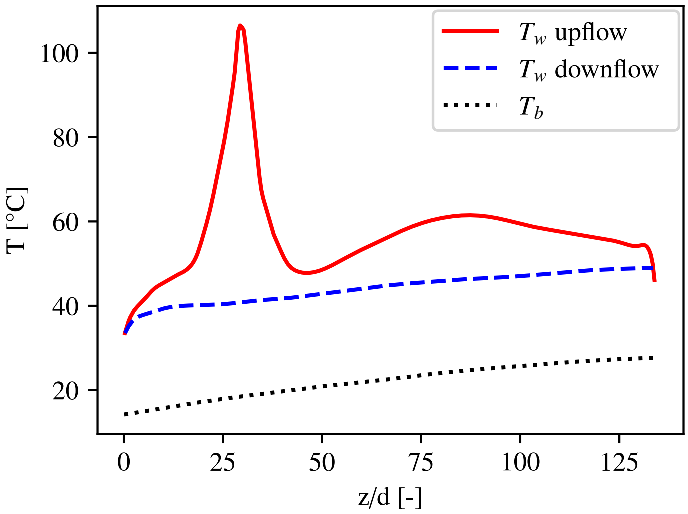

Figure 2.8: Experimental wall temperature for upward and downward flow at $p = 7.58\ MPa$, $\dot{q}_w = 56.9\ kW/m^2$, $Re_0 = 1.13 \cdot 10^5$ *and* $d_i = 19\ mm$ *(J. D. Jackson et al., 1989)*

$$Bu = \frac{\overline{Gr_b}}{Re_b^{2.7}} < 10^{-5} \tag{2.21}$$

with

$$\overline{Gr_b} = \frac{(\rho_b - \overline{\rho})\, g d_i^3}{\rho_b \nu_b^2} \tag{2.22}$$

and

$$\overline{\rho} = \frac{1}{T_w - T_b}\int_{T_b}^{T_w} \rho dT \tag{2.23}$$

In (J. Jackson, 2013), it is stated that equation 2.21 is valid for conditions where the wall temperature exceeds the pseudocritical temperature. Additionally, for conditions with wall temperatures below the pseudocritical temperature, the following criteria was added, for which the buoyancy effect on the heat transfer is smaller than 5%:

$$Bu = \frac{\overline{Gr_b}}{Re_b^{2.7} Pr^{0.5}} < 10^{-5} \tag{2.24}$$

As mentioned above, the DHT is caused by local laminarisation of the flow. The turbulence of a flow is generated by the shear stress in the turbulent boundary layer. Based on the variation of the shear stress distribution in the thermal boundary layer, due to variations in the density which cause buoyancy effects, (D. E. Kim & Kim, 2010) derived a dimensionless parameter for the buoyancy effect on the heat transfer:

$$\Delta\tau_{bu} = (\rho_b - \overline{\rho})\, g\delta_T \tag{2.25}$$

, in which δ_T is the thickness of the thermal boundary layer and g the gravitational constant. The buoyancy parameter Bu_K is finally given as the ratio of the shear stress reduction due to buoyancy $\Delta\tau_{bu}$ and the wall shear stress τ_w:

$$Bu_K = \frac{\Delta\tau_{bu}}{\tau_w} = C\frac{Gr_q}{Re_b^{3.425} Pr_b^{0.8}}\left(\frac{\mu_w}{\mu_b}\right)\left(\frac{\rho_b}{\rho_w}\right)^{0.5} \tag{2.26}$$

Here, Gr_q is the Grashof number based on the heat flux:

$$Gr_q = \frac{\dot{q}_w g \beta_b d_i^4}{\lambda_b \nu_b^2} \tag{2.27}$$

(D. E. Kim & Kim, 2010) used the non-dimensional parameter Bu_K in a Nusselt correlation which they proposed. (J. Jackson, 2013) gives a similar definition, together with a threshold value, under which the effect of buoyancy can be neglected:

$$Bu_{J2} = \left(\frac{Gr_b}{Re_b^{2.7}}\right)\left(\frac{\mu_w}{\mu_b}\right)\left(\frac{\rho_w}{\rho_b}\right)^{0.5} \approx 10^{-4} \tag{2.28}$$

In addition, a similar definition of the buoyancy parameter can be found in (Liu et al., 2017a).

Finally, (J. Jackson, 2017) derived a semi empirical model for the influence of the buoyancy on the heat transfer, which is given in implicit form:

$$\left(\frac{Nu_B}{Nu_F}\right)\left(\frac{F_{VP_3}}{F'_{VP_3}}\right) = \underbrace{\left[\left|1 \mp (CBuF_{VP,B})\left\{\left(\frac{Nu_B}{Nu_F}\right)\left(\frac{F_{VP_3}}{F'_{VP_3}}\right)\right\}^{-2.1}\right|\right]^{0.45}}_{\Psi_{Bu}(CBuF_{VP,B})} \tag{2.29}$$

All of the different F_{VP} factors are factors that take into account variations in thermophysical properties and can be viewed in the given reference. The definition of Bu in equation 2.29 is given in equation 2.24. Nu_F denotes the Nusselt number under forced convection conditions, while Nu_B is the Nusselt number for a flow with buoyancy effect. Since the term $\left(\frac{Nu_B}{Nu_F}\right)\left(\frac{F_{VP_3}}{F'_{VP_3}}\right)$ is only a function of the parameter $(CBuF_{VP_B})$, it is written as a function $\Psi_{Bu}\left(CBuF_{VP_B}\right)$. Now, assigning a series of values to $\left(\frac{Nu_B}{Nu_F}\right)\left(\frac{F_{VP_3}}{F'_{VP_3}}\right)$, the corresponding values of $(CBuF_{VP_B})$ can be calculated. Figure 2.9 (a) shows the predictions of the model. It can be seen that, for downward flow, heat transfer is predicted to be improved when buoyancy is present. For upward flow, with an increasing effect of buoyancy, heat transfer changes slightly, until it reaches a rapid decrease around $(CBuF_{VP_B}) \approx 0.2$, meaning the models predicts strong DHT for that value of $(CBuF_{VP_B})$, with a local minimum at $(CBuF_{VP_B}) = 0.26$. From this point on, for an increasing effect of buoyancy, the model predicts a recovery of heat transfer, until heat transfer is even improved for very large values of $(CBuF_{VP_B})$. Unfortunately, in (J. Jackson, 2017), no assessment of the model with experimental data was shown. Therefore, data from (J. D. Jackson et al., 1989), is compared to an earlier version of the model in 2.9 (b).

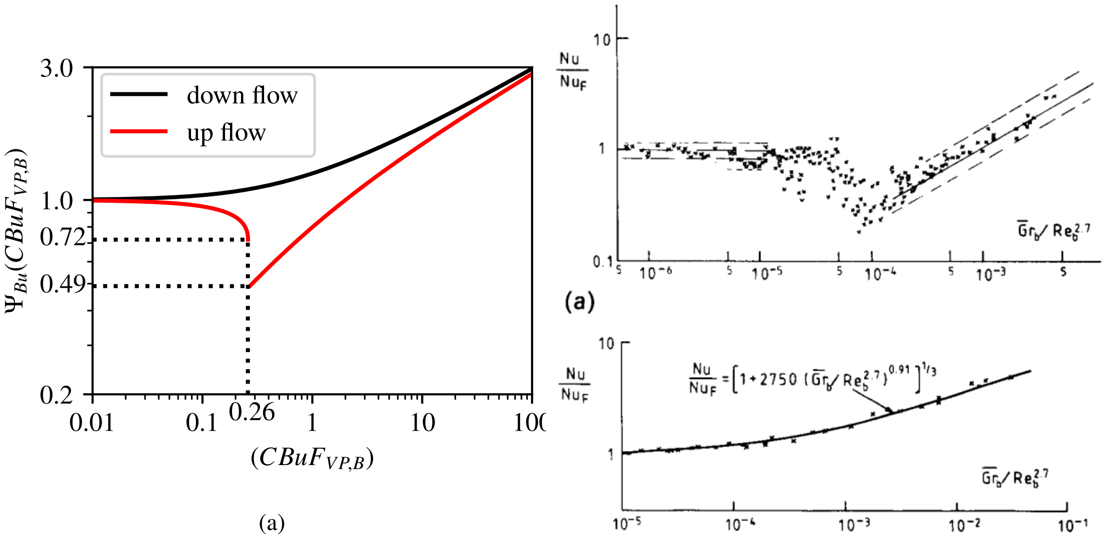

(a)

(b)

Figure 2.9: Variation of heat transfer due to buoyancy (a) predicted by Jackson Model and (b) experimental results (J. D. Jackson et al., 1989)

2.2.1.3 The effect of thermally induced flow acceleration

Compared to the buoyancy effect, which is caused by gravity and the lower density close to the wall, due to heating, the acceleration effect is caused by the increase in the bulk temperature, resulting in a lower bulk flow density. The reduction of the density must result in a larger velocity of the fluid, since the volume of the fluid expanses, hence the flow is accelerated. To accelerate the fluid, an additional axial pressure gradient is required. This acceleration does not happen uniformly across the flow. In the core region, where the velocity is already high, the fluid responds more directly to the pressure gradient. However, near the tube wall the velocity is much lower because of viscous effects. Since the pressure gradient acts equally at all points across the tube's cross-section, the near-wall fluid experiences a force that is greater than what is needed to match the acceleration of the bulk flow. However, because of viscosity, this excess force does not translate into a proportional increase in velocity. Instead, it alters the velocity profile, requiring an adjustment in the shear stress distribution across the near-wall layer. One consequence of this adjustment is that the shear stress at the outer edge of the boundary layer decreases compared to the case without bulk flow acceleration. This reduction in shear stress leads to less turbulence generation, which in turn impairs heat transfer efficiency (J. Jackson, 2013), (J. Jackson, 2017). The criterion for which acceleration effects on the heat transfer can be neglected is given by (J. Jackson, 2013) as:

$$Ac_b = \frac{Q_b}{Re_b^{1.625} Pr_b} < 4 \cdot 10^{-6} \tag{2.30}$$

with

$$Q_b = \frac{\dot{q}_w \beta_b d_i}{\lambda_b} \tag{2.31}$$

, where β is the isobaric thermal expansion coefficient. (D. E. Kim & Kim, 2010) derived a similar non-dimensional parameter, based on the reduction of the shear stress in the boundary layer:

$$\Delta\tau_{ac} = \rho_b u_b \frac{du_b}{dx} \delta_{ac} \tag{2.32}$$

The final nondimensional parameter is given as the ratio of the reduction of the shear stress in the boundary layer due to acceleration $\Delta\tau_{ac}$ and the wall shear stress τ_w:

$$Ac_{b,KK} = C \frac{q^+}{Re_b^{0.625}} \left(\frac{\mu_w}{\mu_b}\right) \left(\frac{\rho_b}{\rho_w}\right)^{0.5} \tag{2.33}$$

with the dimensionless heat flux

$$q^+ = \frac{\dot{q}_w}{G} \frac{\beta_b}{c_{p,b}} \tag{2.34}$$

(D. E. Kim & Kim, 2010) do not give a threshold value for which acceleration effects can be neglected, but they applied the non-dimensional parameter in 2.33 to their Nusselt correlation, together with the buoyancy parameter in 2.26. A similar non-dimensional parameter was derived by (Liu et al., 2017a).

Similar to the model for the effect of buoyancy in equation 2.29, (J. Jackson, 2017) derived an implicit model for the effect of bulk flow acceleration on the heat transfer, which is given by:

$$\left(\frac{Nu_A}{Nu_F}\right)\left(\frac{F_{VP_3}}{F'_{VP_3}}\right) = \underbrace{\left[1 - (C_A Ac_b F_{VP_A}) \left\{\left(\frac{Nu_A}{Nu_F}\right)\left(\frac{F_{VP_3}}{F'_{VP_3}}\right)\right\}^{-1.1}\right]^{0.45}}_{\Psi_{Ac}(C_A Ac_b F_{VPA})} \tag{2.35}$$

Here, Nu_A is the Nusselt number of flow in which acceleration effects on the heat transfer are present, which is put into relation to the Nusselt number Nu_F for a forced convection flow in which acceleration effects can be neglected. The factors F_{VP} take into account the variation of thermophysical properties and Ac_b is given in equation 2.30. $\left(\frac{Nu_A}{Nu_F}\right)\left(\frac{F_{VP_3}}{F'_{VP_3}}\right)$ is only depending on $(C_A Ac_b F_{VP_A})$, thus it can be written as the function $\Psi_A\left(C_A Ac_b F_{VP_A}\right)$. The assignment of values to

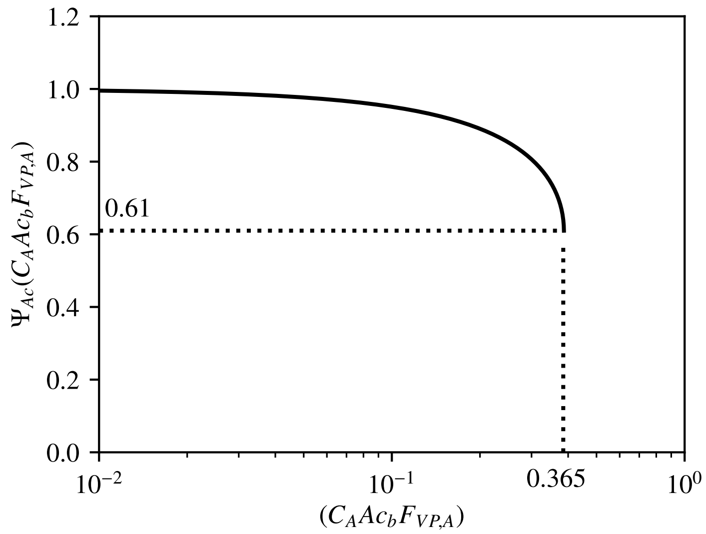

Figure 2.10: Variation of heat transfer due to flow acceleration according to model of (J. Jackson, 2017)

$\left(\frac{Nu_A}{Nu_F}\right)\left(\frac{F_{VP_3}}{F'_{VP_3}}\right)$ and the calculation of the corresponding values of $(C_A Ac_b F_{VP_A})$ yields Figure 2.10. The model predicts a slight impairment of the heat transfer for the increasing acceleration effect, with a relatively sharp decrease of around $(C_A Ac F_{VP}) \approx 0.3$ and at $(C_A Ac F_{VP}) = 0.365$ the flow is considered totally laminarised.

2.2.1.4 Combined effect of buoyancy and bulk flow acceleration

Both, the buoyancy effect and the acceleration effect are caused by density variations, the first in the near wall region and the latter in the core region of the flow. It is therefore obvious that the effects can also appear together. (J. Jackson, 2017) derived a implicit model for the combined effect of buoyancy and acceleration, based on the following equation:

$$\Delta\tau_{BA} = \left[\rho_b u_b \frac{du_b}{dx} \mp (\rho_b - \overline{\rho})\right] \delta_T \tag{2.36}$$

The model is given by:

$$\begin{aligned}\left(\frac{Nu_{BA}}{Nu_F}\right)\left(\frac{F_{VP_3}}{F'_{VP_3}}\right) = \Bigg[1 &\mp (C_B Bu F_{VP_B})\left\{\left(\frac{Nu_{BA}}{Nu_F}\right)\left(\frac{F_{VP_3}}{F'_{VP_3}}\right)\right\}^{-2.1} \\ &- r\,(C_B Bu F_{VP_B})\left\{\left(\frac{Nu_{BA}}{Nu_F}\right)\left(\frac{F_{VP_3}}{F'_{VP_3}}\right)\right\}^{-2.1}\Bigg]^{0.45}\end{aligned} \tag{2.37}$$

with

$$r = \frac{8Q_b}{Ga_b Re_b^{0.8} Pr_b} \tag{2.38}$$

in which Ga_b is the Galilei number, which expresses the ratio of gravitational to viscous forces:

$$Ga_b = \frac{gd_i^3}{\nu_b^2} \tag{2.39}$$

$\left(\frac{Nu_{BA}}{Nu_F}\right)\left(\frac{F_{VP_3}}{F'_{VP_3}}\right)$ can be regarded as a function $\Phi_{BA}\left(C_B Bu F_{VP_B}\right)$ and can be evaluated for different values or r. Figure 2.11 shows the predictions of the model for $r = 0$, 0.5, and 0.8. Obviously, for $r = 0$, the result must be the same as for the pure buoyancy model, as shown in Figure 2.9. For upward flow, an additional acceleration effect leads to deterioration of heat transfer, shifted to lower values of $(C_B Bu F_{VP_B})$. For $r = 0.8$, the strongest deterioration is shifted to $(C_B Bu F_{VP_B}) = 0.14$, compared to $(C_B Bu F_{VP_B}) = 0.26$ for $r = 0$. For downward flow, the improvement of heat transfer is weakened as a result of the bulk flow acceleration effect. In summarizing Sections 2.2.1.2 to 2.2.1.4, it can be concluded that buoyancy influences heat transfer differently in upward and downward flows, primarily due to local laminarization in the upward direction, leading to DHT, while in downward flow, heat transfer may be improved. The acceleration effect can only have a deteriorating effect on heat transfer.

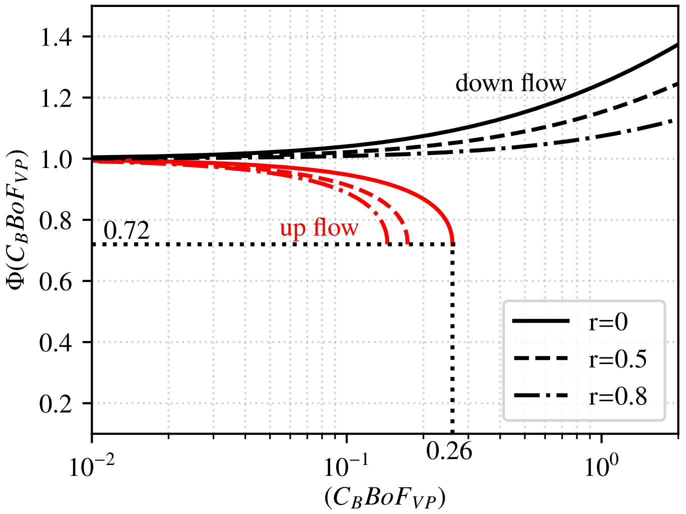

Figure 2.11: Variation of heat transfer due to combined effect of buoyancy and flow acceleration according to model of (J. Jackson, 2017)

2.2.2 Experimental investigations on heat transfer to fluids at supercritical pressure

(Pioro & Duffey, 2005) conducted an extensive survey of the experimental investigations conducted so far on heat transfer to water at supercritical pressure. The first reported experiments were conducted in the 1950s, such as (McAdams et al., 1950), (Randall, 1956) and (Dickinson & Welch, 1958). Increasing the thermal efficiency of fossil-fired power plants appears to be the motivation for the works carried out in that time period. In the former USSR, Shitsman conducted a large number of experimental investigations, published in (Shitsman, 1962), (Shitsman, 1963), (Shitsman, 1967), (Shitsman, 1968), and several more. Most of the experiments reported in (Pioro et al., 2004) have been conducted in circular tubes, mostly vertically oriented with upward flow, but also work with downward flows or horizontal orientation of the tube can be found. In addition, 5 experimental investigations with flow turbulizers are mentioned, (Kamenetskii, 1980), for instance. Further, 4 experiments which are conducted in annuli are reported, such as (Ornatskiy et al., 1972). Although a large number of experiments have been reported so far, not all of the data are publicly available. (M. F. Löwenberg, 2007) collected the experimental data points available for heat transfer to water at supercritical pressure and reported 9300 available data points by 2007. More recently, (T. R. J. Gschnaidtner, 2023) conducted experiments for the typical operating range of SCWRs.

Since the critical point of water is at a high pressure of $p = 22.064\ MPa$ and a high temperature of $T = 373.94\ °C$, construction and operation of such experimental facilities is expensive. Hence, the application of model fluids, which critical point is at much lower pressure and temperature are frequently applied. Common model fluids are carbon dioxide or the refrigerant R134a, which is also used in the present work. (Duffey & Pioro, 2005) performed a literature review of heat transfer experiments performed with supercritical pressure carbon dioxide. In the 1950s, (Bringer & Smith, 1957) chose CO_2 as working fluid due to its comparably low critical temperature and the fact that the thermophysical properties of that fluid were well established at that time. Among that early work, the survey presents a list of 27 experimental references on CO_2 flow in circular tubes, along with 4 references for experiments involving turbulence-enhancing inserts. More recently, the experimental investigations of (Y.-Y. Bae & Kim, 2009), (Mokry et al., 2009), (Zahlan, Groeneveld, & Tavoularis, 2015), (Eter et al., 2017) and (Kline, 2017) have to be mentioned, which mainly focus on buoyancy effects and the onset of DHT. Further, there are some experiments with R134a, such as (Kang & Chang, 2009), (S. Zhang et al., 2014), and especially to mention (Feuerstein, 2019), which was also conducted at the KIT Model Fluid Facility (KIMOF).

Recently, an extensive review of the literature on the experiments performed on rough walls was carried out by (Copping & Yaras, 2022). The number of experiments conducted at rough or transitionally rough conditions is very small, and among those, not all are revealing a description of the surface roughness. Instead, (Copping & Yaras, 2022) calculated the present surface roughness based on the pressure drop measurements. Table 2.1 gives an overview of some heat transfer experiments to supercritical pressure fluids at rough walls.

The experimental investigation of (Touba & McFadden, 1966) did not consider the surface roughness, but pressure drops under adiabatic conditions were published, allowing the surface roughness to be estimated. (Copping & Yaras, 2022) are comparing the results of (Touba & McFadden, 1966) with the experimental results of (Herkenrath, 1967), which have been performed under similar conditions, but with negligible effects of surface roughness. Figure 2.12 presents a comparison of the experimental results from (Touba & McFadden, 1966) (p = 22.8 MPa, G = 3400 kg/m²s, q = 590 kW/m²) and (Herkenrath, 1967) (p = 22.5 MPa, G = 3500 kg/m²s, q = 1200 kW/m²), which were digitized from (Copping & Yaras, 2022). In addition to the experimental data, the figure also includes the heat transfer coefficients and wall temperatures calculated using the correlation for smooth surfaces proposed by (V. Kurganov et al., 2013b). It is evident that the heat transfer coefficients measured by (Touba & McFadden, 1966) in a test section with a rough surface significantly exceed the calculated values—by more than 50%. In contrast, the heat transfer coefficients

Table 2.1: Heat transfer experiments with fluids at supercritical pressure at rough walls (Copping & Yaras, 2022)

Source	Working Fluid	Surface Roughness Characteristics
(Touba & McFadden, 1966)	Water	Not profiled. Estimated from pressure drop: $k_s/d \approx 7 \cdot 10^{-4}$
(Tanaka et al., 1971)	CO2	smooth tube: $k/d = 3 \cdot 10^{-5}$, rough tube: $k/D = 2 \cdot 10^{-3}$
(Niino et al., 1980)	Hydrogen	$k_s/d = 5 \cdot 10^{-5}$, $k_s/d = 5 \cdot 10^{-5}\ 1 \cdot 10^{-4}$, $k_s/d = 2 \cdot 10^{-3}\ 3 \cdot 10^{-3}$
(D. Wang, Dai, et al., 2019) & (D. Wang, Tian, et al., 2019)	R134a	micro-fin, $k/d = 0.015$
(J. Chen et al., 2022)	CO2	smooth tube: $k/d = 3.28 \cdot 10^{-4}$ $k/d = 2.19 \cdot 10^{-3}$ $k/d = 4.38 \cdot 10^{-3}$ $k/d = 6.56 \cdot 10^{-3}$ $k/d = 8.75 \cdot 10^{-3}$

measured by (Herkenrath, 1967) in a test section with a smooth pipe wall are lower than the predicted values. From this, (Copping & Yaras, 2022) conclude that surface roughness substantially enhances heat transfer. However, since the experimental data cannot be directly compared due to the differing heat fluxes, it becomes clear that there is still a lack of suitable experimental data to systematically investigate the influence of surface roughness on heat transfer under supercritical pressure conditions. In the report of (Copping & Yaras, 2022), some more cases are shown, but the number of data points available is limited.

In the experimental work of (Tanaka et al., 1971), two different tubes are used and the rough-

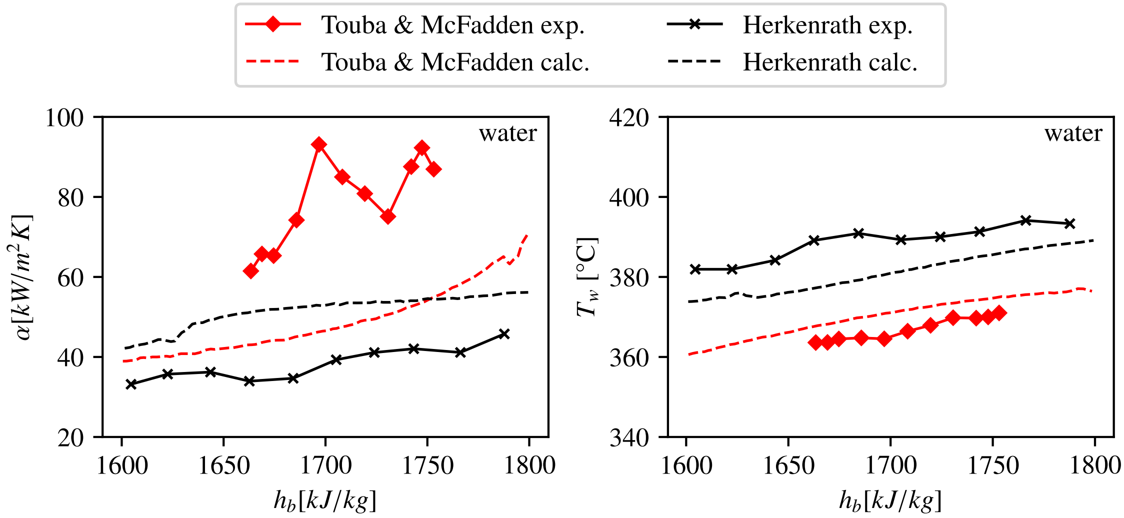

Figure 2.12: Comparison of the experimental results of (Touba & McFadden, 1966) (p=22.8 MPa, G=3400 kg/m²s, q=590 kW/m²) and (Herkenrath, 1967) (p=22.5 MPa, G=3500 kg/m²s, q=1200 kW/m²), digitized from (Copping & Yaras, 2022)

ness values are reported in the reference. Unfortunately, no further description of the reported values is given, besides the values of $k = 0.2\ \mu m$ and $k = 14\ \mu m$. Most likely, this is the mean roughness height R_a. The results show that heat transfer is generally enhanced by surface roughness and DHT is shifted to larger bulk enthalpies.

In the work of (Niino et al., 1980), the mean roughness height R_a was reported for three different tubes, called "fully rough" ($R_a = 4.2\ \mu m$) and "semi-rough" ($R_a = 0.25\ \mu m$ and $R_a = 0.55\ \mu m$). However, the scope of the work was not the investigation of the effect of the surface roughness on the heat transfer, and hence, no direct comparison of the heat transfer coefficient or wall temperature measurements are shown in between the different tubes.

Compared to all other experiments with rough surfaces, in the work of (D. Wang, Dai, et al., 2019) and (D. Wang, Tian, et al., 2019) instead of an irregular rough surface, a microfin tube is used, which is horizontally oriented and compared to a smooth tube. The working fluid in the experiments is R134a. The relative roughness k/D in these experiments is by far the largest among the investigations summarized here. However, this serves as a good example for strong surface roughness effects. Wang et al. found that the onset of buoyancy forces to have an impact on heat transfer is increased by factor 20 in the microfin tube, which means that the buoyancy force is heavily suppressed by the microfins. In the microfin tube in the investigated parameter range, the heat transfer coefficients are 1.68 times higher at the top site and 1.59 times higher at the bottom site of the tube, compared to the smooth tube.

The experimental work of (J. Chen et al., 2022) focuses on the effect of surface roughness on heat transfer. Five different tubes are used, with a roughness of $k = 1.5, 10, 20, 30$ and $40\ \mu m$. Again, no further description of the roughness is made, so it is assumed to be the mean roughness height R_a. The results show that heat transfer is generally enhanced with increasing surface roughness. Furthermore, the critical heat load (q/G) for the onset of DHT increased with increasing roughness and the maximum peak of wall temperatures is reduced for greater surface roughness. Additionally, a new correlation for heat transfer to supercritical pressure fluid, considering the surface roughness is proposed, which will be discussed in chapter 2.2.3.1. Some results are shown in Figure 2.13. However, the experimental campaign was limited to rather small mass fluxes, in the range of 300 to 500 kg/m²s, which is significantly lower than the flow conditions in a SCWR. Also, the ranges of inlet temperatures from 15 °C to 25 °C and of the heat flux, from 40 to 70 kW/m² are small.

In summary, there have been very few experimental studies on the effect of surface roughness on heat transfer to a fluid under supercritical pressure conditions. While the fundamental influence of surface roughness — namely, an improvement in heat transfer — is well understood for single-phase flow below the critical pressure, further research is needed to address the unique characteristics of heat transfer under supercritical conditions. Most previous studies have not directly examined the effect of roughness. In the most recent study of (J. Chen et al., 2022), roughness was explicitly investigated, but the flow parameter range differs from that relevant to SCWR applications. E.g. experimental data at larger mass flux is required. This study aims to bridge this gap and provide a reference for further research on heat transfer modifications resulting from corroded fuel rods.

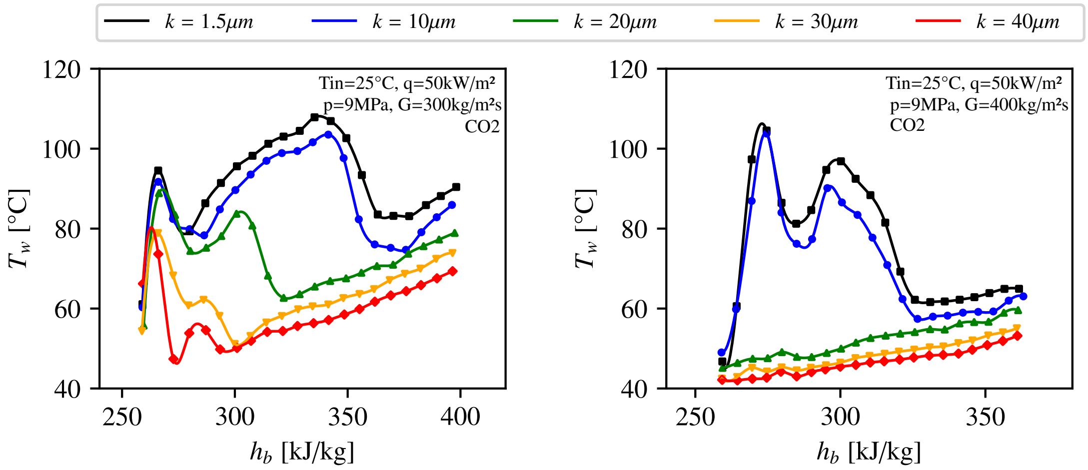

Figure 2.13: Measured wall temperatures for different surface roughness, digitized from (J. Chen et al., 2022)

2.2.2.1 Reproducibility of experiments

Heat transfer under supercritical pressure conditions is very sensitive to experimental boundary conditions. In the early work of (W. B. Hall et al., 1967), the experimental results of similar experimental conditions have been compared and a discrepancy between the measurements is reported. Under DHT conditions, the sensitivity to experimental boundary conditions becomes more significant. This sensitivity can be seen exemplarily in Figure 2.14 (a), where the results of (Feuerstein, 2019) from $p = 4.19\ MPa$ and $p = 4.23\ MPa$ are compared, for the same mass flux of $G = 500\ kg/m^2s$, the same heat flux of $\dot{q}_w = 40\ kW/m^2$ and the same inlet temperature of $T_{in} = 80\ °C$. The heat transfer coefficients are in good agreement far before the pseudocritical enthalpy and also after that point. However, there is a region before the pseudocritical point, in which the deviation is much larger than 50%. Thus, slight changes in the pressure, when the experiments are repeated, can have a considerable influence on the result. Furthermore, in (Feuerstein, 2019), the results he obtained at the Karlsruhe Institute of Technlogy (KIT) are also compared to results from the Shanghai Jiao Tong University (SJTU), which were obtained under similar conditions. An example is shown in Figure 2.14 (b). The experiments were all conducted at a mass flux of $G = 2000\ kg/^2s$ and a heat flux of $\dot{q}_w = 100\ kW/m^2$, but with slightly different inlet temperatures and pressures. Additionally, the KIT results are repeated, after post-dryout experiments have been performed in the same test section, which have led to deposits on the inner wall of the test tube. Although the conditions in the KIT and the SJTU experiment are quite similar, a huge deviation in the results is observed. The deposits on the inner wall of the tubes have a significant influence on heat transfer.

In (Zahlan, Groeneveld, & Tavoularis, 2015), experimental results of (Fewster & Jackson, 2004) have been reproduced. Here, excellent agreement was achieved. In addition, the results of (J. Song et al., 2008) have also been reproduced, where there are considerable discrepancies.

The examples mentioned here show that the reproducibility of the results obtained in this ex-

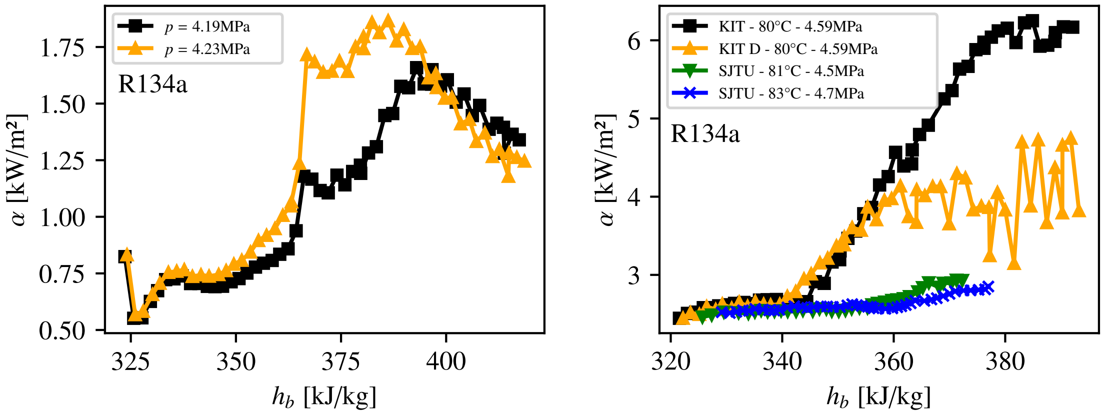

(a)

(b)

Figure 2.14: Repeated experiments with slightly varying pressure (a) and repeated experiments with slightly changed surface and compared to similar conditions in different experimental facility (b), digitized from (Feuerstein, 2019)

perimental investigation must be checked, which is done in the chapter 4.4.3.

2.2.3 Models for heat transfer prediction at supercritical pressure

As described in the previous sections, the heat transfer to fluids at supercritical pressure is, due to the variation of the thermophysical properties in the vicinity of the pseudocritical temperature, a very complex phenomenon. When the difference from wall temperatures to bulk temperatures is large, a strong variation of the fluid properties is present in the flow cross section. To the present day, no analytical solution to the problem of heat transfer to supercritical pressure fluids is known, and conventional correlations also fail. Nevertheless, a great amount of empirical correlations have been proposed so far which take into account the strong variation of the fluid properties. In addition to that, a semi-empirical model based on the two-layer theory was established (Laurien, 2016). On the other hand, methods based on available experimental data have been proposed, such as lookup tables (M. Löwenberg et al., 2007), or models based on machine learning (Wen et al., 2024). In the following, the different modeling approaches will be discussed in detail.

2.2.3.1 Empirical correlations

In the open literature, many reviews have been performed on empirical correlations for heat transfer under supercritical pressure conditions. Among those, the book of (Pioro & Duffey, 2007) is one of the most relevant, covering a large number of correlations. More recently, a state of the art report was published (Vasic et al., 2023), in which 194 different correlations are reported, making it the most complete review of correlations known to the author. Many evaluations of existing correlations have been performed, using experimental data, such as (Pioro et al., 2004), (H. Kim et al., 2006), (Y.-Y. Bae et al., 2010), (Y. Bae et al., 2011), (Zhalan et al., 2011), (W. Chen & Fang, 2014), (International Atomic Energy Agency (IAEA), 2014), (C. Wang & Li, 2014), (W. Chen et al., 2015), (Churkin et al., 2015), (Zhao et al., 2017), (Feuerstein, 2019), and (Z. Ye et al., 2022).

Considering the fact that the experimental data is very sensitive to small changes in the boundary conditions, as shown before and further, that the heat transfer under the given conditions is very complex, it is not surprising that all the existing empirical correlations only perform good in the range of parameters, for which they have been defined, and huge deviations in the predictions of different correlations are possible. Nevertheless, empirical correlations are still the standard in engineering. As summarized in (Vasic et al., 2023), the correlations have in common that they address one or more of the following points:

- Constant properties heat transfer
- Entrance effect correction factors
- Property variation correction factors
- Splitting by temperature/ enthalpy regions
- Buoyancy parameter
- Acceleration parameter
- Flow direction effect

Constant property correlations

Generally, Nusselt correlations for heat transfer to fluids under supercritical pressure conditions consist of a conventional term Nu_0, for constant property flows, and an additional term which takes into account the variation of thermophysical properties, or effects such as buoyancy or acceleration. Nu_0 is commonly formulated according to the Dittus-Boelter equation (Dittus & Boelter, 1930), (Winterton, 1998):

$$Nu_0 = C \cdot Re^m \cdot Pr^n \tag{2.40}$$

Besides that, the constant property correlation proposed by (Petukhov & Kirillov, 1958) is used frequently for Nu_0, here generally expressed as:

$$Nu_0 = \frac{\left(\frac{c_f}{8}\right) \cdot Re_1 \cdot Pr_1}{A + B \cdot \sqrt{\frac{c_f}{8}} \left(Pr_2^{2/3} - 1\right)} \tag{2.41}$$

In the same form, a correlation was also proposed by (Gnielinski, 1975), which further consists of a term for inlet effects. It has to be mentioned here, since this publication is famous for engineering applications. In equation 2.41, c_f is the wall friction coefficient. As shown later, the wall friction coefficient depends on the wall roughness. Thus, correlations of the Petukhof & Kirillov form are already addressing the wall roughness.

Entrance effect

The heat transfer can be significantly enhanced in the entrance region of a heated tube. To take that into account, in some correlations, an additional term is multiplied. There are different forms of the entrance effect, but all have in common that they are expressed as a function of the local distance z from the entrance, and the hydraulic diameter (inner diameter of the tube. Widely used is

$$F_e = \left[1 + c_1\left(\frac{d_i}{z}\right)\right] \tag{2.42}$$

, for example in the correlations proposed by (Bishop et al., 1965) or (Liu et al., 2017b). The similar form,

$$F_e = \left[1 + c_1\left(\frac{d_i}{z}\right)^{c_2}\right] \tag{2.43}$$

is used e.g. in (Gnielinski, 1975). In the correlation proposed in (Gupta et al., 2011), the correction factor for the entrance effect has an exponential form:

$$F_e = \left[1 + exp\left(c_1\left(\frac{d_i}{z}\right)\right)\right]^{c_3} \tag{2.44}$$

Property variation correction factors

When the temperature difference from the wall to the bulk flow is large, especially when the pseudocritical temperature is crossed, there is a strong variation of the thermophysical properties. For the evaluation of Nusselt correlations, thermophysical properties, such as the Prandtl number or the kinematic viscosity, to determine the Reynolds number, are required. For conventional single phase heat transfer applications, the fluid properties at the bulk temperature, or the film temperature $T_{film} = \frac{T_w+T_b}{2}$ are considered. However, due to the sharp variation of the fluid properties in the vicinity of the pseudocritical temperature, such an approach is not sufficient. In most of the heat transfer correlations for supercritical pressure conditions, the Nusselt number Nu_0 is calculated for the bulk properties and correction factors, based on the ratio of the thermophysical properties at wall and at bulk temperature are multiplied to it:

$$\left(\frac{\rho_w}{\rho_b}\right)^{n_1}, \left(\frac{\mu_w}{\mu_b}\right)^{n_2}, \left(\frac{\bar{c}_p}{c_{p,b}}\right)^{n_3}, \left(\frac{k_w}{k_b}\right)^{n_4} \tag{2.45}$$

Mostly, the ratio is formed from the wall temperature to the bulk temperature, but instead of the wall temperature, some authors, (H. Wang et al., 2014) for instance, also use the film temperature in their correction factors. Instead of the specific heat at wall temperature $c_{p,w}$, often the average specific heat $\overline{c_p}$ is used for the ratio of the specific heat capacity c_p, where the mean value is calculated as:

$$\bar{c}_p = \frac{h_w - h_b}{T_w - T_b} \tag{2.46}$$

, in which h_w and h_b are the enthalpy at wall and at bulk temperature respectively. Figure 2.15 shows different property variation ratios, exemplary for water at $p = 25\ MPa$, for a wall temperature 20 K higher than the bulk temperature, in the region around the pseudocritical temperature. It can be seen that the ratio c_p is the only one which can yield values larger than 1 (thus, also the ratio of the Prandtl number), while the application of any of the other correction factors would decrease the predicted heat transfer coefficient. In many correlations, some of the non-dimensional factors are combined. For instance the $\left(\frac{\bar{c}_p}{c_{p,b}}\right)$ and the $\left(\frac{\rho_w}{\rho_b}\right)$ are often used in combination, like in the correlations

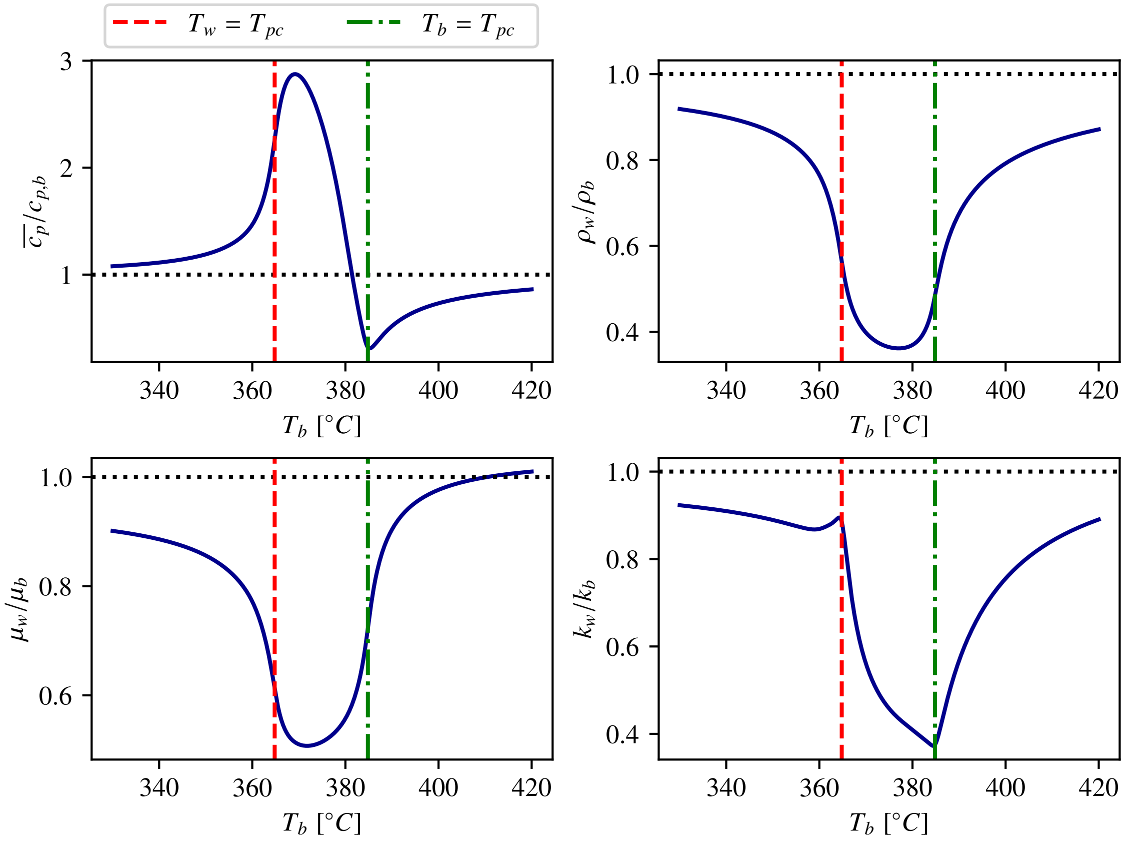

Figure 2.15: Different correction factors for the effect of varying thermophysical properties for water at 25 MPa and wall temperatures 20 K larger than the bulk temperature

proposed by (Kransoshchekov & Protopopov, 1966), (J. Jackson, 2008) and (Ghajar & Asadi, 1986). Some authors only use one dimensionless correction factor, like the $\left(\frac{\mu_w}{\mu_b}\right)$ (Sieder & Tate, 1936), (Petukhov & Kirillov, 1958) or $\left(\frac{\rho_w}{\rho_b}\right)$ (Bishop et al., 1965), (Swenson et al., 1965). In recently proposed correlations, the trend is to used more fluid property ratios. In (Pizzarelli, 2016), (Badea et al., 2018) and (J. Zhu et al., 2019), $\left(\frac{\rho_w}{\rho_b}\right)$, $\left(\frac{\mu_w}{\mu_b}\right)$, $\left(\frac{\bar{c}_p}{c_{p,b}}\right)$ and $\left(\frac{k_w}{k_b}\right)$ are used, making the correlations more complicated and hence more specific to the data used for the fitting of the coefficients and the exponents. Further, such correlations have the tendency to be less robust to the problem of no- or multi-solutions, which is explained later. Besides the ratio of the fluid properties at wall and at bulk temperature, also the ratio of the temperatures $\left(\frac{T_w}{T_b}\right)$ (Taylor, 1968), (Meyer, 1995), the ratio of the bulk temperature and the pseudocritical temperature $\left(\frac{T_b}{T_{pc}}\right)$ (Yang, 2013) or also the ratio of the pressure and the critical pressure $\left(\frac{p}{p_c}\right)$ (Yang, 2013), (Pizzarelli, 2016) are used by some authors.

Temperature and enthalpy regions

Since it is difficult to cover the entire enthalpy range with one correlation, some authors defined different correlations for different enthalpy regions. In the open literature, different approaches are common. (Kransoshchekov & Protopopov, 1966) defined 4 sub-regions, 1. for $T_b < T_w < T_{pc}$, which is the liquid-like region of supercritical fluids, having a high density, 2. for $T_b < T_{pc} < T_w$, which is in the transition region and the maximum of the specific heat is located in the flow cross section, 3. for $T_{pc} < T_b < 1.2T_{pc}$ and $T_b < T_w$, also in the transition region but with the bulk heat capacity decreasing from the maximum value and 4. for $1.2T_{pc} < T_b < T_w$, which is the gas-like region with low-density fluid. According to the enthalpy region, the exponent applied to the ratio $\left(\frac{\bar{c}_p}{c_{p,b}}\right)$ is varied. This approach is applied to the correlations proposed, for instance, by (Kransoshchekov & Protopopov, 1966), (J. Jackson, 2008), (Y. Bae et al., 2007), (H. Kim et al., 2008), and (V. Kurganov et al., 2013b).

Another method was proposed by (Bringer & Smith, 1957), who defined 3 sub regions, based on the Eckert number, which is defined as:

$$Ec = \frac{T_{pc} - T_b}{T_w - T_b} \tag{2.47}$$

The three regions are namely the liquid-like region for $Ec > 1$, where T_b is significantly lower than T_{pc}, the transition region for $1 \leq Ec \leq 0$, in which a significant drop of the density and a peak of the specific heat occurs and the gas-like region fro $Ec < 0$, where due to the bulk temperature significantly over T_{pc} low density fluid is present. This approach is applied in (Bringer & Smith, 1957) and (Yamagata et al., 1972). More approaches for the definition of different temperature/ enthalpy regions can be found in (Vasic et al., 2023).

Buoyancy parameter

In Section 2.2.1.2, different formulations for nondimensional parameters, describing the effect of buoyancy on heat transfer are introduced. Some authors, such as (Watts & Chou, 1982), (Liao & Zhao, 2002), (Y. Bae et al., 2007), (Kuang et al., 2008), (J. Jackson, 2008), (D. E. Kim & Kim, 2010), (W. Chen & Fang, 2014), (Liu et al., 2017a), (Liu et al., 2017b), (Cui & Wang, 2018), and (Q. Zhang et al., 2018), directly applied those parameters or similar parameters, based on the Grashof number or a combination of the Grashof number and the Reynolds number to their correlations. An overview can be found in (Vasic et al., 2023).

Acceleration parameter

Several correlations have been developed considering the effect of the acceleration of bulk flow, such as (Yu et al., 2008), (Kuang et al., 2008), (Saltanov et al., 2014), (Liu et al., 2017a), (Deev et al., 2017). Among all of those, the correlation proposed by (Cheng et al., 2009b) is outstanding, since the wall temperature T_w is not required and hence the iterative solution procedure can be avoided, for applications where the wall temperature is not known a priori. The correlations reads as:

$$Nu = 0.023 \cdot Re^{0.8} \cdot Pr^{1/3} \cdot F \tag{2.48}$$

$$F = min\left(F_1, F_2\right) \tag{2.49}$$

$$F_1 = 0.85 + 0.776\left(\pi_A \cdot 10^3\right)^{2.4} \tag{2.50}$$

$$F_2 = \frac{0.48}{\left(\pi_{A,pc} \cdot 10^3\right)^{1.55}} + 1.21 \cdot \left(1 - \frac{\pi_A}{\pi_{A,pc}}\right) \tag{2.51}$$

, in which π_A is the acceleration parameter, which is defined as (compare q^+, equation 2.34):

$$\pi_A = \frac{\beta}{c_p} \frac{q}{G} \tag{2.52}$$

Heat transfer correlations for application to smooth walls

The Nusselt correlations for heat transfer at supercritical conditions can be summarized as follows:

$$Nu = Nu_0 \cdot F_{VP} \cdot F_{Bu} \cdot F_{Ac} \cdot F_e \tag{2.53}$$

, addressing the constant property Nusselt number Nu_0, which is either based on the Dittus-Boelter equation (see equation 2.40) or on the Petukhov & Kirillov equation (see equation 2.41). In the appendix, a list of correlations can be found. Table 2.2 exemplary shows some correlations that are based on the Dittus-Boelter equation.

Table 2.2: Selected Nusselt correlations based on Dittus-Boelter equation

Author	C	Re	Pr	F_{VP}	F_{Bu}	F_{Ac}	F_e
A.3.1	0.027	$Re_b^{0.8}$	$Pr_b^{1/3}$	$\left(\frac{\mu_b}{\mu_w}\right)^{0.14}$	-	-	-
A.3.2	0.023	$Re_b^{0.8}$	$Pr_b^{0.4}$	$\left(\frac{T_b}{T_w}\right)^{0.3}$	-	-	-
A.3.3	0.0069	$Re_b^{0.9}$	$\overline{Pr}_b^{0.66}$	$\left(\frac{\rho_w}{\rho_b}\right)^{0.43}$	-	-	$\left(1 + 2.4\frac{d}{z}\right)$
A.3.4	0.00495	$Re_w^{0.923}$	$\overline{Pr}_w^{0.613}$	$\left(\frac{\rho_w}{\rho_b}\right)^{0.231}$	-	-	-
A.3.5	0.0183	$Re_b^{0.82}$	$\overline{Pr}_b^{0.5}$	$\left(\frac{\rho_w}{\rho_b}\right)^{0.3}$	-	-	-
A.3.6	0.534	$Re_b^{0.8}$	$Pr_b^{0.4}$	$\left(\frac{\rho_w}{\rho_b}\right)^{1.297}\left(\frac{\bar{c}_p}{c_{p,b}}\right)^{0.296}$	$\left(\frac{\overline{Gr}_b}{Re_b^{2.7}}\right)^{0.157}$	-	-
A.3.7	0.0239	$Re_b^{0.759}$	$\overline{Pr}_b^{0.833}$	$\left(\frac{\rho_w}{\rho_b}\right)^{0.31}\left(\frac{\mu_w}{\mu_b}\right)^{0.832}\left(\frac{k_w}{k_b}\right)^{0.863}$	$Gr_q^{0.014}$	$\pi_{Ac}^{-0.021}$	-
A.3.9	0.021	$Re_b^{0.8}$	$Pr_b^{0.4}$	$\left(\frac{\rho_w}{\rho_b}\right)^{0.3}\left(\frac{\bar{c}_p}{c_{p,b}}\right)^{n}$	-	-	-
A.3.10	0.004	$Re_w^{0.923}$	$\overline{Pr}_w^{0.773}$	$\left(\frac{\rho_w}{\rho_b}\right)^{0.186}\left(\frac{\mu_w}{\mu_b}\right)^{0.366}$	-	-	$\left[1 + exp\left(\frac{z}{1.5d}\right)\right]^{0.0648}$
A.3.11	2.0514	$Re_b^{0.928}$	$Pr_b^{0.742}$	$\left(\frac{\rho_w}{\rho_b}\right)^{1.305}\left(\frac{\mu_w}{\mu_b}\right)^{-0.669}\left(\frac{\bar{c}_p}{c_{p,b}}\right)^{0.888}$	-	$\pi_{Ac}^{0.792}$	-
A.3.12	α_1	$\mathrm{Re}_b^{\alpha_2}$	$Pr_b^{\alpha_3} Pr_w^{\alpha_4}$	$\left(\frac{\rho_w}{\rho_b}\right)^{\alpha_5}\left(\frac{\lambda_w}{\lambda_b}\right)^{\alpha_6}\left(\frac{\nu_w}{\nu_b}\right)^{\alpha_7}\left(\frac{c_{p,w}}{c_{p,b}}\right)^{\alpha_8}$	-	$\frac{\pi_{Ac}}{\pi_{Ac,pc}}$	-
A.3.13 (q)	0.023	0.8	1/3	F_2	-	F_1	-
A.3.13 (T)	0.023	0.8	1/3	$F_3 \cdot F_4 \cdot F_5$	-	-	-

Frequently, the Prandtl number appears to be an averaged Prandtl number, which is defined as (Vasic et al., 2023)

$$\overline{Pr}_b = \frac{\bar{c}_p \cdot \mu_b}{\lambda_b} \tag{2.54}$$

$$\overline{Pr}_w = \frac{\bar{c}_p \cdot \mu_w}{\lambda_w} \tag{2.55}$$

The Grashof number $\overline{Gr}_b$ is used e.g. by (Liao & Zhao, 2002), considering the integrated mean density ρ, which is integrated from the bulk temperature to the wall temperature (see equation 2.22), and further, the Grashof number based on the heat flux

$$Gr_q = \frac{g\beta_b q_w d^4}{\lambda_b \nu_b^2} \tag{2.56}$$

is used by (Kuang et al., 2008). Table 2.3 summarizes the correlations based on the Petukhov & Kirillov correlation. For further details, refer to the appendix.

Table 2.3: Selected Nusselt correlations based on Petukhov Kirillov equation

Author	A	B	Re	Pr_1	Pr_2	F_{c_f}	F_{VP}	F_e
A.2.1	1.07	12.7	Re_b	Pr_b	$Pr_b^{2/3}$	-	$\left(\frac{\mu_w}{\mu_b}\right)^{0.11}$	-
A.2.2	1.07	12.7	Re_b	Pr_b	$Pr_b^{2/3}$	-	$\left(\frac{\mu_w}{\mu_b}\right)^{-0.11}\left(\frac{\lambda_w}{\lambda_b}\right)^{0.33}\left(\frac{\bar{c}_p}{c_{p,b}}\right)^{0.35}$	-
A.2.3	1.07	12.7	Re_b	Pr_b	$Pr_b^{2/3}$	-	$\left(\frac{\rho_w}{\rho_b}\right)^{0.3}\left(\frac{\bar{c}_p}{c_{p,b}}\right)^{n}$	-
A.2.4	1.07	12.7	Re_w	Pr_w	$Pr_w^{2/3}$	-	$\left(\frac{\rho_w}{\rho_b}\right)^{n}\left(\frac{\bar{c}_p}{c_{p,w}}\right)^{m}$	-
A.2.5	1.07	12.7	Re_b	Pr_b	$Pr_G^{2/3}\frac{c_{p,b}}{c_{p,G}}$	-	-	-
A.2.6	1	12.7	$Re_b - 1000$	Pr_b	$Pr_b^{2/3}$	-	K	$\left[1+\left(\frac{d}{z}\right)^{2/3}\right]$
A.2.7	$1+\frac{900}{Re_b}$	12.7	Re_b	Pr_b	$\overline{Pr}_b^{2/3}$	$\left(\frac{\rho_w}{\rho_b}\right)^{0.4}\left(\frac{\mu_w}{\mu_b}\right)^{0.2}$	-	-
A.2.9	1.07	12.7	Re_b	Pr_b	$Pr_b^{2/3}$	$\left(\frac{\mu_w}{\mu_b}\frac{\rho_w}{\rho_b}\right)^{0.18}$	$\left(\frac{\bar{c}_p}{c_{p,b}}\right)^{0.65}$	-
A.2.11	1.07	12.7	$Re_b - 1000$	Pr_b	$Pr_b^{2/3}$	-	C_{vp}	$\left[1+\left(\frac{d}{z}\right)^{2/3}\right]$

Heat transfer correlations for rough walls

The correlations based on the Petukhov & Kirillov correlation can be applied to rough surfaces, since the friction factor c_f is used there. The dependency of the friction factor on the surface roughness will be shown in a later chapter. The number of correlations which directly consider the roughness is very small. All the correlations known to the author are addressed in the following.

The first work has been performed by (J. McCarthy et al., 1968), in the scope of rocket engine development, using hydrogen at supercritical pressure. The correlation is valid for large Reynolds numbers from 500.000 to 4.000.000 and for relatively small relative roughness of maximum $k_s/D = 0.0005$. The correlation is given by:

$$Nu_b = 0.025 Re_b^{0.8} Pr_b^{0.4} \left(\frac{T_w}{T_b}\right)^{-0.55} \left[1 + 1000\frac{k_s}{D}\left(log_{10} Re_b - 5.625\right)\right] \tag{2.57}$$

Another correlation was proposed by (Cook, 1984), where methane was used as experimental working fluid. Again, the Reynolds numbers in the corresponding experiments were comparably large, ranging from 820.000 to 3.800.000. The proposed correlation reads as:

$$Nu_b = \frac{0.4\left(\frac{c_f}{8}\right) Re_b Pr_b}{1 + \sqrt{\frac{c_f}{8}}\left[5.19 k_s^{0.2} Pr_b^{0.44} - 8.5\right]} \tag{2.58}$$

In both equations, k_s is the equivalent sand grain roughness, which will be explained in section 2.3. Both correlations do not consider the variations of the thermophysical properties. The correlation of McCarthy only addresses the ratio of the wall temperature to the bulk temperature. Thus, it can be expected that those correlations do not perform well under conditions with drastic variation in the fluid properties, e.g. close to the pseudocritical point. The latest proposed correlation in the other hand, is considering a very large number of different thermophysical properties (J. Chen et al., 2022):

$$Nu_b = 0.0107 Re_b^{0.838} \overline{Pr}_b^{0.815} \left(\frac{\overline{c}_p}{c_{p,b}}\right)^{0.18} \left(\frac{\rho_w}{\rho_b}\right)^{0.176} \left(\frac{\mu_w}{\mu_b}\right)^{1.03} \left(\frac{\lambda_w}{\lambda_b}\right)^{-0.455} \left(1 + \frac{S_z}{S_{z0}}\right)^{0.135} \tag{2.59}$$

In this correlation, S_z is the actual roughness and $S_0 = 1.5\ \mu m$ is the reference roughness, referring to the roughness of the smooth reference tube in the experiments on which the correlation is based on. It has to be pointed out, that there is no description of which roughness parameter exactly is given in the paper. The roughness of the investigated tubes is reported as 10, 20, 30, and 40 µm. Compared to the two previous correlations, the experiments used here are conducted at a comparably small Reynolds number, with a maximum of around 100.000.

No- and multi-solutions

As summarized in the previous section, the vast majority of correlations applicable to heat transfer to fluids under supercritical pressure conditions are taking the fluid properties at bulk temperature as well as at wall temperature into account, in order to address the strong variation in the thermo-physical properties. This is suitable for many thermal hydraulics system codes. However, in some system codes or engineering applications, the wall heat flux is known and the wall temperature needs to be predicted. Thus, an iterative solution procedure has to be applied, so that the following criterion is fulfilled:

$$\frac{q \cdot D}{\lambda_b \left(T_w - T_b\right)} = Nu_{corr}\left(T_w, T_b\right) \tag{2.60}$$

As already discussed e.g. by (Cheng et al., 2009a), (Churkin & Deev, 2013), (Cheng & Liu, 2018) and (T. Gschnaidtner et al., 2018), for some cases, multi or no solutions to equation 2.60 are possible. The problem of multi-solutions is shown exemplarily in Figure 2.16 for the correlation proposed by (D. E. Kim & Kim, 2010), for water flowing in a tube with $d_i = 10\ mm$, with a mass flux of $G = 1000\ kg/m^2s$, heat flux of $\dot{q}_w = 1000\ kW/m^2$, inlet temperature of $T_{in} = 350\ °C$ and pressure of $p = 25\ MPa$. The definition of the Nusselt number (left site of equation 2.60 and the Nusselt correlation proposed by Kim & Kim have two intersections, the first at $T_w = 384.3\ °C$ and

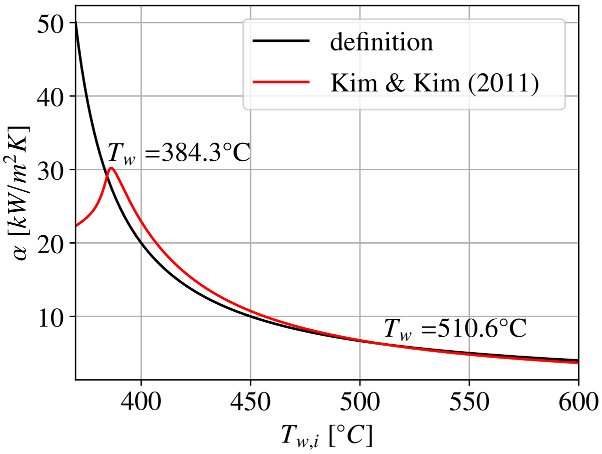

Figure 2.16: Example for multi solutions of Nusselt correlation

the second at $T_w = 510.6\ °C$. It remains an open question, whether such an ambiguity is physically correct, or it is just a problem of the correlation. Similar to the different boiling phenomena film boiling and nucleate boiling, multi-solutions could also be physical for heat transfer to supercritical pressure fluids.

2.2.3.2 Two-layer model

The idea of the two-layer model goes back to the work of Ludwig Prandtl (Prandtl, 1904). The Prandtls idea is that the flow, when the Reynolds number is sufficiently large, can be divided into two regions, which are the bulk flow, where the viscosity of the fluid can be neglected and the thin boundary layer close to the wall, where the viscosity has to be considered.

Based on the two-layer theory (that is, the viscous sublayer and the turbulent logarithmic layer), (Laurien, 2016) developed a model for the transfer of heat to fluids under supercritical pressure conditions. For clarification of the idea, the dimensionless velocity profile is shown in Figure 2.17. Close to the wall ($y = 0$), in the laminar sublayer, viscous forces are dominant and $u^+ = y^+$. Following a transition region, the logarithmic turbulent layer attaches about $y^+ = 70$. The idea behind the model is that in the laminar sublayer, heat transfer is mainly characterized by conduction, whereas in the turbulent logarithmic layer, the turbulent motion of the fluid drives the heat transfer, and the conduction can be neglected. Further, a relation of the thickness of the viscous sublayer to the non-dimensional wall roughness k_s^+ is derived (Laurien, 2016):

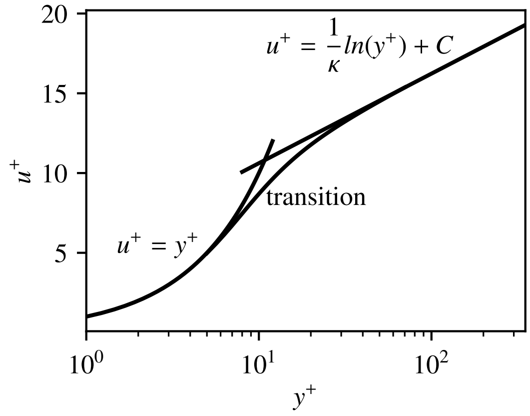

Figure 2.17: Non-dimensional velocity profile

$$y_{vs}^+ = \frac{1}{\kappa} ln y_{vs}^+ + 5.78 - \frac{1}{\kappa} ln\left(1 + \frac{k_s^+}{3.28}\right) \tag{2.61}$$

with:

$$k_s^+ = \frac{k_s \rho u_\tau}{\mu} \tag{2.62}$$

Based on y_{vs}^+, the thickness y_{cs}^+ of the conductive sublayer can be calculated, using the Prandtl number (Laurien, 2016):

$$y_{cs}^+ = \frac{y_{vs}^+}{Pr^{1/3}} \tag{2.63}$$

The dimensionless temperature can now be expressed as:

$$T^+ \left(y^+\right) = \underbrace{\int_0^{y^+_{cs}} Prdy^+}_{conduction} + \underbrace{\int_{y^+_{cs}}^{y^+} \frac{Pr_T}{\kappa \cdot y^+} dy^+}_{turb.convection} \tag{2.64}$$

, where the dimensionless temperature T^+ is defined as:

$$T^+ = \frac{\left(T_w - T_b\right) u_\tau \rho c_p}{q_w} \tag{2.65}$$

Finally, the heat transfer is calculated, summing up the temperature change in the conductive sublayer and in the turbulent layer:

$$T_w = T_b + \Delta T_{turb} + \Delta T_{cs} \tag{2.66}$$

2.2.3.3 Look-up table

As summarized in the previous sections, the prediction of the heat transfer coefficient under supercritical pressure conditions is challenging, as the variation in thermophysical properties is strong. On the other hand, large number of experimental data has been obtained so far under such conditions. The idea of the look-up table is to collect the available experimental data and predict the heat transfer coefficient based on interpolation in between the available data points. The first supercritical pressure water look-up table was published in (M. Löwenberg et al., 2007) and is applicable to upward flows in vertical tubes and covers a mass flux range of 700-3500 kg/m²s, a heat flux range of 300-1600 kW/m²s, a pressure range of 22.5-25 MPa, a tube diameter range of 8-20 mm and a bulk enthalpy range of 1200-2700 kJ/kg. The authors state that the accuracy of the look-up table in the vicinity of the pseudocritical point is significantly higher than the conventional correlations. Since the look-up table is limited to water in circular tubes, the heat transfer coefficient is only a function of the dimensional parameters pressure, mass flux, heat flux, bulk enthalpy, tube diameter and orientation of the flow direction to the gravity field. The method of creating look-up tables has been adapted from (Groeneveld et al., 2003) and (Groeneveld et al., 2005), who already successfully created a look-up table for film-boiling heat transfer or the critical heat flux, which determines the onset of a boiling crisis. The experimental data have been selected from publications, which allow an estimation of the accuracy of the published data. The look-up table is independent of the axial distance from the inlet and therefore only valid for fully developed flow and can not consider inlet effects.

Despite the generally good performance of the look-up table, it is also not capable of predicting the deterioration of heat transfer. As noted in (M. Löwenberg et al., 2007), the deterioration of heat transfer depends on the history of the upstream flow. Thus, data points with considerable effect of buoyancy have been excluded in the development of the look-up table. Furthermore, data at similar experimental conditions, resulting in inconsistent results for the wall temperature, are excluded. Since experimental data always contain random noise, the data need to be smoothed by applying splines, avoiding numerical instabilities when the look-up table is used. This is done using the smoothing method introduced by (Huang & Cheng, 1994). The smoothed experimental data are copied into the look-up table at discrete grid points in the five dimensions p (4 points), G (5 points), q (7 points), d_i (4 points) and h_b (15 points). The data for grid points in between those ones are interpolated, using non-dimensional heat transfer correlations, which are adjusted for the given small ranges in between the given grid points.

Later, the given look-up table was extended to the sub-critical pressure range by (Zahlan, Tavoularis, & Groeneveld, 2015). The table was created with the same methods for the selection of the experimental data, as well as for the smoothing of the data and interpolation in between the grid points. The main difference of this look-up table is that the wall temperature, instead of the wall heat flux in the look-up table of (M. Löwenberg et al., 2007) is given, making it applicable to a different use-case.

Another look-up table for heat transfer to water at supercritical pressure has been proposed by (F. Chang et al., 2021). The approach is again similar to the ones mentioned before, but covering a larger number of experimental data and also more different heat transfer correlations are considered. All three works (M. Löwenberg et al., 2007; Zahlan, Tavoularis, & Groeneveld, 2015; F. Chang et al., 2021) show that look-up tables perform better, compared to the predictions of conventional Nusselt correlations. All of these lookup-tables have in common, that they are designed for water and cannot be applied to other fluids.

2.2.3.4 Machine Learning

As noted in the previous sections, heat transfer to fluid at supercritical pressure is influenced by many factors, whose dependencies are complex and nonlinear and therefore not easy to understand. Machine learning approaches, such as a artificial neural network (ANN) are making use of available data, autonomously understanding the versatile dependencies in the data set. Since this work aims to produce a reference database on the influence of wall roughness on heat transfer to a fluid under supercritical pressure conditions, it is an opportunity to use the generated data to train an ANN. The general idea of an ANN is an artificial representation of the structures in a human brain. An ANN consists of different layers, each of which has a number of neurons. For the case of fully connected Deep Neural Network (DNN), all the neurons form one layer are connected to all neurons in the next layer, and so on. On each of the connection lines in between the neurons, a simple linear relation:

$$z_0 = w \cdot r + b \tag{2.67}$$

The optimization of the weight vectors w and biases b of each neuron is called *training* of the neural network. Here, the training procedure is called *supervised learning*, which means that training data $\hat{y}_i\,(x1, x2, ..., x_n)$ is required. The training data $\hat{y}$ is the *gold standard* data, thus needs to be of good quality. The accuracy of the neural network can be evaluated for the n data points, using the loss function $L\,(w, b)$:

$$L\,(w, b) = \frac{1}{n} \sum_{i=1}^{n} (\hat{y}_i(x) - y_i(x, w, b))^2 \tag{2.68}$$

This example is the mean squared error (MSE) loss function, but also mean squared logarithmic error (MSLE), mean absolute error (MAE) or others can be applied. The goal of the training of the network is to find w and b which minimize $L(w,b)$.

The application of neural networks to supercritical pressure heat transfer is rather new, compared to the classical Nusselt correlations. An early work is performed by (Scalabrin & Piazza, 2003), using experimental data of carbon dioxide. The task is to select the input variables x_i, to predict the Nusselt number or the heat transfer coefficient. Scalabrin et al. made four different selections:

- **dimensionless numbers:** $x = \left(Re,\ Pr,\ Ec = \frac{u^2}{c_p(T_w - T_b)}\right),\ y = Nu$
- **physical variables:** $x = (p/p_c,\ T/T_c,\ \dot{m},\ \dot{q}),\ y = \alpha$
- **accounting for property variations - directly:** $x = \left(Re,\ Pr,\ \left(\frac{\rho_w}{\rho_b}\right),\ \left(\frac{\bar{c}_p}{c_{p,b}}\right)\right),\ y = Nu$
- **accounting for property variations - indirectly:** $x = \left(p/p_c,\ T/T_c,\ \dot{m},\ \left(\frac{T_w}{T_b}\right)\right),\ y = \alpha$

All of the four different architectures yield better results, compared to a convectional Nusselt correlation. However, for three of the four neural networks, the input parameters are containing the wall and the bulk temperature, while as already mentioned, in many applications and especially in nuclear engineering, prediction of the wall temperature for given heat flux and flow conditions is desired. Only the second model could be applied for this kind of problem. More recently (Chu et al., 2018) proposed a neural network, which has been trained using data from DNS with carbon dioxide. Here, the input parameters are chosen to be the inlet temperature T_{in}, the heat flux $\dot{q}$, the inlet pressure p_{in}, the inner tube diameter d_i and the bulk specific enthalpy h_b. The model is capable to predict the wall temperature T_w and the wall shear stress τ_w as well. For the wall temperature, a mean error of 0.07% with a standard deviation of 0.13% and for the wall shear stress a mean error of 1.02% with a standard deviation of 1.98% can be achieved on the validation data. A very similar work was proposed by (W. Chang et al., 2018), with the difference, that DNS data of water is used for training and only T_w is predicted by the DNN. In this work, the results are compared to the predictions of convectional Nusselt correlation, showing that the neural network predictions are much better.

At the current state, there are many more publications, which are similar to those described above, such as (Ma et al., 2017), (K. Ye et al., 2019), (Tao et al., 2022), (Xiao et al., 2023) and (Wen et al., 2024). Among those, the work of (R. Zhang et al., 2023) is to point out, since the ANN proposed there is trained with data for water and CO2. Other works to point out are (Sun et al., 2021), and (Yan et al., 2023), who combined a genetic algorithm with the back propagation algorithm, to find the optimum wights and biases, to reduce the loss function. On the other hand, (Kumar et al., 2023) was using a genetic algorithm to optimize the learning rate, momentum factor, coefficients of activation functions and the number of neurons in the hidden layer.

2.3 Effect of roughness on flows

In chapter 2.2.3 was already shown, that the surface roughness can play a role in the heat transfer. More precise, the frictional resistance is depending on the wall roughness and many heat transfer correlations depend on the frictional resistance, such as the correlations summarized in Table 2.3. Further, it was shown in chapter 2.2.3.2, that the velocity distribution in the boundary layer is effected by the wall shear stress, which again is depending on the frictional resistance of the flow on the wall. In this chapter, the effect of the wall roughness will be described in detail.

2.3.1 Roughness effect on flows at adiabatic conditions

Under adiabatic conditions, the frictional resistance is depending on the Reynolds number and the surface roughness. There have been experimental investigations performed by (Nikuradse, 1933), focusing on the frictional pressure drop and the velocity distribution in tubes. Nikuradse was preparing the tubes inner surface with sand grains of the same size. This was achieved for example for an averaged grain size of 0.8 mm by sifting the sand with a sieve with 0.82 mm openings and then with a sieve with 0.78 mm openings, etc. Then, the tubes inner surface are covered by a thin layer of lacquer and afterwards sand of the desired grain size is filled into the tubes. In the experiments, the pressure drop, defined as the difference from the inlet pressure p_{in} and the outlet pressure p_{out} was obtained. The frictional resistance can be described by the Darcy friction factor c_f, which can be obtained from the tube length L to diameter D ratio, the bulk flow velocity u_b and the measured pressure drop Δp:

$$\Delta p = \frac{\rho}{2} \cdot u_b^2 \cdot \frac{L}{D} \tag{2.69}$$

It has to be noted here, that in the literature also the Fanning friction factor f is used, which is 4 times smaller than the Darcy friction factor c_f ($4f = c_f$). Based on the experimental results of Nikuradse and prior theoretical considerations of (Prandtl, 1933) and (von Karman, 1930), Coloebrook ((Colebrook & White, 1937), (Colebrook, 1939)) developed an equation for the calculation of the Darcy friction factor, based on the Reynolds number and the relative roughness k/D of the tube.

$$\frac{1}{\sqrt{c_f}} = -2log\left(\frac{k}{3.71d} + \frac{2.51}{Re\sqrt{c_f}}\right) \tag{2.70}$$

In this equation, k is the roughness, which is defined as the diameter of the sand grains which were used in the experiments of Nikuradse. (Schlichting, 1937) introduced the concept of the equivalent sand-grain roughness k_s, which referrers to the size of the sand-grains, used in the experiments of (Nikuradse, 1933), which needs to be used instead of k, when the shape of the roughness elements is different from the sand-grains used in the experiments of Nikuradse. Later, (Moody, 1944) compiled the available equations for the friction factor for different relative roughness as function of the Reynolds number into the so-called *Moody-Diagram*, which can be seen on Figure 2.18. In the laminar regime, for $Re < Re_{crit} = 2300$ the Hagen-Poiseuille law is used to calculate the friction factor:

$$c_f = \frac{64}{Re} \tag{2.71}$$

In the range from $2300 < Re < 4000$ is a critical zone for which the exact friction factor cannot be determined, but the minimum for the friction factor is given by the dotted extension of the laminar line. According to Moody, in the critical zone, the conditions may be affected by instabilities due to pressure waves. For $Re > 4000$, c_f can be calculated for perfectly smooth tubes by:

$$\frac{1}{\sqrt{cf}} = 2log\frac{\sqrt{c_f}Re}{2.51} \tag{2.72}$$

, which is indicated by the blue line in Figure 2.18. This region is called the transition zone, where the friction factor strongly depends on the Reynolds number. The transition zones upper bound is given by

$$\frac{1}{\sqrt{c_f}} = \frac{200}{Re}\frac{k}{d} \tag{2.73}$$

, which is represented by the dashed red line in Figure 2.18. For rough tubes, the Colebrook equation (2.70) is used. In the transition zone, c_f is not only depending on Re, but also on the relative roughness k/D. When the Reynolds number becomes large enough, in the rough pipe zone, the friction factor depends only on the relative roughness. In this zone, the second addend in equation 2.70 becomes negligible. Regarding the equations presented here, wall roughness increases the frictional resistance of the flow and thus the pressure drop in a tube increases with increasing surface roughness. Further, the surface roughness also affects the thickness of the laminar sublayer, which can be calculated according to (Schlichting & Gersten, 2016) as:

$$\delta_v = \frac{\nu}{u_\tau} = \frac{\nu}{\sqrt{\tau_w/\rho}} \tag{2.74}$$

The wall shear stress τ_w increases with increasing wall friction and hence the boundary layer thickness decreases. This can was also seen in equation 2.61.

(Hama, 1954) has shown, that the general logarithmic law of the wall can be extended by a

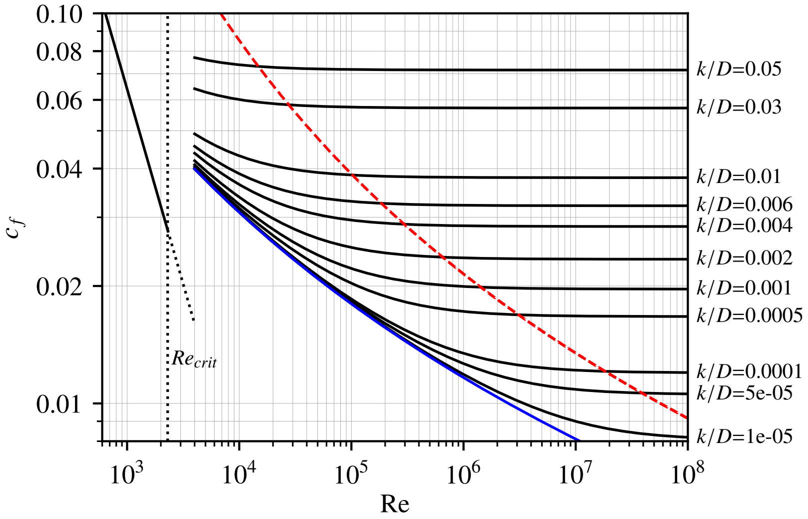

Figure 2.18: Moody Diagram: Friction factor depending on Reynolds number for different wall roughness

roughness function Δu^+, to be applicable to flows over rough surfaces:

$$u^+ = \frac{1}{\kappa} ln\left(y^+\right) + C - \Delta u^+ \tag{2.75}$$

According to (Granville, 1987), the roughness function can be obtained from the difference of the friction coefficient from a smooth tube an a rough tube in the following way:

$$\Delta u^+ = \left(\sqrt{\frac{8}{c_f}}\right)_{smooth} - \left(\sqrt{\frac{8}{c_f}}\right)_{rough} \tag{2.76}$$

The friction factor in the smooth tube can be obtained, using the Colebrook equation 2.70, with $k_s = 0$. In the literature, the *Nikuradse-type* (Nikuradse, 1933) and the *Colebrook-type* (Colebrook, 1939) roughness functions are commonly used, which are presented in Figure 2.19 (b). Using equation 2.76 and Colebrook equation 2.70, the *Colebrook-type* roughness function can be obtained. According to (Andersson et al., 2020), the *Nikuradse-type* roughness function can be expressed as:

$$\Delta u^+ = \begin{cases} 0 & k_s^+ \le k_{smooth}^+ \\ \frac{1}{\kappa} ln\left(C_s k_s^+\right) \cdot sin\left(\frac{\pi}{2} \frac{ln\left(k_s^+\right) - ln\left(k_{smooth}^+\right)}{ln\left(k_{rough}^+\right) - ln\left(k_{smooth}^+\right)}\right) & k_{smooth}^+ < k_s^+ \le k_{rough}^+ \\ \frac{1}{\kappa} ln\left(C_s k_s^+\right) & k_s^+ > k_{rough}^+ \end{cases} \tag{2.77}$$

According to (Schlichting & Gersten, 2016), the onset of roughness effects is for $k_s^+ > 5 = k_{smooth}^+$ and fully rough conditions are present for $k_s^+ > 70 = k_{rough}^+$. (Cebeci & Bradshaw, 1977) suggested a roughness constant of $C_s = 0.253$. For $k_s^+ > 70$, bot of the roughness functions collapse into the fully rough asymptote, which is given by:

$$\Delta u^+ = \frac{1}{\kappa} ln\left(k_s^+\right) + C - 8.5 \tag{2.78}$$

Figure 2.19 (a) shows the downward shift of the dimensionless velocity due to roughness and Figure 2.19 (b) shows the different approaches for the roughness function.

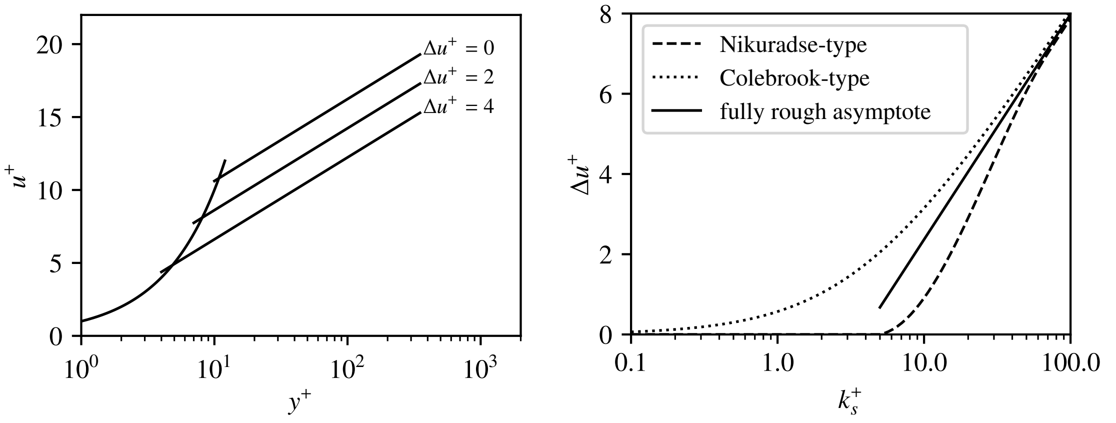

(a)

(b)

Figure 2.19: Velocity shift due to roughness (a) and different roughness functions (b)

Further details on the roughness function can be found in the review paper (Kadivar et al., 2021), as well as in the publications of Flack et al. (K. A. Flack & Schultz, 2010; K. A. Flack et al., 2012; K. Flack et al., 2016).

2.3.2 Roughness effect on heated flows

Generally, it appears reasonable to assume, that surface roughness has an impact on the heat transfer, when the peaks of the surface roughness are larger than the laminar sublayer and thus the laminar layer is disturbed by the roughness. The induced turbulence in the near wall layer thus is expected to enhance the heat transfer. The impact of the surface roughness on the heat transfer is reflected in the empirical correlations based on Petukhov & Kirillov (equation 2.41), by application of the friction factor c_f. With $c_f/8$ in the numerator and $\sqrt{c_f/8}$ in the denominator it is obvious, that this Nusselt correlations predict enhanced heat transfer when the friction at the wall increases.

Similar to the logarithmic law of the non-dimensional velocity, also a logarithmic law for the non-dimensional temperature can be formulated (Schlichting & Gersten, 2016):

$$T^+ = \frac{1}{\kappa_\theta} ln\left(y^+\right) + C_\theta\left(Pr\right) \tag{2.79}$$

, where κ_θ is defined with the von Karman constant κ and the turbulent Prandtl number (Schlichting & Gersten, 2016):

$$Pr_t = \frac{\nu_t}{a_t} = \frac{\kappa}{\kappa_\theta} = \frac{0.41}{0.47} = 0.87 \tag{2.80}$$

and (for smooth wall):

$$C_\theta\left(Pr\right) = 13.7Pr^{2/3} - 7.5 \tag{2.81}$$

Using equation 2.79 and the definition of the non-dimensional temperature (see equation 2.65, as well as the definition of the Nusselt number (see equations 2.3 and 2.2), the following can be obtained (Schlichting & Gersten, 2016):

$$Nu = \frac{\frac{f}{2}RePr}{\frac{\kappa}{\kappa_\theta} + \sqrt{\frac{f}{2}}D_\theta(Pr)} \tag{2.82}$$

$D_\theta(Pr)$ is shown in (Schlichting & Gersten, 2016) for a smooth wall. A similar approach is used later in this work, in order to consider the effect of the wall roughness in a Nusselt correlation.

Similar to the shift of the velocity due to roughness, the logarithmic temperature is also shifted due to the roughness by ΔT^+ (Aupoix, 2015):

$$T^+ = \frac{1}{\kappa_\theta} ln\left(y^+\right) + C_\theta\left(Pr\right) - \Delta T^+ \tag{2.83}$$

In a similar way as the velocity shift in equation 2.76, the temperature shift can be calculated based on the differences of the friction coefficient and the Stanton number $St = Re \cdot Pr$ in between a smooth and a rough tube:

$$\Delta T^{+} = \left(\frac{\sqrt{\frac{f}{2}}}{St}\right)_{smooth} - \left(\frac{\sqrt{\frac{f}{2}}}{St}\right)_{rough} \tag{2.84}$$

(Kays & Crawford, 1993) proposed an empirical equation for the temperature shift ΔT^{+}:

$$\Delta T^{+} = \frac{1}{\kappa_\theta} ln \frac{k_s^{+}}{32.6} + C_\theta (Pr) - 1.25 Pr^{0.44} k_s^{+0.2} \tag{2.85}$$

2.3.3 Features of rough surfaces

The structure of a surface can be described, using several different parameters, which are summarized in Table 2.4. All of them can be obtained from a measurement of the elevation of the surface along a line. Let the elevation of the discrete points on such a measurement line be y_i, then the different surface parameters are calculated as shown in Table 2.4 and visualized in Figure 2.20. In addition, a histogram of the roughness heights from that exemplary roughness profile is shown in Figure 2.21, to visualize the skewness and the kurtosis. The skewness would be 0, if the median of the values would equal the mean. The kurtosis expresses the peakedness or flattness of the surface, and equals to 3 if the histogram would be a normal distribution. As shown in section 2.3.1,

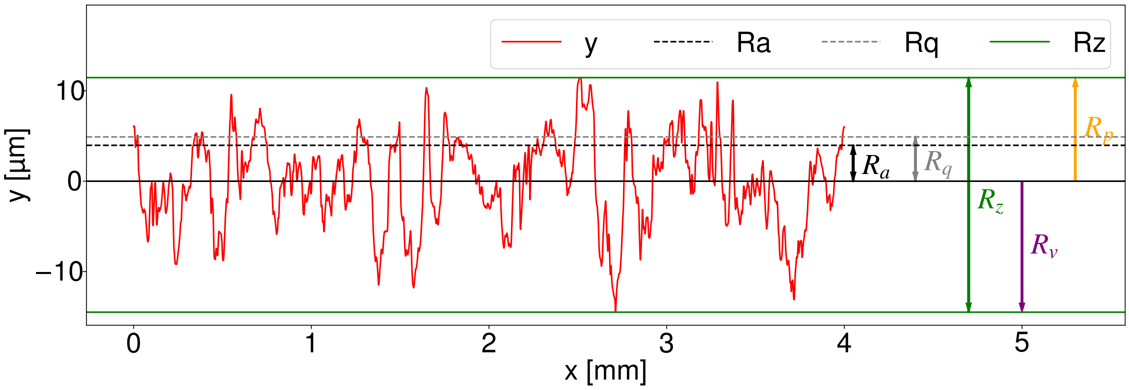

Figure 2.20: Visualization of different roughness parameters

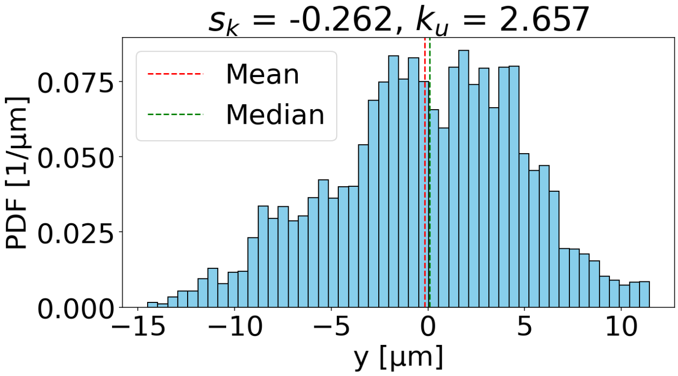

Figure 2.21: Probability Density Distribution of roughness height

Table 2.4: Surface roughness parameters

Parameter	Description	Equation
R_a	mean elevation of surface form the mean line	$\frac{1}{N}\sum_{i=1}^{N}\lvert y_i\rvert$
R_q	root mean squared elevation from mean line	$\sqrt{\frac{1}{N}\sum_{i=1}^{N} y_i^2}$
R_v	maximum valley depth below the mean line	$\lvert min\ y_i\rvert$
R_p	maximum peak height above the mean line	$max\ y_i$
R_z	maximum peak to valley height	$R_v + R_p$
s_k	skewness	$\frac{1}{(NR_q)^3}\sum_{i=1}^{N} y_i^3$
k_u	kurtosis	$\frac{1}{(NR_q)^4}\sum_{i=1}^{N} y_i^4$

the frictional resistance depends on the surface roughness and experiments in tubes which inner walls had been prepared with sand grains of equal size have been conducted, on which following theoretical work was based. E.g. in equation 2.70, a single length scale for the roughness is used, corresponding to the sand grain diameter in the Nikuradse experiments. Thus, the question arises, which of the listed surface roughness parameters in Table 2.4 is an appropriate measure of the roughness effect on the flow and thus should be applied in the Colebrook equation 2.70.

As mentioned before, (Schlichting, 1937) introduced the concept of the equivalent sand-grain roughness, which aims to find for every kind of rough surface an equivalent value k_s, which represents the effect of the roughness on the flow, caused by the sand-grains of size k in the Nikuradse experiment. To find the equivalent sand-grain roughness k_s for a given roughness geometry, empirical correlations have to be found. This is done for different kinds of regular shaped roughness, e.g. by (Dirling, 1973), who used hemispheres, spherical segments and cones, and correlated the equivalent-sand grain roughness to the shape Λ, expressed by the projected surface area A_p and the windward surface area A_s, as well as to the mean spacing of the roughness elements Ψ and the mean roughness element height k.

$$\Lambda = \left(\frac{\Psi}{k}\right)\left(\frac{A_p}{A_s}\right)^{-4/3} \tag{2.86}$$

However, for this work, irregular shaped roughness, such as it would be caused by corrosion of a steel surface is important.

(Bottros, 2016) conducted tests in 13 different commercial steel pipes, using natural gas in a range of Reynolds numbers from $9 \cdot 10^6$ to $16 \cdot 10^6$ and found a correlation of the equivalent sand-grain roughness k_s to the root meas square of the elevation of the roughness profile R_q. The authors differentiated in between the Colebrook type roughness, which is more suitable for real applications like steel tubes, and Nikuradse type roughness, which is a more theoretical type, which better fits to a sand-grain like roughness, as it was used in the Nikuradse experiments. (See the different roughness functions in Figure 2.19). (Bons, 2002) studied nearly 100 samples taken from land-based gas turbines, which cover deposits, thermal barrier coating (TBC), erosion and pitting. The samples, which are plates, where put to the bottom wall of a wind tunnel and test where conducted at $Re = 5 \cdot 10^5$ and $Re = 9 \cdot 10^5$. Finally, the equivalent sand-grain roughness was correlated to the root mean squared (RMS) of the surface slope angles α_{rms} between each measurement points of the roughness profile. In a following work (Bons, 2005), the authors proposed an updated version of the correlation. Further experiments, using turbulent flow in tubes where carried out by (Shockling et al., 2006). The inner surface of the tubes was prepared by a honing tool. The Reynolds number is in the range of $57 \cdot 10^3$ to $21 \cdot 10^6$ and k_s is correlated to the RMS of the roughness. Another experimental work, using commercial steel pipes was conduced by (Langelandsvik et al., 2008). Here, the Reynolds number varies from $150 \cdot 10^3$ to $20 \cdot 10^6$ and again, a correlations of k_s to the RMS roughness R_q was found. (Boyle & Stripf, 2009) used experimental data of (Stripf et al., 2005) and proposed a revised form of the correlation, which has previously developed by (Koch & Smith, 1976), using R_q and the skewness of the roughness profile s_k. (K. A. Flack & Schultz, 2010) proposed a similar correlation, based on experimental data obtained, using sandpaper (K. A. Flack et al., 2007), honed pipe (Shockling et al., 2006), commercial pipe (Langelandsvik et al., 2008), medium and coarse gravel (Castro, 2007), different sized pyramids (Schultz & Flack, 2009), packed spheres and packed spheres with grid (Schultz & Flack, 2005). Compared to other correlations, the one proposed by (K. A. Flack & Schultz, 2010) is covering a wide range of different surfaces and operating conditions. Later, (K. Flack et al., 2016) added an additional form of the correlation, applicable to rough surfaces with negative skewness s_k and in (K. Flack et al., 2020) also a correlation for surfaces with zero skewness is proposed. Table 2.5 gives an overview of the mentioned correlations for the equivalent sand-grain roughness k_s.

Table 2.5: Correlations for the equivalent sand-grain roughness k_s

Author	type of roughness	k_s
(Bons, 2002)	deposits, thermal barrier coating erosion and pitting at samples from gas turbines	$k_s = -0.0261\alpha_{rms} + 0.0138\,(\alpha_{rms})^2$
(Bottros, 2016)	commercial steel pipes	$(k_s)_{Colebrook} = 1.306R_q + 0.078R_q^2$ $(k_s)_{Nikuradse} = 2.294R_q$
(Boyle & Stripf, 2009)	evenly spaced truncated cones with varying height	$k_s = 4.3R_q\,(1 + C_{sk}s_k)$ for $s_k > 0$
(Dirling, 1973)	hemispheres, spherical segments, cones	$\frac{k_s}{R_a} = 0.0164\Lambda^{3.78}$ for $\Lambda < 4.93$, $\frac{k_s}{R_a} = 139\Lambda^{-1.9}$ for $\Lambda > 4.93$
(Koch & Smith, 1976)	sandpaper	$k_s = 6.2R_a$ or $k_s = 4.3R_q$
(K. A. Flack & Schultz, 2010)	sandpaper, honed tubes, commercial pipes, small and medium gravel, different sized pyramids, packed spheres	$k_s = 4.43R_q\,(1 + s_k)^{1.37}$
(K. Flack et al., 2016)	rough surfaces with negative s_k	$k_s = 2.91R_q\,(2 + s_k)^{-0.284}$
(Langelandsvik et al., 2008)	commercial steel pipes	$k_s \simeq 1.6$
(Shockling et al., 2006)	honed steel tubes	$k_s \simeq 3R_q$

2.4 Knowledge gaps and need for research

The environment inside of an SCWR core is, due to nature of water at high temperatures, very corrosive. Typically, the fuel rods will stay for several years in the reactor core, which will result in a transition of the initial smooth surface structure, towards a rough heat transfer surface. However, as the literature review presented in the previous sections has shown, heat transfer to a fluid at supercritical pressure conditions is, due to the strong variation of the thermophysical properties, an overly complex phenomenon, and the correct prediction is still challenging. In order to guarantee safe operation of a future SCWR, it is indispensable to correctly predict the heat transfer, not only for fresh fuel with a smooth surface, but also for used fuel, which has a more rough surface. The work aims to address the following:

- At the current state of the art, experimental investigations in which the surface roughness is considered are rare and in most of the cases, the aim of the studies was not the investigation of the effect of the surface roughness on the heat transfer. Therefore, this work aims to generate an experimental database, which can be used to assess the effect of the surface roughness on the heat transfer. The new experimental data is covering a range of Reynolds numbers, which are relevant to SCWR applications. To the current day, there is no other published data, which directly compares heat transfer for different roughness for these flow conditions.

- By comparison of results, obtained in a smooth tube, with results obtained at the same boundary conditions in a rough tube, the impact of the surface roughness on the heat transfer will be pointed out and discussed.

- The number of empirical correlations, which are applicable to heat transfer at rough surfaces is quite small. Usually, the surface roughness is only indirectly considered, via the skin friction coefficient. Therefore, in the present work, a new empirical correlation will be proposed, making use of the newly generated reference data, in which the surface roughness is directly considered.

- Recently, the application of machine learning models has led to promising results. The newly obtained experimental reference data is used to establish a neural network model for the prediction of the heat transfer to fluid at supercritical pressure conditions at a rough wall. A conventional neural network, as well as a hybrid neural network are established and the performance is compared to the new and existing empirical correlations.

3 Experimental Setup

In this chapter, the experimental setup is described. The KIMOF, which is located at the Institute for Applied Thermofluidics (IATF) is presented, as well as the configuration of the test section, with the measurement devices. Further, the surface roughness in the rough test tube is described.

3.1 Experimental facility

The KIMOF is designed as a closed loop facility and uses the refrigerant Freon R134a as surrogate fluid. The critical temperature of $T_c = 101.06\ °C$ and the critical pressure of $p_c = 4.059\ MPa$ of R134a are well below the critical values of water ($T_c = 373.95\ °C$ and $p_c = 22.064\ MPa$), which results in significantly decreased erection costs for the facility and further drastically reduces the energy consumption during the operation of the loop. A scheme of the KIMOF is shown in Figure 3.1.

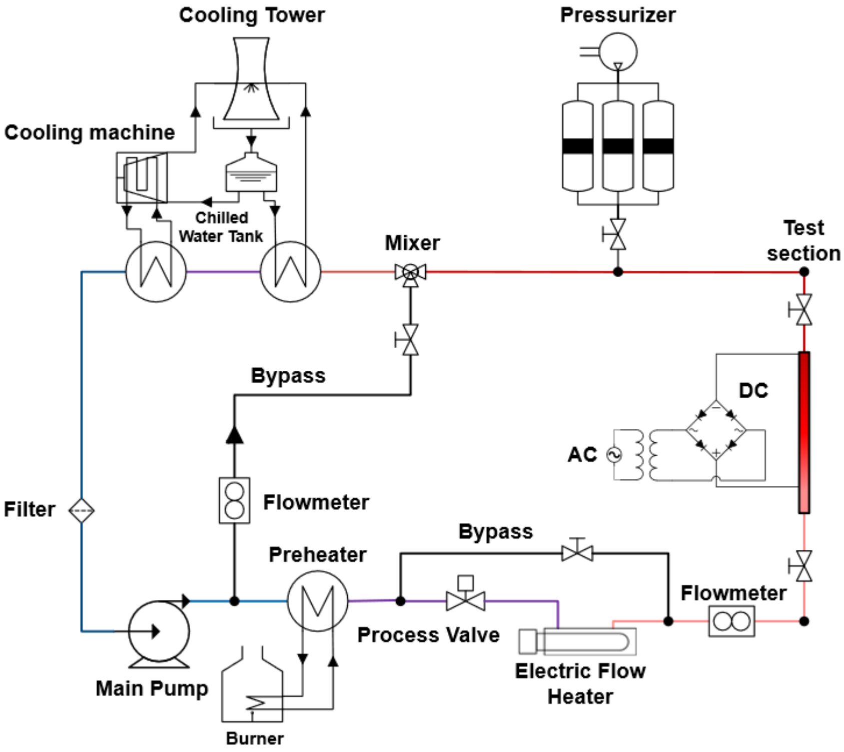

Figure 3.1: Scheme of the KIMOF

The coolant flow is driven by the main pump and the mass flow rate through the test section is adjusted by a process valve. The flow is separated into the flow through the test section and the flow through the bypass, in order to operate the pump at it's optimum design point. The mass flow rate is measured by a Coriolis flow meter. The inlet temperature into the test section is adjusted, using two pre-heating systems. The first pre-heater consists of a gas burner, a 500 liters storage tank, which buffers the effect of the gas burner on the temperature in the main pipe, and a heat exchanger with water at the secondary site. The temperature of the main R134a flow is controlled by adjusting the temperature in the storage tank, using the gas burner, and adjusting the mass flow rate of water, through the secondary side of the heat exchanger. Especially for large mass flow rates of R134a, this system is required to reach high inlet temperatures. The second pre-heater is a simple electric flow heater, in which the desired temperature of the R134a flow can directly be adjusted. Bulk flow temperatures of up to 95 °C can be reached. The bypass to the process valve and the electric flow heater is generally closed during the experiments. The test section is heated, using direct current (DC), which is provided by a power converter. The device can deliver DC of up to 600 A and 1000 V, while the voltage is limited to ~30 V in the experiments, since then a current of 600 A is reached. Downstream of the outlet of the test section, at the top of the facility, the pressurizer is located, which consists of three cylindrical tanks with hydraulic oil in the secondary site. A hydraulic pump is used to push the hydraulic oil in the secondary site, and a valve is used to control the actual pressure in the system. Further downstream, the flow is mixed with the colder flow coming from the bypass. Finally, in order to maintain a constant inlet temperature, and further maintain the flow below the maximum operating temperature of of 60 °C of the pump, a cooling machine as well as a cooling tower can be used to dissipate the heat to the environment. Both of the devices are connected to the R134a loop by heat exchangers with water as working fluid of the secondary side. The pump, pre-heaters, process valve, pressurizer as well as the cooling towers are controlled by a PC, using programmable logic controllers. The measurement data is acquired, using 5 data loggers, using LABVIEW software.

3.2 Test section and instrumentation

In the present investigation, two different test sections are used, of which one is called *smooth* and one is called *rough*. Both of the test sections mainly consist of a simple cylindrical hydraulic tube, made from stainless steel 1.4571. The smooth tube's inner surface is just as received from the manufacturer, while the rough tube's inner surface was artificially roughened. The surfaces will be described later in section 3.2.7. The tubes have an inner diameter of 9 mm and an outer diameter of 12 mm and the heated length is 2800 mm. A scheme of the test section can be seen in Figure 3.2. Electrical insulation flanges are used, preventing the electrical current to be conducted into the rest of the facility.

3.2.1 Wall temperature measurement

For measuring the heat transfer, 68 thermocouples (TCs) of type T, class 1, with a measurement uncertainty of max(+/-0.5 K, 0.4% of the measured value in °C), are mounted on the outside of

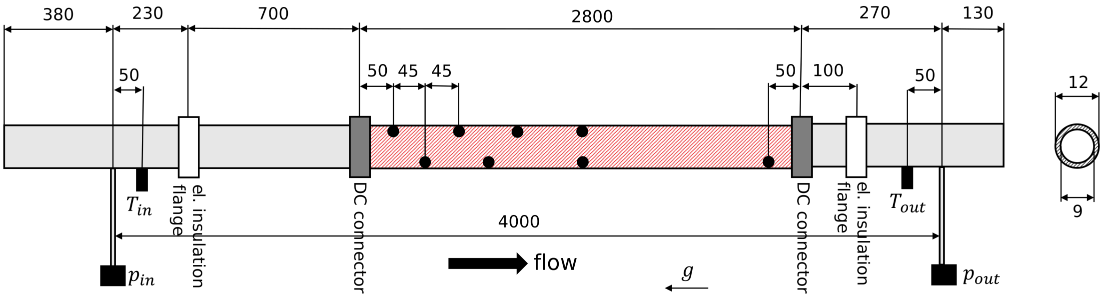

Figure 3.2: Scheme of the test section

the tube, on alternating sites along the heated section. As indicated in Figure 3.2, the first TC is located 50 mm downstream of the center of the DC connector. The following thermocouples are mounted with an axial spacing of 45 mm, which is corresponding to 5 hydraulic diameters of the test tube. At the axial distances of 500 mm, 950 mm, 1850 mm and 2300 mm from the beginning of the heated section, the TCs are mounted on both sides of the tube. The thermocouples need to be electrically insulated from the test tube. Therefore, exactly one layer of self adhesive fiber glass tape is placed underneath each TC measurement tip, as indicated in Figure 3.3. Another layer of the same self adhesive fiber glass tape is used, to fix the TC at the desired measurement location.

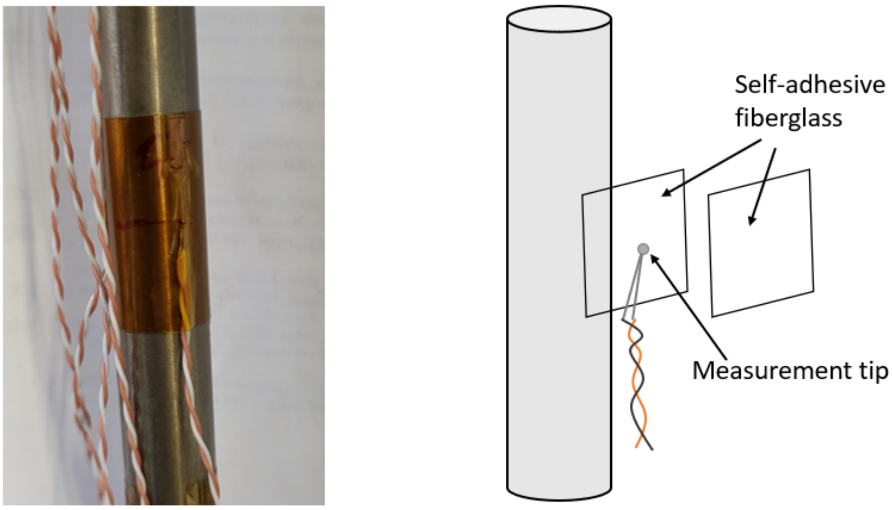

Figure 3.3: Mounted thermocouples for wall temperature measurement

3.2.2 Fluid temperature measurement

The temperature of the fluid is measured at the inlet, as well as at the outlet of the test section, using sheathed thermocouples of type T, class 2, with an measurement uncertainty of max(+/-1.0 K, 0.75 % of the measured value in °C) The exact axial position of the TC is indicated in Figure 3.2. As can be seen in Figure 3.4, the measurement tip of the TC are placed in the center of the tube. Since there are several bends in the tubing in between the pre-heaters and the inlet temperature measurement position, the flow is fully mixed, thus the temperature profile is homogeneous. Also

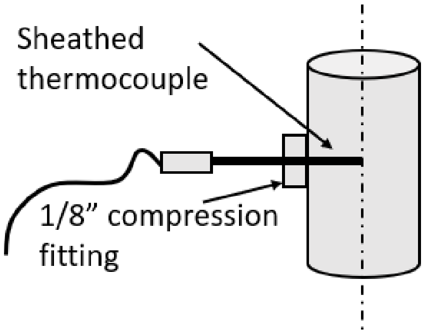

Figure 3.4: Thermocouples for fluid inlet and outlet temperature

downstream of the heated section, the distance of ~25 hydraulic diameters is sufficient, to consider the flow temperature as homogeneous. The TC are mounted, using a 1/8" compression fitting. A clamping ring inside of the compression fitting is providing the sealing.

3.2.3 Pressure sensors

The pressure is measured by PAA-33X pressure sensors, from Keller, which have a measurement range of 0..6 MPa. The sensors are measuring the absolute pressure. The analog channel is used, which has a measurement uncertainty of 0.1 % of the measurement range, which is 6000 Pa. The measurement of the fluid pressure is sensitive to the temperature, present at the transducer. Therefore, the applied PAA-33X sensors are compensated for the temperature within the range of 10..40 °C. To ensure that the devices are always operated in the temperature compensated range, a coiled tubing is mounted on the test tube, and the sensors are installed at the end of that. Figure 3.5 shows the coiled tubing with the pressure sensor. The sensors have been calibrated by the manufacturer and the calibration protocols are considered in the data acquisition procedure. The measured pressure is transferred to the data acquisition system in form of a voltage. The linear relation in between that voltage and the pressure contains the information from the calibration.

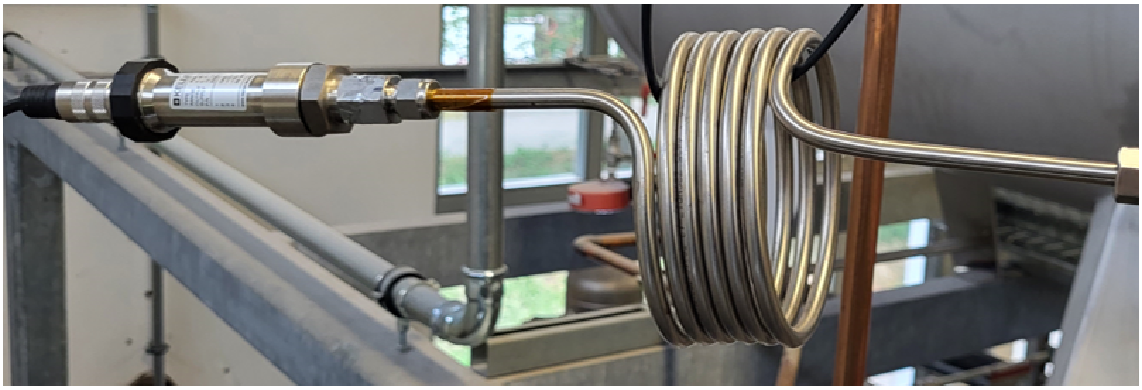

Figure 3.5: Coiled tubing and pressure sensor

3.2.4 Flow meter

The R134a mass flow rate through the test section is measured, using the YOKOGAWA RCUS34S-20TG90-0C6A-NN00-4-JA1/L005 Coriolis flow meter. The measurement uncertainty is 0.15 % for most of the experimental conditions. Details are provided in section 4.3.

3.2.5 Heat power measurement

The voltage drop over the heated part of the test section is measured parallel to it, using an input channel of the data logger. The electrical current is measured directly by the power supply. From the measured values of voltage drop and current, the heating power is calculated.

3.2.6 Heat loss

In order to reduce the heat loss during the experiments to a minimum, the test section is insulated, using a layer of mineral wool with a thickness of 50 mm. However, the heat loss needs to be estimated. In principal, the temperature difference of the test section to the environment is driving the heat loss. In order to obtain data at the test section, it is first evacuated, since in a vacuum, no heat convection is present and all the heat which is supplied to the test section will be released to environment. Then, a small electrical power is applied to the test section. After sufficient time, the temperature of the test section becomes stable, since a thermal equilibrium is reached. The electrical power equals now the heat, which is lost to the ambient. At the stable conditions, the power and the wall temperature measurements are recorded and the arithmetic mean of the wall temperatures, $T_{w,m}$ is calculated. This was repeated afterwards for a larger electrical power, until mean temperatures $T_{w,m}$ of ~200 °C are reached, which is more than the maximum average temperature which is expected in the experimental campaign. In total the data is recorded at zero electrical power and at four data points with different electrical power. The results can be seen on Figure 3.6. A polynomial

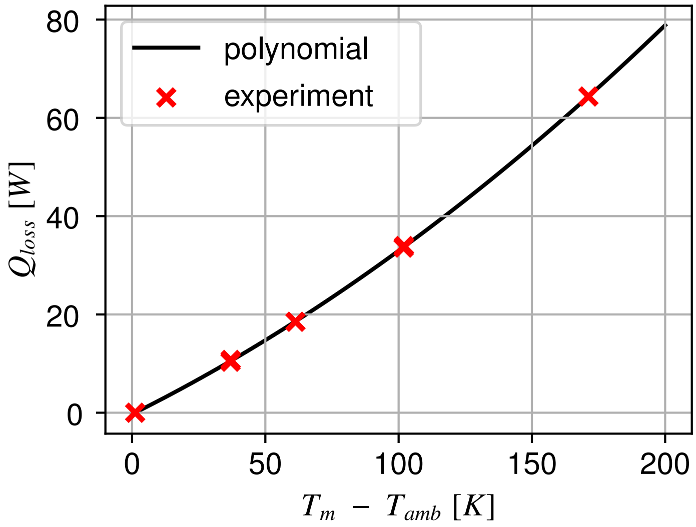

Figure 3.6: Experimentally obtained heat loss and polynomial fit

fit of second order, which is applied in the post processing of the experimental data later on, fits well to the obtained heat loss data, as a function of the mean test section temperature $T_{w,m}$ and the ambient temperature T_{amb}:

$$\dot{Q}_{loss} = 0.00063091\,(T_{w,m} - T_{amb})^2 + 0.26959\,(T_{w,m} - T_{amb}) - 0.31 \tag{3.1}$$

3.2.7 Surface roughness

In the present experimental investigation, a *smooth* reference tube, and a *rough* tube, which inner surface has been artificially roughened are used. The smooth tube is a conventional hydraulics tube. A second tube, coming from the same charge of the same manufacturer, was cut into pieces, and 6 samples, which where uniformly distributed over the length of the tube where taken out for measurement of the surface roughness profile. Project partners within the ECC-SMART project where using a contact profilometer to obtain the surface structure at the 6 specimen (Otic et al., 2024). Table 3.1 summarizes some parameters of the surface roughness in the smooth tube. Definition of the parameters are given in Table 2.4. At the lines 4 and 5, local irregularities of the surface from manufacturing process are leading to a very large value of R_z and also to a large skewness. However, since this is a local effect, it is not representative for the whole inner surface of the tube. For the evaluation of the data later on, one single parameter shall be used, to describe the surface roughness. Thus, lines 4 and 5 have been excluded from the evaluation. Now, a correlation to calculate the equivalent sand-grain roughness has to be chosen, among the ones summarized in section 2.3.3. The correlation of (K. Flack et al., 2016) (see Table 2.5) is the only one explicitly dedicated to surfaces with negative skewness, as they are present here. Further, water is used in the experiments, which fits best to the application here, even though it is not optimal. The equivalent sand grain roughness k_s is calculated for each of the lines, and then the arithmetic average is calculated, which is $k_s = 0.96\ \mu m$.

Table 3.1: Surface roughness of the smooth tube

Line	R_a $[\mu m]$	R_z $[\mu m]$	R_q $[\mu m]$	s_k $[\mu m]$
1	0.194	1.505	0.252	-0.724
2	0.29	2.024	0.371	-0.791
3	0.334	2.132	0.416	-1.038
4	0.301	5.258	0.575	2.495
5	0.231	3.709	0.242	2.129
6	0.207	1.964	0.281	-1.357

The inner surface of the rough tube has been manufactured and measured by the same project partners, within the ECC-SMART project. Figure 3.7 is a sketch of the manufacturing procedure. The tube has been mounted on 8 bearings and was clamped in a drilling machine at one end. At the other end, a tool with a sandpaper was injected into the tube with defined linear feed. Also the rotational speed of the drilling machine was defined. Several tests at different parameters have been performed by the project partners. After a test, the tube was cut at the locations indicated in Figure

3.7. The desired roughness which should be modeled on the inner surface of the tubes is derived from results of static autoclave experiments of the project partners (Marusakova et al., 2025), (Vit & Sipova, 2025), (Otic et al., 2024), conducted with supercritical water at high temperature, corresponding to actual conditions in an SCWR core. The results are comparable to previously published corrosion tests, such as in (L. Zhang et al., 2009) or (Guo et al., 2019). The mass flow rate in the autoclave is very low and only has the purpose of keeping the water chemistry constant. On the other hand, in the reactor, the large mass flow rate will induce flow accelerated corrosion, which will result in further increased surface roughness. Thus, a reasonably larger surface roughness than reported in the autoclave experiments was used in the current experiments. Once the desired surface parameters where achieved, the procedure was repeated, to make sure it is reproducible. Finally, the

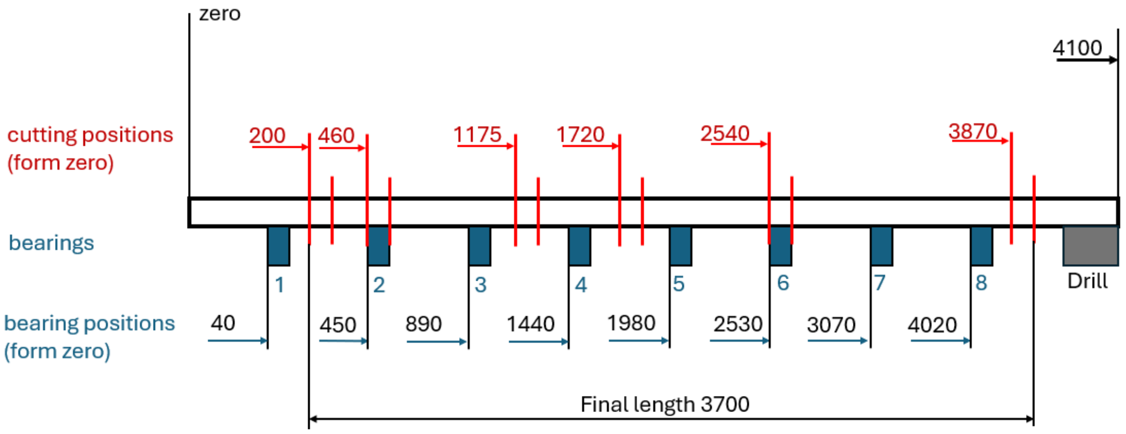

Figure 3.7: Manufacturing and sampling of the rough tubes inner surface

Table 3.2: Surface roughness of the rough tube

Line	R_a [μm]	R_z [μm]	R_q [μm]	s_k [μm]	k_s [μm]
1-1	3.417	24.253	4.357	-0.365	11.027
1-2	3.482	22.745	3.308	-0.395	10.96
1-3	3.34	20.312	3.816	-0.198	9.394
2-1	3.507	20.932	4.193	-0.262	10.429
2-2	3.203	19.784	3.839	-0.294	9.599
2-3	3.941	20.315	3.941	-0.103	9.526
3-1	4.097	25.565	5.082	-0.247	12.609
3-2	4.168	24.64	5.288	-0.304	13.244
3-3	4.103	23.878	4.813	-0.34	12.128
4-1	3.423	22.561	4.141	-0.289	10.346
4-2	3.65	27.765	4.655	-0.348	11.746
4-3	3.356	23.243	4.215	-0.555	11.048
5-1	3.597	22.367	4.521	-0.381	11.747
5-2	3.082	19.922	3.691	-0.301	9.24
5-3	3.404	26.628	4.757	-0.696	12.383
6-1	2.832	24.084	3.844	-0.615	10.198
6-2	2.734	16.035	3.471	-0.332	8.599
6-3	3.212	19.492	3.879	-0.282	9.68

surface roughness was measured at the sample locations, cut from the latest tube, which surface has been produced with the exact same parameters as the tube used in the experiments here. The results of contact profilometer measurements, which are repeated 2 times in each sample are reported in Table 3.2. Using the correlation proposed by (K. Flack et al., 2016), dedicated to surfaces with negative skewness, the equivalent sand-grain roughness is calculated at each sample, for each of the obtained contact profilometer data rows. Then, the arithmetic mean is calculated, which is $k_s = 10.78\ \mu m$.

For evaluation of the experimental results, it is useful to express the roughness height in terms of non-dimensional distance, which is achieved by:

$$k_s^+ = \frac{k_s \rho u_\tau}{\mu} \tag{3.2}$$

with the friction velocity u_τ:

$$u_\tau = \sqrt{\frac{\tau_w}{\rho}} \tag{3.3}$$

4 Experimental methodology

In this chapter, the experimental procedure will be explained. It includes specification of the test matrix and the procedure for the data post processing is explained. Further, the experimental setup is validated.

4.1 Test parameters and procedure

The experimental data is acquired at steady state conditions, which means the pressure, mass flux, inlet temperature and heat flux need to be stable. The data is recorded within 60 seconds, with a acquisition frequency of 2 Hz. Change of the operating pressure is challenging for the components of the experimental facility, especially for seals. In order to reduce changes of pressure to a minimum, the pressure is kept constant within a day of measurements. After the pressure is set, the mass flow rate is adjusted to the desired value. Then, the desired inlet temperature is set. While the inlet temperature increases, the process valve which controls the mass flow rate needs to be carefully adjusted, since the flow rate depends on the density of the fluid at the valve, which in turn depends on the temperature of the fluid. In the mean time, the heat flux is increased in small steps, until the lowest value of the experimental matrix is reached. Once the desired parameters are reached, the facility is operated at stable conditions for at least 15 minutes, to ensure the flow to be fully developed. Then, the data is recorded. Afterwards, the heat flux is increased to the next higher desired value. After the largest heat flux is reached, the inlet temperature is increased to the next larger value of the matrix and the heat flux is reduced to the smallest corresponding value. Then the heat flux is increased again. On one day, the experiments of two different inlet temperatures can be carried out.

The experimental database created in this work should be representative to the application of supercritical pressure water in the core of an SCWR. In the given project, the thermodynamic parameters of the reactor design proposed by (Schulenberg & Otic, 2021) are exemplarily considered, but the horizontal rod bundle is replaced by a vertical tube. The system pressure is 25 MPa. Using the fluid-to-fluid scaling model of (Cheng et al., 2011):

$$\left(\frac{p}{p_c}\right)_{water} = \left(\frac{p}{p_c}\right)_{R134a} \tag{4.1}$$

the corresponding pressure in R134a is 4.6 MPa. For the scaling of the temperature, the following rule is applied:

$$\left(\frac{T - T_{pc}}{T_{pc} - T_c}\right)_{water} = \left(\frac{T - T_{pc}}{T_{pc} - T_c}\right)_{R134a} \tag{4.2}$$

The proposed reactor design consists of 7 horizontal flow passes, in which the coolant is heated up. The core inlet temperature is 310 °C and the core outlet temperature is 500 °C. Applying equation 4.2, the corresponding temperature range in R134a is 64 °C to 174 °C. The experimental inlet temperature and heat flux are varied on order to cover that temperature range as much as possible. The heat flux is scaled by:

$$\left(\frac{\dot{q}_w D}{\lambda_b \left(T_{pc} - T_c\right)}\right)_{water} = \left(\frac{\dot{q}_w D}{\lambda_b \left(T_{pc} - T_c\right)}\right)_{R134a} \tag{4.3}$$

The sub-channel hydraulic diameter in the proposed design is 4.61 mm and the heat flux for an average channel is 775 kW/m². In the hot channel, the heat flux is 1550 kW/m². Using equation 4.3, the corresponding heat flux in the 9 mm experimental tube, using R134a is 28 kW/m² for the average channel and 56 kW/m² for the hot channel. The mass flow rate is scaled by:

$$\left(\left(\frac{G \cdot D}{\mu_b}\right)^{0.8} \cdot Pr_b\right)_{water} = \left(\left(\frac{G \cdot D}{\mu_b}\right)^{0.8} \cdot Pr_b\right)_{R134a} \tag{4.4}$$

The mass flux of 2042 kg/m²s in an assembly of the reactor core is scaled to 900 kg/m²s in the R134a experiment.

Nevertheless, the goal of this experimental investigation is not to represent exactly the conditions of a specific reactor design, but to create a reference database, covering a wide range of operating conditions, to investigate the effect of the surface roughness on the heat transfer. Therefore, the experimental matrix is set up to cover those conditions. Also, the database shall be applicable to validation of e.g. Computational Fluid Dynamics (CFD) simulations. A second pressure of 4.35 MPa is investigated, since this is closer to the critical pressure of R134a and therefore, the variation of the thermophysical properties is stronger. The experiments are conducted at each mass flux and heat flux combination shown in Table 4.1, at each given pressure and at each given inlet temperature. The experiments are conducted in the smooth tube and at the same conditions in the rough tube.

Table 4.1: Experimental matrix for heat transfer experiments

p [MPa]	T_{in} [°C]	G [kg/m²s]	$\dot{q}_w$ [kW/m²]
4.6 4.35	50 60 70 80	500	20, 25, 30, 35, 40, 45, 50, 55, 60, 65, 70
		750	30, 35, 40, 45, 50, 55, 60, 65, 70, 75
		1000	40, 50, 60, 70, 80, 90, 100, 110, 120, 130
		1250	50, 60, 70, 80, 90, 100, 110, 120, 130, 140, 150
		1500	60, 70, 80, 90, 100, 110, 120, 130, 140, 150, 160, 170, 180
		1750	70, 80, 90, 100, 110, 120, 130, 140, 150, 160, 170, 180, 190
		2000	80, 90, 100, 110, 120, 130, 140, 150, 160, 170, 180, 190, 200

4.2 Data reduction

From the parameters measured in the experimental campaign, finally the heat transfer coefficient α and the Nusselt number Nu have to be calculated:

$$\alpha_n = \frac{\dot{q}_{w,n}}{T_{wi,n} - T_{b,n}} \tag{4.5}$$

$$Nu_n = \frac{\alpha_n d_h}{\lambda_{b,n}} \tag{4.6}$$

Here, $\dot{q}_w$ is the wall heat flux, T_{wi} is the wall temperature at the inner side of the tube, T_b is the bulk temperature of the coolant flow, d_h is the hydraulic diameter of the tube and λ_b is thermal conductivity of the fluid at bulk temperature. The index n refers to the measurement location. The wall heat flux $\dot{q_w}$ results from the voltage drop U and the electrical current I within the heated part of the test tube. Since the electrical resistivity of steel is depending on the temperature, the local voltage-drop and thus the locally released heat is depended on the local temperature of the test section. This results in a slight variation of the local released heat over the heated length. Taking the ratio of the local electric resistivity $\rho_{el,n}$ to the total electric resistivity $\rho_{el,tot}$ into account, the locally released heat is calculated as:

$$\dot{Q}_n = U \cdot I \cdot \frac{\rho_{el,n}}{\rho_{el,tot}} \frac{L_n}{L_{heat}} \tag{4.7}$$

with L_{heat} as the heated length and L_n as the distance from one to another thermocouple. A small fraction of the released heat is dissipated to the environment, as heat loss $\dot{Q}_{loss}$, which is determined as a function of the difference of mean test section temperature to the ambient (see equation 3.1). Assuming the heat loss is distributed uniformly over the test section, the local heat flux is calculated:

$$\dot{q}_{w,n} = \frac{\dot{Q}_n - \frac{L_n}{L_{heat}} \dot{Q}_{loss}}{\pi \cdot d_i \cdot L_n} \tag{4.8}$$

Further, in equations 4.5 and 4.6 the bulk temperature is required to calculate the heat transfer coefficient α or the Nusselt number Nu respectively. This is obtained from the bulk enthalpy h_b, using the National Institute of Standards and Technology (NIST) Standard Reference Database 23, Version 10 (Lemmon et al., 2018). The bulk enthalpy in turn is obtained, using the energy balance:

$$h_{b,n+1} = h_{b,n} + \frac{\dot{Q}_n - \frac{L_n}{L_{heat}} \dot{Q}_{loss}}{\dot{m}} \tag{4.9}$$

where $\dot{m}$ is the mass flow rate which is measured in the experiment. Initially, this requires the inlet enthalpy, which is obtained from the NIST database, using the measured inlet temperature T_{in} and the measured pressure at the inlet p_{in}. Then, the bulk temperature T_b is obtained, using the bulk enthalpy h_b from equation 4.9 and the arithmetic mean p_m of the measured pressure at the inlet p_{in} and at the outlet p_{out}.

Furthermore, the temperatures T_{wi} at the inner side of the tube need to be calculated from the measured temperatures T_{wo} at the outer side of the wall. As shown in (Feuerstein, 2019) and also shown for the present experimental investigation in section 4.3.1, the axial heat conduction can be neglected. Thus, the problem is described by the one-dimensional heat conduction in the radial direction of the tube.

$$\frac{1}{r}\frac{d}{dr}\left(r\frac{dT}{dr}\right)+\frac{\dot{q}_v}{\lambda_s}=0 \tag{4.10}$$

Here, r is the radius of the tube, λ_s is the thermal conductivity of the steel and $\dot{q}_v$ is the volumetric heat, released in the tube wall due to the electrical power. The boundary conditions required to solve the differential equation 4.10 are the measured outer wall temperature and the beforehand determined heat loss to the ambient from the outer wall of the tube:

$$T(r_{wo})=T_{wo} \tag{4.11}$$

$$-\lambda_s\left.\frac{dT}{dr}\right|_{r=r_{wo}}=\dot{q}_{loss} \tag{4.12}$$

The volumetric heat flux $\dot{q}_v$ is calculated locally as:

$$\dot{q}_v=\frac{4\dot{Q}_n}{\pi\left(d_o^2-d_i^2\right)\cdot L_n} \tag{4.13}$$

Finally, the inner wall temperature is calculated as:

$$T_{wi,n}=T_{wo,n}+\frac{\dot{q}_v}{16\lambda_s}\left(d_o^2-d_i^2\right)+\frac{d_o}{2\lambda_s}\left(\frac{\dot{q}_v\cdot d_o}{4}-\dot{q}_{loss}\right)ln\left(\frac{d_i}{d_o}\right) \tag{4.14}$$

4.3 Uncertainty analysis

All measurement devices have a measurement uncertainty, which is defined here as the standard deviation σ of the measured values around the true value. As the previous section 4.2 shows, the measured quantities obtained in the experiment are post-processed through as series of equations, until the final results, the inner wall temperature $T_{w,i}$, the heat transfer coefficient α and the Nusselt number Nu are obtained. Thus, it is necessary to propagate the uncertainties of the measured input values to the final calculated quantities. Table 4.3 summarizes the uncertainties of the measurement devices. The measurement uncertainty of the mass flow rate increases, when the mass flow rate is

Table 4.2: Uncertainty of the measurement devices

Parameter	Uncertainty [%]
Fluid temperatures	max(1 K, 0.75 % of the measured value in °C)
Wall temperatures	max(0.5 K, 0.4 % of the measured value in °C)
Pressure	0.1 % (of full sensor range)
Flow rate	0.15 % - 0.26 %
Data logger voltage	0.03 %
Data logger temperature	0.5 K
Current	1.5 %
Length	0.5 mm
Tube inner diameter	0.03 mm

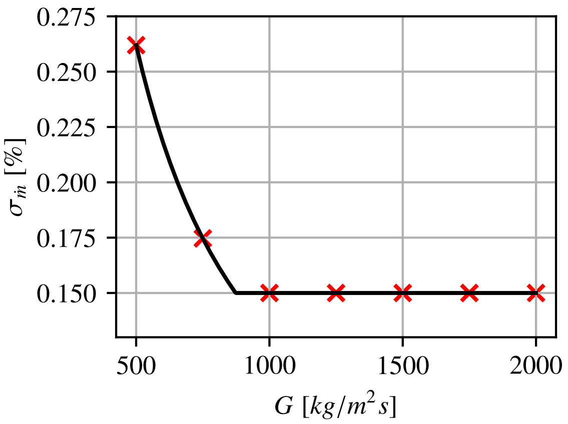

Figure 4.1: Variation of uncertainty of the mass flow rate with the mass flux

smaller than 200 kg/h. In the present test section, this corresponds to a mass flux of 873.3 kg/m²s. The variation in the uncertainty of the Coriolis flow meter measurement is shown as a function of the mass flux in the given test section in Figure 4.1. Based on the individual measurement uncertainties σ_i of the input quantities, the uncertainty of a derived parameter is calculated under the assumption that the measurement errors are normally distributed and independent of each other:

$$\sigma_f^2 = \sum_{i=1}^{n} \left(\frac{\partial f}{\partial P_i} \sigma_i \right)^2 \tag{4.15}$$

Here, $(\partial f / \partial P_i)$ is the sensitivity of the function f to a change of the parameter P_i, which has an uncertainty of σ_i. For example, the uncertainty of the heat transfer coefficient α, which is calculated by equation 4.5, the uncertainty is calculated as:

$$\sigma_\alpha^2 = \left(\frac{1}{T_{w,i} - T_b} \cdot \sigma_{\dot{q}_w} \right)^2 + \left(\frac{-q}{(T_{w,i} - T_b)^2} \cdot \sigma_{T_{w,i}} \right)^2 + \left(\frac{q}{(T_{w,i} - T_b)^2} \cdot \sigma_{T_b} \right)^2 \tag{4.16}$$

In this way, the uncertainties σ_i were computed step by step, storing the results of the intermediate steps. The propagation of the measurement uncertainty is performed for every experimental data point and is given as a percentage of the actually measured or calculated value. Table 4.3 shows the minimum, maximum and arithmetic mean of all the uncertainties σ_i of the boundary conditions

Table 4.3: Summary of the uncertainties of the derived measurement parameters for all obtained data points

Parameter	σ_{min} [%]	σ_{max} [%]	$\overline{\sigma}$ [%]
$\overline{p}$	0.92	0.98	0.95
G	0.68	0.72	0.69
$\dot{q}_w$	2.04	2.27	2.16
T_{in}	1.38	2.25	1.76
h_b	0.36	0.62	0.5
$T_{w,i}$	0.47	1.11	0.67
α	0.98	42.44	5.65
Nu	1.21	42.44	5.77

among all the obtained data points, of both the boundary conditions and key derived parameters, given as percentages of the respective values. It can be seen, that the maximum uncertainties of the heat transfer coefficient α and of the Nusselt number Nu are large, compared to the uncertainties of the other parameters. As can be seen in equation 4.16, this occurs when the temperature difference between the wall and the bulk fluid, $T_{w,i} - T_b$, becomes small. However, the mean uncertainty of the heat transfer coefficient is 5.56 % and of the Nusselt number is 5.77 %. Figure 4.2 shows the percentage distribution of the respective uncertainties across all measured data. The y-axis indicates the percentage of data points with uncertainty values less than the corresponding x-axis values. It can be seen that 91. 1 % of the data points have an uncertainty of the heat transfer coefficients less than 10 % and only very few data points have an uncertainty greater than 20 %. The uncertainties of the Nusselt numbers are distributed similarly, but shifted to slightly larger uncertainties. 90.9 % of the data points have an uncertainty of the Nusselt number, which is smaller than 10 %. Figure 4.3 shows the variation of the uncertainty of the heat transfer coefficient with the temperature difference from the wall to the bulk. It clearly shows that the uncertainty of the heat transfer coefficient, σ_α, is

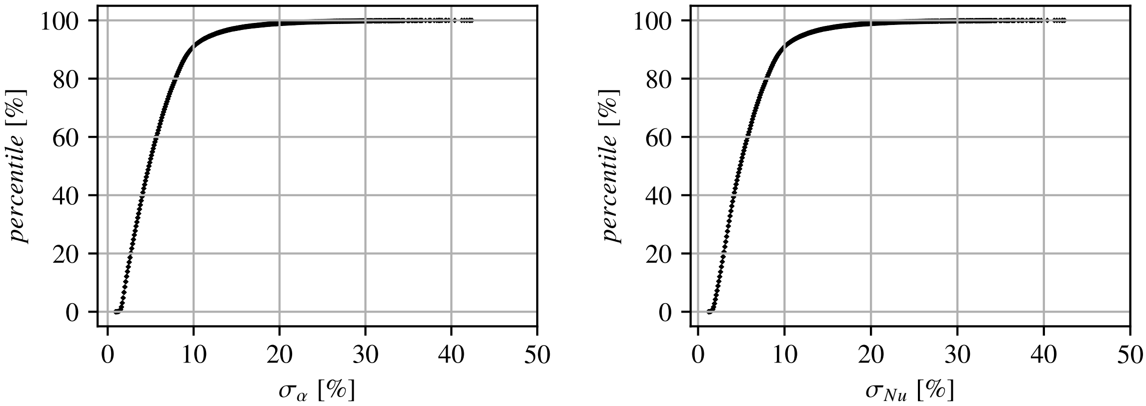

(a)

(b)

Figure 4.2: Distribution of the uncertainties of the heat transfer coefficient (a) and of the Nusselt number (b) for all data points

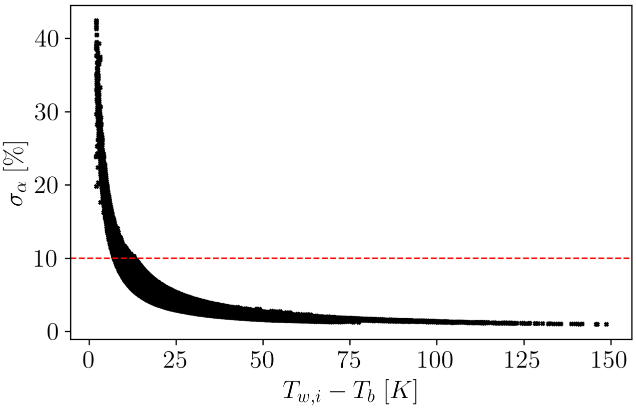

Figure 4.3: Variation of the uncertainty of the heat transfer coefficient for all experimental data with the temperature difference between wall and bulk

only large when the temperature difference between the wall and the bulk is small.

4.3.1 Axial heat conduction

As mentioned in Section 4.2, the axial conduction of heat is neglected. In this section, it is proven that heat conduction is negligible throughout the entire experimental campaign. The heat flux conducted in a steel tube is calculated as:

$$\dot{Q}_{cond} = -\lambda_s \cdot A\frac{dT}{dx} \tag{4.17}$$

, where A is the cross section of the tube, λ_s is the thermal conductivity of steel and x is the coordinate in streamwise direction. The amount of conducted heat in between all thermocouple positions is calculated for all experimental cases, using all of the actual experimental data and put into relation to the electrical heat which is released in the same section of the tube. In most cases, the maximum amount of heat conducted between two measurement locations is less than 0. 3% of the electrical heat released in that section. In the most severe case, the heat conducted is 1. 38% of the electrical heat. Thus, the axial conduction of heat is negligible throughout the experimental campaign.

4.4 Verification of the measurement system

Besides the evaluation of uncertainty propagation presented in the previous section, the experimental results for sub-critical pressure conditions can be compared with predictions of well-accepted correlations. In addition, the heat balance is checked. Finally, the assumption that the thermal conduction in the steel tube can be neglected in axial direction, is proven. This procedure ensures that there is no major failure of the measurement system.

4.4.1 Test of sub-critical pressure heat transfer

For single phase pipe flow at sub-critical pressure conditions, the Dittus-Boelter correlation (Dittus & Boelter, 1930) as well as the Gnielinski correlation (Gnielinski, 1975) are well accepted. In order to proof that the measurement system is set up properly, experiments with single phase flow at subcritical pressure (3.6 MPa) are conducted and the measured heat transfer coefficients are compared to the heat transfer coefficients predicted by the correlations. Figure 4.4 exemplarily shows the results obtained for a small mass flux and a small heat flux obtained in the (a) smooth tube and (c) rough tube, as well as the results obtained for a large mass flux and a large heat flux in the (b) smooth tube and (d) rough tube. The measurement uncertainty is given by the orange error bars. It can be seen, that the trend is captured well by both of the correlations, and is almost perfectly reproduced by the Gnielinksi correlation. This indicates that the experimental setup is correct. Furthermore, the predictions of the correlations against all conducted sub-critical pressure cases are evaluated, in terms of the mean error (ME) μ, the MAE $|\mu|$ and the standard deviation (STD) σ,

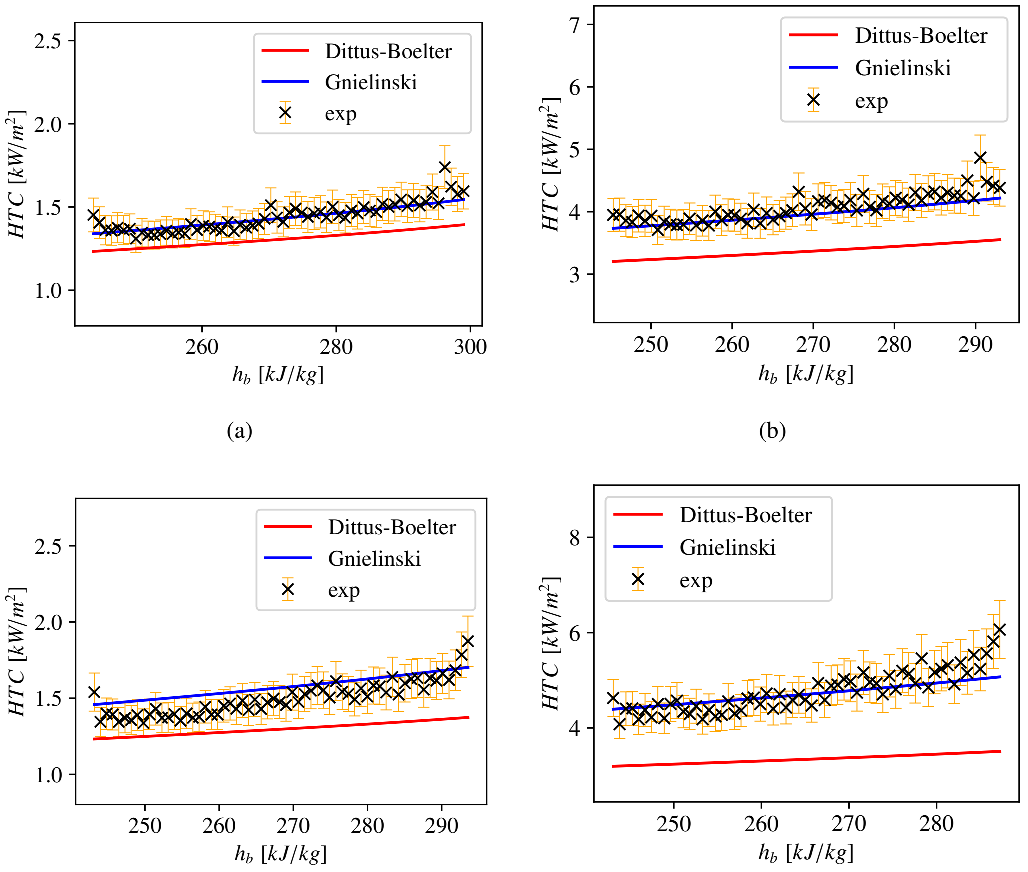

(a) (b) (c) (d)

Figure 4.4: Experiment at 3.6 MPa in smooth tube with (a) mass flux of 600 kg/m²s and heat flux of 26 kW/m² and (b) mass flux of 2000 kg/m²s and heat flux of 74 kW/m² and in rough tube with (c) mass flux of 600 kg/m²s and heat flux of 26 kW/m² and (d) mass flux of 2000 kg/m²s and heat flux of 74 kW/m²

which are defined as:

$$\mu = \frac{1}{N} \sum_{i=1}^{N} \frac{\alpha_{c,i} - \alpha_{exp,i}}{\alpha_{exp,i}} \cdot 100 \tag{4.18}$$

$$|\mu| = \frac{1}{N} \sum_{i=1}^{N} \frac{|\alpha_{c,i} - \alpha_{exp,i}|}{\alpha_{exp,i}} \cdot 100 \tag{4.19}$$

$$\sigma = \sqrt{\frac{1}{N-1} \sum_{i=1}^{N} \left(\frac{\alpha_{c,i} - \alpha_{exp,i}}{\alpha_{exp,i}} \cdot 100 - \mu \right)^2} \tag{4.20}$$

The results are shown in Table 4.4, separately for the smooth tube and for the rough tube. The heat transfer coefficients predicted by the Gnielinski correlation are very close to the experimental results. Since the wall friction is considered in that correlation, a good agreement in the smooth, as well as in the rough tube is achieved. This is an indication, that the experimental setup as well as the data reduction as presented in section 4.2 are correct. The Dittus-Boelter correlation has the tendency to under-predict the experimentally obtained heat transfer coefficient. Since the enhanced heat transfer due to wall roughness is not considered by the Dittus-Boelter correlation, the heat transfer is underestimated a bit more in the rough tube.

Table 4.4: Comparison of Gnielinski and Dittus-Boelter correlations with results of sub-critical experiments

Correlation	smooth			rough		
	μ [%]	$\lvert\mu\rvert$ [%]	σ [%]	μ [%]	$\lvert\mu\rvert$ [%]	σ [%]
Gnielinski	-3.76	6.44	8.0	1.35	6.19	8.98
Dittus Boelter	-13.8	15.53	8.33	-19.5	21.38	10.96

4.4.2 Reproducibility of sub-critical pressure experiments

Furthermore, reproducibility of experimental results needs to be demonstrated beforehand the experimental campaign. Of course, also reproducibility of results at supercritical pressure is important and will be discussed in Chapter 4.4.3. This is also done beforehand with single phase sub-critical pressure heat transfer experiments, which are conducted at different days. Figure 4.5 shows the measured wall temperatures and heat transfer coefficients. It can be seen, that the results almost overlap with each other, thus reproducibility is proven.

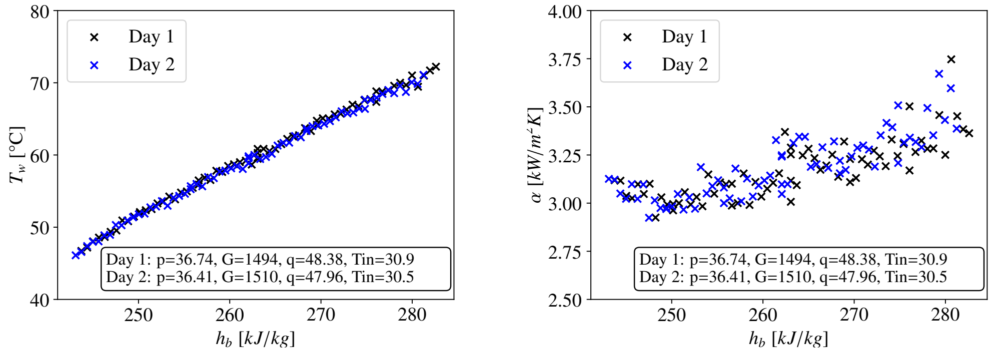

(a) (b)

Figure 4.5: Reproduced sub-critical heat transfer experiment

4.4.3 Reproducibility of supercritical pressure experiments

Reproducibility of experimental results is important in order to guaranty the reliability of the obtained experimental results. Therefore, some cases throughout the whole range of experimental conditions have been reproduced. Some of the repeated cases from the rough tube are shown exemplarily in Figures 4.6 - 4.8. Under normal heat transfer conditions, the results are always accurately reproducible, as shown in Figure 4.6 for (a) p=4.35 MPa, G=1000 kg/m²s, q=40 kW/m² and (b) p=4.6 MPa, G=1750 kg/m²s and q=100 kW/m². In general, results for cases with heat transfer deterioration are also reproducible. Exemplarily, the heat transfer coefficients obtained for p=4.35 MPa and (a) G=500 kg/m²s, q=70 kW/m² and (b) G=1000 kg/m²s, q=130 kW/m²s are shown in Figure 4.7. Along most parts of the tube, the heat transfer coefficients can be reproduced accurately. Some small deviations can be observed at the onset point of the heat transfer deterioration. In Figure 4.7 (a), heat transfer coefficient drops down to a lower level, close to the inlet. In the repetition of the case in the second day, heat transfer coefficient drops at slightly larger

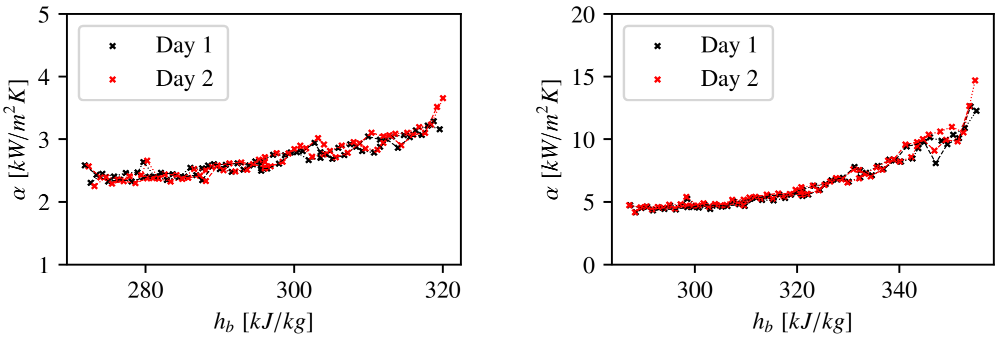

(a) (b)

Figure 4.6: Reproducibility of heat transfer coefficients in normal heat transfer regime at (a) p=4.35 MPa, G=1000 kg/m²s, q=40 kW/m² and (b) p=4.6 MPa, G=1750 kg/m²s and q=100 kW/m²

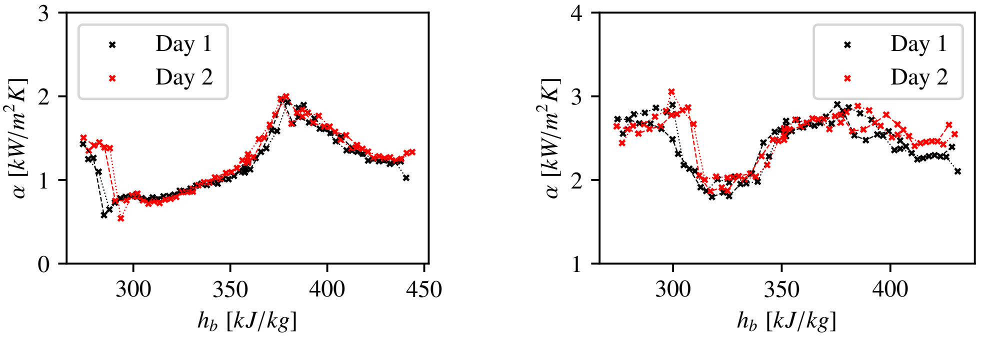

(a) (b)

Figure 4.7: Reproducibility of heat transfer coefficients in DHT regime at p=4.35 MPa and (a) G=500 kg/m²s, q=70 kW/m² and (b) G=1000 kg/m²s, q=130 kW/m²s

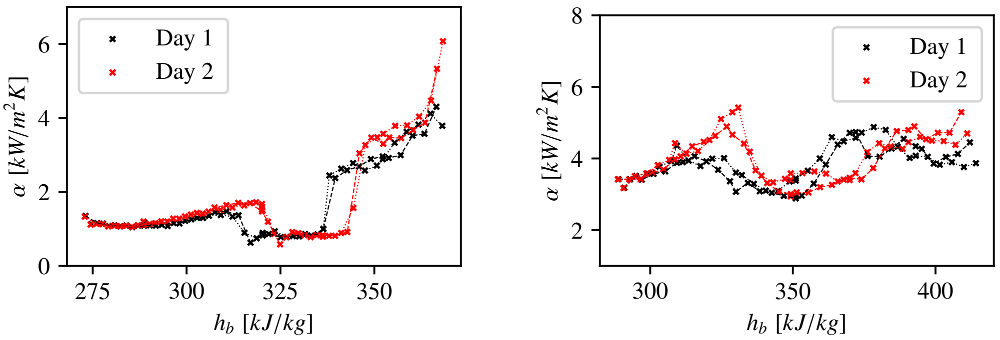

(a) (b)

Figure 4.8: Examples for bad reproducibility of heat transfer coefficients in DHT regime at (a) p=4.35 MPa, G=500 kg/m²s, q=40 kW/m² and (b) p=4.6 MPa, G=1250 kg/m²s, q=130 kW/m²

bulk enthalpy, but down to the same level. Further downstream, (at larger bulk enthalpy), the results obtained at day 1 are matching with the results obtained later at day 2. However, sometimes the experimental results within the deteriorated heat transfer regime could not exactly be reproduced.

Figure 4.8 shows heat transfer coefficients obtained for (a) p=4.35 MPa, G=500 kg/m²s, q=40 kW/m² and (b) p=4.6 MPa, G=1250 kg/m²s, q=130 kW/m². In (a), it can be seen that the onset of heat transfer deterioration on the second day was shifted by about 10 kJ/kg to larger bulk enthalpy. Also the point where the heat transfer recovers to the normal level was shifted by the same amount. Upstream of the part of the tube where DHT is present, the results are in good agreement. Also the amount by what the heat transfer is reduced remains the same in the repeated experiment. Figure 4.7 (b) is one of the examples with the most significant deviations in between the results obtained at day 1 and day 2. However, at least qualitatively, the trend is reproduced well. First, heat transfer coefficient increases, then it drops down and later it recovers. Within all repeated experiments, the mean deviation of the heat transfer coefficients is 3.8% with a standard deviation of 3.6%, even though locally, like in Figure 4.8 (a), the deviations can be large, when the onset of DHT is shifted along the tube to a different bulk enthalpy. The reproducibility in the smooth tube is similar to the examples shown here for the rough tube.

5 Results and discussion

In this chapter, first, general findings of the experiments, such as different heat transfer regimes and reproducibility, are addressed. The following discussion of the experimental results in separated into two parts: In the first part, results of the smooth tube are shown and the influence of the experimental boundary conditions on the heat transfer is discussed. In the second part, the results of the rough tube are compared to the results of the smooth tube, in order to highlight the effect of the wall roughness on the heat transfer under supercritical pressure conditions. The data are available from the Institute of Applied Thermofluidics (IATF) at KIT upon reasonable request.

5.1 General findings and overview

As introduced in Section 2.2.1, heat transfer at supercritical pressure conditions can be categorized into three regimes of normal heat transfer (NHT), deteriorated heat transfer (DHT) and improved heat transfer (IHT). In the following, examples for NHT and DHT are given and the characteristics are pointed out. The category of IHT is not distinguished from the others in this investigation due to the unclear definition.

5.1.1 Normal heat transfer

At low heat fluxes, wall temperature profiles in supercritical pressure heat transfer experiments appear to be very similar like those, obtained for single phase heat transfer at sub-critical pressures.

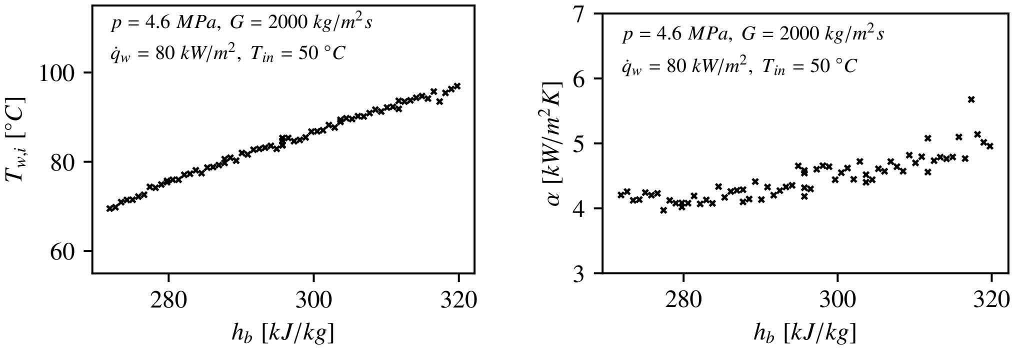

(a)

(b)

Figure 5.1: Profiles of (a) wall temperature and (b) heat transfer coefficient in the normal heat transfer regime for p=4.6 MPa, G=2000 kg/m²s and q=80 kW/m²

This is referred as the NHT regime. Figure 5.1 shows experimentally obtained wall temperature and heat transfer coefficient at $p = 4.6\ MPa$, $G = 2000\ kg/m^2s$ and $\dot{q}_w = 80\ kW/m^2$, exemplarily for the NHT regime. The characteristic of that heat transfer regime is a almost linear increasing wall temperature profile, with slightly decreasing slope at larger bulk enthalpies. This is caused by slightly increased heat transfer coefficient, due to increasing bulk Reynolds number, which is attributed to the decrease of the viscosity with increase in the bulk enthalpy.

5.1.2 Deteriorated heat transfer

When the heat flux, applied to a fluid at supercritical pressure is large enough, heat transfer deterioration can appear. Although there is no exact definition available, in general, heat transfer deterioration is related to a local decrease in the heat transfer coefficient, which results in a wall temperature peak. Figure 5.2 exemplarily shows the wall temperature profiles at (a) $p = 4.6\ MPa$, $G = 750\ kg/m^2s$ and $\dot{q}_w = 60\ kW/m^2$ and (b) $p = 4.6\ MPa$, $G = 2000\ kg/m^2s$ and $\dot{q}_w = 180\ kW/m^2$. At the smaller mass flux, DHT is clearly identifiable by a wall temperature peak. On the other hand, at a larger mass flux, DHT manifests as a more gradual rise in the wall temperature profile rather than a distinct peak. Generally, there is no clear border, which separates the DHT regime from the NHT regime. In addition to checking the wall temperature profiles for temperature peaks, the criterion of (Koshizuka et al., 1995), which was introduced in section 2.2.1.1, can also be used. In order to identify DHT, the local heat transfer coefficient is related to the heat transfer at normal conditions. In the present investigation, the heat transfer coefficient α_G, predicted by the Gnielinski correlation (Gnielinski, 1975) is reasonable to chose, since wall friction is considered here. Figure 5.3 shows measured heat transfer coefficients related to heat transfer coefficients, predicted by the Gnielinski correlation at pressure of $p = 4.6\ MPa$ and (a) mass flux of $G = 1000\ kg/m^2s$ and (b) mass flux of $G = 2000\ kg/m^2s$. The vertical dashed black line indicates the pseudocritical bulk enthalpy and the horizontal blue dashed line indicates the value of 0.3, which was proposed by (Koshizuka et al., 1995) to distinguish NHT from DHT. The value of 0.3 is a choice, made by Koshizuka, but does not have a physical meaning. For the present experimental data, it seems to be reasonable to set the threshold value to a larger value, like e.g. 0.7. Apart from that, the results

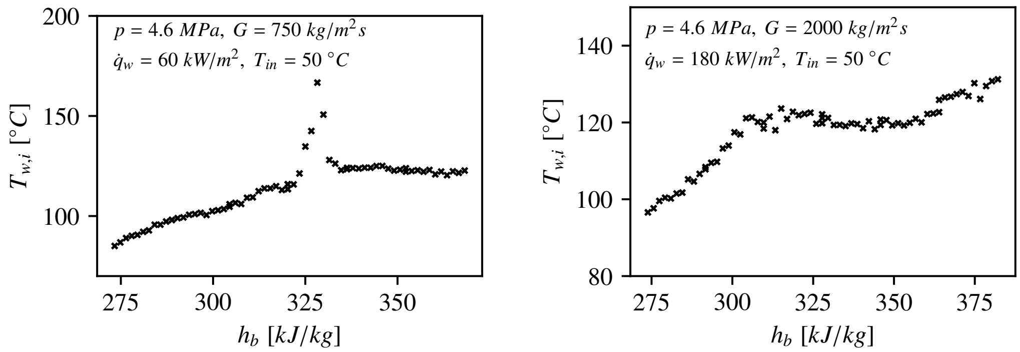

(a)

(b)

Figure 5.2: Wall temperature profiles with heat transfer deterioration at (a) small mass flux (p=4.6 MPa, G=750 kg/m²s and q=60 kW/m²) and (b) large mass flux (p=4.6 MPa, G=2000 kg/m²s and q=180 kW/m²)

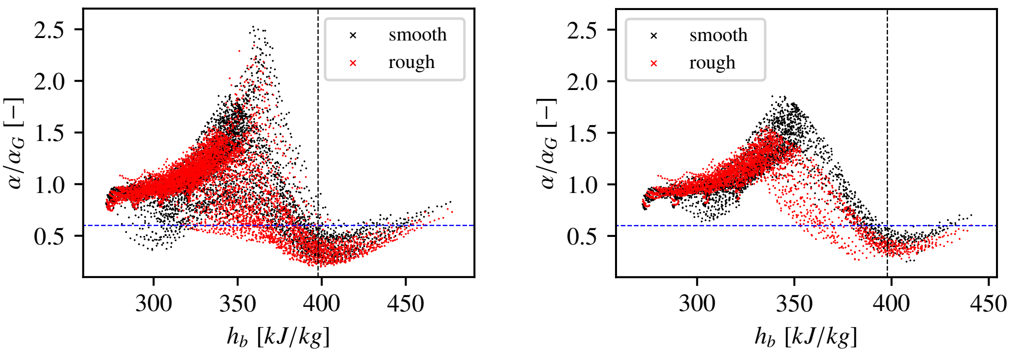

(a)

(b)

Figure 5.3: Ratio of measured heat transfer coefficient to Gnielinski heat transfer coefficient at mass flux of (a) 1000kg/m²s and (b) 2000 kg/m²s

shown in Figure 5.3 can be discussed in a qualitative manner. When the bulk enthalpy is far lower than the pseudocritical value, the ratio of experimentally obtained heat transfer coefficient α to normal condition heat transfer coefficient α_G is close to 1, thus the NHT regime is present. Around the pseudocritical point, the ratio of heat transfer coefficients becomes the smallest. Typically, DHT appears, slightly before the bulk flow reaches the pseudocritical point, and heat transfer recovers at larger bulk enthalpies. The results in Figure 5.3 indicate, that DHT is appearing in the smooth tube as well as in the rough tube, but also differences can be observed. This will be discussed in detail in section 5.3. The phenomenon of heat transfer deterioration is of great scientific and technical importance. From an engineering point of view, temperature peaks are problematic, since when designing a technical component, it has to be made sure that the temperatures will always stay below the limitations of the material. On the other hand, DHT is hard to be predicted by existing models and correlations.

Besides DHT, data points in Figure 5.3 with $\alpha/\alpha_G > 1$ could be referred as improved heat transfer. Typically, heat transfer is improved first and deteriorates when the bulk enthalpy approaches the pseudocritical value. IHT is of less significance, since from engineering point of view, a design will be conservative in terms of limitations of the materials, when those effects would be neglected. All the three, NHT, DHT and IHT have in common, that there is no clear definition to distinguish those regimes from the normal heat transfer regime.

In the evaluation of the present experimental results, heat transfer deterioration is identified by peaks in the trend of the wall temperatures, which are corresponding to valleys in the trend of heat transfer coefficients. Further, buoyancy and acceleration effects are quantified.

5.2 Experimental results - smooth tube

In this section, the influence of the experimental boundary conditions, namely the mass flux, heat flux, inlet temperature and pressure on the heat transfer to supercritical R134a are discussed. To provide a general overview, first, only results in the smooth tube are considered. In section 5.3, the impact of the surface roughness will be pointed out.

5.2.1 Effect of the mass flux

The influence of the mass flux on the heat transfer is investigated by comparing results at constant pressure, heat flux and inlet temperature and varying mass flux. Figure 5.4 shows experimentally obtained (a) wall temperature, (b) heat transfer coefficient and (c) buoyancy parameter, obtained for $p = 4.6\ MPa$, $\dot{q}_w = 60\ kW/m$ and $T_{in} = 50\ °C$. The buoyancy parameter (Figure 5.4 (c)) is calculated, using equations 2.21 and 2.24. According to (J. Jackson, 2013), heat transfer is affected by buoyancy for $Bu > 10^{-5}$. When for a constant heat flux the mass flux is reduced, the range of bulk enthalpy which is covered in the test tube obviously becomes larger. The inlet enthalpy is around 275 kJ/kg for all of the three cases presented in the figure and the outlet enthalpy is around 350 kJ/kg for the mass flux of 1000 kg/m²s, around 370 KJ/kg for the mass flux of 750 kg/m²s and around 420 kJ/kg for the mass flux of 500 kg/m²s, which is the only case, where the pseudocritical point (indicated as gray dotted vertical line in the figure) is exceeded in the bulk. Looking in the cross-section of the tube, it can be seen that for mass flux of 1000 kg/m²s the pseudocritical temperature is just reached at the wall close to the outlet. In this case, normal heat transfer behavior is observed. In contrast to that, for a lower mass flux of 750 kg/m²s, a sharp temperature peak is

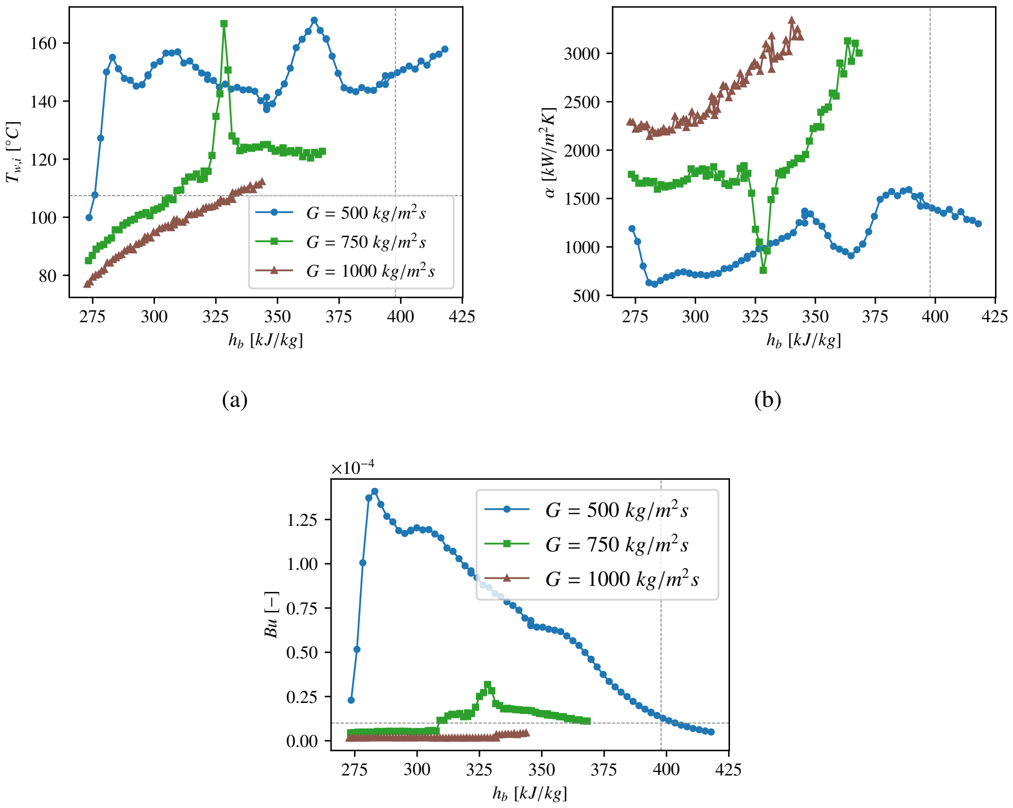

(a)

(b)

(c)

Figure 5.4: (a) Wall temperature, (b) heat transfer coefficient and (c) buoyancy parameter at p=4.6 MPa, q=60 kW/m², Tin=50°C and different mass flux (Legend in (a) and (c))

observed around a bulk enthalpy of 325 kJ/kg. This temperature peak refers to the effect of heat transfer deterioration. It corresponds to a sharp drop in the heat transfer coefficient (Figure 5.4 (b)), and to a peak in the buoyancy parameter (Figure 5.4 (c)). In this case, the pseudocritical temperature is exceeded at the wall, shortly downstream of the location that shows the wall temperature peak. The effect of laminarisation due to the buoyancy effect may explain the sharp drop in the heat transfer coefficient. Finally, at the lowest mass flux of 500 kg/m^{2}s, the wall temperature immediately jumps to a higher level and forms a plateau, which is also dedicated to the effect of DHT. The buoyancy parameter clearly exceeds the threshold of $1 \cdot 10^{-5}$ for which the effect of buoyancy cannot be neglected. At this point, it can be concluded that for low mass flux - and thus low Reynolds number - DHT can appear. On the other hand, this is obvious, since due to larger heat per mass of fluid, the fluid temperature is larger. As the pseudocritical temperature is exceeded, the variations of the thermophysical properties becomes significant, which actually is the prerequisite for DHT.

Therefore, also the results obtained at a constant rate of heat per mass of fluid $\dot{q}_w/G$ are compared in Figure 5.5, for different combination of heat flux and mass flux at $\dot{q}_w/G = 0.08$. In this case, the range of bulk enthalpy is the same for all the cases compared. Looking at Figure 5.5 (a), sharp temperature peaks for the low mass fluxes $G = 500\ kg/m^s$ and $G = 750\ kg/m^2s$ are observed, which are clearly related to DHT. As before, the fluid temperature is crossing the pseudo-critcal

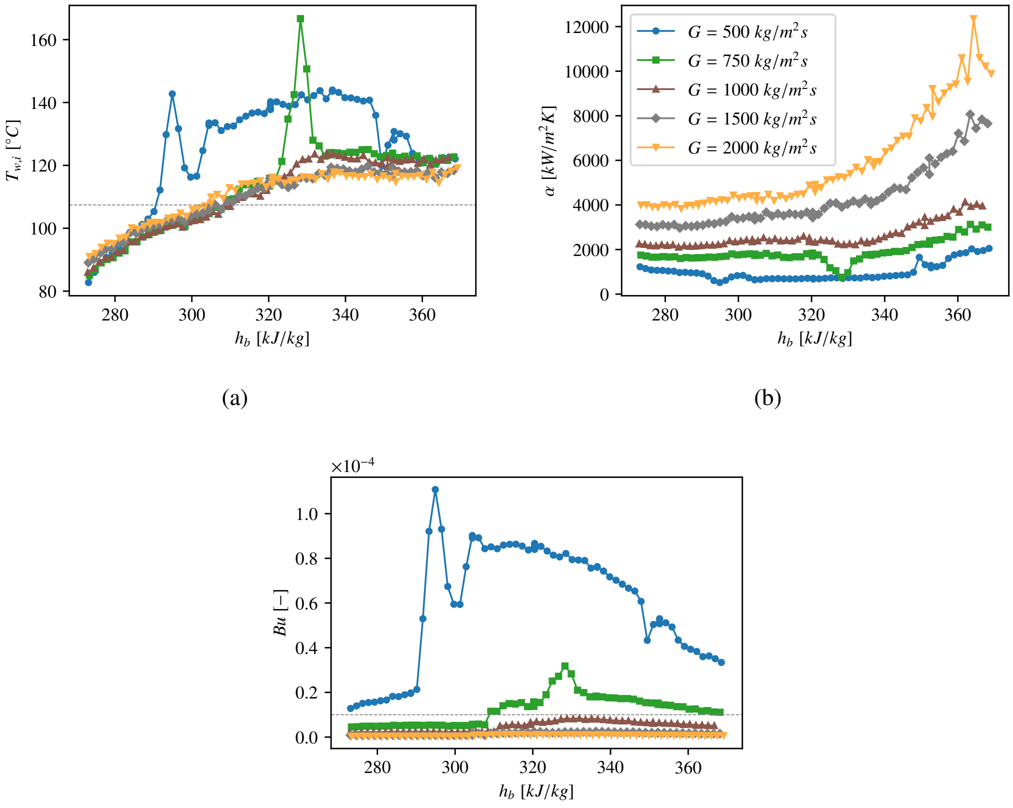

(a)

(b)

(c)

Figure 5.5: (a) Wall temperature, (b) heat transfer coefficient and (c) buoyancy parameter at q/G=0.08 (Legend in (b))

temperature, resulting in significant variation of the thermophysical properties, which can cause DHT. However, the pseudocritical temperature is exceeded at the wall for all of the cases shown here, while the bulk temperature is below the pseudocritical value. This means strong variation of the properties is present in all of the cases. As the Reynolds number is larger, for larger mass flux, the effect of buoyancy is reduced (see equations 2.21 and 2.24). Figure 5.5 shows that the threshold value of $1.0 \cdot 10^{-5}$ is not exceed for the cases with mass flux of 1000, 1500 and 2000 kg/m²s. Also, the heat transfer coefficient is larger for larger mass flux, which is obviously the case for larger Reynolds numbers.

In conclusion, DHT due to buoyancy is more likely to appear for small mass flux. The pseudocritical temperature needs to be crossed, so that strong variation of the fluid properties is present, but this does not necessarily trigger the DHT. If the Renolds number is large, the effect of buoyancy on the heat transfer remains still low and NHT is present.

5.2.2 Effect of heat flux

Figure 5.6 shows experimentally obtained (a) wall temperature, (b) heat transfer coefficient and (c) buoyancy parameter, obtained for $p = 4.6\ MPa$, $G = 500\ kg/m^2s$ and $T_{in} = 50\ °C$, with different heat flux. The buoyancy parameter (Figure 5.6 (c)) is calculated, using equations 2.21 and 2.24. For the smallest heat flux of $\dot{q}_w = 20\ kW/m^2$, normal heat transfer is present. The temperature profile looks like sub-critical single phase heat transfer. In this case, the wall temperatures stay below the pseudocritical temperature of 107.3 °C, which is indicated by a gray dashed line in the figure All other cases shown in Figure 5.6 show sharp temperature peaks, followed by a plateau of larger wall temperatures, which corresponds to a sudden decrease in heat transfer coefficient. Heat transfer remains deteriorated for a certain enthalpy range, and that range increases with increasing heat flux. Further, increasing heat flux shifts the temperature peak to lower bulk enthalpy level. It can be observed, that temperature peaks form, right after the pseudocritical temperature is exceeded. The bulk temperature is below the pseudocritical temperature within the entire tube, for all the cases shown here. Therefore, strong variation of the thermophysical properties are present in radial direction of the tube. The strong variation of the density leads to a reduction of the turbulence in the near wall layer, deteriorating the heat transfer, which in turn further increases the wall temperature, followed by lower density, which further enhances this effect and a pronounced temperature peak is formed. Even local laminarisation near the wall may occur here. Figure 5.6 shows the corresponding buoyancy parameter. The threshold value of $Bu > 10^{-5}$, proposed by (J. Jackson, 2013), for which heat transfer is affected by buoyancy is exceeded by an order of magnitude around the temperature peaks and decreases over the following plateau of large temperatures. As the impact of buoyancy on the heat transfer diminishes, heat transfer recovers to a normal level, which can be observed for the cases with $\dot{q}_w = 40$ and $50\ kW/m^2$.

In addition, results obtained for $G = 2000\ kg/^2s$, which are shown in Figure 5.7, are discussed here as well. In contrast to the results obtained for lower mass flux of 500 kg/m²s, no sharp peak of wall temperature is observed for any of the results here. The results obtained for the heat fluxes $\dot{q}_w = 80$, 100, 120 and 140 kW/m^2 show monotonically increasing wall temperature profiles, and

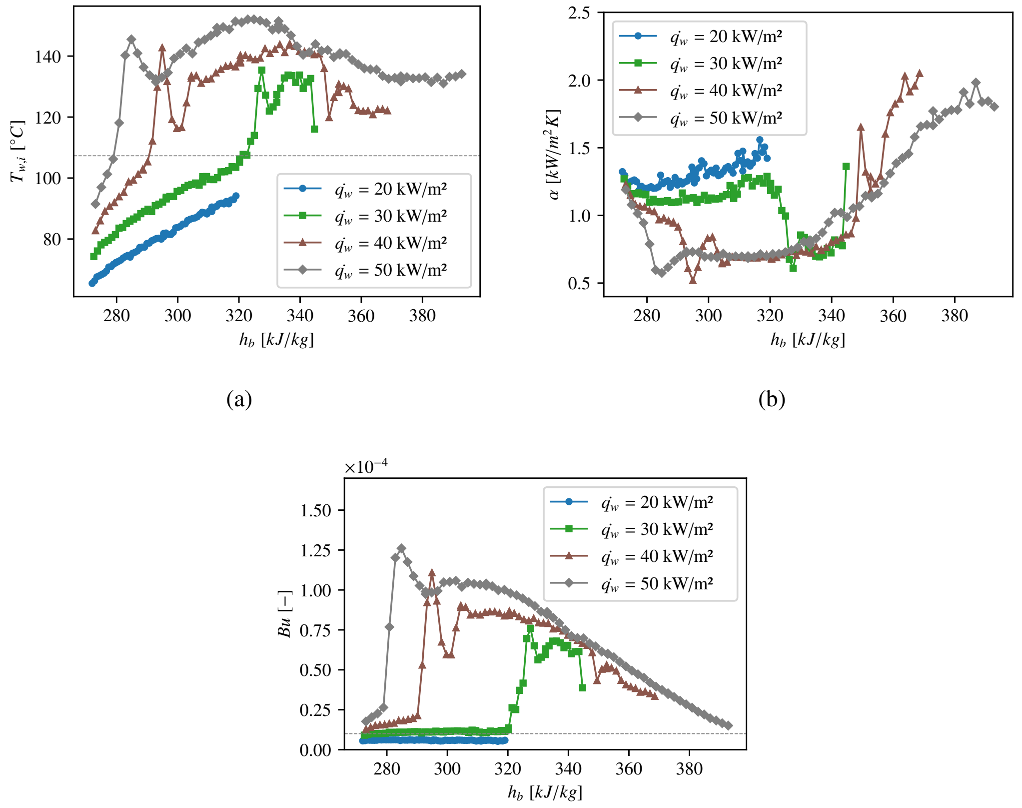

(a)

(b)

(c)

Figure 5.6: (a) Wall temperature, (b) heat transfer coefficient and (c) buoyancy parameter at p=4.6 MPa, G=500 kg/m²s, Tin=50°C and different heat flux

the heat transfer coefficients increase along the heated section, as the Reynolds number increases. These results are in the normal heat transfer regime. The wall temperature profile obtained for $\dot{q}_w = 160\ kW/m^2$ first monotonically increases, but the slope increases, when the wall temperature passes by the pseudocritical value. Following that, the temperature profile remains almost flat, indicating that heat transfer is very efficient. The flat temperature profile in the bulk enthalpy range from around 320 kJ/kg to 360 kJ/kg corresponds to a strongly increasing heat transfer coefficient. The results for $\dot{q}_w = 180\ kW/m^2$ and $\dot{q}_w = 200\ kW/m^2$ show a valley of the heat transfer coefficient, as the wall temperature exceeds to pseudocritical temperature, corresponding to some increase of wall temperature profile. The buoyancy parameter reaches at most $Bu = 0.25 \cdot 10^{-5}$, which is lower than the threshold of $1.0 \cdot 10^{-5}$. (Feuerstein, 2019) found in experimental results, which are obtained with the same model fluid, R134a, that buoyancy starts to have an effect on heat transfer for $Bu > 0.2 \cdot 10^{-5}$, which would explain occurrence of DHT in the present results as well. This is only the case for the largest heat flux, while for all the others, Bu is smaller. The elevation of the wall temperature can be explained by the effect of the variation of the specific heat capacity c_p around the pseudocritical temperature. The specific heat capacity shows its maximum at the pseudocritical points, which means that the fluid needs to absorb a lot of heat to change it's temperature. However, once the pseudocritical temperature is exceeded at the wall, with further increasing temperature, the specific heat capacity of the fluid near the wall starts to decrease.

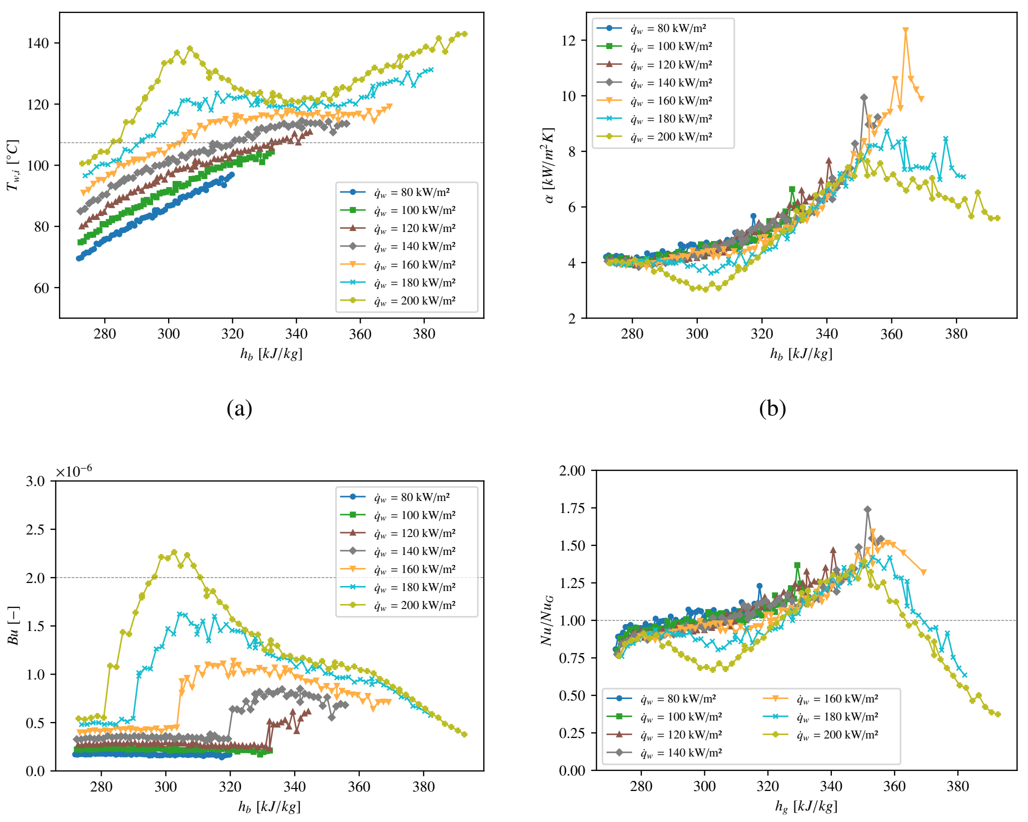

(a) (b)

(c) (d)

Figure 5.7: (a) Wall temperature, (b) heat transfer coefficient, (c) buoyancy parameter and (d) Nu/NuG at p=4.6 MPa, G=2000 kg/m²s, Tin=50 °C and different heat flux

Transferring a given amount of heat to the fluid will increase the temperature more strong, than compared to close to the critical temperature. Therefore, the temperature of the wall increases. Figure 5.7 (d) shows the ratio of the experimentally obtained Nusselt number Nu to the NHT Nusselt number Nu_G, predicted by the Gnielinski correlation (see A.2.6). It can be seen that the data points with $Bu > 2.0 \cdot 10^{-6}$ are corresponding to $Nu/Nu_G < 0.7$, which indicated DHT according to the selected threshold. Further, Nu/Nu_G drops, when the bulk enthalpy becomes larger than ~360 kJ/kg.

It can be concluded, that the effect of heat flux on the heat transfer at supercritical pressure conditions strongly depends on the mass flux. For lower mass flux - and thus less turbulence - DHT appears, if the heat flux reaches a sufficiently large value, which manifests itself in sharp temperature peaks. Buoyancy is playing a role for such flow conditions. On the other hand, for larger mass flux - and thus strong turbulence - effects of buoyancy become less significant. Nevertheless, temperature peaks still appear of the heat flux is large enough, but the temperature rise appears less sudden.

5.2.3 Effect of pressure

The effect of the pressure on the heat transfer is discussed exemplarily for the mass flux of $G = 750\ kg/m^2s$. Figure 5.8 exemplarily shows the trends of (a) wall temperatures and (b) heat transfer coefficients at different pressures, for heat flux of $\dot{q}_w = 50\ kW/m^2$ and (c) wall temperatures and (d) heat transfer coefficients for $\dot{q}_w = 60\ kW/m^2$. The pseudocritical temperature for each pressure is indicates as horizontal dashed line in the corresponding color. For the lower pressure of $p = 4.35\ MPa$, the pseudocritical temperature is $T_{pc} = 104.5\ C$, while for the pressure of $p = 4.6\ MPa$, it is a bit larger at $T_{pc} = 107.3\ C$. Therefore, pseudocritical temperature is exceeded at slightly smaller bulk enthalpy for both of the examples shown here. For the heat flux of $\dot{q_w} = 50\ kW/m^2$, at $p = 4.35\ MPa$, a small but clear temperature peak, corresponding to a sharp decrease in the heat transfer coefficient is observed, after which heat transfer immediately recovers. For the larger pressure of $p = 4.6\ MPa$, heat transfer coefficient also slightly reduces after the pseudocritical temperature is exceeded at the wall, which corresponds of an elevation of wall temperatures. For both of the pressures DHT is present, but is is more pronounced for the smaller pressure, which is closer to the critical pressure of $p_c = 4.059\ MPa$. Therefore, such a behavior is expected, since the thermophysical properties, which in turn are causing DHT, vary stronger around the pseudocritical temperature, the closer the pressure is to the critical value. For the larger heat flux of $\dot{q}_w = 60kW/m^2$, wall temperatures show a pronounced peak for both of the pressures. Due to the same reasons as explained before, the temperature peak is smaller for the larger pressure. The temperature peak is shifted to larger bulk enthalpy with increased pressure, since the corresponding pseudocritical temperature is larger, and exceeding that value is required to

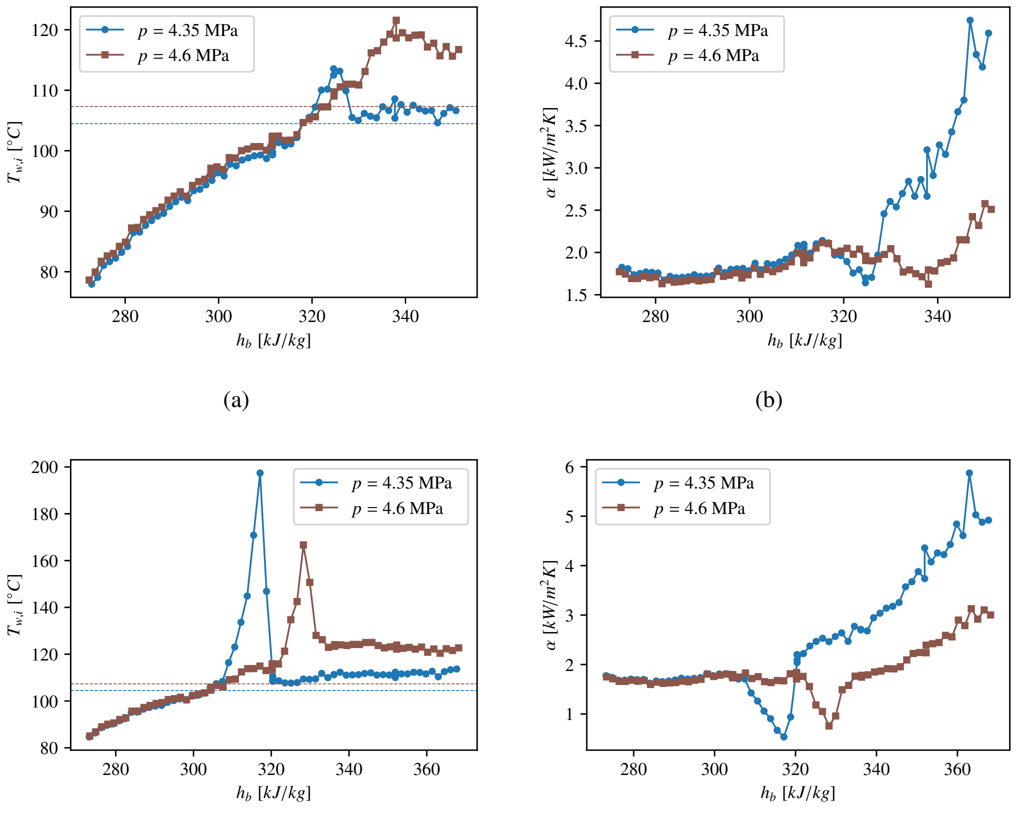

(a)

(b)

(c)

(d)

Figure 5.8: Trends of (a) wall temperature and (b) heat transfer coefficient at q=50 kW/m² and (c) wall temperature and (d) heat transfer coefficient at q=60 kW/m² for different pressures at mass flux of G=750 kg/m²s

trigger the heat transfer deterioration.

As effects like heat transfer deterioration are dedicated to strong variation of the fluid properties, and the variation of the properties are showing a larger gradient around T_{pc}, when the pressure is closer to p_c, the results are not surprising. It can be concluded, that more strong variation of the fluid properties due to a different pressure leads to more severe DHT.

5.2.4 Effect of inlet temperature

Figure 5.9 shows experimentally obtained wall temperatures and Figure 5.10 shows the heat transfer coefficients at $p = 4.6\ MPa$, $G = 500\ kg/m^2s$ and (a) $\dot{q}_w = 20\ kW/m^2$ and (b) $\dot{q}_w = 40\ kW/m^2$, with different inlet temperatures. For the smaller heat flux in Figures 5.9 and 5.10 (a), only normal heat transfer is present. The measured heat transfer coefficients are overlapping, since for a given bulk enthalpy, all local parameters such as Reynolds number, Prandtl number or other fluid properties are the same. Thus, also the heat transfer coefficient must be the same. This shows, that there is no general local effect of the inlet temperature. However, inlet effects can be observed in Figures

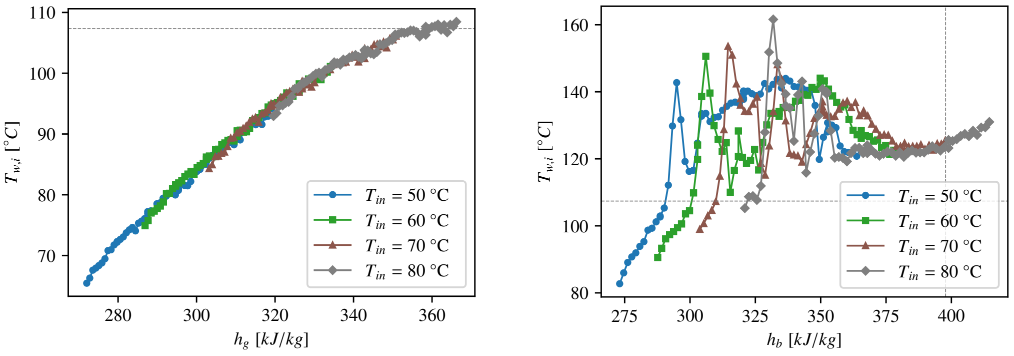

(a) (b)

Figure 5.9: Trends of wall temperature at p=4.6 MPa, G=500 kg/m²s and (a) q=20 kW/m² and (b) q=40 kW/m² for different inlet temperatures

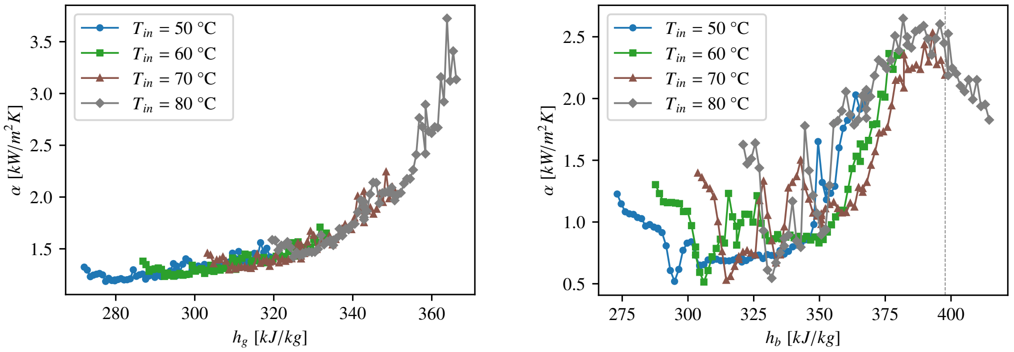

(a) (b)

Figure 5.10: Trends of heat transfer coefficient at p=4.6 MPa, G=500 kg/m²s and (a) q=20 kW/m² and (b) q=40 kW/m² for different inlet temperatures

5.9 (b) and 5.10 (b). In this case, the heat flux is large enough, that the pseudocritical temperature is exceeded close to the inlet and heat transfer deteriorates in the following. As observed in the previous example (Figure 5.6, the fluid needs to move for some distance, before the heat transfer can recover. If now the inlet temperature is changed, the starting point of DHT is shifted to another bulk enthalpy level, and thus also the enthalpy range which the heat transfer needs to recover. For larger bulk enthalpy, when heat transfer is recovered, the heat transfer coefficients obtained for cases with different inlet temperatures are becoming more close to each other. The appearance of such inlet effect are challenging for development of correlations, which typically only consider local parameters (*Re*, *Pr*, ratio of thermophysical properties, distance from the inlet, ...), but this results show, that the history of the flow can play a significant role on the local eat transfer coefficient.

Figure 5.11 exemplarily shows trends of (a) wall temperature and (b) heat transfer coefficient obtained for $p = 4.6\ MPa$, $G = 2000\ kg/m^2s$ and $\dot{q}_w = 180\ kW/m^2$. Up to a bulk enthalpy of around 330 kJ/kg, the results obtained for the two lower inlet temperatures, $T_{in} = 50$ and $60\ °C$, are well overlapping. The temperature trend shows a peak due to DHT around $h_b = 315\ kJ/kg$. Downstream of that peak, heat transfer recovers better for the case with inlet temperature of $T_{in} = 60\ °C$. The two cases have in common, that the wall temperature at the inlet is smaller than the pseudocritical value, but for the case of $T_{in} = 60\ °C$, the first wall temperature is already very close to the pseudocritical point. As seen before, the history of the flow affects the results in the wake of the DHT regime. For the case of $T_{in} = 70\ °C$, the wall temperature at the inlet is already above T_{pc}. A temperature peak due to DHT forms immediately. The location of the peak, as well as the magnitude is in agreement with the results obtained for $T_{in} = 50\ °C$ and $T_{in} = 60\ °C$. In the following region with recovering heat transfer, results obtained for inlet temperatures of 60°C and 70°C are overlapping. The case with the largest inlet temperature of $T_{in} = 80\ °C$ is different, since the inlet enthalpy is larger than 315 kJ/kg, where the temperature peak is appearing for the other cases, thus for that case, no temperature peak exists. Overall, the trend agrees with the results obtained for $T_{in} = 50\ °C$.

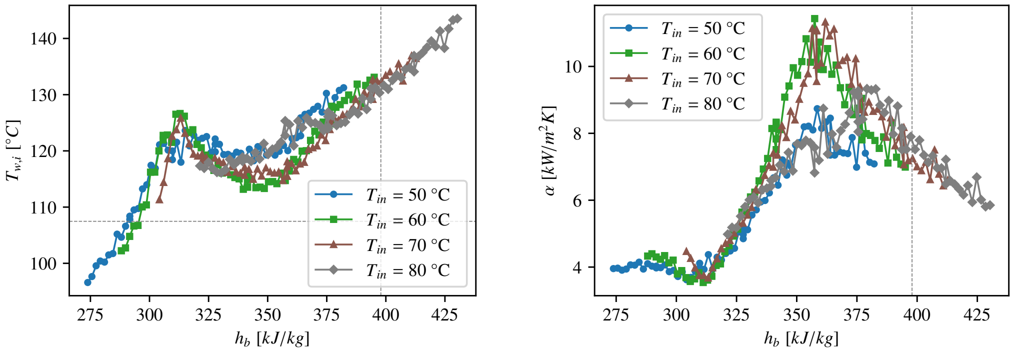

(a) (b)

Figure 5.11: Trends of (a) wall temperature and (b) heat transfer coefficient p=4.6 MPa, G=2000 kg/m²s, q=180 kW/m² and different inlet temperatures

5.3 Experimental results - rough tube

In the following, the effect of wall roughness on heat transfer under supercritical pressure conditions will be evaluated, by comparing the results obtained for the same flow conditions in the smooth tube to the results obtained in the rough tube. Different effects of the roughness are observed, corresponding to the normal heat transfer regime and the deteriorated heat transfer regime. Therefore, the following discussion is divided accordingly.

5.3.1 Roughness effect in the normal heat transfer regime

Figure 5.12 shows trends of wall temperature, heat transfer coefficient and non-dimensional roughness height in the NHT regime, obtained in the smooth tube and in the rough tube, for (a, b, c) $G = 500\ kg/m^2s$, $\dot{q}_w = 20\ kW/m^2$, (d, e, f) $G = 1000\ kg/m^2s$, $\dot{q}_w = 40\ kW/m^2$ and (g, h, i) $G = 2000\ kg/m^2s$, $\dot{q}_w = 80\ kW/m^2$. Within the examples, the heat flux related to the mass flux is constant at $q/G = 0.04$, in order to have comparable heat transfer conditions. Comparing the results obtained in the smooth tube (black), to the results obtained in the rough tube (red), for the

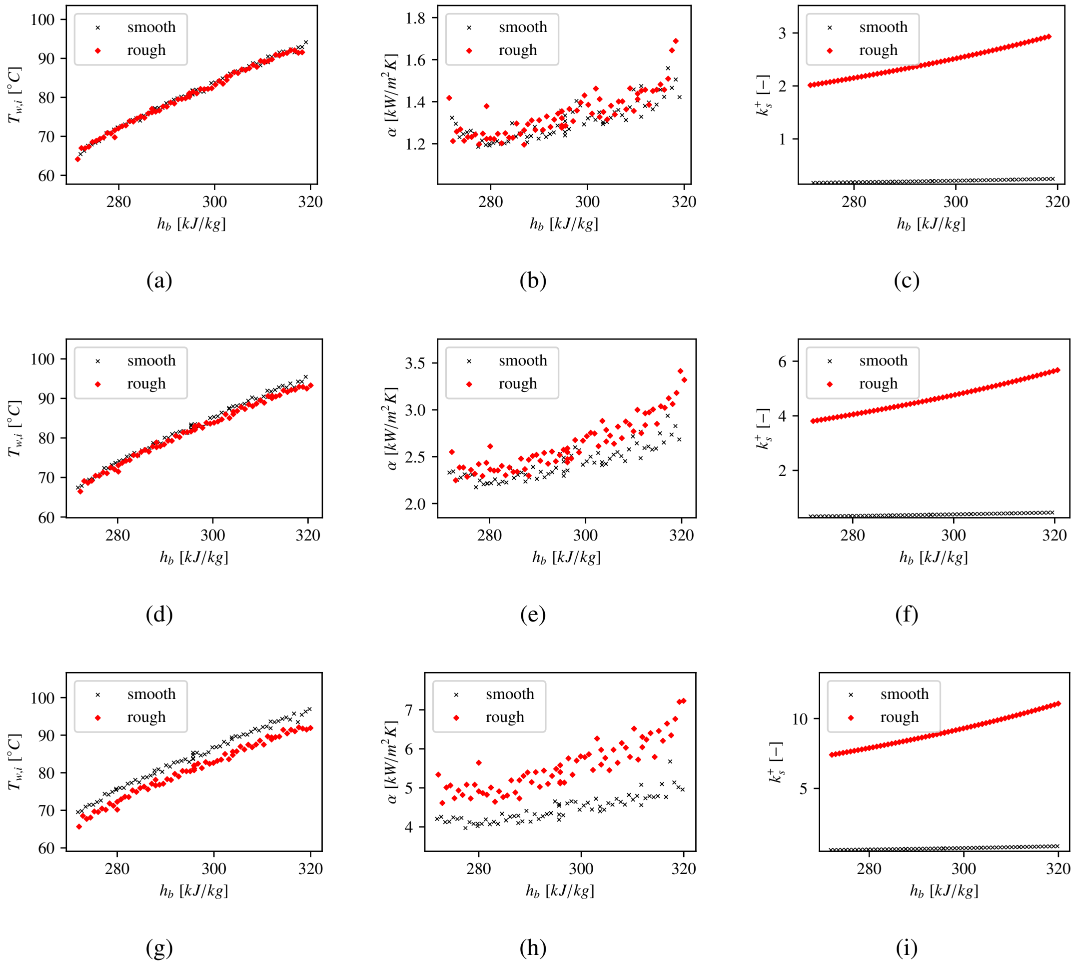

(a) (b) (c)

(d) (e) (f)

(g) (h) (i)

Figure 5.12: Comparison of trends of wall temperatures, heat transfer coefficients and non-dimensional roughness height in NHT regime at (a, b, c) G=500 kg/m²s and q=20 kW/m², (d, e, f) G=1000 kg/m²s and q=40 kW/m² and (g, h, i) G=2000 kg/m²s and q=80k W/m²

smallest mass flux, no effect of the wall roughness can be observed, the results are almost exactly overlapping. In that case, the non-dimensional roughness height varies from 2 to 3, which means, that the roughness elements are about half of the size of the viscous sublayer, which extents from the wall to $y^+ \approx 5$. The thickness of the viscous sublayer is related to the Reynolds number, which ranges from about $30 \cdot 10^3$ to $43 \cdot 10^3$. For the larger mass flux of $G = 1000\ kg/m^2s$ (d, e, f), where the Reynolds number ranges from $59 \cdot 10^3$ to $85 \cdot 10^3$, the impact of surface roughness on the heat transfer becomes noticeable. Around the bulk enthalpy value of 290 kJ/kg, the trends of wall temperatures and heat transfer coefficients, obtained in the rough tube start to deviate from the corresponding trends in the smooth tube. The non-dimensional roughness approaches a value of $k_s^+ = 5$ in the rough tube, meaning that the roughness elements are about the same height as the edge of the viscous sublayer. Now, near wall turbulence is sufficiently enhanced due to perturbations caused by the roughness element, that enhances heat transfer. Additionally, in Figure 5.12 (g, h, i), results obtained for $G = 2000\ kg/m^2s$ and $\dot{q}_w = 80\ kW/m^2$ are shown. Here, Reynolds number ranges from about $120 \cdot 10^3$ to $18 \cdot 10^3$ and the non-dimensional roughness height in the rough tube ranges from about 7 to 11. In this case, the roughness elements are penetrating the buffer layer. A significant increase of heat transfer coefficient is observed in the rough tube, compared to in the smooth tube. The enhances heat transfer in the rough tube is leading to 4-5 K lower wall temperatures.

In order to get an overall view of the obtained experimental data, the entire range of Reynolds numbers covered in the experiment for $\dot{q}_w/G = 0.04$ and $T_{in} = 50\ °C$ is split into 100 evenly spaced intervals. For each interval, the obtained heat transfer coefficients are averaged to determine a representative mean value for the corresponding Reynolds number. This is shown in Figure 5.13 (a), for the smooth and for the rough tube. For Reynolds numbers of smaller than 50,000, heat transfer coefficients obtained in smooth and in rough tube are almost the same. For larger Reynolds numbers, a deviation becomes noticeable, the heat transfer coefficients obtained in the rough tube become larger, compared to the smooth tube. Figure 5.13 (b) shows the ratio of heat transfer coefficient obtained in the smooth tube to heat transfer coefficient obtained in the rough tube. For small Reynolds numbers, that ratio is around 1 or slightly above. At a Reynolds number of 71,000, indicated by the black dashed line, the roughness enhances the heat transfer by 10%. At the same Reynolds number, as can be seen in Figure 5.13 (c), the non-dimensional roughness height is $k_s^+ = 4.6$. As discussed before, it can be concluded that when the roughness elements significantly penetrate the viscous sublayer, near wall turbulence is considerably enhanced, which is leading to considerably enhanced heat transfer coefficient. It is worth mentioning, that there is a small effect of roughness on the heat transfer, already for the smallest non-dimensional roughness height of $k_s^+ = 2$, obtained in the rough tube, which further increases, when the non-dimensional roughness height increases. Comparing this to the roughness functions, shown in Figure 2.19 (b) in section 2.3.1, the behavior seems to be more close to the Colebrook-type roughness function. In Contrast to that, in the Nikuradse type roughness function, a threshold value needs to be exceeded, before any effect of the roughness can be seen. Since the heat transfer is linked to the turbulence, and therefore to the velocity field, it is plausible to say that the obtained results follow the Colebrook-type roughness function.

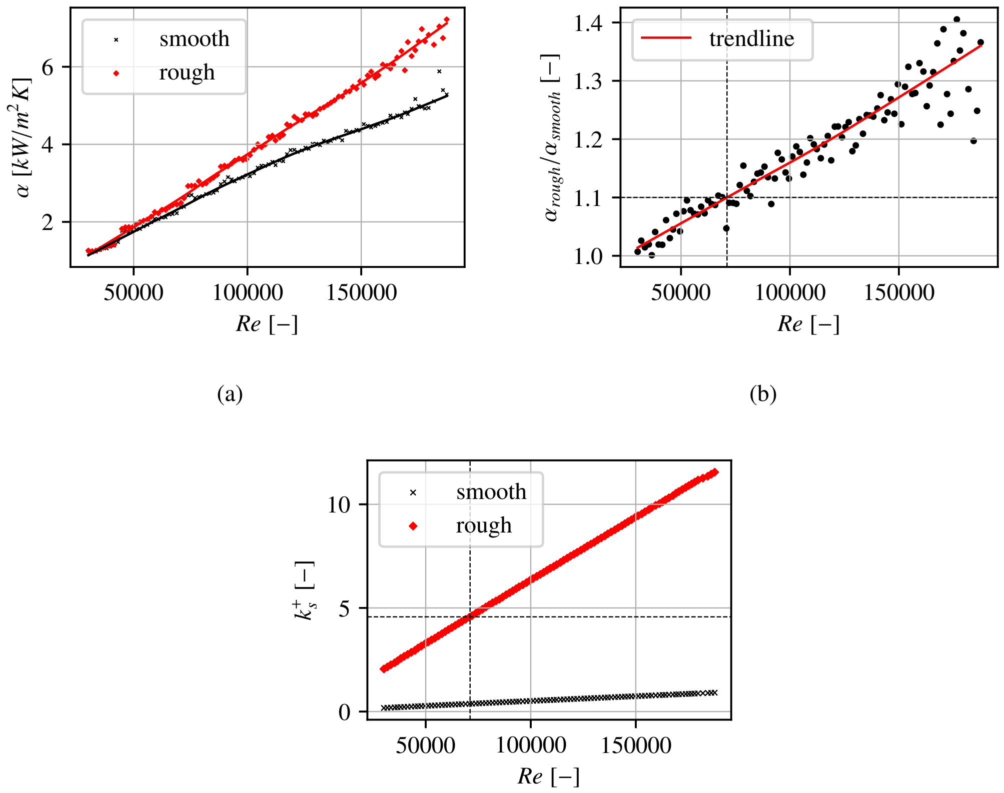

(a)

(b)

(c)

Figure 5.13: Enhancement of heat transfer due to wall roughness in the normal heat transfer regime: (a) Comparison of heat transfer coefficients, (b) ratio of heat transfer coefficients and (c) non-dimensional roughness height.

The effect of the wall roughness on heat transfer to fluid under supercritical pressure conditions, can be summarized for the normal heat transfer regime as follows: For small Reynolds numbers, when the thickness of the viscous sublayer is large, compared to the height of the roughness elements, no, or only little effect of wall roughness on the can be observed. With increasing Reynolds number - and consequently decreasing thickness of the viscous sublayer - Roughness effect gradually increases, which is expressed in enhances heat transfer and thus reduced wall temperatures. No clear threshold for the onset of roughness effect on heat transfer is observed. However, the results show that the effect of the wall roughness becomes considerable strong (more then 10%), when the non-dimensional roughness height k_s^+ reaches a value of about 5, which means the roughness elements have about the same height as the viscous sublayer.

5.3.2 Roughness effect in the buoyancy controlled deteriorated heat transfer regime

This section presents the results for cases where DHT is mainly driven by buoyancy effects. These mainly occur at low mass fluxes (500 and 750 kg/m²s), where the Reynolds number is small enough for natural convection and density gradients to significantly alter flow behavior. In the following, the effect of the surface roughness on DHT in the presence of the buoyancy effect is discussed, separately for results obtained at mass fluxes of 500 and 750 kg/m²s.

5.3.2.1 Mass flux of 500 kg/m²s

The effect of wall roughness on heat transfer in the DHT regime is first shown for some cases obtained for $p = 4.6\ MPa$ and $G = 500\ kg/m^2s$ and different heat flux. Trends in wall temperature and heat transfer coefficient are shown in Figure 5.14. The results obtained in the smooth tube are marked as a black x, and the results obtained in the rough tube are indicated as a red diamond. The thermocouples are mounted at alternating sites on the tube, as described in Section 3.2.1. The different sites are indicated in the results by a dashed and a dotted line, respectively. For the smallest heat flux shown, $\dot{q}_w = 30\ kW/m^2$ in Figure 5.14 (a, b), the smooth tube results show a

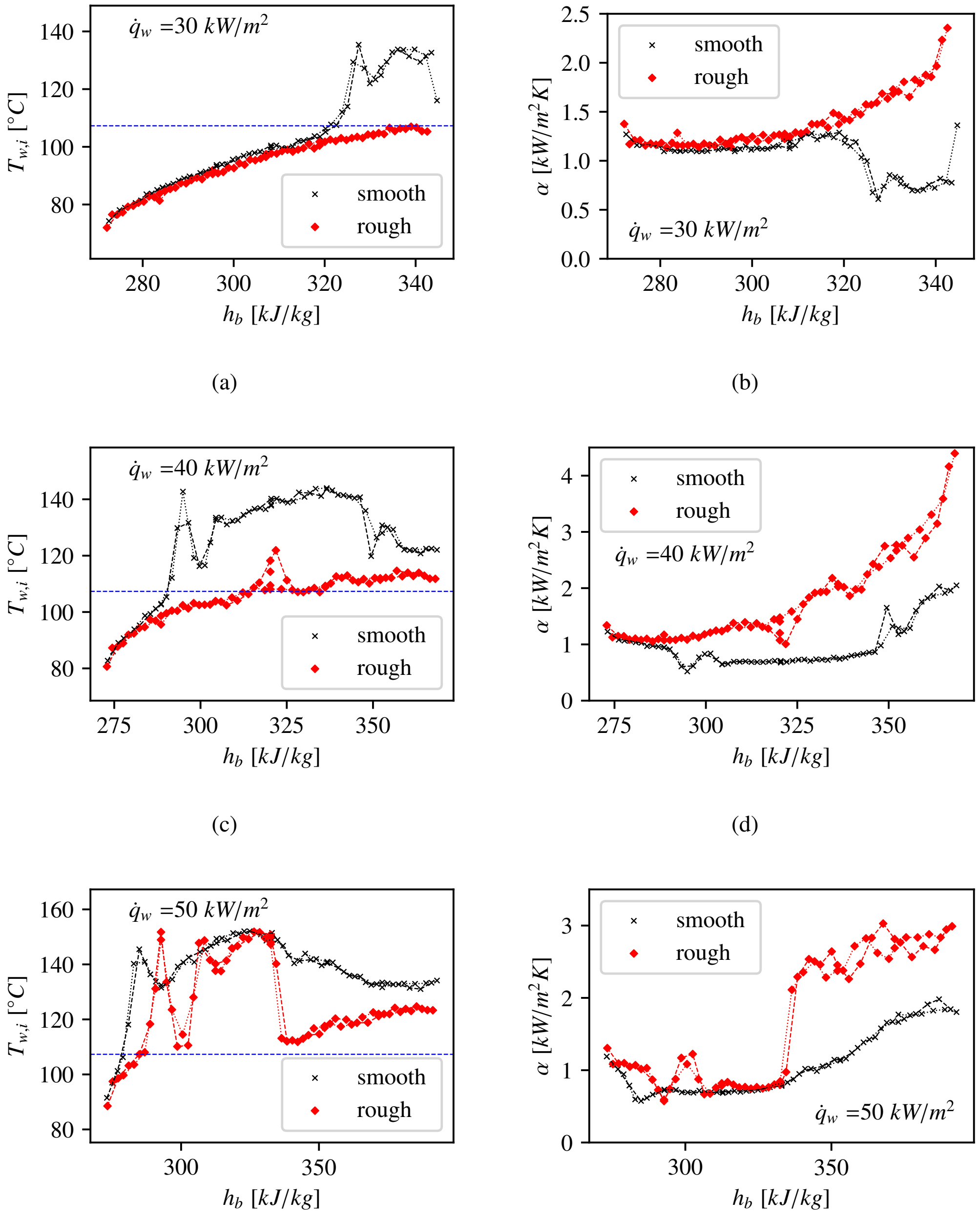

(a) (b)

(c) (d)

(e) (f)

Figure 5.14: Trends of wall temperature and heat transfer coefficient at p=4.6 MPa, G=500 kg/m²s and (a, b) q=30 kW/m², (c, d) q=40 kW/m² and (e, f) q=50 kW/m².

sharp temperature peak, corresponding to a sharp decrease in the heat transfer coefficient, followed by a plateau of high wall temperatures and low heat transfer coefficient. This is clearly deteriorated heat transfer, as discussed in section 5.2.2. However, the results from the rough tube show neither any peak in the wall temperature nor a drop in the heat transfer coefficient. Under the present conditions, the roughness suppresses the heat transfer to deteriorate. For the discussion of this observation, the corresponding trends of the buoyancy parameter *Bu* and the non-dimensional wall roughness k_s^+, based on bulk properties and also based on wall properties, are shown in Figure 5.15. Since for DHT conditions, large gradients of fluid properties are present from the wall to the bulk, the non-dimensional wall distance is expressed in terms of wall properties, to describe the

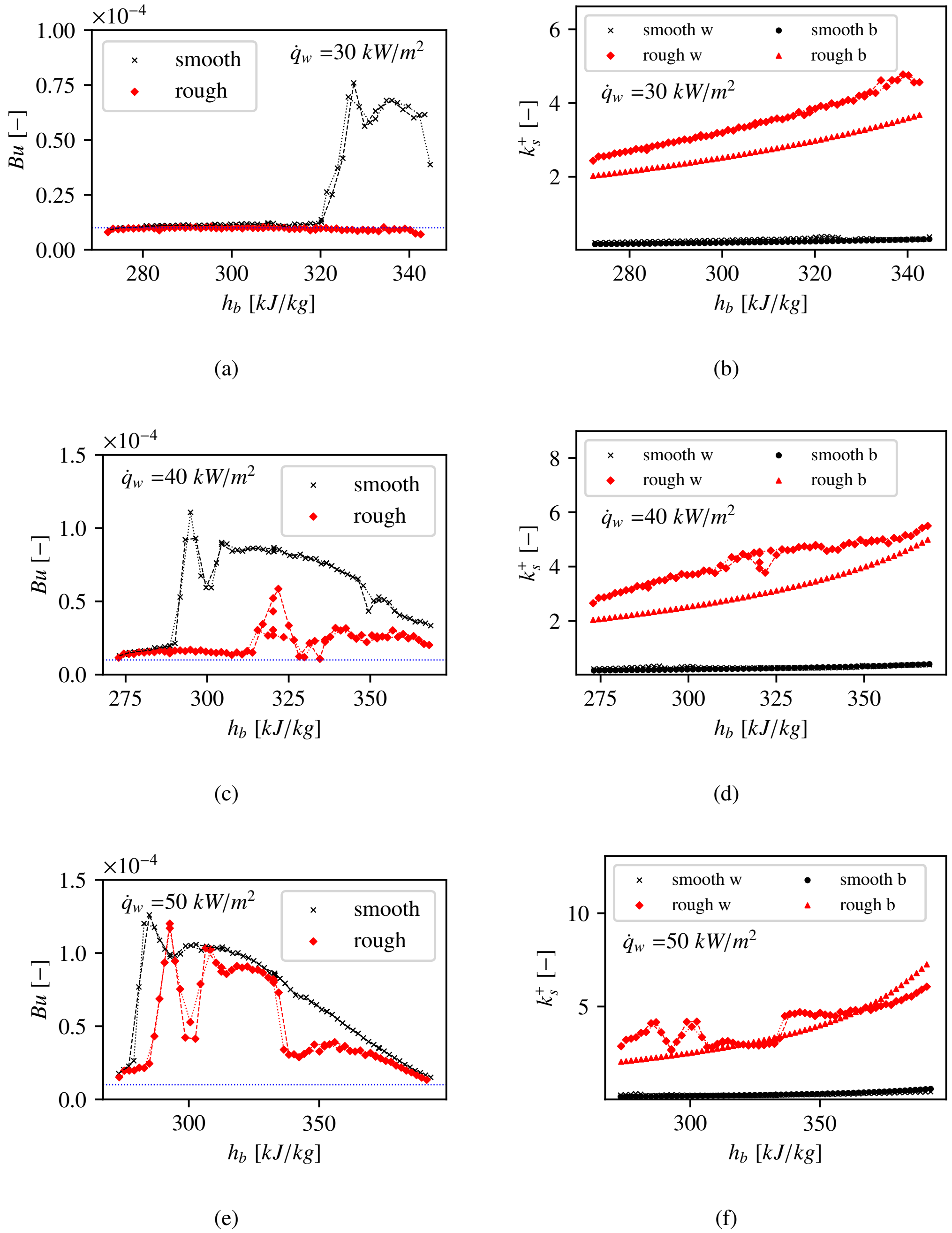

(a) (b)

(c) (d)

(e) (f)

Figure 5.15: Trends of buoyancy parameter and wall-property based non-dimensional roughness height at p=4.6 MPa, G=500 kg/m²s and (a, b) q=30 kW/m², (c, d) q=40 kW/m² and (e, f) q=50 kW/m².

situation that is actually present in the near-wall layer. It can be seen, that the DHT conditions in the smooth tube are corresponding to a sharply increasing buoyancy parameter, and the buoyancy parameter in the rough tube remains almost flat. The non-dimensional roughness height is around 4 in the corresponding region of the tube. As discussed in section 5.3.1 for the normal heat transfer regime, heat transfer is slightly enhanced due to the roughness. This leads to wall temperatures lower than the pseudocritical temperature, which is indicated by the blue dashed line in the figure. Since a strong variation of the fluid properties in the flow cross section is therefore avoided, DHT is suppressed. When the heat flux increases to $\dot{q}_w = 40\ kW/m^2$, as shown in Figure 5.14 (c, d), the temperature plateau in the smooth tube expands over a significant part of the test section - DHT regime is present there. The temperature profile obtained in the rough tube shows a small temperature peak, once the pseudocritical temperature is exceeded at the wall, corresponding to a drop in the heat transfer coefficient. After a short distance, heat transfer recovers to the normal regime. In Figure 5.15 it can be seen that buoyancy plays a significant role, also in the rough tube, at the corresponding location. However, the turbulence induced by the roughness elements is strong enough to counteract the effect of the local laminarisation due to the buoyancy and heat transfer can recover. It is noticeable that the non-dimensional wall roughness height shows a small decrease at the location of the small temperature peak in the rough tube. Due to the increased wall temperature, the density and viscosity decrease quite sharply, which thickens the viscous sublayer at that location. This becomes important when the heat flux is increased further to $\dot{q}_w$, as shown in Figures 5.14 (e, f) and 5.15 (e, f). Now, in the rough tube, also a sharp temperature peak, followed by a plateau is observed, and heat transfer is deteriorated in significant parts of the test section. In the corresponding part of the test section, the non-dimensional wall roughness is significantly reduced, as a result of a thicker viscous sublayer, which is a result of the larger wall temperature. At the same time, there is a strong effect of buoyancy. In that situation, the effects of increasing wall temperature, buoyancy, and increasing sublayer thickness reinforce each other. This is illustrated in Figure 5.16. For further evaluation of the effect of the surface roughness, all experimentally obtained data points for $p = 4.6\ MPa$ and $G = 500\ kg/m^2s$, the ratio of the actually measured heat transfer coefficient α, to the heat transfer coefficient α_G, which represents normal heat transfer conditions, are plotted over the bulk enthalpy. The Gnielinski correlation (Gnielinski, 1975) is used for reference for NHT, since the wall friction c_f is considered, which takes the wall roughness into

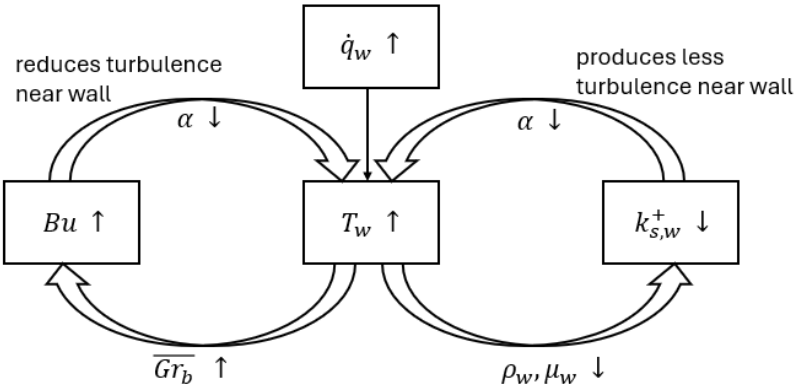

Figure 5.16: Reinforced effects of increasing temperature, increasing buoyancy and decreasing non-dimensional roughness

account. Figure 5.17 (a) shows α/α_G for the smooth tube and (b) for the rough tube. The data points are colored according to the buoyancy parameter Bu. The pseudocritical bulk enthalpy is indicated by the vertical black dashed line, the threshold value for DHT conditions is represented by the horizontal red dashed line. In the present investigation, the threshold value is given by:

$$\frac{\alpha}{\alpha_G} = 0.7 \tag{5.1}$$

Both of the results, obtained in the smooth, as well as in the rough tube, show data with deteriorated heat transfer, corresponding to strong buoyancy around a bulk enthalpy of 280 to 350 kJ/kg. It can be seen, that in the rough tube are less points with DHT, dedicated to the buoyancy effect, compared to the smooth tube. That shows, that roughness is capable to suppress DHT, but not under all conditions. Figure 5.17 (c) shows α/α_G in the rough tube, but the points are colored by the non-dimensional roughness height, based on wall properties. It can be seen, that all the points with heat transfer deterioration, which are dedicated to the buoyancy effect, show values of $k^+_{s,w}$ around 2. This is not sufficient to counteract the reduction of turbulence due to buoyancy in a sufficient manner to prevent the heat transfer from deterioration. Further, around the pseudocritical bulk enthalpy, the heat transfer is deteriorated in the smooth tube, as well as in the rough tube. As Figure 5.17 (c) shows, the non-dimensional wall roughness is about 5 or more at the corresponding

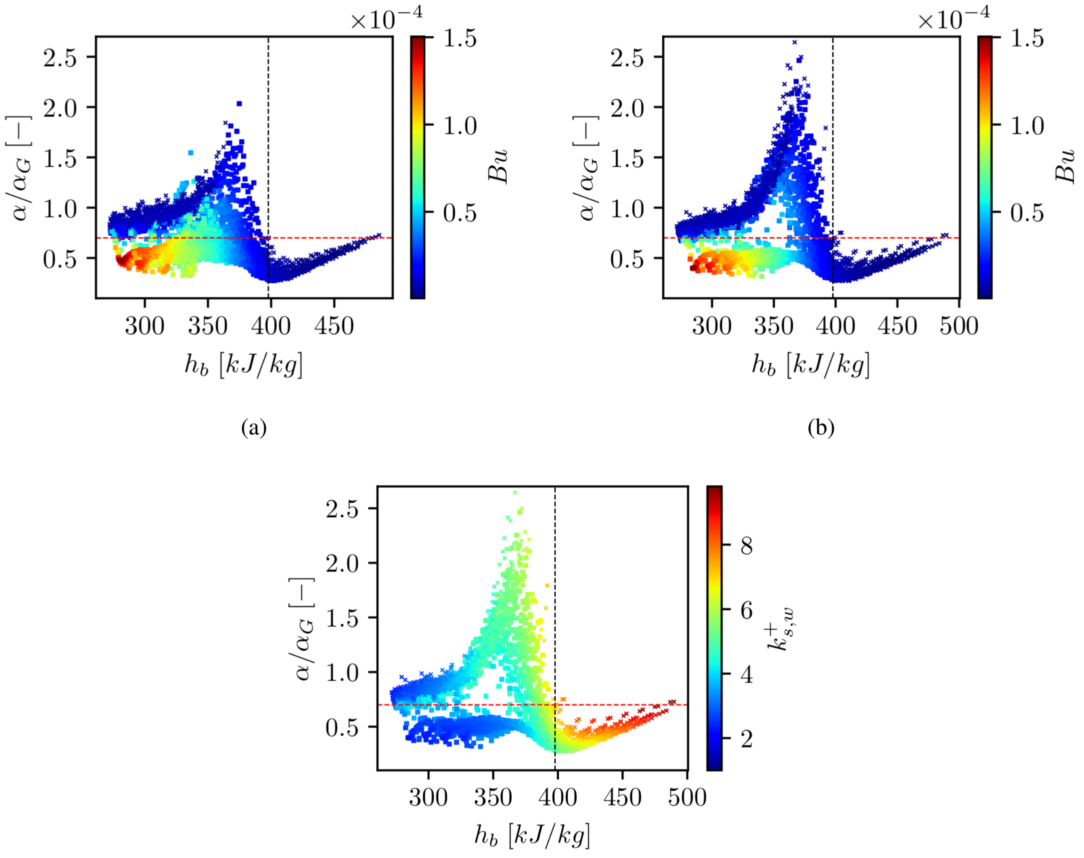

(a)

(b)

(c)

Figure 5.17: Ratio of experimentally obtained to normal conditions heat transfer coefficients for p=4.6 MPa and G=500 kg/m²s in the (a) smooth tube and (b, c) rough tube

data points. However, the DHT around the pseudocritical temperature seems to be unaffected by the wall roughness.

5.3.2.2 Mass flux of 750 kg/m²s

For the next larger mass flux of $G = 750\ kg/m^2s$, the roughness effect becomes stronger, since larger Reynolds numbers are present and therefore the viscous sublayer is thinner and consequently the non-dimensional roughness height is larger. Figure 5.18 shows trends of wall temperature and heat transfer coefficient obtained for $p = 4.6\ MPa$ and $G = 750\ kg/m^2s$ at heat flux of (a,

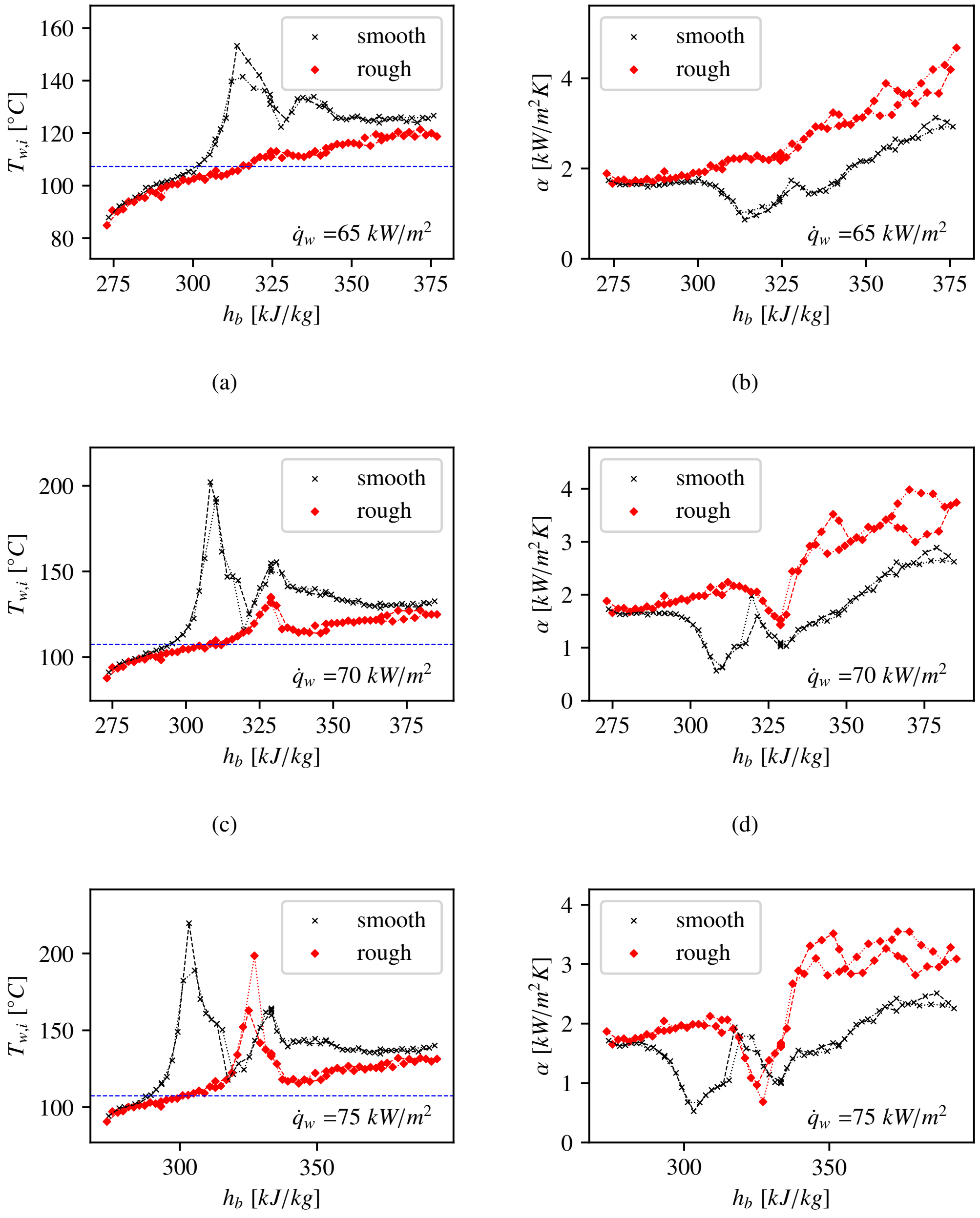

(a) (b)

(c) (d)

(e) (f)

Figure 5.18: Trends of wall temperature and heat transfer coefficient at p=4.6 MPa, G=750 kg/m²s and (a, b) q=65 kW/m², (c, d) q=70 kW/m² and (e, f) q=75 kW/m².

b) $\dot{q}_w = 65$, (c, d) 70 and (d, e) 75 kg/m^2. Similar to the results obtained for $G = 500\ kg/m^2s$, the onset of heat transfer deterioration is delayed to larger heat flux in the rough tube. However, results are different there from the ones at the smaller mass flux: For $\dot{q}_w = 65\ kW/m^2$, the wall temperature is exceeding the pseudocritical value in both tubes, so also in the rough tube, by more than 10K. Therefore, strong variation of the thermopyhsical properties are present in the flow cross-section. Also buoyancy plays a role, since $Bu > 1.0 \cdot 10^{-5}$ as can be seen in Figure 5.19 (a). On the other hand, as Figure 5.19 (b) shows, the non-dimensional roughness height based on wall properties is above 5 in most of the tube. No sudden widening of the viscous sublayer can be observed. In the given situation, the perturbation of the flow due to the roughness elements

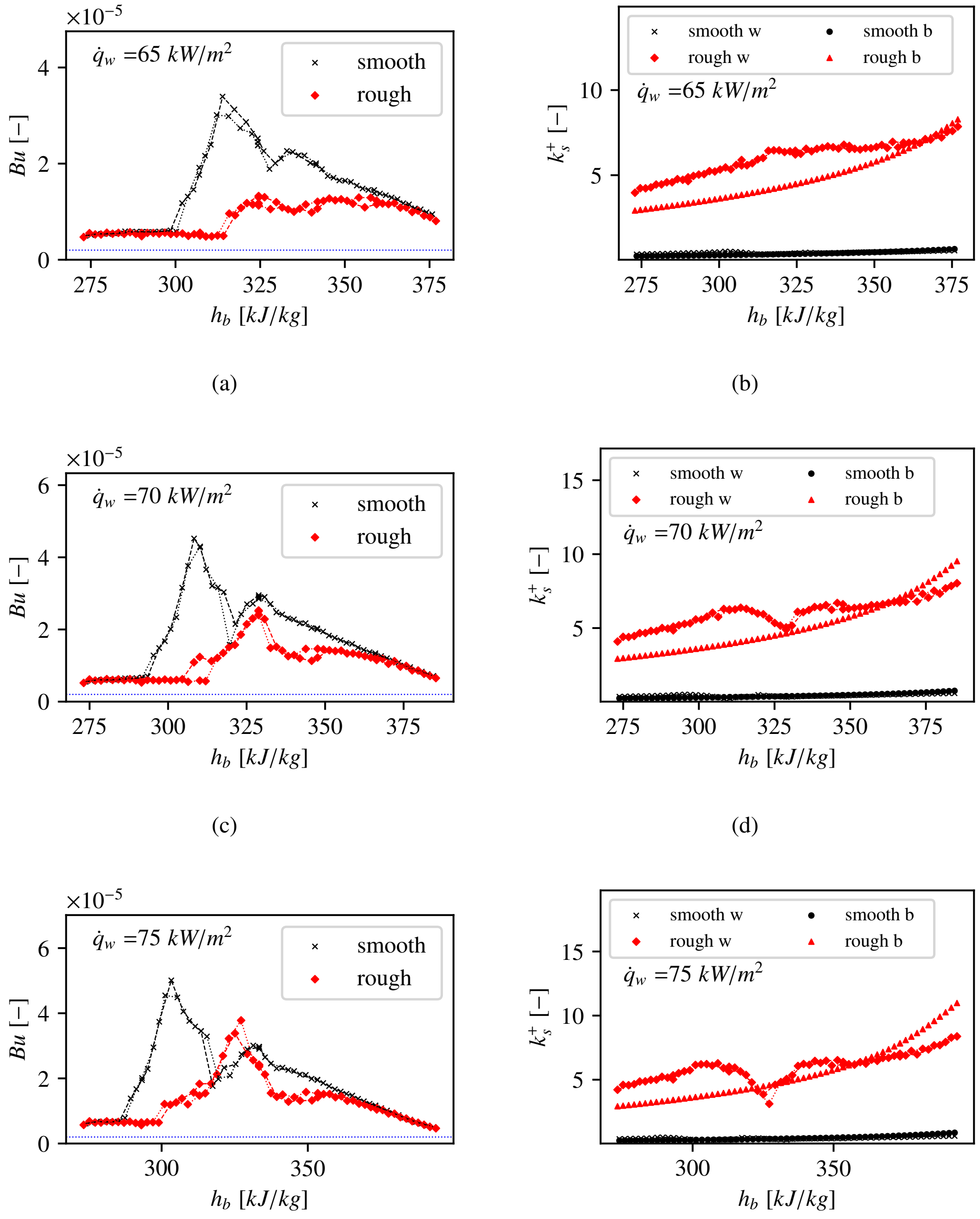

(a) (b)

(c) (d)

(e) (f)

Figure 5.19: Trends of buoyancy parameter and wall-property based non-dimensional roughness height at p=4.6 MPa, G=750 kg/m²s and (a, b) q=65 kW/m², (c, d) q=70 kW/m² and (e, f) q=75 kW/m².

induces turbulence, strong enough to counteract the effect of the buoyancy. For the next larger heat flux of $\dot{q}_w = 65\ kW/m^2$, in Figure 5.18 (c) trend of wall temperature and (d) trend of heat transfer coefficient can be seen. A temperature peak is forming, which corresponds to a sudden decrease in the heat transfer coefficient. As seen in Figure 5.19 (c), buoyancy plays a significant role. In the same time, as illustrated in Figure 5.16, the increased wall temperature results in locally enlarged sublayer thickness and thus decreased non-dimensional roughness height. However, the roughness effect is still sufficient to prevent a significant peak of the wall temperature. Nevertheless, according to the definition of heat transfer deterioration as a temperature peak, these data points are considered to be in the DHT regime. Another observation is the shift of the heat transfer deterioration to a larger bulk enthalpy. While in the smooth tube, the wall temperature shows a sudden increase around the bulk enthalpy of 300 kJ/kg, the peak is shifted to around 325 kJ/kg in the rough tube. The explanation is the same is previously discussed for the results for $G = 500\ kg/m^2s$: Heat transfer is slightly enhanced due to the roughness in the normal heat transfer regime, which is present, when the wall temperature is below T_{pc}. Therefore, the wall temperature in the rough tube exceeds the pseudocritical temperature at a larger bulk enthalpy. Since the buoyancy related DHT requires the wall temperature to be larger, and the bulk temperature to be smaller than T_{pc}, the temperature peak is shifted towards larger bulk enthalpy. When the heat flux is further increased to $\dot{q}_w = 75\ kW/m^2$, as presented in Figures 5.18 (e, f) and 5.19 (e, f) the reinforcing effects of increasing wall temperature, increasing buoyancy, and decreasing non-dimensional roughness height are leading to significant deterioration of heat transfer. The non-dimensional roughness height based on wall properties is reduced to less than 3. The heat transfer coefficient drops down to the same level as in the smooth tube and a sharp temperature peak is observed. The ratio of $\alpha/_G$ for all obtained data points for $p = 4.6\ MPa$ and $G = 750\ kg/m^2s$ is shown in Figure 5.20 (a) for the smooth tube and (b), for the rough tube. Again, DHT dedicated to buoyancy effect is observed in the smooth tube from around $h_b = 300\ kJ/kg$. In contrast to the results obtained for $G = 500\ kg/m^2s$, presented in Figure 5.17, here, in the rough tube, DHT is always shifted to larger bulk enthalpies. The first buoyancy related deterioration of heat transfer appears around $h_b = 325\ kJ/kg$. Furthermore, significantly less data points show DHT in the rough tube, then in the smooth tube. Over all, for $G = 750\ kg/m^2s$, roughness suppresses DHT more efficient, than for $G = 500\ kg/m^2s$. As Figure 5.20 (c) shows, where the data points are colored by the wall property-based non-dimensional roughness, the buoyancy related heat transfer deterioration is corresponding to reduced wall roughness relative to the sublayer thickness. The dependency illustrated in Figure 5.16 - increased wall temperature, increased buoyancy, decreased non-dimensional roughness height - is appearing. Furthermore, consistent to the results for $G = 500\ kg/m^2s$, around the pseudocritical enthalpy DHT is present, which is not related to buoyancy effect. In that case, roughness does not show any effect on the heat transfer. This is particularly to highlight, since the non-dimensional roughness height is the larges, for the corresponding data points. With values above $k_s^+ > 7$, the roughness elements penetrate the buffer layer, but the deterioration of heat transfer can not be suppressed. Nevertheless, roughness is enhancing the heat transfer, even though deterioration can not be avoided, which is shown in the following.

At this point, the conclusion is that the roughness of the wall alters the heat flux, for which DHT is observed. For the cases discussed here, where the deterioration of heat transfer is related to

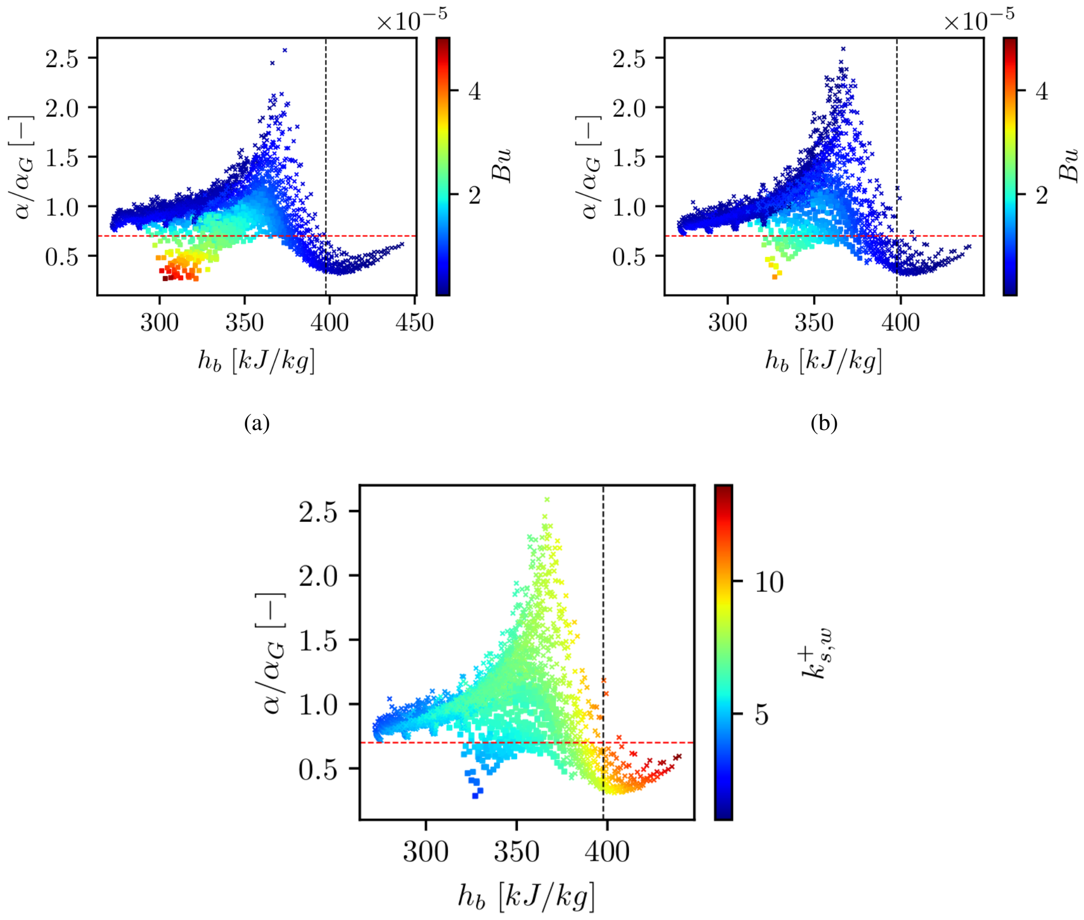

(a)

(b)

(c)

Figure 5.20: Ratio of experimentally obtained to normal conditions heat transfer coefficients for p=4.6 MPa and G=750 kg/m²s in the (a) smooth tube and (b, c) rough tube

the effect of buoyancy, roughness shows a significant impact on the onset of heat transfer deterioration. Table 5.1 shows the minimum heat flux, for which the buoyancy parameter exceeds the threshold of $Bu > 1.0 \cdot 10^{-5}$. This is the minimum required heat flux to have a significant effect of buoyancy at each given flow condition. As was shown before, these conditions are related to deteriorated heat transfer and usually show sharp peaks in the trend of the wall temperature and deep valleys in the trend of the heat transfer coefficient. In Table 5.1, the minimum heat flux for which buoyancy becomes significant is compared for the smooth and for the rough tube. First of all, it can be seen that only for the smaller mass fluxes is buoyancy relevant. It can be seen that for almost all of the cases, the minimum heat flux to reach conditions with $Bu > 1.0 \cdot 10^{-5}$ is increased by the roughness. For mass flux of 1250 kg/m²s, for none of the investigated heat fluxes it was possible to reach flow conditions with significant buoyancy.

5.3.3 Roughness effect in the property controlled deteriorated heat transfer regime

In the following results, heat transfer deterioration is mainly driven by sharp variation of the properties such as c_p near the pseudocritical point. Sure, the buoyancy effect is also due to variation of the density, but in contrast the the results discussed in the previous section, buoyancy is negligible

Table 5.1: Minimum heat flux for buoyancy-related heat transfer deterioration in the smooth tube and in the rough tube

		smooth tube				rough tube			
p $[MPa]$	T_{in} $[°C]$	G $[kg/m^2 s]$				G $[kg/m^2 s]$			
		500	750	1000	1250	500	750	1000	1250
4.35	50	25	45	80	-	30	55	100	-
	60	25	45	80	-	25	55	100	-
	70	20	40	90	140	30	55	90	-
	80	20	40	100	130	25	50	100	-
4.6	50	30	45	100	-	30	60	100	-
	60	25	45	90	-	30	60	110	-
	70	25	45	90	140	30	55	110	-
	80	20	45	110	150	35	55	110	-

here. Results obtained for mass flux of 1000 kg/m²s and 2000 kg/m²s are discussed exemplarily.

5.3.3.1 Mass flux of 1000 kg/m²s

The results obtained for $p = 4.6\ MPa$, $G = 1000\ kg/m^2 s$ and different heat flux are shown in Figures 5.21 and 5.22. For a larger mass flux, heat transfer deterioration appears to be different from for small mass flux. For $\dot{q}_w = 70\ kW/m^2$, the slope of the wall temperature profile in the smooth tube increases, when T_w exceeds T_{pc}, which corresponds to slightly decreasing heat transfer coefficient. This is where the results obtained on the rough tube start to differ significantly, from the results obtained in the smooth tube, since the slope of the wall temperature trend in the rough tube does not show that much of an increase. The non-dimensional roughness height - either based on wall or on bulk properties - is above 5, when the pseudocritical wall temperature is reached. The thickness of the viscous sublayer is not growing under that conditions, so the roughness can induce turbulence near the wall and heat transfer is enhanced. The buoyancy parameter *Bu* stays below the limit of (J. Jackson, 2013) of $1.0 \cdot 10^{-5}$, but it exceeds the limit of $0.2 \cdot 10^{-5}$, which was found by (Feuerstein, 2019) for R134a. A transitional behavior is observed, where buoyancy plays a minor role. At the larger heat flux of $\dot{q}_w = 90\ kW/m^2$, the wall temperature increases with a steeper gradient in the smooth tube, until the profile becomes more or less flat. The trends of heat transfer coefficient shows a clear valley. Compared to that, in the rough tube, no reduction of the heat transfer coefficient is observed. Except for the inlet region of the tube, the temperature profile shows roughly the same slope over the whole test section. In contrast to the results from the smooth tube, this can be regarded as suppressed heat transfer deterioration. According to the definition of the buoyancy parameter, there is a jump of buoyancy impact, once $T_w > T_{pc}$. However, the buoyancy effect is weak and in the same time the roughness elements clearly penetrate the buffer layer, and heat transfer is therefore clearly enhanced. For the largest heat flux shown in Figures 5.21 and 5.22, A sharp temperature peak, right after the inlet is observed. As Figure 5.22 (e) shows, buoyancy effect plays a significant role here. In the same time, the roughness, which extends into the buffer layer, suppressed the heat transfer deterioration. However, as Figure 5.22 (f) shows, from a bulk enthalpy of about 300 kJ/kg to about 350 kJ/kg, the viscous sublayer slightly increases - the non-dimensional roughness height decreases and the impact of the surface roughness on the heat transfer consequently reduces a bit. The temperature profile shows a small elevation, while the heat transfer coefficient shows a slight reduction in that enthalpy range, thus heat transfer is deteriorated. It is important to mention that the temperature curves as well as the curves of the heat transfer coefficient depend on the location of the TCs on the circumference of the tube, indicated with a dashed and a dotted line for each location. Such appearance of a hot site and a cold site of the tube was also observed by (Feuerstein, 2019). After the experiments where completed, the tube was cut into pieces and analysis has shown that eccentricity of the tube is leading to that observation. The effect of tube eccentricity is stronger in the rough tube. However, it is not clear, since the tubes

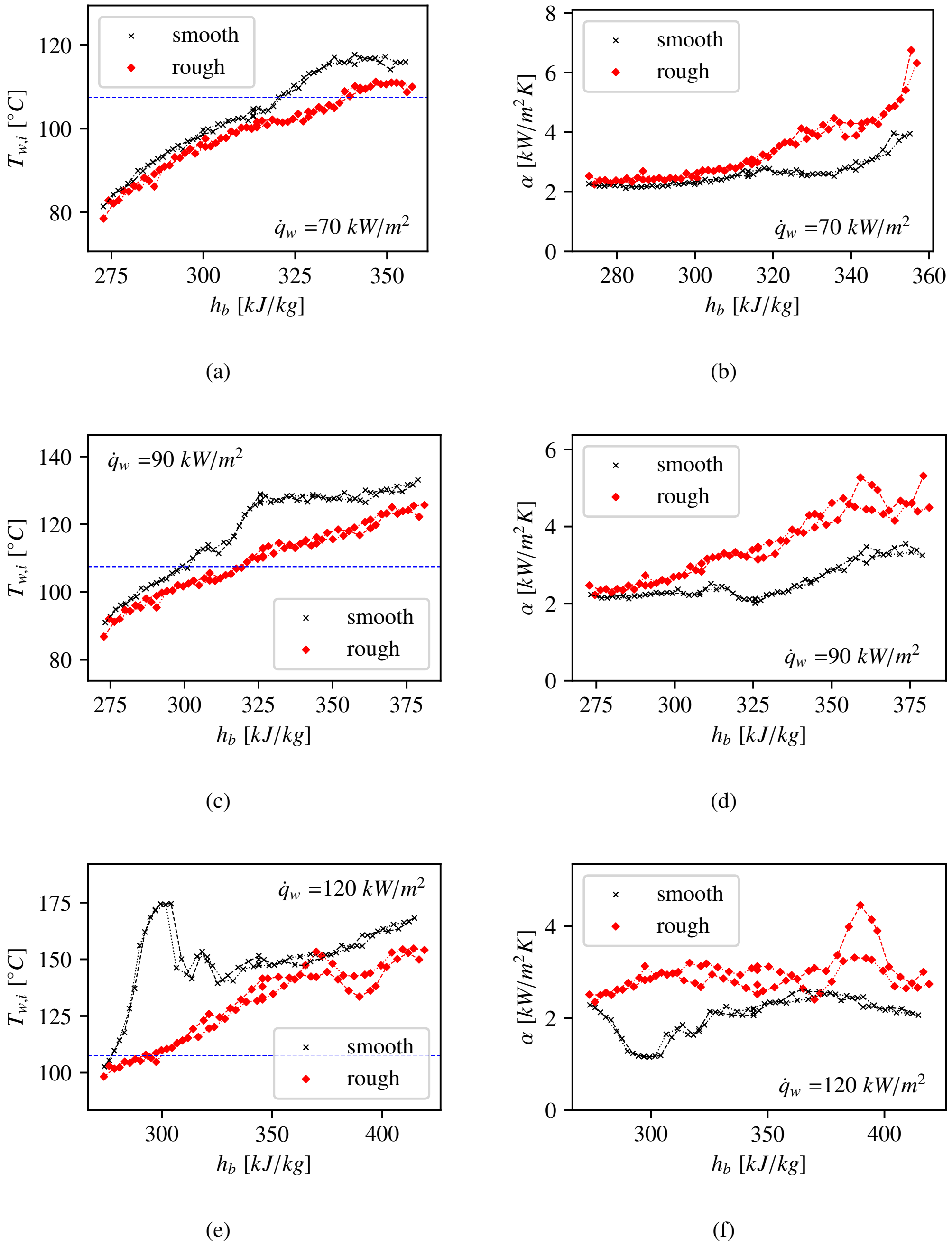

Figure 5.21: Trends of wall temperature and heat transfer coefficient at p=4.6 MPa, G=1000 kg/m²s and (a, b) q=70 kW/m², (c, d) q=90 kW/m² and (e, f) q=120 kW/m².

from this investigation have not been cut, how the TCs are oriented relative to the eccentricity of the tube. So the difference might just come from different orientation. It could also be related to the preparation of the rough inner surface. Summarizing the results for the mass flux of 1000 kg/m²s, Figure 5.23 shows all obtained data-points for (a) the smooth tube and (b, c) the rough tube. Comparing the results, it becomes obvious that in the enthalpy range from 280 kJ/kg to 320 kJ/kg, DHT due to buoyancy is totally suppressed by the roughness. From bulk enthalpy of 320 kJ/kg to about 360 kJ/kg, the rough tube shows data points with buoyancy related DHT, but with larger values of α/α_G, meaning deterioration is less strong. The non-dimensional roughness height is reduced at these data points, but the values are still above 5, which can explain that heat transfer

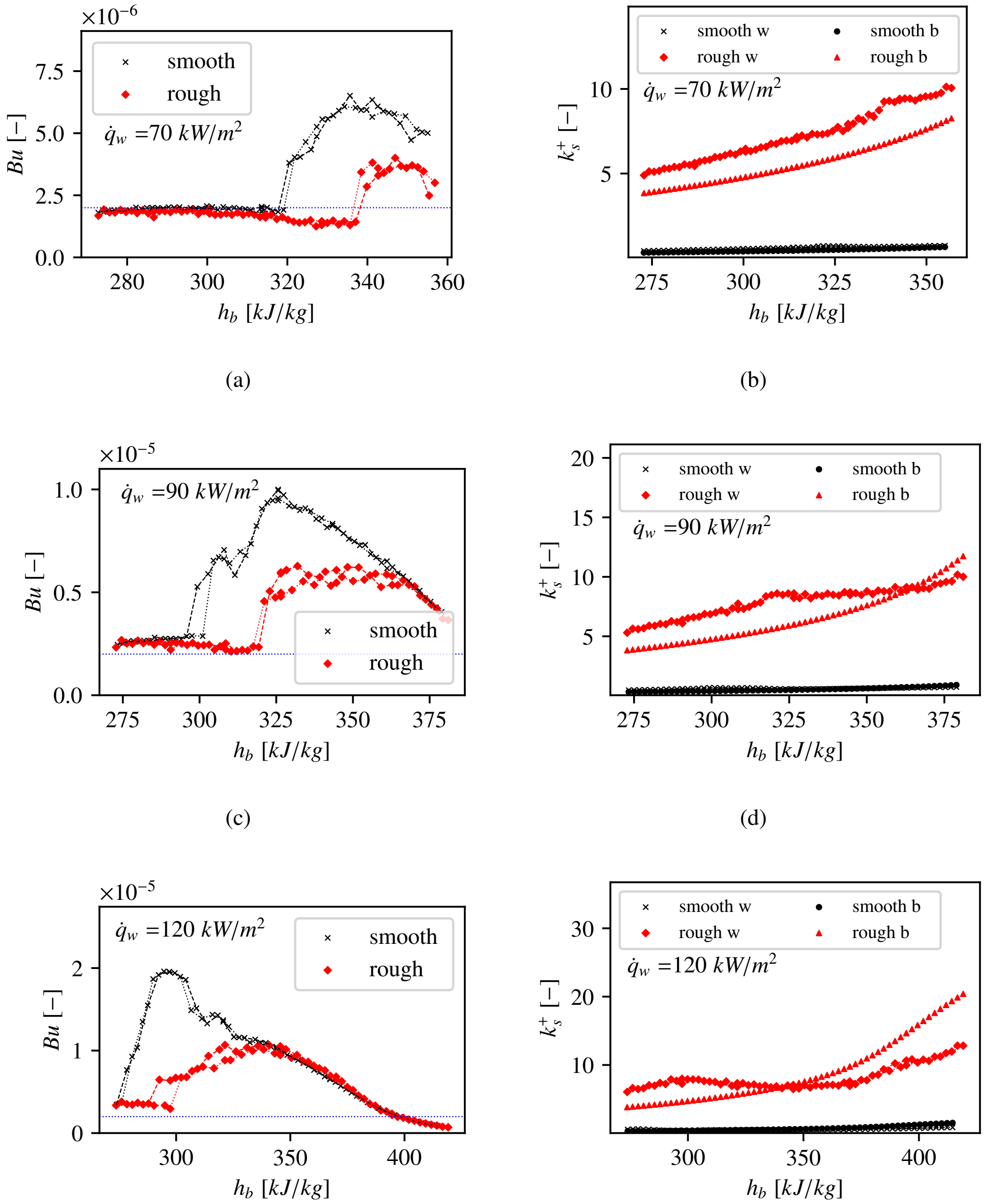

(a) (b)

(c) (d)

(e) (f)

Figure 5.22: Trends of buoyancy parameter and wall-property based non-dimensional roughness height at p=4.6 MPa, G=1000 kg/m²s and (a, b) q=70 kW/m², (c, d) q=90 kW/m² and (e, f) q=120 kW/m².

is still enhances due to the roughness, even though deterioration can not be suppressed. Consistent with the results obtained at all the other mass flux shown before, a second region of DHT, which is unrelated to buoyancy, is appearing in both of the tube. The roughness does not suppress DHT, but still heat transfer is enhanced.

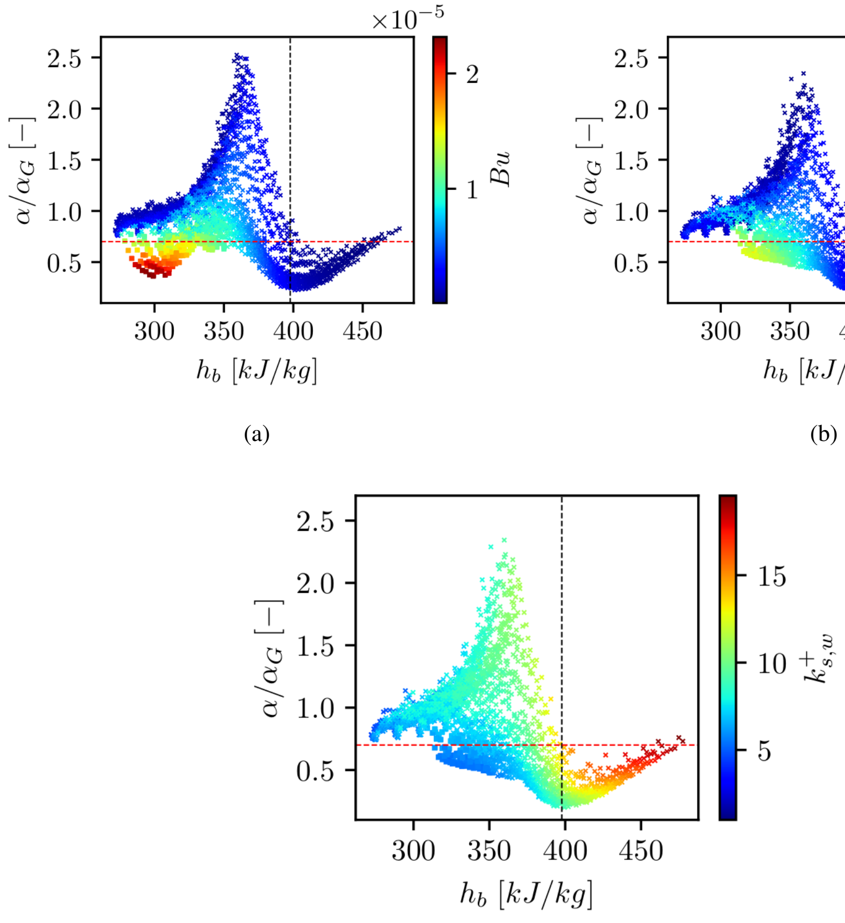

(a)

(b)

(c)

Figure 5.23: Ratio of experimentally obtained to normal conditions heat transfer coefficients for p=4.6 MPa and G=1000 kg/m²s in the (a) smooth tube and (b, c) rough tube

5.3.3.2 Mass flux of 2000 kg/m²s

The results obtained for the largest mass flux of $G = 2000\ kg/m^2s$, at the pressure of $p = 4.6\ MPa$ are shown, as trends of wall temperature and heat transfer coefficient in Figure 5.24 and the corresponding buoyancy parameter as well as non-dimensional roughness height are shown in Figure 5.25. The results obtained for $\dot{q}_w = 160\ kW/m^2$, shown in Figure 5.24 (a, b) show a significant enhancement of heat transfer, over the part of the test section where the wall temperature is below the pseudocritical value. However, as soon as T_w exceeds T_{pc} in the rough tube, a jump of the wall temperature trend can be observed, which is corresponding to a decreased heat transfer coefficient. In contrast to the results obtained in the smooth tube, it seems that the enhancement of the heat transfer due to the roughness becomes less efficient, as soon as $T_w > T_{pc}$. It is observed, that the difference of the heat transfer coefficients obtained in the rough tube, to the the heat transfer coefficients obtained in the smooth tube is significantly reduced, from the location where the wall temperature in the rough tube exceeds the pseudocritical value. On the other hand, as Figure 5.25 (b) shows, the non-dimensional roughness height does not collapse at the same point, as it was observed for other flow conditions before. There is even a small peak at the point where T_w crosses T_{pc}. Thus, the reduction of the effect of the roughness on the heat transfer has to be explained with something else than the penetration depth into the buffer layer. A possible explanation is illustrated in Figure 5.26. The roughness elements are deflecting fluid parcel, close to the wall, which have a temperature close to the wall temperature. These fluid parcels transfer the momentum to other fluid parcels, which can also be more far from the wall, having a temperature of the bulk

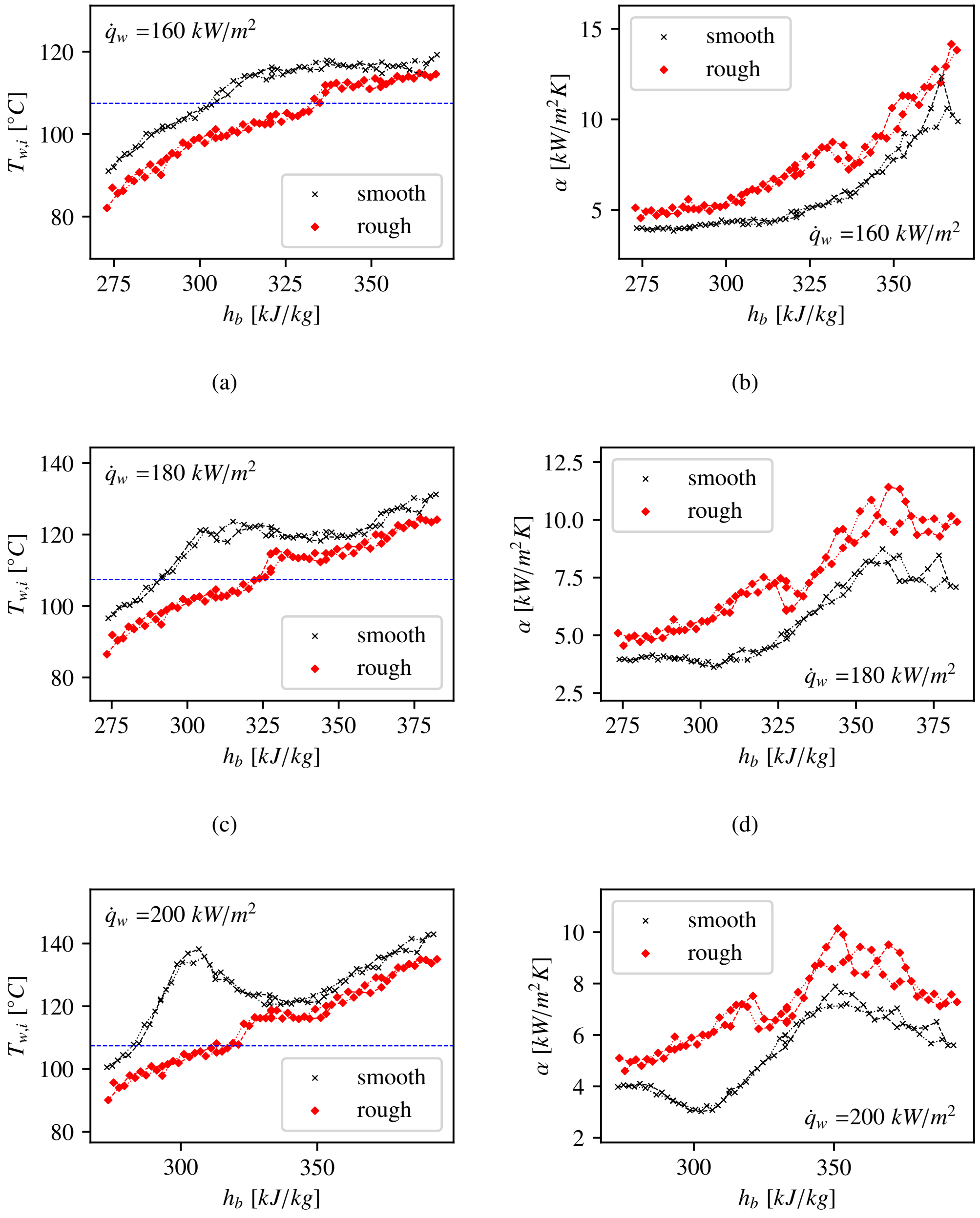

(a) (b)

(c) (d)

(e) (f)

Figure 5.24: Trends of wall temperature and heat transfer coefficient at p=4.6 MPa, G=2000 kg/m²s and (a, b) q=160 kW/m², (c, d) q=180 kW/m² and (e, f) q=200 kW/m².

temperature, in a first approximation. In Figure 5.26, the size of a circle represents the density. In the case of $T_{w,i} < T_{pc}$, as shown in Figure 5.26 (a), the difference between the density at the wall temperature and at bulk temperature is small. Thus, a fluid parcel, having velocity u_1 due to deflection by the roughness elements, transferring its momentum to another parcel further away from the wall, with similar density, will result in a similar velocity u_2 of the other parcel. In other words: The induced perturbations of the velocity field due to the roughness have an impact on the flow. The resulting turbulence enhances heat transfer. The situation with $T_{w,i} > T_{pc}$ and $T_b < T_{pc}$ is illustrated in Figure 5.26 (b). Since density is decreasing significantly around T_{pc}, the difference between density near the wall and fluid parcels further away from the wall becomes

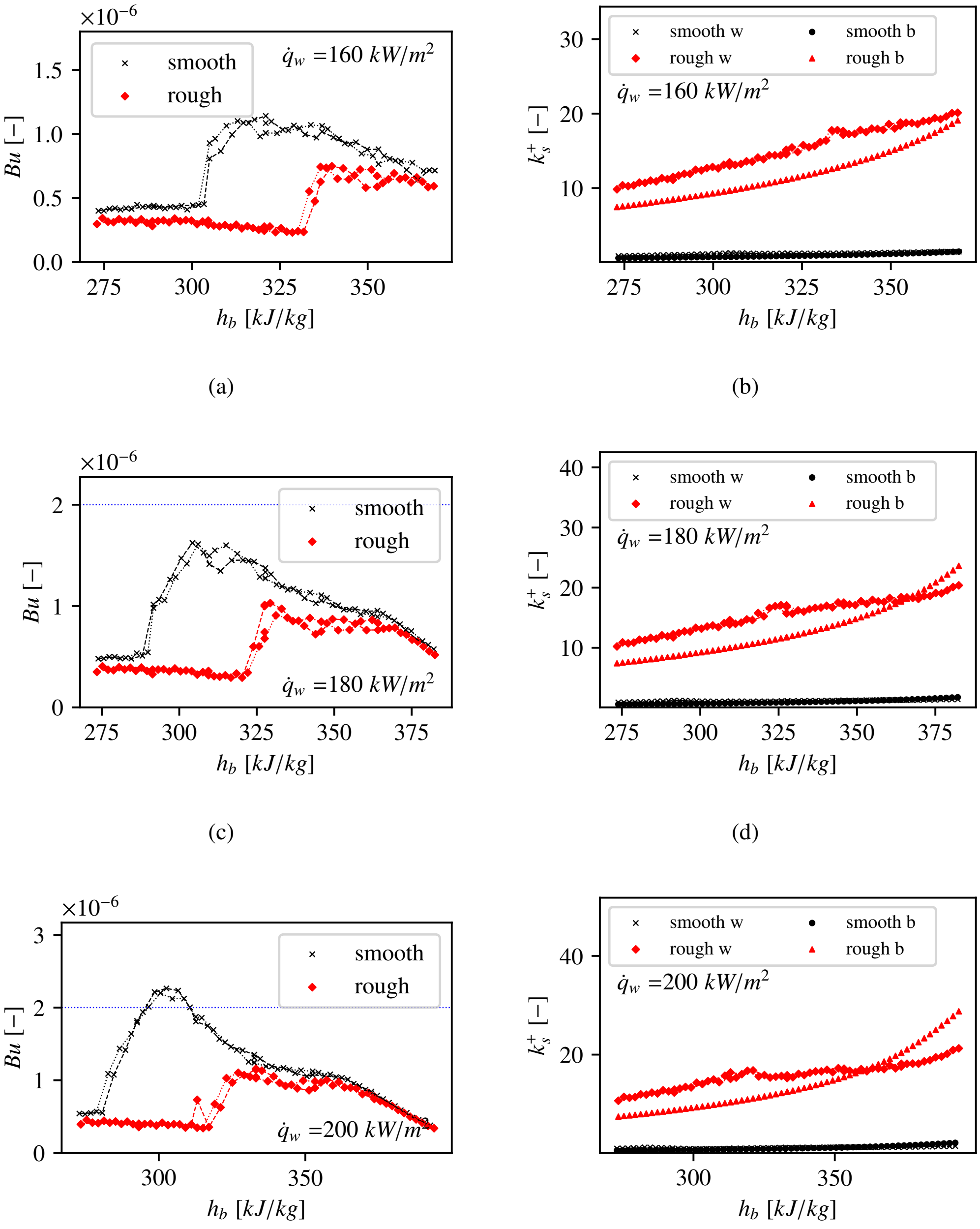

(a)

(b)

(c)

(d)

(e)

(f)

Figure 5.25: Trends of buoyancy parameter and wall-property based non-dimensional roughness height at p=4.6 MPa, G=2000 kg/m²s and (a, b) q=160 kW/m², (c, d) q=180 kW/m² and (e, f) q=200 kW/m².

relevant. When the momentum from the deflected fluid parcel close to the wall is transferred to another parcel further away from the wall, it is transferred from a small density parcel to a larger density parcel. Consequently, the velocity u_2 of the second parcel will be significantly less, compared to the velocity u_1 of the initially deflected parcel. This means that perturbations due to the roughness will not propagate into the flow. Turbulence can not be enhanced as much as in the scenario with similar densities. Thus, even though the roughness elements have a significant penetration depth into the flow, the effect of the roughness of the wall on the heat transfer is reduced.

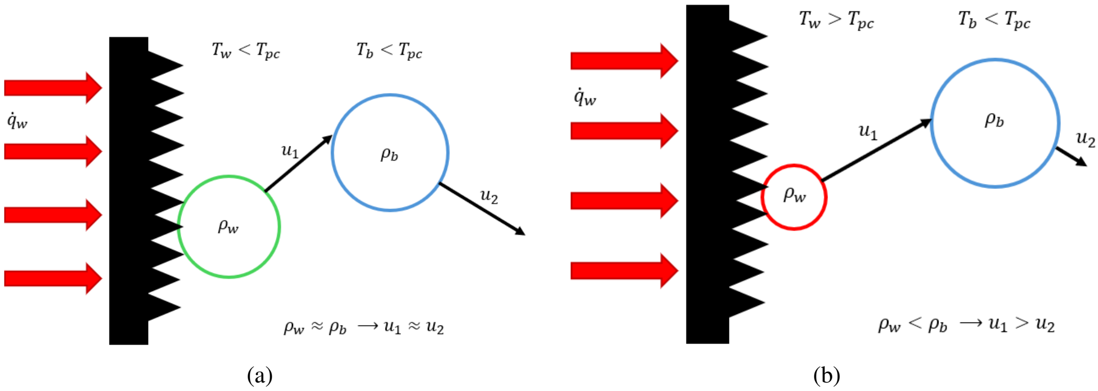

(a) (b)

Figure 5.26: Illustration of momentum transfer from the wall to the bulk at (a) $T_{w,i} < T_{pc}$ and $T_b < T_{pc}$ and (b) $T_{w,i} > T_{pc}$ and $T_b < T_{pc}$

For a larger heat flux of $\dot{q}_w = 180\ kW/m^2$, as shown in Figures 5.24 (c, d) and 5.25 (c, d), in the smooth tube, a slight deterioration of heat transfer is observed. In the rough tube, this is suppressed. However, the effect of less efficiently enhanced heat transfer due to roughness is also observed here, expressed in the jump of the wall temperature over the pseudocritical value, corresponding to a reduced heat transfer coefficient. Further, even for the larges obtained heat flux of $\dot{q}_w = 200\ kW/m^2$, which is shown in Figure 5.24 (e, f) and 5.25 (e, f), no DHT can be observed in the rough tube, while on the other hand the heat transfer is clearly deteriorated in the smooth tube. This is the only case at large mass flux, for which the threshold proposed by (Feuerstein, 2019) for R134a was exceeded, but that only happens in the smooth tube. Further it can be seen, that for the large mass flux, no significant changes of the non-dimensional wall roughness can be observed anymore, especially there are no sudden increases in the sublayer thickness.

For a global picture of the results obtained for $p = 4.6\ MPa$ and $G = 2000\ kg/m^2s$, the ratio of the experientially obtained heat transfer coefficient α to the normal condition heat transfer coefficient α_G is shown in Figure 5.27 for (a) the smooth tube and (b, c) the rough tube. In the rough tube, heat transfer deterioration is only observed in the vicinity of the pseudocritical point in the bulk. In contrast to that, few data points with deteriorated heat transfer are observed in the smooth tube in the bulk enthalpy range of about 300 kJ/kg to 320 kJ/kg. At these points, the threshold value of $0.2 \cdot 10^{-5}$ for buoyancy effect, as proposed by (Feuerstein, 2019) for R134a is exceeded. As the deterioration of heat transfer in that enthalpy range was clearly dedicated to buoyancy, for the smaller mass flux, these results for $G = 2000\ kg/m^2s$ support the proposed threshold value for R134a, as it was proposed by (Feuerstein, 2019). The non-dimensional roughness height, as shown

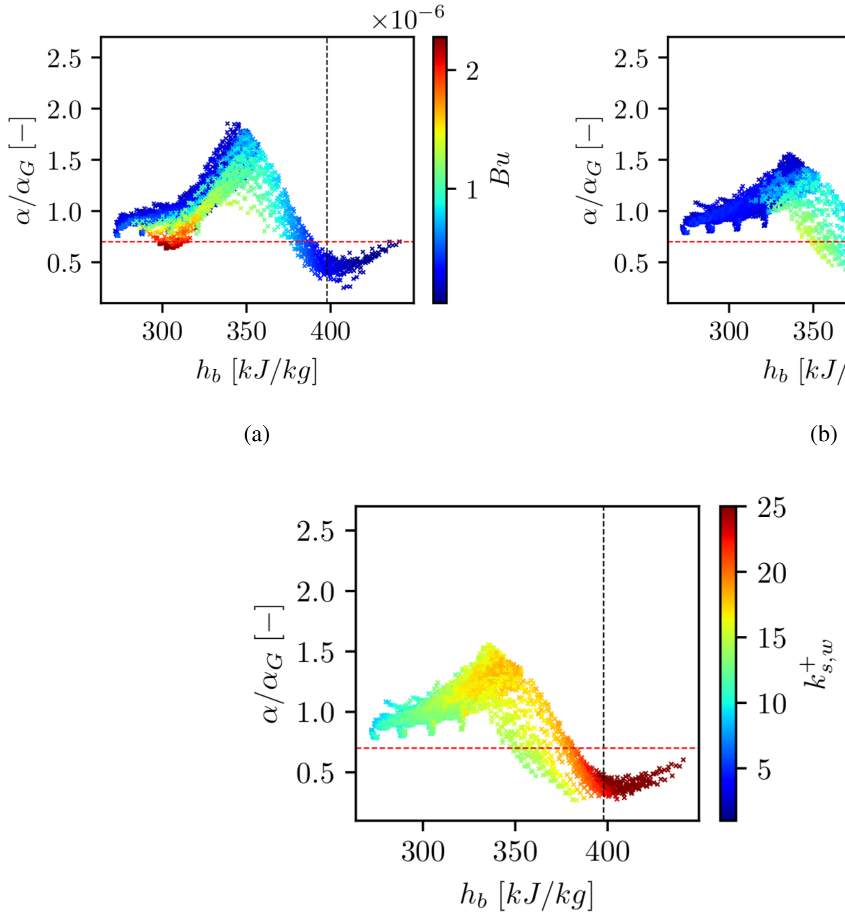

(a)

(b)

(c)

Figure 5.27: Ratio of experimentally obtained to normal conditions heat transfer coefficients for p=4.6 MPa and G=2000 kg/m²s in the (a) smooth tube and (b, c) rough tube

based on wall properties in Figure 5.27 (c), is above 10 for almost all the data points. Especially for the data-points with heat transfer deterioration around the pseudocritical bulk enthalpy, the non-dimensional roughness is large and the roughness elements are deeply penetrating the buffer layer. However, DHT cannot be suppressed by the effect of roughness.

The discussion above shows, that roughness also alters to onset of the property controlled heat transfer deterioration. To summarize the results, the criterion proposed by (Koshizuka et al., 1995) with a threshold value of 0.7 is applied to all results where the buoyancy parameter *Bu* is smaller than the threshold value of $1.0 \cdot 10^{-5}$. For $\alpha/\alpha_G < 0.7$ and $Bu < 1 \cdot 10^{-5}$, heat transfer is called property controlled deteriorated. The minimum heat flux for DHT according to this criterion is shown in Table 5.2. It can be seen, that for the smaller mass fluxes, the onset of heat transfer deterioration is shifted to larger heat flux. On the other hand, for larger mass flux, no effect is observed, or the minimum heat flux for which deterioration is present is slightly reduced. This is especially the case for the lower pressure of 4.35 MPa. However, in this case, heat transfer deterioration is just defined as a significantly lower experimentally obtained heat transfer coefficient, compared to a predicted heat transfer coefficient for normal conditions. E. g. the roughness effect is only considered via the skin friction coefficient, which is not necessarily sufficient. Therefore, this evaluation does not clearly show that a deterioration of heat transfer really exists at smaller heat flux, when roughness is present. Furthermore, as the results show, the roughness still enhances heat transfer, even though deteriorated heat transfer is present.

Table 5.2: Minimum heat flux for property controlled heat transfer deterioration in the smooth tube and in the rough tube (values are $\dot{q}_{DHT,smooth}/\dot{q}_{DHT,rough}$)

p $[MPa]$	T_{in} $[°C]$	G $[kg/m^2s]$						
		500	750	1000	1250	1500	1750	2000
4.35	50	35/ 35	55/ 70	90/ 90	100/ 110	130/ 130	150/ 140	170/ 170
	60	25/ 35	55/ 60	80/ 80	100/ 100	120/ 120	140/ 130	160/ 160
	70	25/ 35	55/ 55	80/ 80	100/ 90	110/ 110	140/ 130	140/ 140
	80	35/ 30	45/ 50	70/ 70	80/ 90	100/ 110	120/ 120	100/ 120
4.6	50	30/ 40	55/ 70	90/ 90	120/ 120	140/ 149	160/ 160	180/ 180
	60	30/ 40	60/ 65	90/ 90	110/ 110	130/ 130	150/ 150	170/ 170
	70	30/ 35	55/ 60	80/ 80	100/ 100	120/ 120	140/ 140	160/ 150
	80	30/ 35	50/ 55	80/ 70	90/ 90	110/ 100	120/ 120	130/ 140

5.3.4 Summary and conclusion for experiments at rough wall

Summarizing the results, the following can be concluded:

- Heat transfer is enhanced in the NHT regime, when the non-dimensional roughness height is large enough. The deeper the roughness elements penetrate the buffer layer, the more heat transfer is enhanced.

- Heat transfer deterioration, which is related to the effect of buoyancy, can be suppressed by the roughness, when the non-dimensional roughness height is sufficiently large. The induces turbulence are counteracting the laminarisation near the wall due to buoyancy. This is the case for moderate heat flux

- For large heat flux, roughness cannot suppress buoyancy related DHT. However, the temperature peak is shifted to larger bulk enthalpies. This can be explained with the enhanced heat transfer at NHT conditions. Due to enhanced heat transfer, the pseudocritical temperature at the wall is reached at larger bulk enthalpy. Consequently, since $T_{w,i} < T_{pc} < T_b$ is the prerequisite for buoyancy related DHT, the peak in the wall temperature is shifted in the rough tube.

- Around the pseudocritical enthalpy in the bulk, heat transfer is deteriorated in the smooth tube and in the rough tube as well. Such conditions are only reached with large heat flux, in the given experimental setup and the investigated inlet temperatures. Even though the roughness cannot suppress DHT, heat transfer is still enhanced.

- At large mass flux, heat transfer is enhanced clearly stronger, when $T_{w,i} < T_{pc}$, compared to situations with $T_{w,i} > T_{pc}$. This could be explained by momentum transfer from near wall fluid to fluid further away from the bulk. Deflected fluid with low density will not have a great impact in the velocity field further from the wall, while if the density near the wall and further from the wall is comparable, perturbations due to roughness will induce turbulence deeper in wall normal direction.

6 Development of empirical model

In this chapter, a new empirical correlation for heat transfer to fluids under supercritical pressure conditions is presented. First, the derivation of the general form of the theoretical considerations of the correlation form is shown. The model is then adjusted to the newly generated experimental data. In the first step, in order to capture the roughness effect on the heat transfer, flow conditions with very limited variations of the thermophysical properties are selected. Then for all of the newly generated data, the correlation is adjusted to strong variations in the fluid properties. In addition, a number of correlations from the literature that are applicable to heat transfer to supercritical pressure fluids at rough walls are evaluated and compared to the new correlation. Further, the correlation is evaluated, using CO_2 data from the literature.

6.1 Derivation of new empirical correlation

In this section, a new empirical correlation for heat transfer to fluid at supercritical pressure conditions, considering the wall roughness will be derived. The effect of the wall roughness on the flow is - as pointed out in the previous chapter - strongly related to the boundary layer, which is disturbed by the roughness elements. Therefore, the new correlation is based on the equation for the non-dimensional temperature in the turbulent boundary layer, which can be described depending on the surface roughness by (Schlichting & Gersten, 2016), (Aupoix, 2015), as introduced in Chapter 2.3.2:

$$T^+ = \frac{1}{\kappa_\Theta} ln\left(y^+\right) + C\left(Pr\right) - \Delta T^+\left(k_s^+\right) \tag{6.1}$$

The term $\Delta T^+\left(k_s^+\right)$ is the roughness function and represents the shift of the non-dimensional temperature profile due to the effect of the roughness on the flow. The constant $C\left(Pr\right)$ is given according to (Schlichting & Gersten, 2016) as:

$$C\left(Pr\right) = A \cdot Pr^m + B \tag{6.2}$$

With the assumption that the bulk temperature T_b is an approximation of the center line temperature T_{cl}, the non-dimensional temperature can be expressed as:

$$T^+ = \frac{T_w - T_b}{T_\tau} = \frac{\rho c_p \left(T_w - T_b\right) u_\tau}{\dot{q}_w} \tag{6.3}$$

According to (Laurien, 2012) and (Laurien, 2016), who is using the assumption for their two-layer model, it introduces an error, especially for large heat flux, but the error was limited to 5 K for

$q_w = 698\ kW/m^2$ in water. This implies that the performance of the correlation has to be evaluated carefully, especially for larger heat flux. Using equation 6.3, together with the definition of the Nusselt number and the definition of the heat transfer coefficient, the following is obtained:

$$Nu = \frac{\alpha D}{\lambda} = \frac{\dot{q}_w D}{\lambda \left(T_w - T_b\right)} = \frac{\rho c_p u_\tau D}{\lambda T^+ \left(y^+\right)} \tag{6.4}$$

where the non-dimensional temperature T^+ is a function of the non-dimensional wall distance y^+. Using the definition of the friction velocity u_τ and of the the wall shear τ_w:

$$u_\tau = \sqrt{\frac{\tau_w}{\rho}} \tag{6.5}$$

$$\tau_w = \frac{c_f}{8} \rho u_b^2 \tag{6.6}$$

the correlation reads:

$$Nu = \frac{\sqrt{\frac{c_f}{8}} \rho u_b D c_p}{\lambda T^+ \left(y^+\right)} \tag{6.7}$$

When the fraction is expanded with the dynamic viscosity μ, the equation can be expressed using the Reynolds and the Prandtl number:

$$Nu = \frac{\sqrt{\frac{c_f}{8}}}{T^+ \left(y^+\right)} \cdot \frac{\rho u_b D}{\mu_b} \cdot \frac{\mu_b c_p}{\lambda} = \frac{\sqrt{\frac{c_f}{8}} Re Pr}{T^+ \left(y^+\right)} \tag{6.8}$$

The non-dimensional temperature $T^+ \left(y^+\right)$, as written in equation 6.1 is introduced:

$$Nu = \frac{\sqrt{\frac{c_f}{8}} Re Pr}{\frac{1}{\kappa_\Theta} ln \left(y^+\right) + C \left(Pr\right) - \Delta T^+ \left(k_s^+\right)} \tag{6.9}$$

At this point, the roughness function $\Delta T \left(k_s^+\right)$ is included into the new empirical correlation. The non-dimensional wall distance y^+ is consistent with the definition of T^+ in equation 6.3, considered to range from the wall to the center line of the tube. Thus, the distance y equals the tube radius R:

$$y^+ = R^+ = \frac{\rho R}{\mu} = \frac{\rho R \sqrt{\tau_w}}{\mu \sqrt{\rho}} = \frac{\rho u_b D}{\mu} \cdot \frac{\sqrt{c_f}}{2\sqrt{8}} = \frac{\sqrt{c_f} Re}{2\sqrt{8}} \tag{6.10}$$

Finally, the constant $C \left(Pr\right)$ is simplified to $C \left(Pr\right) = A \cdot Pr^m$ and the roughness function is expressed as a linear function $\Delta T \left(k_s^+\right) = B \cdot k_s^+$. The constant property form of the new empirical model reads as:

$$Nu = \frac{\sqrt{\frac{c_f}{8}} Re Pr}{\frac{1}{\kappa_\Theta} ln \left(\frac{\sqrt{c_f} Re}{2\sqrt{8}}\right) + A \cdot Pr^m - B \cdot k_s^+} \tag{6.11}$$

In the following, the coefficients A and B, as well as the exponent m have to be determined. This is first done for experimental data with low variation of the thermophysical properties in the wall normal direction, in order to confirm that the correlation is generally capable for predicting the heat transfer, and especially the impact of the wall roughness on the heat transfer correctly (see Chapter 6.2). Then, in a second step (see Chapter 6.3), all newly obtained experimental data, so also data with strong variation of the thermophysical properties in wall normal direction is used, in order to introduce a correction factor for the fluid property variation.

6.2 Correlation for constant property heat transfer

First, in order to capture the roughness effect, data within the normal heat transfer regime, where only a slight variation of the thermophysical properties is present in the normal direction of the wall, are selected from the experimental database obtained. The data is selected by screening the experimental results for heat transfer deterioration, which is detected by temperature peaks. In addition, all data with $Bu > 1.0 \cdot 10^{-5}$ is also excluded. Further, data points which have a measurement uncertainty greater than 15% for the Nusselt number have been sorted out. There are 5092 data points selected from the rough tube and 5097 data points selected from the smooth tube, fulfilling those requirements. However, there is always some variation in the properties of the fluid. To take this into account, the averaged Prandtl number $\overline{Pr}$ is used.

$$\overline{Pr} = \frac{\overline{c_p}\mu_b}{\lambda_b} \tag{6.12}$$

with

$$\overline{c_p} = \frac{h_w - h_b}{T_w - T_b} \tag{6.13}$$

The non-dimensional roughness height is calculated as:

$$k_s^+ = \frac{\rho_w u_{\tau_w} k_s}{\mu_w} \tag{6.14}$$

and

$$u_{\tau_w} = \sqrt{\frac{c_f}{\rho_w}} \tag{6.15}$$

This will become relevant in the next step, when the correlation has to become applicable to cases with strong variation of thermophysical properties. As was shown in Chapter 5.3, the thickness of the boundary layer can be significantly influenced under deteriorated conditions, indicating that the application of wall properties will be required later when the correlation is adapted to these conditions. However, for the sake of application to cases with a small variation in fluid properties in the normal direction of the wall, this is obviously not relevant. Fitting the correlation with the mentioned data in the NHT regime and with a small variation in fluid properties yields $A = 10.63$, $B = 0.17$ and $m = 0.46$. The correlation for NHT and small variation of properties is therefore finally:

$$Nu = \frac{\sqrt{\frac{c_f}{8}} Re \overline{Pr}}{\frac{1}{\kappa_\Theta} ln\left(\frac{\sqrt{c_f} Re}{2\sqrt{8}}\right) + 10.63 \cdot \overline{Pr}^{0.46} - 0.17 \cdot k_s^+} \tag{6.16}$$

For a first assessment, the same data is used. Since the new correlation also depends on the wall temperature and the bulk temperature, an iterative solution of the equation 2.60, as explained in the paragraph 2.2.3.1, is obtained. For the flow conditions present in these data, the problem of no- or multi-solution does not exist. Table 6.1 shows the mean deviation μ, the mean absolute deviation

Table 6.1: Accuracy of basic correlation for data with small variation of thermophysical properties

Data set	μ [%]	$\|\mu\|$ [%]	σ [%]
smooth	1.78	6.3	8.03
rough	0.88	7.8	10.16

$|\mu|$ and the standard deviation σ of the predictions of the new correlation with the experimental data. The mean deviation μ, the mean absolute deviation $|\mu|$ and the standard deviation σ are defined as shown in equations 4.18, 4.19, 4.20, but are calculated based on the Nusselt number here. Furthermore, Figure 6.1 shows the predicted Nusselt number and the predicted wall temperature, exemplarily for the case of $p = 4.6\ MPa$, $G = 2000\ kg/m^2s$ and $\dot{q}_w$. It can be seen that the correlation captures the effect of the roughness on heat transfer well for the given flow conditions with a small variation of the thermophysical properties. From this point on, the correlation can be further adjusted to flow conditions with strong variations in fluid properties.

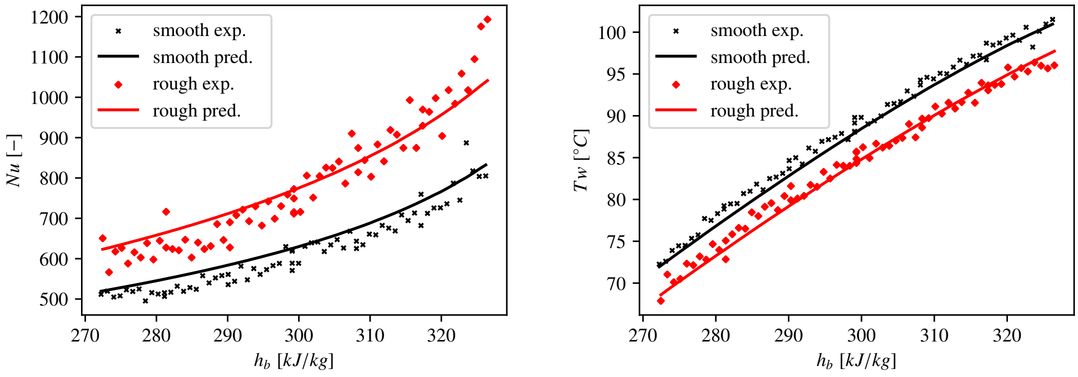

(a)

(b)

Figure 6.1: Predicted (a) Nusselt number and (b) wall temperature in comparison to experimental data for p=4.6 MPa, G=2000 kg/m²s, q=90 kW/m²

6.3 Correlation for non-constant property heat transfer

To adjust the correlation for cases with a strong variation of fluid properties, a correction factor, considering the variation of the properties from the wall to the bulk, is added to the basic correlation presented in the previous section. In Chapter 2.2.3.1, the possible ratios of the fluid properties are listed and their trend over varying bulk and wall temperature is shown. Generally, the ratio of the density ρ, the viscosity μ and the thermal conductivity λ form the wall temperature to the bulk temperature follows a similar trend, where only a reduction of the heat transfer by the correction factor can be captured, since these ratios are always smaller than 1. In contrast to that, the ratio of specific heat c_p can also increase to values larger than 1. As the analysis in Chapter 5 has shown, buoyancy often plays a role that is related to the variation of the density. Therefore, the ratio of the density at the wall temperature to the density at the bulk temperature is chosen for the analysis. Furthermore, the variation of the specific heat is chosen, since this correction factor can also be larger than 1. According to the trends of the property ratios presented in Figure 2.15 in Chapter 2.2.3.1, application of more than 2 correction factors should not be necessary. All available experimental data, sorting out some outlier data points with experimental uncertainty of the Nusselt number of more than 15 %, is used for a systematic analysis of all possible combinations of the chosen correction factors

$$F_{VP} = \left(\frac{\rho_w}{\rho_b}\right)^{n_1} \cdot \left(\frac{\overline{c_p}}{c_{p,b}}\right)^{n_2} \tag{6.17}$$

The exponents n_1 and n_2 are either fitted both, or one of them is forced to be 0. Furthermore, the analysis in Chapter 5.3.3 has shown that heat transfer is enhanced less strongly when the wall temperature exceeds the pseudocritical temperature and the bulk temperature is still subcritical. This could be explained with less effective momentum transfer, as illustrated in Figure 5.26. This emphasizes the application of another correction factor to the roughness function ΔT^+ (k_s^+), in the form of:

$$F_{\Delta T^+} = \left(\frac{\rho_w}{\rho_b}\right)^{n_3} \tag{6.18}$$

In the analysis, $F_{\Delta T^+} = 1$ and equation 6.18 are considered. As can be seen in Table 2.3, some authors of existing correlations also apply correction factors to the friction factor, such as (Razumovskiy et al., 1990):

$$F_{c_f} = \left(\frac{\mu_w}{\mu_b}\frac{\rho_w}{\rho_b}\right)^{n_4} \tag{6.19}$$

or (V. Kurganov, 1998)

$$F_{c_f} = \left(\frac{\rho_w}{\rho_b}\right)^{n_4} \tag{6.20}$$

The application of either equation 6.19, 6.20 or no correction of c_f is considered in the analysis, and the exponent n_4 is fitted respectively. In order to find the best combination of the correction factors under consideration, the correlation is fitted to all the experimental data, applying each combination of the correction factors F_{VP}, $F_{\Delta T^+}$ and F_{c_f}:

$$Nu = \frac{\sqrt{\frac{c_f}{8}}Re\overline{Pr}}{\frac{1}{\kappa_\Theta}ln\left(\frac{\sqrt{c_f}Re}{2\sqrt{8}}\right) + 10.63 \cdot \overline{Pr}^{0.46} - F_{\Delta T^+} \cdot 0.17 \cdot k_s^+} \cdot F_{VP} \tag{6.21}$$

with

$$c_f = c_{f,0} \cdot F_{c_f} \tag{6.22}$$

The method of non-linear least squares is applied to it all possible combinations of F_{VP}, $F_{\Delta T^+}$ and F_{c_f} to find the correlation with the best prediction accuracy, in terms of the mean deviation μ, the mean absolute deviation $|\mu|$ and the standard deviation σ. Further it is important, that number of data-points for which no or multi-solutions are possible is minimized. Finally, the best correlation is found by:

$$Nu = \frac{\sqrt{\frac{c_f}{8}}Re\overline{Pr}}{\frac{1}{\kappa_\Theta}ln\left(\frac{\sqrt{c_f}Re}{2\sqrt{8}}\right) + 10.63 \cdot \overline{Pr}^{0.46} - 0.17 \cdot k_s^+ \left(\frac{\rho_w}{\rho_b}\right)^{0.68}} \cdot \left(\frac{\rho_w}{\rho_b}\right)^{0.18} \tag{6.23}$$

with

$$c_f = c_{f,0} \cdot \left(\frac{\rho_w}{\rho_b} \frac{\mu_w}{\mu_b} \right)^{0.29} \tag{6.24}$$

In Figure 6.2, the predicted Nusselt number for a unknown wall temperature, using equation 6.23, is compared to the experimental data, for all the experimental data obtained in (a) the rough tube and (b) the smooth tube. Generally, the correlation yields reasonable predictions, but some systematic deviations can also be observed. For small Nusselt numbers, there is a tendency for over-prediction of the experimental data. This is the case for the data obtained in the rough tube and for the data obtained in the smooth tube as well. Further, for the data obtained in the smooth tube, the new correlations tend to under-predict the Nusselt number, for data points with large experimentally obtained Nusselt number. Since the focus of the present work is to develop a correlation, capable of predicting heat transfer to supercritical pressure fluid at a rough wall, this can be accepted at this point. Additionally, Figure 6.3 shows the predicted Nusselt number for a unknown wall heat flux, compared to the experimental values. Since the wall temperature is applied to the correlation, the Nusselt number can be calculated explicitly and the predictions are less scattered compared to the

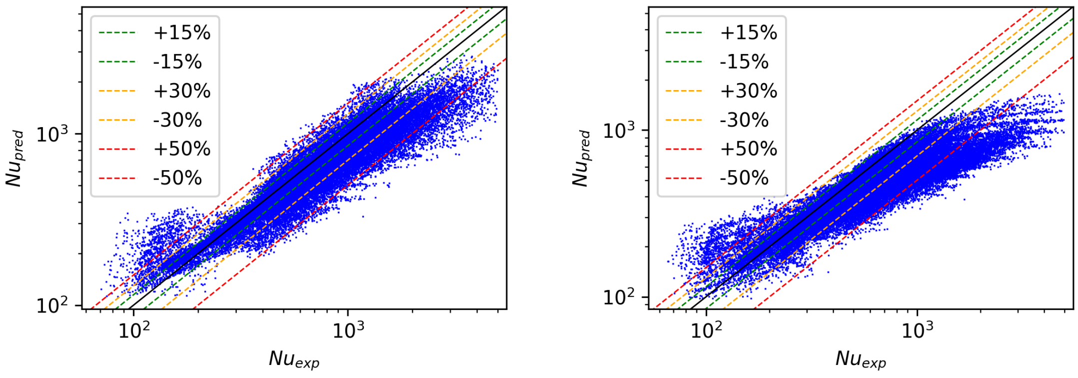

(a) (b)

Figure 6.2: Predicted Nusselt number with unknown wall temperature compared to experiment for data obtained in the (a) rough tube and (b) smooth tube

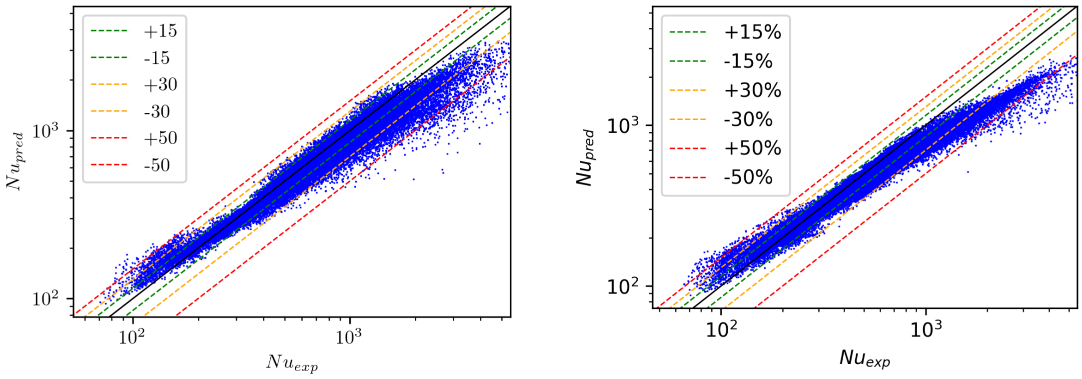

(a) (b)

Figure 6.3: Predicted Nusselt number with unknown wall heat flux compared to experiment for data obtained in the (a) rough tube and (b) smooth tube

implicit predictions with unknown $T_{w,i}$. Besides that, the conclusions are the same as for Figure 6.2.

As mentioned before, the assumption of $T_b = T_{cl}$, (T_{cl} is temperature at the centerline of the tube) which was used to derive the new Nusselt correlation, introduces an error for cases with large heat flux. Therefore, the performance of the correlation for cases with large heat flux has to be evaluated carefully. As an example, Figure 6.4 shows the predicted (a) Nusselt number and (b) wall temperature versus experimental data, for $p = 4.6\ MPa$, $G = 500\ kg/m^2s$ and $\dot{q} = 70\ kW/m^2$, which is the largest heat flux in the database, for the smallest mass flux. In addition to the prediction of the correlation, the recalculated Nusselt number and wall temperature are also shown for comparison. Recalculated means that the experimentally obtained wall temperature and the known bulk temperature are used in the correlation to calculate the Nusselt number, and thus this is not a prediction. It can be seen, that DHT which happens close to the inlet of the tube can be recalculated well. Comparing the recalculated wall temperature to the experimental data, qualitatively nice agreement is achieved, but the temperatures are under predicted. In contrast to that, the prediction just roughly follows the experimental data. In general, the correlation yields a reasonable recalculation for large heat flux, qualitatively capturing the rise in temperature due to DHT. On the other hand, prediction of DHT remains challenging for conventional correlations, which is addressed in the following chapter.

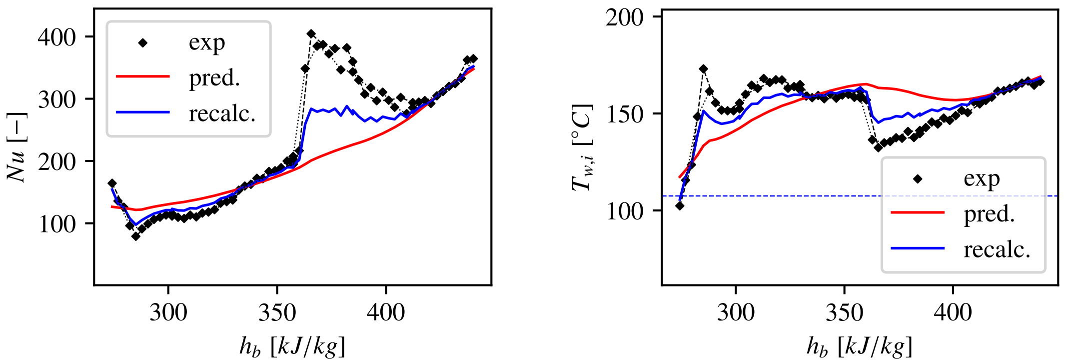

(a)

(b)

Figure 6.4: Predicted (a) Nusselt number and (b) wall temperature in comparison to experimental data for p=4.6 MPa, G=500 kg/m^2*s, q=70 kW/m*^{2}*, rough tube*

For a larger mass flux of $G = 750\ kg/m^2s$, the largest heat flux is $\dot{q} = 75\ kW/m^2$. Figure 6.5 shows the trends of the predicted (a) Nusselt number and (b) wall temperature for these conditions. The experimental data clearly shows DHT, in form of a sharp temperature peak, which can be properly recalculated by the correlation. The DHT can be qualitatively predicted to some extent, as a small drop in the Nusselt number and a small temperature peak are predicted, but quantitatively the effect is underestimated.

Figure 6.6 shows the trends of the predicted (a) Nusselt number and (b) wall temperature, for heat flux $\dot{q}_w = 130\ kW/m^2$ at $G = 1000\ kg/m^2s$. The predicted wall temperature is larger than T_{pc} throughout the test section. The experimental results show DHT, which is recalculated well. At

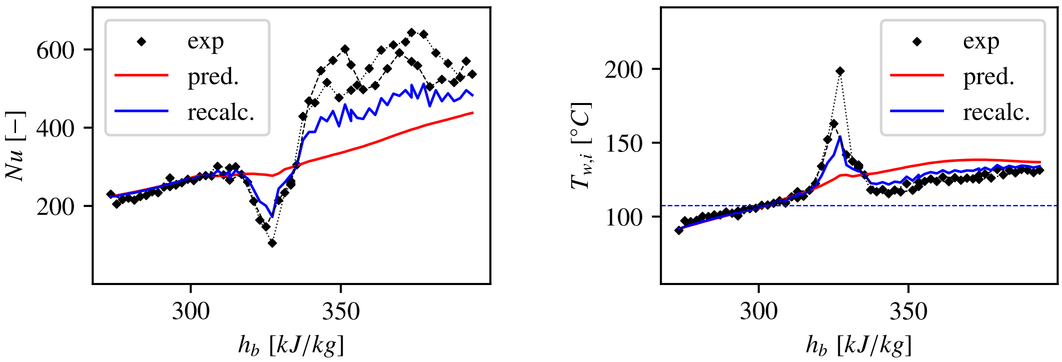

(a)

(b)

Figure 6.5: Predicted (a) Nusselt number and (b) wall temperature in comparison to experimental data for p=4.6 MPa, G=750 kg/m²s, q=75 kW/m², rough tube

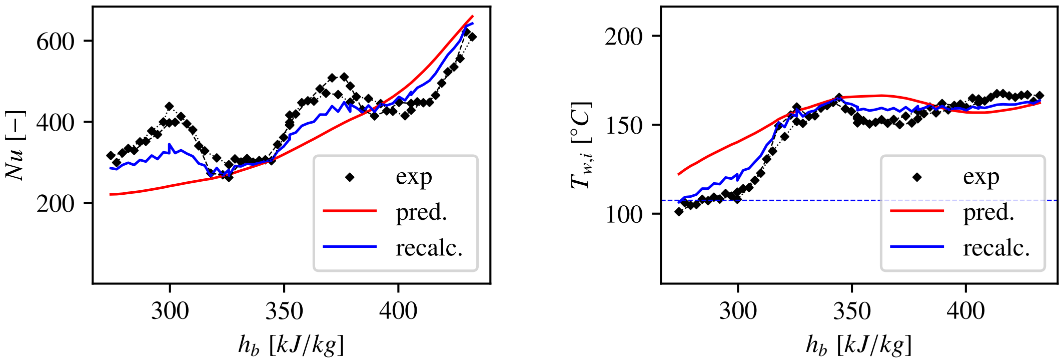

(a)

(b)

Figure 6.6: Predicted (a) Nusselt number and (b) wall temperature in comparison to experimental data for p=4.6 MPa, G=1000 kg/m²s, q=130 kW/m², rough tube

these conditions, also the predicted wall temperature shows a small elevation. Qualitatively, the prediction agrees well with the experimental results.

In summary, it can be said that the proposed correlation for heat transfer to supercritical pressure fluid at rough surface yields reasonable results, even for large heat flux, despite the assumption of $T_b = T_{cl}$ in the derivation of it. Heat transfer deterioration cannot be predicted but qualitatively recalculated.

For further evaluation of the correlation, the prediction accuracy is compared to correlations presented in the literature, which are applicable to heat transfer at rough walls. As discussed in Chapter 2.2.3.1, the number of correlations that are directly applicable to heat transfer is limited, but some more correlations exist, in which the wall roughness can be considered by calculating the skin-friction coefficient as a function of the wall roughness, using e.g. the Colebrook equation eq. 2.70 (Colebrook, 1939). Table 6.3 summarizes the precision of the prediction for unknown wall temperature $T_{w,i}$, in terms of the mean deviation μ, the mean absolute deviation $|\mu|$ and the standard deviation σ of the predictions versus the experimental data, separately for the data obtained in the smooth tube and the data obtained in the rough tube. The same is shown for the precision of the prediction for unknown wall heat flux $\dot{q}_w$. The correlations from the literature are shown in the Appendix, as indicated in the table. The correlations in the table are sorted by the mean absolute deviation $|\mu|$ for the data obtained in the rough tube. It can be seen that the new correlation is most accurate in terms of the mean absolute deviation for the rough tube. Also, the standard deviation σ is the smallest for the new correlation. It is noticeable that correlations, in which the variation of the fluid properties is considered for the skin-friction coefficient, such as (Razumovskiy et al., 1990), (V. Kurganov, 1998) are among the most precise correlations, either for the rough or for the smooth tube.

Table 6.2: Comparison of accuracy of predictions of new correlation and correlations from the literature against all new experimental data, for unknown wall temperature

	rough tube			smooth tube		
Author	μ [%]	$\lvert\mu\rvert$ [%]	σ [%]	μ [%]	$\lvert\mu\rvert$ [%]	σ [%]
New correlation	-12.3	19.7	23.3	-19.0	25.8	28.1
(Razumovskiy et al., 1990), A.2.9	-3.4	21.4	29.6	9.7	23.4	31.1
(V. Kurganov, 1998), A.2.10	-2.6	23.0	33.6	-10.7	22.4	29.3
(Kransoshchekov & Protopopov, 1966), A.2.3	-5.3	26.6	34.3	-12.4	25.1	30.2
(Kirillov et al., 1990), A.2.8	-25.0	30.0	27.1	-35.8	36.6	57.1
(Petukhov et al., 1961), A.2.2	17.9	32.3	46.7	14.1	29.3	41.6
(J. Chen et al., 2022), A.1.3	-10.0	35.9	39.7	-46.6	50.3	28.7
(J. McCarthy et al., 1968), A.1.1	-10.7	42.8	53.3	5.5	38.4	57.1
(Petukhov & Kirillov, 1958), A.2.1	14.9	50.4	81.3	8.8	43.3	68.6
(Gnielinski, 1975), A.2.6	41.0	59.6	97.7	36.4	52.2	82.1
(Cook, 1984), A.1.2	85.6	95.5	182.9	56.3	71.0	132.8

This supports the decision to apply a correction factor for the variation of the thermophysical

Table 6.3: Comparison of accuracy of predictions of new correlation and correlations from the literature against all new experimental data, for unknown wall heat flux

	rough tube			smooth tube		
Author	μ [%]	$\lvert\mu\rvert$ [%]	σ [%]	μ [%]	$\lvert\mu\rvert$ [%]	σ [%]
New correlation	-11.3	14.3	13.2	11.6	15.2	15.5
(Razumovskiy et al., 1990), A.2.9	-4.9	15.8	19.6	-7.8	16.5	20.0
(V. Kurganov, 1998), A.2.10	-3.6	16.4	20.4	-8.1	15.3	18.8
(Kirillov et al., 1990), A.2.8	-15.2	18.5	16.9	-21.3	22.0	16.3
(Kransoshchekov & Protopopov, 1966), A.2.3	-6.4	19.0	22.4	-10.3	18.0	20.8
(Petukhov et al., 1961), A.2.2	13.0	26.6	36.4	11.6	24.3	32.7
(J. Chen et al., 2022), A.1.3	-25.9	27.4	16.9	-38.9	38.9	15.1
(Petukhov & Kirillov, 1958), A.2.1	17.9	48.3	79.8	10.9	41.8	67.6
(J. McCarthy et al., 1968), A.1.1	-56.8	73.6	55.3	0.5	37.0	52.7
(Gnielinski, 1975), A.2.6	50.8	68.1	115.4	45.1	60.5	97.9
(Cook, 1984), A.1.2	87.8	96.0	183.2	58.1	60.5	97.9

properties for c_f in the new correlation. Looking at the results obtained for the smooth tube, the correlations proposed by (Razumovskiy et al., 1990), (V. Kurganov, 1998) and (Kransoshchekov & Protopopov, 1966) show a lower mean absolute deviation $|\mu|$, but the standard deviation σ is the smallest among those for the proposed new correlation. This shows how challenging it is to develop a correlation, which is valid for smooth and rough walls together. The correlations, which directly consider the roughness of the wall, (J. McCarthy et al., 1968), (J. Chen et al., 2022), and (Cook, 1984), are among the least accurate correlations. In the McCarthy correlation, the variation of the fluid properties is considered only by the ratio of wall temperature to bulk temperature, which appears to be insufficient for the present data. Cook did not consider the variation of the thermopyhsical properties at all. In contrast to this, Chen et al. used the ratio of density ρ, specific heat c_p, viscosity μ, and thermal conductivity λ. Therefore, the correlation has a comparably larger number of free parameters for fitting, which usually helps to create a good fit to the underlying data, but also comes with the risk that the correlation performs worse for different data sets, which is the case for the present experimental data. The majority of the correlations perform better for a known wall heat flux, when the wall temperature can be directly applied to them. In summary, it can be stated that the new correlation yields acceptable results, especially for NHT conditions. The accurate prediction of DHT still remains challenging, which shall be addressed be application of machine learning in the following Chapter.

6.4 Evaluation against literature data

The new correlation yields reasonable results for the R134a data, which has been used to develop it. Nevertheless, an evaluation of the new correlation against different data from the literature is necessary. The study of (J. Chen et al., 2022), using CO_2 as working fluid and 5 different tubes with different surface roughness is well suited for an evaluation. A total of 2268 data points have been digitized from the publication. The digitized data covers boundary conditions in the range of $7.5\ MPa \leq p \leq 10\ MPa$, $300\ kg/m^2s \leq G \leq 500\ kg/m^2s$, $30\ kW/m^2 \leq \dot{q}_w \leq 70\ kW/m^2$ and $15\ °C \leq T_{in} \leq 25\ °C$. Table 6.4 shows mean deviation μ, mean absolute deviation $|\mu|$ and standard deviation σ of the predictions of the new correlation to the experimental data, separately for unknown $T_{w,i}$ and for unknown $\dot{q}_w$.

Additionally, Figure 6.7 shows the predicted Nusselt number, compared to the experimental results for the data of Chen at al., for (a) unknown wall temperature $T_{w,i}$ and for (b) unknown wall heat flux $\dot{q}_w$. If the heat flux is unknown and the wall temperature can be applied to the correlation, the performance is reasonably good. Generally, the correlation tends to over predict the experimental

Table 6.4: Comparison of accuracy of predictions of new correlation and correlations from the literature against all new experimental data, for unknown wall temperature

Mode	μ [%]	$\|\mu\|$ [%]	σ [%]
unknown $T_{w,i}$	54.83	57.22	65.1
unknown $\dot{q}_w$	19.79	20.89	18.22

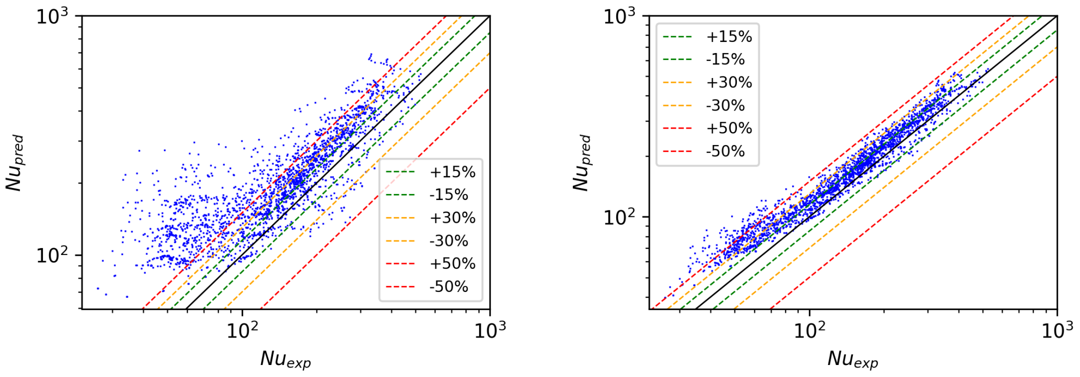

(a) (b)

Figure 6.7: Predicted Nusselt number compared to data of Chen et al. for (a) unknown wall temperature and (b) unknown wall heat flux

Nusselt number, but on the other hand, the standard deviation is small, which can also be seen in the low scatter of the predictions in Figure 6.7 (b). On the other hand the results are quite poor for unknown $T_{w,i}$.

7 Neural network model for heat transfer

In the recent years, machine learning models have become more and more important. The large amount of experimental data can be used to train machine learning models that promise to be more accurate compared to conventionally used empirical correlations. As pointed out in the previous chapter, especially the prediction of heat transfer deterioration is challenging by means of conventional methods. In the following, neural network-based machine learning shall be tested. The newly generated experimental database of heat transfer to supercritical pressure R134a at a smooth and rough surface shall be used to train and evaluate a neural network-based machine learning model. First, it needs to be analyzed, which input and output parameters can be used for the neural network model. Then, the model architecture and optimization of the structure, the training and validation procedure is discussed. Finally, the neural network approach and conventional correlations are compared in terms of prediction accuracy.

7.1 Model parameter selection

In heat transfer experiments, the wall temperature T_w is measured, for a given pressure p, mass flow rate $\dot{m}$, heat flux $\dot{q}_w$ and inlet temperature T_{in}, in a tube with hydraulic diameter d_h, wall roughness k_s and heated length L_h. From the energy balance, the local bulk enthalpy h_b or local bulk temperature T_b respectively, can be calculated. In the most simple case, a neural network could be trained to predict wall temperature as a function of these parameters. However, such a model would be limited to application to problems, where the same fluid as in the training data is used, and a training database with different fluids would contain ambiguous results. Therefore, it seems desirable to create a neural network based on non-dimensional input and output features. Instead of predicting the wall temperature, it makes sense to use the Nusselt number Nu, representing the non-dimensional heat transfer coefficient as the output feature. For a given fluid, the pressure determines how sharp the thermophysical properties are varying in the vicinity of the pseudocritical temperature. As explained in Chapter 2.1 and visualized in Figure 2.3 for density ρ and specific heat c_p, the variation in fluid properties is sharper, the closer the pressure to the critical pressure, and the change becomes more subtle for larger pressures. This is taken account by a scaling of the pressure, using the critical pressure of the fluid:

$$p^+ = \frac{p}{p_c} \tag{7.1}$$

The mass flow rate $\dot{m}$, in combination with the local viscosity μ and the hydraulic diameter d_h, is determining, weather the flow is turbulent, and also indicates how strong the turbulence is. This can be represented by the Reynolds number, as given in equation 2.4. Additionally, the Prandtl number Pr, as defined in 2.5, as a measure of dominance of convection or conduction respectively, contains useful information which can be used for the training of the neural network, as it it also included in empirical heat transfer correlations. The heat flux can be expressed, applying the acceleration number proposed by (Cheng et al., 2009b), which is in this context called the non-dimensional heat flux q^+:

$$\dot{q}_w^+ = \frac{\dot{q}_w}{G} \frac{\beta}{c_p} \tag{7.2}$$

Further, a local parameter is required, which is given by a non-dimensional form of the bulk enthalpy h_b. This is taken from (Pucciarelli et al., 2020):

$$h_b^+ = \left(h_b - h_{pc}\right) \frac{\beta_{pc}}{c_{p,pc}} \tag{7.3}$$

As the analysis of the experimental results in Chapter 5.2 has shown, the "history" of the flow can also play a role. To address this issue, the difference from the inlet enthalpy to the pseudocritical enthalpy is considered, also in non-dimensional form:

$$h_{in}^+ = \left(h_{in} - h_{pc}\right) \frac{\beta_{pc}}{c_{p,pc}} \tag{7.4}$$

Finally, the effect of the wall roughness has to be considered. As explained in Chapter 5.3, the effect of the wall roughness on the heat transfer is directly related to the ratio of the sand grain roughness height k_s to the thickness of the laminar sublayer, which is expressed in the non-dimensional roughness height k_s^+. In order to avoid an iterative procedure, k_s^+ has to be defined on bulk properties, as given in equation 3.2. Thus, the task of the neural network training is to find the function:

$$Nu = f\left(p^+,\ Re,\ Pr,\ \dot{q}_w^+,\ h_b^+,\ h_{in}^+,\ k_s^+\right) \tag{7.5}$$

On the first glance, it seems that application of p^+ and Pr is ambiguous, but nevertheless, application of both of the input parameters yields slightly better results (about 1 % difference in MAE and STD), as tests have shown. For the following, all available experimental data from the smooth and the rough tube are used, excluding data points with experimental uncertainty of more than 15%. For training of neural network, it is beneficial, when the distribution of the training data follows a Gaussian normal distribution. However, a real existing experimental dataset usually does not follow such a distribution. Nevertheless, the data can be prepared to be more close to a Gaussian distribution. This is shown exemplarily for the Nusselt number and the Reynolds number in Figure 7.1, where the distribution of the Reynolds number and the Nusselt number respectively are shown, and also the distribution of the natural logarithm of these parameters is shown. It can be seen, that this results in a distribution of data, which is more close to a standard distribution. This is applied to all the parameters where applicable and useful, so that the target of the neural network training is changed to find the function:

$$ln\left(Nu\right) = f\left(p^+,\ ln(Re),\ Pr,\ ln\left(\dot{q}_w^+\right),\ h_b^+,\ h_{in}^+,\ ln\left(k_s^+\right)\right) \tag{7.6}$$

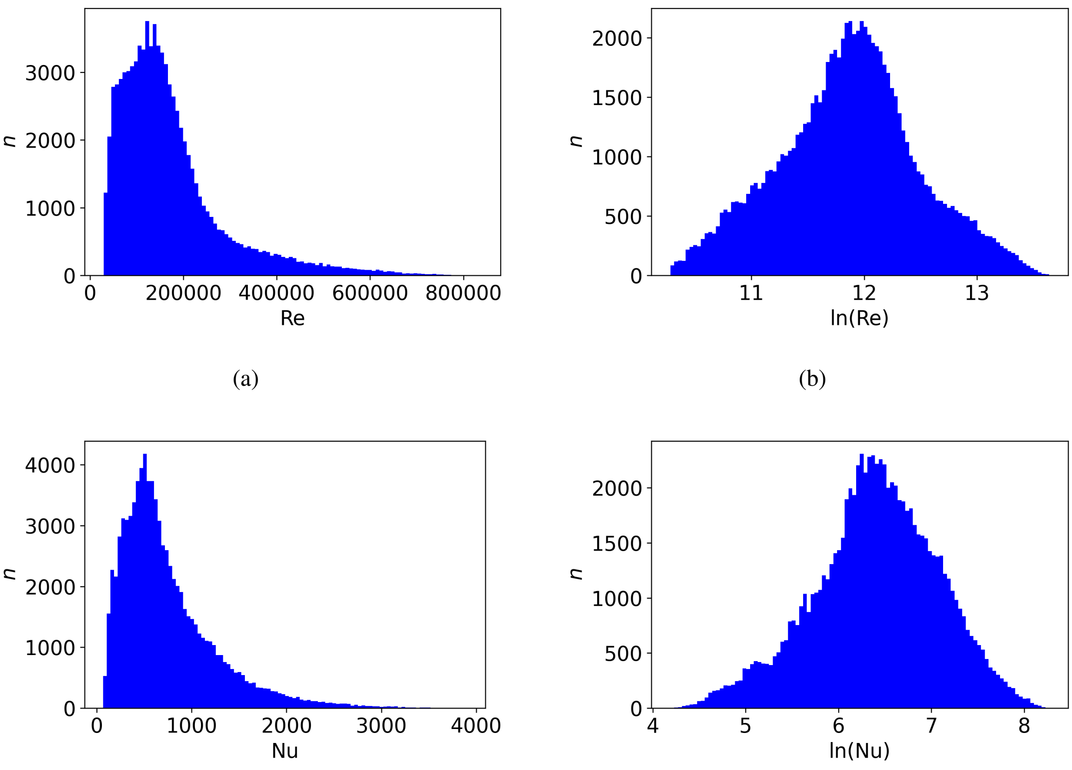

(a) (b)

(c) (d)

Figure 7.1: Distribution of (a) Reynolds number, (b) natural logarithm of Reynolds number, (c) Nusselt number and (d) natural logarithm of Nusselt number

This means, the neural network will predict the natural logarithm of the Nusselt number, which can simply be reverted by the exponential function.

7.2 Model architecture

In Chapter 2.2.3.4, the general structure of a neural network is explained. For practical application, the choice of the so-called hyperparameters is challenging, since there are no best-practice guidelines, of, for example, how many hidden layers to choose or how many neurons there should be in each layer. It just can be said that one should start with a smaller model and increase model complexity step by step, until a satisfying result is achieved. The following hyperparameters have to be chosen:

- **Number of hidden layers N:** Each neural network needs an input layer and an output layer. The number of neurons is simply defined by the number of input and output parameters. All the layers between are called hidden layers. A deep neural network has at least 1 hidden layer

- **Number of neurons in each layer n:** In each hidden layer, number of neurons can be freely chosen, independently from the number of neurons in the previous or the following layer. Each neuron is connected to each neuron from the previous layer and from the following layer. At each connection, the simple linear function $y = w_i + b$ is calculated, where every connection has its own weight w_i and the bias b is usually the same for all connections on each neuron. (b can also be 0).

- **Activation function:** In addition to the linear equation, each neuron can also have an activation function, for example rectified linear unit (ReLU) or sigmoid. Theoretically, each hidden layer can have it's own activation function or no activation function.

- **Loss function:** The target in training a neural network is minimizing the loss function. Depending on the problem which is addressed by the neural network, the loss function can be chosen from a large number of different formulations. However, for data regression problems, MSE, MAE or MSLE are commonly used.

- **Learning rate η:** The learning rate determines how much the trainable parameters w_i and b are updated in each training step. Generally, at the beginning of the training, a higher learning rate can be used to speed up the process, and later smaller values are required to find the global minimum of the loss function.

- **Optimizer:** The optimizer is an algorithm used to update w_i and b, with the aim of reducing the loss function. For regression problem, stochastic gradient descent algorithms are used. Many tests within this work have shown that for heat transfer problems, Adam optimizer (Kingma & Ba, 2015) should be used.

- **Dropout rate:** A dropout layer randomly sets connections to the next layer to 0, according to the dropout rate r_d. This helps prevent overfitting. The inputs, which are not set to zero, are scaled by $1/(1-r_d)$, so the overall inputs are unchanged.

- **Kernel regularization**: By adding a penalty term, based on the magnitude of the weights to the loss function, overfitting can be prevented. This discourages the model from heavily relying on specific parameters, encouraging simpler and more general solutions. L1 regularization adds the sum of the absolute values of the weights ($\lambda \sum |w_i|$) to the loss function. As some weights will be set so exactly zero, the model is encouraged to be sparse. On the other hand, L2 regularization adds the sum of the squared values of the weights $\left(\lambda \sum w_i^2\right)$, which discourages large weights, but does not set them to 0. The hyperparameter λ needs to be chosen. Tests have shown, that for heat transfer problems, L2 regularization can be beneficial, while L1 regularization is more likely leading to worse performance of the model.

As can be seen from this breakdown, a large number of hyperparameters need to be chosen in combination. One may choose 1 hidden layer with, e.g. 20, 50, 100, 200 neurons, 2 hidden layers or even more, and within each layer again different numbers. For all the hyperparameters in combination, many different network architectures can be tested and evaluated by the final loss on the training data and also on unseen test data. This procedure is called grid search, which is obviously very time consuming. The Optuna framework (Akiba et al., 2019) offers a more efficient method for hyperparameter optimization, based on a pruning algorithm. In this framework, the parameter search space can be defined for each desired hyperparameter. The algorithm constructs a trial for a combination of hyperparameters, evaluates the model based on a defined metric (validation loss in the present case) and iteratively improves the search by learning from past trials. Table

Table 7.1: Search space for hyperparameter optimization

Hyperparameter	search space
Number of hidden layers N	1 - 5
Number of neurons per layer n_i	4 - 512
Activation function	ReLU, sigmoid, tanh
Dropout rate r_d	0.001 - 0.5
L2 regularization λ	$1 \cdot 10^{-10}$ - $1 \cdot 10^{-3}$

7.1 gives the search space, applied in this study: In order to reduce the effort for the optimization algorithm, the other hyperparameters are selected by experience. The loss function is the MSE, as given in equation 2.68. For training, the Adam optimizer is used, with an initial learning rate of $\eta = 1 \cdot 10^{-3}$. The Optuna algorithm was run for 500 trials, using the same data which are used for the training of the final model in the next step, and ultimately suggested a model with 4 hidden layers. The hyperparameters for each layer are shown in Table 7.2.

Table 7.2: Hyperparameters of optimized neural network

Hyperparameter	Layer 1	Layer 2	Layer 3	Layer 4
Number of neurons n_i	365	214	124	392
Activation function	ReLU	ReLU	ReLU	ReLU
Dropout rate r_d	$1.54 \cdot 10^{-3}$	$12.2 \cdot 10^{-3}$	$2.01 \cdot 10^{-3}$	$2.35 \cdot 10^{-3}$
L2 regularization λ	$3.12 \cdot 10^{-8}$	$1.69 \cdot 10^{-7}$	$9.13 \cdot 10^{-8}$	$2.76 \cdot 10^{-9}$

7.3 Model training

For machine learning, a set of data must always be kept out in the training procedure, since a large neural network is usually able to fit a given dataset very well, since the number of trainable parameters can be very large. However, a model which fits perfectly to a given dataset may perform very badly on any other dataset. The performance of a machine learning model can only be evaluated by comparing the predictions with data that have not been used in the training of the model. In addition, it shall be tested whether the neural network is able to predict temperature trends, especially temperature peaks due to DHT. Therefore, 41 of the experimental cases are randomly selected from the experimental database, covering NHT and DHT conditions. For every selected case, the data from the smooth tube and from the rough tube is taken, that the predictions can be directly compared, and it can be evaluated, how well the effect of the roughness is predicted by the model. These test cases contain 5450 data points, which corresponds to 6% of the available data. Another 14% (11802 data points) are randomly selected, among all the rest of the available data, regardless of which experimental case they belong to. These are the validation data, which are used after each training iteration to calculate the validation loss. The other 80% (68059) of available data are the training data.

At the beginning of the training, all weights w_i and bias b are initialized with random values. The training data set is split into batches and in a training iteration, all batches are fed into the neural network. After each batch, the loss function (equation 2.68 is calculated, based on the network output $y_i(x, w, b)$ and the corresponding experimental result $\hat{y}_i(x)$. Then, the gradient descent algorithm updates the weights w_i and the bias b, in order to reduce the loss function, which is repeated for each batch. The batch size has an impact on the results and is also a hyperparameter. In general, a smaller batch size offers potentially better generalization, while a larger batch size speeds up the training, but comes with the risk of overfitting. By gained experience in many tests, batch size of 32 is chosen. In the gradient descent algorithm, the learning rate η is initially set to $1 \cdot 10^{-3}$. After all batches have been fed to the neural network, the training iteration terminates. Now, the weights w_i and bias b are fixed, and the validation data is fed into the neural network to calculate the validation loss. This procedure is repeated up to 5000 times. The validation loss is monitored and used to do two different things: First, if the validation loss does not decrease for 50 training iterations, the learning rate is multiplied by factor 0.8, which helps to further decrease the loss in the following training iterations. Once the learning rate reaches the limit of $1 \cdot 10^{-6}$, it no longer decreases. The second use of the validation loss is to stop training if the validation loss does not decrease anymore. After 100 training iterations without improvement, the training is stopped, which happens after 1048 iterations. Figure 7.2 shows the training loss and the validation loss of the neural network for the whole training process.

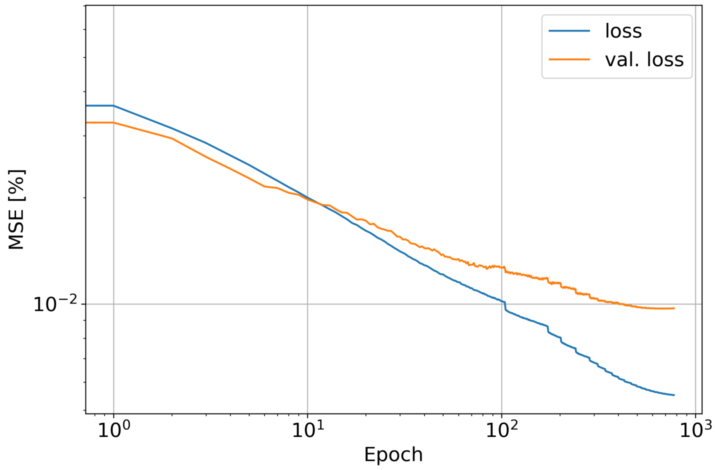

Figure 7.2: Training and validation loss

7.4 Evaluation of machine learning model

The machine learning model is evaluated separately for all the data points in the test cases, the validation data and also for the training data. The new correlation, as given in equation 6.23 is also evaluated on these data sets, separately. Table 7.3 gives an overview of the mean deviation μ, mean absolute deviation $|\mu|$ and standard deviation σ for the correlation and for the neural network. Obviously, the neural network shows the best performance in terms of $|\mu|$ and σ for the training data, independent of the tube in which the data was obtained. More interesting are the deviations of the predictions in the validation data and on the test cases. The accuracy of the neural network is very

Table 7.3: Comparison of prediction accuracy of neural network and correlation

		rough tube			smooth tube		
data set	model	μ [%]	$\lvert\mu\rvert$ [%]	σ [%]	μ [%]	$\lvert\mu\rvert$ [%]	σ [%]
test cases	Neural Network	0.76	6.04	9.18	1.09	6.15	10.2
	Correlation	-9.49	20.18	26.45	-15.04	24.27	30.35
validation data	Neural Network	0.27	5.33	7.3	0.2	3.85	5.67
	Correlation	-9.85	18.06	22.32	-17.54	24.81	27.46
training data	Neural Network	0.22	3.94	5.21	0.18	2.75	3.79
	Correlation	-9.78	18.12	22.47	-17.06	24.62	28.09

similar in the smooth and in the rough tube, which indicates that the effect of the wall roughness on the heat transfer is captured well. Compared to the correlation, only one neural network model is able to perform well on smooth and rough walls, while the correlation has some limitations for the application to smooth heat transfer walls. It can be seen clearly, that the neural network can predict heat transfer more accurate, compared to the empirical correlation. Figure 7.3 shows the Nusselt number, predicted by (a) the neural network and (b) the empirical correlation, for the validation data obtained in the rough tube. Figure 7.4 shows the same for the validation data obtained in the smooth tube. The red line indicates a deviation of the prediction of +/- 20%. As can be seen, the neural

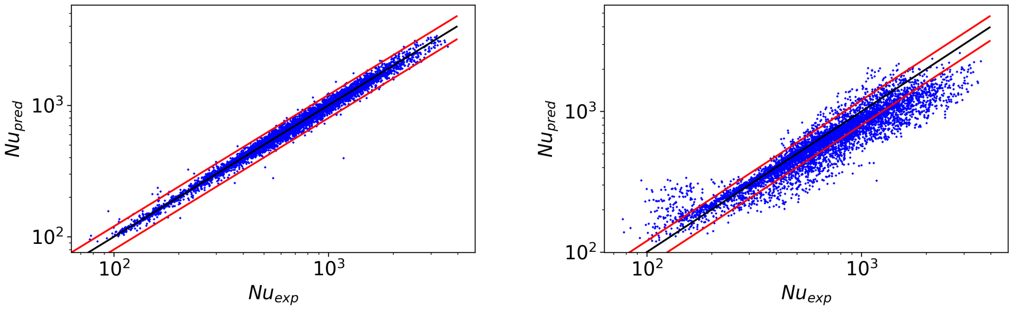

(a) (b)

Figure 7.3: Predicted Nusselt number of (a) neural network and (b) empirical correlation for the rough tube

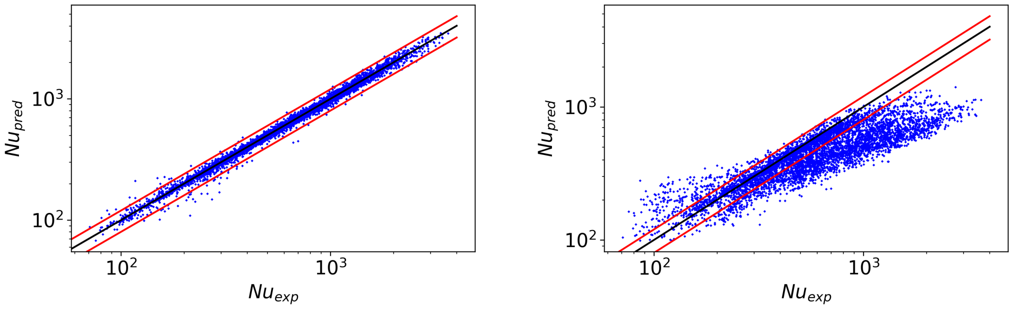

(a) (b)

Figure 7.4: Predicted Nusselt number of (a) neural network and (b) empirical correlation for the smooth tube

network can predict, except a small number of outliers, almost all data points with a deviation of less than 20%. The correlation can also predict the majority of data points within that range, but

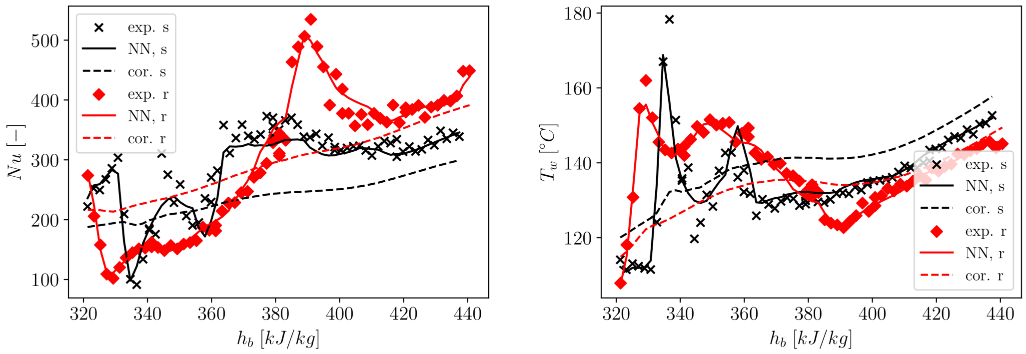

(a)

(b)

Figure 7.5: Predicted (a) Nusselt number and (b) wall temperature compared to experimental data for p=4.6 MPa, G=500 kg/m²s, q=50 kW/m² (r: rough tube, s: smooth tube)

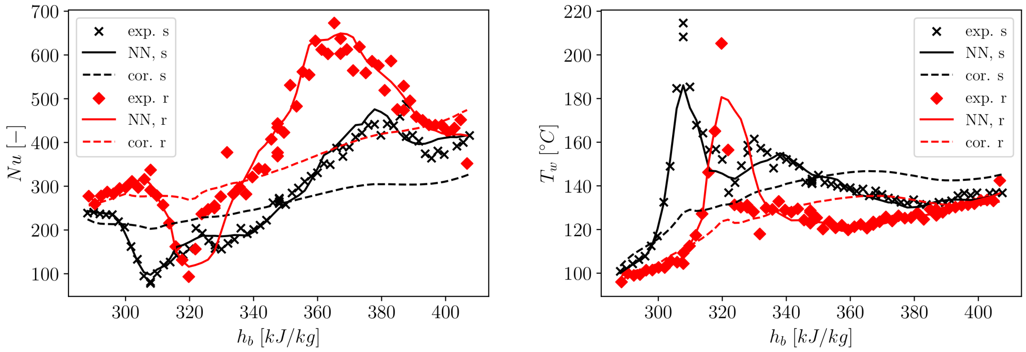

(a)

(b)

Figure 7.6: Predicted (a) Nusselt number and (b) wall temperature compared to experimental data for p=4.35 MPa, G=750 kg/m²s, q=75 kW/m² (r: rough tube, s: smooth tube)

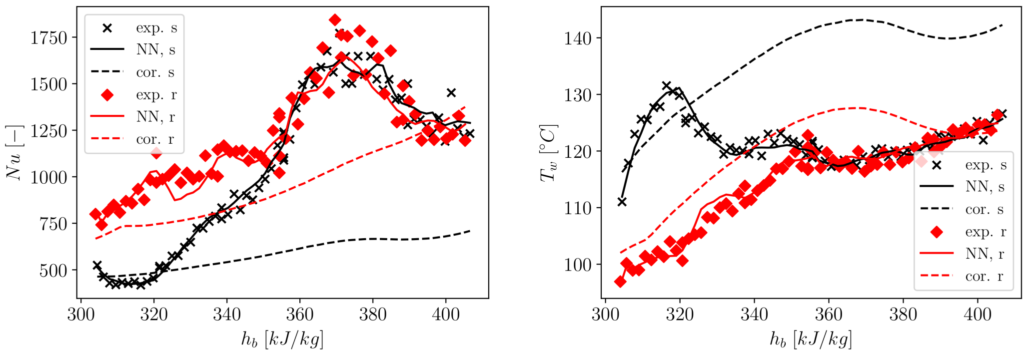

(a)

(b)

Figure 7.7: Predicted (a) Nusselt number and (b) wall temperature compared to experimental data for p=4.35 MPa, G=1750 kg/m²s, q=150 kW/m² (r: rough tube, s: smooth tube)

the number of points outside of that bound is much larger. Figures 7.5 to 7.7 show trends in the predicted Nusselt number and wall temperature, from the neural network and correlation, compared to the experimental data. In the legend of the figures, r indicates the rough tube, and s indicates the smooth tube. These results clearly show the difference of the machine learning approach from the empirical correlation. The correlation captures the global trend of the Nusselt number or the wall temperature profile, but DHT is, as discussed in Chapter 6, not predicted well. In contrast to that, the neural network is capable to predict the trend of Nusselt number or wall temperature quite precisely, even sharp changes in the trends are captured well.

Further, the machine learning model is used to generate a Nukiyama Diagram, which is the wall heat flux $\dot{q}_w$ plotted over the temperature difference $\Delta T = T_{w,i} - T_b$. Figure 7.8 shows the Nukiyama Diagram obtained by the Neural network, compared to the experimental data, exemplarily for $p = 4.6\ MPa$, $G = 500\ kg/m^s$ and $h_b = 320\ kJ/kg$. It can be seen that in the smooth tube, for a wall heat flux of around 30 kW/m², the wall temperature increases strongly, with only small further increase of the heat flux. The temperature difference increases from around 25K to more than 60K, with a variation of less than 10 kW/m² of the wall heat flux. This is, where heat transfer is deteriorated. In the rough tube, the same behavior is observed but shifted to larger heat flux. For a wall heat flux of 40 kW/m², the temperature difference is again around 25K, and it increases to more than 60, when the heat flux is increased by less than 10 kW/m². This shows, that the machine learning model is able to capture the effect of roughness-enhanced heat transfer and of increased heat flux for the onset of DHT. For large ΔT, the machine learning model predicts better heat transfer for the smooth tube. This is also observed for one of the experimental points, which appears to be an outlier. It seems that the neural network tends to be over-fitted here, since there is no physical explanation for the better heat transfer in the smooth tube.

In summary, neural network approaches are promising, as a large amount of experimental data

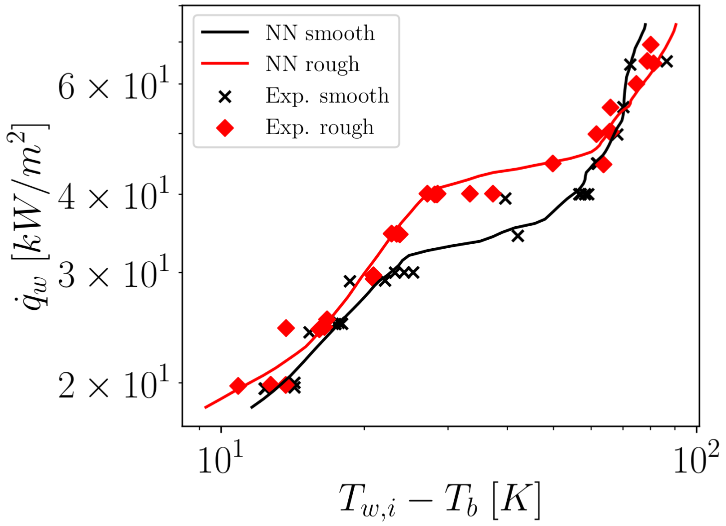

Figure 7.8: Nukiyama diagram at p=4.6 MPa, G=500 kg/m²s and h$_b$*=320 kJ/kg*

is available in the research community. For a given set of data, better results can be obtained, in contrast to conventional correlations. Especially the prediction of DHT, which is a great challenge for empirical correlations, is successful with the neural network approach presented here. However, it is obvious that such a data-driven approach can only be as good as the underlying data set.

7.5 Application to $\mathrm{CO_2}$ data

The non-dimensional setup of the machine learning model allows it to be applied also for different fluids, except R134a. Nevertheless, just applying the model which was only trained with R134a data will not yield good results. Therefore, the 2268 data points from (J. Chen et al., 2022) and new R134a are combined which has previously been used, to a new database. This new database is again split into 80% train data and 20% validation data. Then, a new neural network is trained, with the exact same hyperparameters as shown in Chapter 7.2. Table 7.4 shows μ, $|\mu|$ and σ separately for the R134a train data, R134a validation data, CO_2 train data and CO_2 validation data. It can be seen, that is is possible to fit the given neural network also to two fluids R134a and CO_2. The model performs slightly better for R134a validation data, which is very likely due to the much larger number of R134a training data. In general this shows, that this machine learning model with non-dimensional input and output features is well suitable for application to different fluids. The key is the availability of the experimental data, or, that the model is able to be continuously trained, as shown in (M. Song et al., 2025).

Table 7.4: Accuracy of the Neural network for R134 and for $\mathrm{CO_2}$ *data*

Dataset	μ [%]	$\lvert\mu\rvert$ [%]	σ [%]
validation data R134a	-0.40	4.88	6.88
validation data CO_2	5.43	8.03	10.45
train data R134a	0.03	3.22	4.38
train data CO_2	5.54	6.19	5.46

8 Conclusion and outlook

In the present work, the transfer of heat to R134a at supercritical pressure was experimentally investigated, with a focus on the impact of the roughness of the wall on the heat transfer. This is important, since the environment in SCWR cores is highly corrosive, fuel rods are exposed to these conditions for years and heat transfer at supercritical pressure conditions is complex and therefore sensitive to even small changes in the surface structure. In the frame of the same research project, autoclave experiments with candidate materials for fuel rod cladding have been conducted. The corroded surfaces of the specimen have been analyzed. For the present study the following steps where performed:

- Reference experiments are conducted in a circular tube with a smooth inner surface, at flow conditions that are relevant for SCWRs.
- Experiments are then performed again in a tube with identical geometry but with a rough inner surface, under the same flow conditions.
- Systematic analysis of the effect of wall roughness on heat transfer under supercritical pressure conditions is performed.
- A new empirical correlation for heat transfer at supercritical pressure conditions was derived from the boundary layer theory, which directly considers the wall roughness.
- To address the problem of poor prediction capabilities of empirical correlations for DHT conditions, a machine learning model is proposed, capable of predicting heat transfer also at DHT conditions.

The main results of the experimental campaign can be summarized as:

- Roughness enhances heat transfer: The height of the roughness elements compared to the thickness of the viscous sublayer is identified as the key parameter, which determines the strength of the effect of the surface roughness on the heat transfer. When the roughness elements are close to or higher than the sublayer, heat transfer is enhanced.
- Roughness suppresses buoyancy induced DHT: The roughness elements induce turbulence near the wall, which enhances heat transfer. This counteracts the effect of buoyancy, which causes relaminarisation near the wall due to sharp variation of the density.
- Delayed DHT to larger heat flux: When the heat flux is increased and the pseudocritical temperature is exceeded at the wall, the effect of buoyancy becomes stronger. At the same

time, because of the reduction in density and viscosity, the thickness of the laminar sublayer expands, which in turn weakens the effect of roughness on heat transfer. In this conditions, DHT exists, but at larger heat flux, compared to a smooth wall.

- No suppression of property-controlled DHT through roughness: Although heat transfer is still enhanced, DHT due to property variation (which is not buoyancy-induced DHT) cannot be suppressed.

- Heat transfer is enhanced more efficient, if $T_{w,i}$ and T_b both are well below T_{pc}, or if both are well above T_{pc}. On the other hand, if $T_{w,i} > T_{pc}$ and $T_b < T_{pc}$, the effect of the roughness on the heat transfer becomes less significant. This is explained by the momentum transfer.

As the analysis has shown, the relative size of the roughness elements compared to the boundary layer is the key parameter to understand the effect of the surface roughness on the heat transfer. Therefore, a new empirical correlation is derived from the boundary layer theory, which directly considers the surface roughness in non-dimensional form. The new experimental data were used to investigate correction factors which can be applied in order to take into account the strong variation of the pseudocritical temperature. The new correlation is given by

$$Nu = \frac{\sqrt{\frac{c_f}{8}} Re \overline{Pr}}{\frac{1}{\kappa_\Theta} ln\left(\frac{\sqrt{c_f} Re}{2\sqrt{8}}\right) + 10.63 \cdot \overline{Pr}^{0.46} - 0.17 \cdot k_s^+ \left(\frac{\rho_w}{\rho_b}\right)^{0.68}} \cdot \left(\frac{\rho_w}{\rho_b}\right)^{0.18} \tag{8.1}$$

with

$$c_f = c_{f,0} \cdot \left(\frac{\rho_w}{\rho_b} \frac{\mu_w}{\mu_b}\right)^{0.29} \tag{8.2}$$

and can predict heat transfer well in the NHT regime, especially in the rough tube. On the other hand, prediction of DHT is generally challenging. In addition to that, a neural network for the prediction of Nu is established, which is trained based on non-dimensional input parameters p^+, Re, Pr, $\dot{q}_w^+$, h_b^+, h_{in}^+ and k_s^+, using the new experimental data. The neural network approach stands out with its capability of even predicting DHT conditions quite accurately.

As an outlook into the future, several directions are suggested:

- Experiment: Future experiments should reflect more realistic flow conditions, particularly relevant to SCWR designs. Especially the roughness height should be addressed. The current roughness profiles, based on low-flow autoclave data may not fully represent corrosion effects in operational reactor systems. Additionally, application of real corroded specimen can provide useful insights, as also the thermal conductivity of a real corroded layer is changed. Furthermore, experiments, using water are suggesteed.

- Data-driven modeling: A coordinated effort within the research community to share, expand, and refine experimental datasets could support development of robust and reliable machine learning models. The concept of "continual learning", where models are re-trained incrementally with new data across institutions, is promising.

- Empirical correlations: The correct prediction of DHT remains still a big challenge. This is yet to be solved for neither smooth nor rough walls. A reliable prediction of whether buoyancy effects are present or not may be a key factor in improving the accuracy of empirical models.

In summary, this study advances both the physical understanding and predictive modeling of heat transfer under supercritical conditions, especially in the presence of wall roughness. Future experiments with water can be conducted, so that the models proposed in this work can be evaluated and probably re-fitted to the water data. Following that, the empirical and data-driven approaches shown in this work, together lay a solid foundation for future design and safety assessment of advanced reactor systems.

References

Ackerman, J. W. (1970, August). Pseudoboiling heat transfer to supercritical pressure water in smooth and ribbed tubes. *Journal of Heat Transfer*, *92*(3), 490–497. doi:10.1115/1.3449698

Akiba, T., Sano, S., Yanase, T., Ohta, T., & Koyama, M. (2019). Optuna: A next-generation hyperparameter optimization framework. In *Proceedings of the 25th ACM SIGKDD international conference on knowledge discovery and data mining* (pp. 2623–2631). ACM. doi:10.1145/3292500.3330701

Alekseev, P., Sedov, A., Teplov, P., & Chibiniaev, A. (2018, June). A concept of VVER-SCP reactor with fast neutron spectrum and self provision by secondary fuel. In *Fast reactors and related fuel cycles: Next generation nuclear systems for sustainable development (FR17).* Vienna, Austria. (Proceedings of international conference held 26–29 June 2017 in Yekaterinburg, Russian Federation; ISBN978-92-0-108618-1, STI/PUB/1836)

Andersson, J., Oliveira, D. R., Yeginbayeva, I., Leer-Andersen, M., & Bensow, R. E. (2020). Review and comparison of methods to model ship hull roughness. *Applied Ocean Research*, *99*, 102119. doi:10.1016/j.apor.2020.102119

Aupoix, B. (2015, December). Improved heat transfer predictions on rough surfaces. *International Journal of Heat and Fluid Flow*, *56*, 160–171. doi:10.1016/j.ijheatfluidflow.2015.07.007

Badea, A. F., Zhao, M., Cheng, X., Feuerstein, F., & Liu, X. (2018, August). Consistency considerations on a large databank and wide-range heat transfer prediction for supercritical water in circular tubes. *Nuclear Engineering and Design*, *335*, 178–185. doi:10.1016/j.nucengdes.2018.05.015

Bae, Y., Hong, S., & Kim, Y. (2011). Assessment of mixed convection heat transfer correlations at supercritcal pressures. In *The 5th international symposium on supercritical water cooled reactors (ISSCWR-5).* Vancouver, British Columbia, Canada. (March 13-16)

Bae, Y., Jang, J., Kim, H., Yoon, H., Kang, H., & Bae, K. (2007). Research activities on a supercritical pressure water reactor in korea. *Nuclear Engineering and Technology*, *39*(4), 273–284. doi:10.5516/NET.2007.39.4.273

Bae, Y.-Y., & Kim, H.-Y. (2009). Convective heat transfer to CO_2 at a supercritical pressure flowing vertically upward in tubes and an annular channel. *Experimental Thermal and Fluid Science*, *33*(2), 329–339. doi:10.1016/j.expthermflusci.2008.10.002

Bae, Y.-Y., Kim, H.-Y., & Kang, D.-J. (2010). Forced and mixed convection heat transfer to supercritical CO_2 vertically flowing in a uniformly-heated circular tube. *Experimental Thermal and Fluid Science*, *34*(8), 1295–1308. doi:10.1016/j.expthermflusci.2010.06.001

Bishop, A., Sandberg, R., & Tong, L. (1965). Forced convection heat transfer to water at near-critical temperatures and supercritical pressures. In *Symposium on chemical engineering under extreme conditions.* London, UK. (June 13-17)

Bons, J. P. (2002). St and Cf augmentation for real turbine roughness with elevated freestream turbulence. *Journal of Turbomachinery*, *124*(4), 632–644. doi:10.1115/1.1505851

Bons, J. P. (2005, 05). A critical assessment of Reynolds analogy for turbine flows. *Journal of Heat Transfer*, *127*(5), 472–485. doi:10.1115/1.1861919

Bottros, K. (2016). Experimental investigation into the relationship between the roughness height used in the Nikuradse and Colebrook roughness functions and the internal wall roughness profile for commercial steel pipes. *Journal of Fluids Engineering*, *138*(12). doi:10.1115/1.4032601

Bourke, P., Pulling, D., Gill, L., & Denton, W. (1970). Forced convective heat transfer to turbulent CO_2 in the supercritical region. *International Journal of Heat and Mass Transfer*, *13*(8), 1339–1348. doi:10.1016/0017-9310(70)90074-8

Boyle, R. J., & Stripf, M. (2009, 07). Simplified approach to predicting rough surface transition. *Journal of Turbomachinery*, *131*(4), 041020-1–041020-10. doi:10.1115/1.3072521

Bringer, R. P., & Smith, J. M. (1957). Heat transfer in the critical region. *AIChE Journal*, *3*(1), 49-55. doi:10.1002/aic.690030110

Castro, I. (2007). Rough-wall boundary layers: mean flow universality. *Journal of Fluid Mechanics*, *585*, 469–485. doi:10.1017/S0022112007006921

Cebeci, T., & Bradshaw, P. (1977). *Momentum transfer in Boundary Layers*. Washington, D.C. USA: Hemisphere Publishing Corporation.

Chang, F., Chan, W., Wang, L., Shang, Y., Feng, Y., & Li, H. (2021). Look-up table for wall temperature of vertically-upward round tube with heat transfer to supercritical water. *Applied Thermal Engineering*, *197*, 117440. doi:10.1016/j.applthermaleng.2021.117440

Chang, W., Chu, X., Fereed, A., Pandey, S., Luo, J., Weigand, B., & Laurien, E. (2018). Heat transfer prediction of supercritical water with Artificial Neural Networks. *Applied Thermal Engineering*, *131*, 815–824. doi:10.1016/j.applthermaleng.2017.12.119

Chen, J., Yang, S.-G., Zhao, R., & Cheng, W.-L. (2022). Experimental study on the effect of wall roughness on heat transfer characteristics of supercritical carbon dioxide in vertical tubes. *International Journal of Heat and Mass Transfer*, *196*. doi:10.1016/j.ijheatmasstransfer.2022.123258

Chen, W., & Fang, X. (2014). A new heat transfer correlation for supercritical water flowing in vertical tubes. *International Journal of Heat and Mass Transfer*, *78*, 156–160. doi:10.1016/j.ijheatmasstransfer.2014.06.059

Chen, W., Fang, X., Xu, Y., & Su, X. (2015). An assessment of correlations of forced convection heat transfer to water at supercritical pressure. *Annals of Nuclear Energy*, *76*, 451–460. doi:10.1016/j.anucene.2014.10.027

Cheng, X., & Liu, X. (2018). Research challenges of heat transfer to supercritical fluids. *Journal of Nuclear Engineering and Radiation Science*, *4*(4). doi:10.1115/1.4037117

Cheng, X., Liu, X., & Gu, H. (2011). Fluid-to-fluid scaling of heat transfer in circular tubes cooled with supercritical fluids. *Nuclear Engineering and Design*, *241*, 498–508. doi:10.1016/j.nucengdes.2010.11.017

Cheng, X., & Schulenberg, T. (2001, May). *Heat transfer at supercritical pressures - literature* *review and application to an HPLWR* (Scientific Report (FZKA-6609)). Karlsruhe, Germany: Forschungszentrum Karlsruhe GmbH. doi:10.5445/IR/270049813

Cheng, X., Yang, Y., & Huang, S. (2009a). A simple heat transfer correlation for SC fluid flow in circular tubes. In *Proceedings of the 13th international topical meeting on Nuclear Reactor Thermal Hydraulics (NURETH-13).* (September 27 - October 2)

Cheng, X., Yang, Y., & Huang, S. (2009b). A simplified method for heat transfer prediction of supercritical fluids in circular tubes. *Annals of Nuclear Energy*, *36*(8), 1120–1128. doi:10.1016/j.anucene.2009.04.016

Cheng, X., Zhao, M., Feuerstein, F., & Liu, X. (2019). Prediction of heat transfer to supercritical water at different boundary conditions. *International Journal of Heat and Mass Transfer*, *131*, 527-536. doi:10.1016/.ijheatmasstransfer.2018.11.028

Chowdhurry, A. S. M. S., & Ehsan, M. M. (2023). A critical overview of working fluids in organic rankine, supercritical rankine, and supercritical Brayton cycles under various heat grade sources. *International Journal of Thermofluids*, *20*, 100292. doi:10.1016/j.ijft.2023.100426

Chu, X., Chang, W., Pandey, S., Luo, J., Weigand, B., & Laurien, E. (2018). A computationally light data-driven approach for heat transfer and hydraulic characteristics modelling of supercritical fluids: From DNS to DNN. *International Journal of Heat and Mass Transfer*, *123*, 629–636. doi:10.1016/j.ijheatmasstransfer.2018.02.115

Churkin, A. N., & Deev, V. (2013). Ambiguity of calculation results of heat transfer to water using empirical correlations in the region of supercritical pressure. In *Proceedings of the 6th international symposium on Supercritical Water-Cooled Reactors (ISSCWR-6).* Shenzen, Guangdong, China. (March 03-07)

Churkin, A. N., Deev, V., & Kharitonov, V. (2015). A new correlation of a heat transfer coefficient on supercritical water. In *Proceedings of the 7th international symposium on Supercritical Water-Cooled Reactors (ISSCWR-7).* Helsinki, Finland. (March 15-18)

Cohen, P. (1979, December). *The chemistry of water and solutions at high temperatures for application to corrosion in power systems* (Technical Report No. WARD-5788). Madison, Pennsylvania: Westinghouse Electric Corporation, Advanced Reactors Division.

Colebrook, C. F. (1939). Turbulent flow in pipes, with particular reference to the transition region between the smooth and rough pipe laws. *Journal of the Institution of Civil Engineers*, *11*(4), 133–156. doi:10.1680/ijoti.1939.13150

Colebrook, C. F., & White, C. M. (1937). The reduction of carrying capacity of pipes with age. *Journal of the Institution of Civil Engineers*, *7*(1), 99–118. doi:10.1680/ijoti.1937.13128

Cook, R. T. (1984, November). *Methane heat transfer investigation technical progress narrative* (Technical Report No. ASR84-72). Canoga Park, California, USA: Rockwell International Corporation, Rocketdyne Division.

Copping, A. W., & Yaras, M. Y. (2022, June). *Convective heat transfer at supercritical pressure in the presence of surface roughness - a literature review* (Scientific Report (CU-SCHT-2022-1)). Ottawa, Canada: Carleton University, Department of Mechanical and Aerospace Engineering.

Cui, Y.-L., & Wang, H.-X. (2018). Experimental study on convection heat transfer of r134a at supercritical pressures in a vertical tube for upward and downward flows. *Applied Thermal Engineering*, *129*, 1414-1425. doi:10.1016/j.applthermaleng.2017.10.120

Dang, C., & Hihara, E. (2004). In-tube cooling heat transfer of supercritical carbon dioxide. part 1. experimental measurement. *International Journal of Refrigeration*, *27*(7), 736-747. doi:10.1016/j.ijrefrig.2004.04.018

Deev, V., Kharitonov, V., & Churkin, A. (2017). Analysis and generalization of experimental data on heat transfer to supercriitcal pressure water flow in annular channels and rod bundles. *Thermal Engineering*, *64*, 142-150. doi:10.1134/S0040601516110021

Dickinson, N. L., & Welch, C. P. (1958, April). Heat transfer at supercritical water. *Transactions of the American Society of Mechanical Engineers*, *80*(3), 746–752. doi:10.1115/1.4012501

Dirling, R. B. (1973). A method for computing roughwall heat transfer rates on reentry nosetips. In *Proceedings of the AIAA 8th thermophysics conference.* Palm Springs, California, USA: American Institute of Aeronautics and Astronautics. (July 16-18) doi:10.2514/6.1973-763

Dittus, F., & Boelter, L. (1930). Heat transfer in automobile radioators of the tubular type. *University of California Publications in Engineering*, *2*(13), 443-461.

Doerffel, C., Thomas, C., & Hesse, U. (2021). Experiences form supercritical CO2 applications in refrigeration and air conditioning systems. In *The 4th European sCO2 Conference for Energy Systems.* Prague. (March 22-26)

Duffey, R. B., & Pioro, I. (2005). Experimental heat transfer of supercritical carbon dioxide flowing inside channels (survey). *Nuclear Engineering and Design*, *235*, 913-924. doi:10.1016/j.nucengdes.2004.11.011

Edwards, T. (1993). Usaf supercritical hydrocarbon fuels interests. In *31st aerospace sciences meeting and exhibit.* Reno, Nevada. (January 11-14)

Eter, A., Groeneveld, D., & Tavoularis, S. (2017). Convective heat transfer in supercritical flows of co2 in tubes with and without flow obstacles. *Nuclear Engineering and Design*, *313*, 162-176. doi:10.1016/j.nucengdes.2016.12.016

Feuerstein, F. (2019). *Investigation of heat transfer near the critical point of R134a* (PhD Thesis, Karlsruher Institut für Technologie (KIT)). doi:10.5445/IR/1000096644

Fewster, J., & Jackson, J. (2004). Experiments on supercritical pressure convective heat transfer having relevance to spwr. In *Proceedings of icapp'04.* Pittsburg, PA, USA. (June 13-17)

Flack, K., Schultz, M., & Barros, J. (2020). Skin friction measurements of systematically-varied roughness: Probing the role of roughness amplitude and skewness. *Flow, Turbulence and Combustion*, *104*, 317-329.

Flack, K., Schultz, M., Barros, J., & Kim, Y. (2016). Skin-friction behavior in the transitionally-rough regime. *International Journal of Heat and Fluid Flow*, *61*, 21-30. doi:10.1016/j.ijheatfluidflow.2016.05.008

Flack, K. A., & Schultz, M. P. (2010, 04). Review of Hydraulic Roughness Scales in the Fully Rough Regime. *Journal of Fluids Engineering*, *132*(4). doi:10.1115/1.4001492

Flack, K. A., Schultz, M. P., & Connelly, J. S. (2007, September). Examination of a critical roughness height for outer layer similarity. *Physics of Fluids*, *19*(9), 095104. doi:10.1063/1.2757708

Flack, K. A., Schultz, M. P., & Rose, W. B. (2012, March). The onset of roughness effects in the transitionally rough regime. *International Journal of Heat and Fluid Flow*, *35*, 160–167. doi:10.1016/j.ijheatfluidflow.2012.02.003

Ghajar, A., & Asadi, A. (1986). Improved forced convective heat transfer correlations for liquids in the near critical region. *AIAA Journal*, *24*, 2030-3037.

Gnielinski, V. (1975). Neue Gleichungen für den Wärme und Stoffübergang in turbulent durchströmten Rohren und Kanälen. *Forschung im Ingenieurwesen*, *41*(1), 8-16.

Granville, P. S. (1987, 03). Three Indirect Methods for the Drag Characterization of Arbitrarily Rough Surfaces on Flat Plates. *Journal of Ship Research*, *31*(01), 70-77. doi:10.5957/JSR.1987.31.1.70

Grass, G., Herkenrath, H., & Hufschmidt, W. (1971). Anwendung des prandtlschen grenzschichtmodells auf den wärmeübergang an flüssigkeiten mit stark temperaturabhängigen stoffeigenschaften bei erzwungener strömung. *Wärme und Stoffübertragung*, *4*, 113-119. doi:10.1007/BF01929761

Groeneveld, D., Leung, L., & Vasic, A. (2003). A look-up table for fully developed film-boiling heat transfer. *Nuclear Engineering and Design*, *225*, 83-97. doi:10.1016/S0029-5493(03)00149-3

Groeneveld, D., Shan, J., & Vasic, A. (2005). The 2005 chf look-up table. In *Proceedings of the 11th international topical meeting on nuclear reactor thermal hydraulics (nureth-11).* Avignon, France. (October 2-6)

Gschnaidtner, T., Schatte, G., Kohlhepp, A., Wang, Y., Wieland, C., & Spliethoff, H. (2018). A new assessment method for the evaluation of supercritical heat transfer correlations, particularly with regard to the "multiple/no solutions" problem. *Thermal Science and Engineering Progress*, *7*, 267-278. doi:10.1016/j.tsep.2018.07.006

Gschnaidtner, T. R. J. (2023). *Experimental and theoretical investigations of heat transfer to supercritical water under low to medium heat loads* (Unpublished doctoral dissertation). Technische Universität München.

Guo, X., Fan, Y., Gao, W., Tang, R., Chen, K., Shen, Z., & Zhang, L. (2019). Corrosion resistance of candidate cladding materials for supercritical water reactor. *Annals of Nuclear Energy*, *127*, 351-363. doi:10.1016/j.anucene.2018.12.007

Gupta, S., Mokry, S., & Pioro, I. (2011). Developing a heat-transfer correlation for supercritical water flowing in vertical tubes and its application in scwrs. In *19th international conference on nuclear engineering.* Chiba, Japan. (May 16-19)

Hall, W., & Jackson, J. (1969). *Laminarization of a turbulent pipe flow by buoyancy forces.* ASME.

Hall, W. B., Jackson, J. D., & Watson, A. (1967). Paper 3: A review of forced convection heat transfer to fluids at supercritical pressures. *Proceedings of the Institution of Mechanical Engineers, Conference Proceedings*, *182*(9), 10-22.

Hama, F. (1954). *Boundary-layer characteristics for smooth and rough surfaces.* Society of Naval Architects and Marine Engineers.

Herkenrath, H. (1967). *Wärmeübergang an wasser bei erzwungener strömung im druckbereich von 140 bis 250 bar.* Ispra, Italy: EURATOM.

Huang, X. C., & Cheng, S. C. (1994). Simple method for smoothing multidimensional experimental data with application to the chf and postdryout look-up tables. *Numerical Heat Transfer, Part B: Fundamentals*, *26*(4), 425–438. doi:10.1080/10407799408914938

International Atomic Energy Agency (IAEA). (2011, July). *Status Report 97 – Advanced Boiling Water Reactor (abwr)* (Status Report No. 97). IAEA Advanced Reactors Information System (ARIS). (Accessed via IAEA ARIS database)

International Atomic Energy Agency (IAEA). (2014). *Heat Transfer Behaviour and Thermohydraulics Code Testing for Supercritical Water Cooled Reactors (SCWRs)* (Tech. Rep.). Vienna, Austria: IAEA–TECDOC 1746.

International Atomic Energy Agency (IAEA). (2015, December). *Status Report – Chinese Supercritical Water-Cooled Reactor (csr1000)* (Status Report No. –). Vienna, Austria: IAEA Advanced Reactors Information System (ARIS) Database.

International Atomic Energy Agency (IAEA). (2019). *Energy, electricity and nuclear power estimates for the period up to 2050* (No. 1). Vienna: International Atomic Energy Agency. Retrieved from `https://www.iaea.org/publications/13591/energy-electricity-and-nuclear-power-estimates-for-the-period-up-to-2050`

Jackson, J. (2008). A semi-empirical model of turbulent convective heat transfer to fluids at supercritical pressure. In *Proceedings of the 16th international conference on nuclear engineering (icone-16).* Orlando, Florida, USA. (May 11-15)

Jackson, J. (2009). Validation of an extended heat transfer equation for fludis at supercritical pressure. In *The 4th international symposium on supercritical water cooled reactors (isscwr-4).* Berlin, Germany. (March 8-11)

Jackson, J. (2013). Fluid flow and convective heat transfer to fluids at supercritical pressure. *Nuclear Engineering and Design*, *264*, 24-40. doi:10.1016/j.nucengdes.2012.09.040

Jackson, J. (2017). Models of heat transfer to fluids at supercritical pressure with influences of buoyancy and acceleration. *Applied Thermal Engineering*, *124*, 1481-1491. doi:10.1016/j.applthermaleng.2017.03.146

Jackson, J., & Fewster, J. (1975). *Forced convection data for supercritical pressure fluids* (Tech. Rep. Nos. Technical Report, HTFS, 21540). Manchester, Great Britain: University of Manchester.

Jackson, J., & Hall, W. (1979). Forced convection heat transfer to fluids at supercritical pressures, in: S. kakac, d.b. spalding (eds.), turbulent forced convection in channels. *Hemisphere Publishing Corporation, USA*, *2*, 563-661.

Jackson, J. D., Cotton, M. A., & Axcell, B. P. (1989, March). Studies of Mixed Convection in Vertical Tubes. *International Journal of Heat and Fluid Flow*, *10*(1), 2–15. doi:10.1016/0142-727X(89)90049-0

Kadivar, M., Tormey, D., & McGranaghan, G. (2021). A review on turbulent flow over rough surfaces: Fundamentals and theories. *International Journal of Thermofluids*, *10*.

Kamenetskii, B. (1980). The effectiveness of turbulence promoters in tubes with nonuniformity heated perimeters under conditions of impaired heat transfer. *Thermal Engineering*, *27*(4), 222-223.

Kang, K.-H., & Chang, S.-H. (2009). Experimental study on the heat transfer characteristics during the pressure transients under supercritical pressures. *International Journal of Heat and Mass Transfer*, *52*, 4946-4955. doi:10.1016/j.ijheatmasstransfer.2009.06.005

Kays, W., & Crawford, M. (1993). *Convective heat and mass transfer* (No. 3rd edition). New York, USA: McGraw-Hill.

Kim, D. E., & Kim, M. H. (2010, 10). Experimental study of the effects of flow acceleration and buoyancy on heat transfer in a supercritical fluid flow in a circular tube. *Nuclear Engineering and Design*, *240*, 3336-3349. doi:10.1016/j.nucengdes.2010.07.002

Kim, D. E., & Kim, M.-H. (2011). Experimental investigation of heat transfer in vertical upward and downward supercritical co2 flow in a circular tube. *International Journal of Heat and Fluid Flow*, *32*(1), 176-191. doi:10.1016/j.ijheatfluidflow.2010.09.001

Kim, H., Kim, H. Y., Song, J. H., & Bae, Y. Y. (2008). Heat transfer to supercritical pressure carbon dioxide flowing upward through tubes and a narrow annulus passage. *Progress in Nuclear Energy*, *50*(2), 518-525. doi:10.1016/j.pnucene.2007.11.065

Kim, H., Song, J., Bae, Y., & Kim, H. (2006). Assessment of heat transfer correlations on supercritical pressure flows for an upward flow of co2 in a circular tube. In *5th korea-japan symposium on nuclear thermal hydraulics and safety.* Jeju, Korea. (November 26-29)

Kingma, D. P., & Ba, J. (2015, May). Adam: A Method for Stochastic Optimization. In *International Conference on Learning Representations (ICLR)* (pp. 1–13). (arXiv:1412.6980) doi:10.48550/arXiv.1412.6980

Kirillov, P., Yuriev, Y., & Bobkov, V. (1990). *Handbook of thermal-hydraulics calculation (in russian).* Moscow, Russia: Energoatoizdat Publication House.

Kline, N. (2017). *An experimental study of heat transfer deterioration at supercritical pressures* (Master Thesis). Ottawa, Canada: Ottawa-Carleton Institute for Mechanical and Aerospace Engineering, University of Ottawa.

Koch, C. C., & Smith, J., L. H. (1976, July). Loss Sources and Magnitudes in Axial-Flow Compressors. *Journal of Engineering for Power*, *98*(3), 411–424. doi:10.1115/1.3446202

Kondrat'ev, N. (1969). Heat transfer and hydraulic resistance with supercritical water flowing in tubes. *Thermal Engineering*, *16*(8), 73-77.

Koshizuka, S., Takano, N., & Oka, Y. (1995). Numerical analysis of deterioration phenomena in heat transfer to supercritical water. *International Journal of Heat and Mass Transfer*, *36*(16), 3077-3084. doi:10.1016/0017-9310(95)00008-W

Kransoshchekov, E., Kuraeva, I., & Protopopov, V. (1969). Local heat transfer of carbon dioxide under supercritical pressure under cooling conditions (english translation). *Teplofizka Vysokikh Temperatur*, *7*, 922-930.

Kransoshchekov, E., & Protopopov, V. (1966). Experimental study of heat exchange in carbon dioxide in the supercritical range at high temperature drops. *High Temperature*, *7*, 856-862.

Kuang, B., Zhang, Y., & Cheng, X. (2008). A new, wide-ranged heat transfer correlation of water at supercritical pressures in vertical upward ducts. In *The 7th international topical meeting on nuclear thermal hydraulics, operation and safety (nuthos-7).* Seoul, Korea. (October 5-9)

Kumar, N., Ghosh, S., & Basu, D. N. (2023). Thermalhydraulic assessment and performance prediction of supercritical minichannel heat sink with airfoil-shaped obstructions using ga-tuned neural network. *Applied Thermal Engineering*, *227*, 120352. doi:10.1016/j.applthermaleng.2023.120352

Kunik, C. (2012). *Cfd-simulationen turbulenter konvektiver strömungen bei überkritischen drücken* (PhD Thesis, Karlsruhe Institute of Technology (KIT)). doi:10.5445/IR/1000029455

Kurganov, V. (1998). Heat transfer and pressure drop in tubes under supercritical presser of the coolant. part 1: Specifics of the thermophysical properties, hydrodynamics and heat transfer of the liquid regimes of normal heat transfer. *Thermal Engineering*, *45*(3), 177-185.

Kurganov, V., Zeigarnik, Y., & Maslakova, I. (2012). Heat transfer and hydraulic resistance of supercritical-pressure coolants. part i: Specifics of thermophysical properties of supercritical pressure fluids and turbulent heat transfer under heating conditions in round tubes (state of the art). *International Journal of Heat and Mass Transfer*, *55*(11), 3061-3075. doi:10.1016/j.ijheatmasstransfer.2012.10.072

Kurganov, V., Zeigarnik, Y., & Maslakova, I. (2013a). Heat transfer and hydraulic resistance of supercritical-pressure coolants. part ii: Experimental data on hydraulic resistance and averaged turbulent flow structure of supercritical pressure fluids during heating in round tubes under normal and deteriorated heat transfer conditions. *International Journal of Heat and Mass Transfer*, *58*(1), 152-167. doi:10.1016/j.ijheatmasstransfer.2012.10.072

Kurganov, V., Zeigarnik, Y., & Maslakova, I. (2013b). Heat transfer and hydraulic resistance of supercritical pressure coolants. part iii: Generalized description of scp fluids normal heat transfer, empirical calculating correlations, integral method of theoretical calculations. *International Journal of Heat and Mass Transfer*, *67*, 535-547. doi:10.1016/j.ijheatmasstransfer.2013.07.056

Kurganov, V., Zeigarnik, Y., & Maslakova, I. (2014). Heat transfer and hydraulic resistance of supercritical pressure coolants. part iv: Problems of generalized heat transfer description, methods of predicting deteriorated heat transfer; empirical correlations; deteriorated heat transfer enhancement; dissolved gas effects. *International Journal of Heat and Mass Transfer*, *77*, 1197-1212. doi:10.1016/j.ijheatmasstransfer.2014.06.014

Kurganov, V. A., Zeigarnik, Y. A., & Maslakova, I. V. (2016, 06). On calculating heat transfer and pressure drop of supercritical-pressure coolants. *Journal of Nuclear Engineering and Radiation Science*, *2*(3), 031012.

Langelandsvik, L., Kunkel, G., & Smits, A. (2008). Flow in a commercial steel pipe. *Journal of Fluid Mechanics*, *595*, 323-339. doi:10.1017/S0022112007009305

Laurien, E. (2012). Semi-analytic prediction of hydraulic resistance and heat transfer in pipe flows of water at supercritical pressure. In *Proceedings of the international conference on advances in nuclear power plants (icapp12).* Chicago, Illinois, USA. (June 24-28)

Laurien, E. (2016). Implicit model equation for hydraulic resistance and heat transfer including wall roughness. *Journal of Nuclear Engineering and Radiation Science*, *2*. doi:10.1115/1.4031948

Lee, R., & K.H.Haller. (1974). Supercritical water heat transfer developments and applications. In *5th international heat transfer conference.* Tokyo, Japan. (September 3-7)

Lemmon, E. W., Bell, I. H., Huber, M. L., & McLinden, M. O. (2018). *Nist standard reference database 23: Reference fluid thermodynamic and transport properties - refprop, version 10* (Tech. Rep.). National Institute of Standards and Technology.

Liao, S., & Zhao, T. (2002). An experimental investigation of convection heat transfer to supercritical carbon dioxide in miniature tubes. *International Journal of Heat and Mass Transfer*, *45*(25), 5025-5034. doi:10.1016/S0017-9310(02)00206-5

Licht, J., Anderson, M., & Corradini, M. (2008). Heat transfer to water at supercritical pressures in a circular and square annular flow geometry. *International Journal of Heat and Fluid Flow*, *29*(1), 156-166. doi:10.1016/j.ijheatfluidflow.2007.09.007

Liu, S., Huang, Y., Liu, G., Wang, J., & Leung, L. (2017b). A predictive-corrective process for predicting forces convective heat trasnfer in heated tubes at supercrical pressures. *International Journal of Heat and Mass Transfer*, *110*, 374-382. doi:10.1016/j.ijheatmasstransfer.2017.03.058

Liu, S., Huang, Y., Liu, G., Wang, J., & Leung, L. K. (2017a). Improvement of buoyancy and acceleration parameters for forced and mixed convective heat transfer to supercritical fluids flowing in vertical tubes. *International Journal of Heat and Mass Transfer*, *106*, 1144-1156. doi:10.1016/j.ijheatmasstransfer.2016.10.093

Löwenberg, M., Laurien, E., Class, A., & Schulenberg, T. (2007). Supercritical water heat transfer in vertical tubes: A look-up table. *Progress in Nuclear Energy*, *20*, 532-538. doi:10.1016/j.pnucene.2007.11.037

Löwenberg, M. F. (2007, December). *Wärmeübergang von Wasser in vertikalen Rohrströmungen bei überkritischem Druck* (Report No. 7320). Karlsruhe, Germany: Wissenschaftliche Berichte des Forschungszentrum Karlsruhe (FZKA). Retrieved from `http://d-nb.info/985070072/34`

Ma, D., Zhou, T., Chen, J., Qi, S., Ali Shahzad, M., & Xiao, Z. (2017). Supercritical water heat transfer coefficient prediction analysis based on bp neural network. *Nuclear Engineering and Design*, *320*, 400-408. doi:10.1016/j.nucengdes.2017.06.013

Marusakova, D., Vit, J., & Sipova, M. (2025). Evaluating of long-term exposure of 310s and 800h under conditions of scw-smr. In *11th international symposium on scwrs (isscwr-11).* Pisa, Italy. (February 3-7)

McAdams, W. H., Kennel, W. E., & Addoms, J. N. (1950, May). Heat Transfer to Superheated Steam at High Pressures. *Journal of Fluids Engineering*, *72*(4), 421-428.

McCarthy, J., Trebes, D., & Seader, J. (1968). *The influence of surface roughness on the heat transfer to geseous hydrogen flowing turbulently in round cross-sectional tubes* (Tech. Rep.). Canoga Part, California: Rocketdyne Div., North Amrerican Aviation.

McCarthy, J. R., & Wolf, H. (1960, December). *The Heat Transfer Characteristics of Gaseous Hydrogen and Helium* (Research Report No. RR-60-12). Canoga Park, California: Rocketdyne Division, North American Aviation.

McTigue, J. D., Farres-Antunez, P., Neises, T., & White, A. (2020). Supercritical co2 heat pumps and power cycles for concentrating solar power: Preprint. In *26th solarpaces conference 2020.* National Renewable Energy Laboratory, Golen, Colorado, USA. (September 28 - October 2)

Meyer, M. (1995). Electrically heated tube investigation of cooling channel geometry effects. In *31st joint propulsion conference and exhibit cosponsored by aiaa, asme sae and asee.* San Diego, California, USA. (July 10-12)

Mokry, S., Pioro, I., & Duffey, R. (2009, April). Experimental heat transfer to supercritical co2 flowing in a bare vertical tube. In *Scco2 power cycle symposium.* Troy, New York, USA. (April 29-30)

Mokry, S., Pioro, I., Farah, A., King, K., Gupta, S., Peiman, W., & Kirillov, P. (2011). Development of supercritical water heat-transfer correlation for vertical bare tubes. *Nuclear Engineering and Design*, *241*, 1126-1136. doi:10.1016/j.nucengdes.2010.06.012

Moody, L. (1944). Friction factors for pipe flows. *Transactions of the American Society of Mechanical Engineers*, *66*(8), 671-678.

Negishi, H., Daimon, Y., Kawashima, H., & Yamanishi, N. (2012, August). Flowfield and heat transfer characteristics of cooling channl flows in a methane-cooled thrust chamber. In *48th aiaa/asme/sae/asee joint propulsion conference and exhibit.* Atlanta, Georgia. (July 30 -

August 1)

Niino, M., Suzuki, A., Kumakawa, A., Sakamoto, H., & Sasaki, M. (1980). Heat transfer in rough tubes to supercritical hydrogen. *Heat Transfer - Jpn. Res.; (United States)*, *9*(2).

Nikuradse, J. (1933). Strömungsgesetze in rauen rohren. *VDI Forschungsheft 361. Beilage zu "Forschung auf dem Gebiete des Ingenieurwesens"*, *4*(B).

Oka, Y., & Mori, H. (Eds.). (2014). *Supercritical-pressure light water reactors*. Japan: Springer. doi:10.1007/978-4-431-55025-9_1

Ornatskiy, A., Glushchenko, L., & Gandzyuk, O. (1972). An experimental study of heat transfer in externally-heated annuli at supercritical pressures. *Heat Transfer-Seviet Res.*, *4*(6), 25-29.

Otic, I., Wiltschko, F., Nava, A., Azih, C., Sipova, M., Vit, J., … He, S. (2024). *Report summarizing the newly generated reference data for natural convection, forced and mixed convection and decay heat removal* (Deliverable D3.1 Report). KIT, Karlsruhe, Germany: ECC-SMART Project (Grant Agreement No.945234, H2020 NFRP-2019-2020).

Paul, I. (1999, April). Supercritical coal fired power plants. *Energy Issues*, *19*.

Pencer, J., & Colton, A. (2013, June). Progression of the physics conceptual design for the canadian supercritical water reactor. In *Proceedings of 34th annual cns conference.* Toronto, Canada. (June 9-12)

Petukhov, B., & Kirillov, V. (1958). On the question of heat transfer to a turbulent flow of fluids in pipes. *Thermal Engineering*, *4*, 63-68.

Petukhov, B., Krasnoshchekov, E., & Protopopov, V. (1961). An investigation of heat transfer to fluids flowing in pipes under supercritical pressure conditions. In *International heat transfer conference.* Boulder, Colorado, USA.

Petukhov, B. S., Kurganov, V. A., & Ankudinov, V. B. (1983, July). Heat transfer and flow resistance in the turbulent pipe flow of a fluid with near-critical state parameters. *Teplofizika Vysokikh Temperatur*, *21*, 92-100.

Pioro, I. L., & Duffey, R. B. (2005). Experimental heat transfer in supercritical water flowing inside channels (survey). *Nuclear Engineering and Design*, *235*, 2407-2430. doi:10.1016/j.nucengdes.2005.05.034

Pioro, I. L., & Duffey, R. B. (2007). *Heat Transfer and Hydraulic Resistance at Supercritical Pressures in Power Engineering Applications*. ASME Press. doi:10.1115/1.802523

Pioro, I. L., Khartabil, H. F., & Duffey, R. B. (2004). Heat transfer to supercritical fluids flowing in channels—empirical correlations (survey). *Nuclear Engineering and Design*, *230*(1), 69-91. (11th International Conference on Nuclear Energy) doi:10.1016/j.nucengdes.2003.10.010

Pizzarelli, M. (2016). A cfd-derived correlation for methane heat transfer deterioration. *Numerical Heat Transfer, Part A: Applications*, *69*(3), 242–264. doi:10.1080/10407782.2015.1080575

Prandtl, L. (1904). Über flüssigkeitsbewegungen bei sehr kleiner reibung. In *Verhandlungen des iii. internationalen mathematiker kongress.* Heidelberg, Germany. (August 8-13)

Prandtl, L. (1933). Neue ergebnisse der turbulenzforschung. *Zeitschrift des Vereins deutscher Ingenieure*, *77*, 105-114.

Protopopov, V., Kuraeva, I., & Antonov, A. (1973). An approach to the determination of the conditions of occurance of deteriorated heat transfer regimes at supercritical pressures. *High Temperature*, *11*(3), 529-532.

PRPPWG, & GIF. (2022, April). *Gif supercritical water-cooled reactor, proliferation resistance* *and physical protection white paper* (Tech. Rep.). Proliferation Resistance and Physical Protection Working Group (PRPPWG) and the Super Critical Water Reactor System Steering Committee of the Generation IV International Forum (GIF).

Pucciarelli, A., He, S., & Ambrosini, W. (2020). A successful local fluid-to-fluid similarity theory for heat transfer to supercritical pressure fluids: merits and limitations. *International Journal of Heat and Mass Transfer*, *157*, 119754. doi:10.1016/j.ijheatmasstransfer.2020.119754

Qu, J., & Oka, Y. (2014). Improved single pass core design for high temperature super lwr. *Nuclear Engineering and Design*, *267*, 100-108. doi:10.1016/j.nucengdes.2013.12.002

Randall, D. (1956). *Some heat transfer and fluid friction experiments with supercritical water. report nda 2051* (Tech. Rep.). United States. Retrieved from `https://digital.library.unt.edu/ark:/67531/metadc1398044`

Razumovskiy, V., Ornatskiy, A., & Mayevskiy, Y. (1990). Local heat transfer and hydraulic behavior in turbulent channel flow of water at supercritical pressure. *Heat Transfer - Soviet Research*, *22*(1), 91-102.

Rowinski, M. K., Zhao, J., White, T. J., & Soh, Y. C. (2018). Safety analysis of super-critical water reactors–a review. *Progress in Nuclear Energy*, *106*, 87-101. doi:10.1016/j.pnucene.2018.03.002

Ryzhov, S., Mohov, V., Nikitenko, M., Kirillov, P., Chetverikov, A., Churkin, V., & Glebov, A. (2011, March). Concept of a single-circuit rp with vessel type supercritical water-cooled reactor. In *Proceedings of the 5th international symposium of supercritical water-cooled reactors (isscwr-5).* Vancouver, Canada. (March 13-16)

Saltanov, E., Pioro, I., Mann, D., Gupta, S., Mokry, S., & Harvel, G. (2014, 07). Study on specifics of forced-convective heat transfer in supercritical carbon dioxide. In *22nd international conference on nuclear engineering (icone-22).* Prague, Czech Republic. (July 7-11)

Scalabrin, G., & Piazza, L. (2003). Analysis of forced convection heat transfer to supercritical carbon dioxide inside tubes using neural networks. *International Journal of Heat and Mass Transfer*, *46*(7), 1139-1154. doi:10.1016/S0017-9310(02)00382-4

Schatte, G. A., Kohlhepp, A., Wieland, C., & Spliethoff, H. (2016). Development of a new empirical correlation for the prediction of the onset of the deterioration of heat transfer to supercritical water in vertical tubes. *International Journal of Heat and Mass Transfer*, *102*, 133-141. doi:10.1016/j.ijheatmasstransfer.2016.06.007

Schlichting, H. (1937). *Experimental investigation of the problem of surface roughness* (No. No. 823). National Advisory Commitee for Aeronautics.

Schlichting, H., & Gersten, K. (2016). *Boundary-layer theory* (9th ed.). Springer Berlin, Heidelberg. doi:10.1007/978-3-662-52919-5

Schulenberg, T., & Otic, I. (2021). Suggestion for design of a small modular scwr. In *10th international symposium on scwrs (isscwr-10).* Prague, Czech Republic. (March 15-19)

Schulenberg, T., & Starflinger, J. (Eds.). (2012). *High performance light water reactor : Design and analyses*. Karlsruhe: KIT Scientific Publishing. doi:10.5445/KSP/1000025989

Schultz, M. P., & Flack, K. A. (2005). Outer layer similarity in fully rough turbulent boundary layers. *Experiments in Fluids*, *38*, 328-340. doi:10.1007/s00348-004-0903-2

Schultz, M. P., & Flack, K. A. (2009, 01). Turbulent boundary layers on a systematically varied rough wall. *Physics of Fluids*, *21*(1), 015104. doi:10.1063/1.3059630

Shitsman, M. (1962). Investigation of heat transfer at water cooling in near critical region. *Thermal Engineering*, *9*(1), 83-86.

Shitsman, M. (1963). Impairment of the heat transfer at supercritical pressures. *Teplofiz. vys. Temp.*, *1*(2), 267-275.

Shitsman, M. (1967). Temperature conditions of evaporative surfaces at supercritical pressures. *Electric. Stations*, *38*(2), 27-30.

Shitsman, M. (1968). Temperature conditions in tubes at supercritical pressures. *Thermal Engineering*, *15*(5), 72-77.

Shnell, J., Elders, W. A., Orcutt, J., & Osborn, W. L. (2019). Exploration and development of supercritical geothermal resrources on the ocean floor. In *Proceedings of the 44th workshop on geothermal reservoir engineering.* Stanford University, Stanford, California. (February 11-13)

Shockling, M., Alledn, J., & Smits, A. (2006). Roughness effects in turbulent pipe flow. *Journal of Fluid Mechanics*, *564*, 267-285. doi:10.1017/S0022112006001467

Sieder, E. N., & Tate, G. E. (1936). Heat transfer and pressure drop of liquids in tubes. *Industrial & Engineering Chemistry*, *28*(12), 1429-1435. doi:10.1021/ie50324a027

Song, J., Kim, H., & Bae, Y.-Y. (2008, 03). Heat transfer characteristics of a supercritical fluid flow in a vertical pipe. *Journal of Supercritical Fluids*, *44*, 164-171. doi:10.1016/j.supflu.2007.11.013

Song, M., Wiltschko, F., Liu, X., Badea, A. F., & Cheng, X. (2025). Development and assessment of the data-informed continuous machine learning approach based on chf prediction. *International Journal of Heat and Mass Transfer*, *252*, 127474. doi:10.1016/j.ijheatmasstransfer.2025.127474

Stripf, M., Schulz, A., & Wittig, S. (2005, 02). Surface Roughness Effects on External Heat Transfer of a HP Turbine Vane. *Journal of Turbomachinery*, *127*(1), 200-208. doi:10.1115/1.1811101

Styrikovich, M., Margulova, T., & Miropolskiy, Z. (1967). Problems in the development of designs of supercritical boilers. *Teploenergetica*, *14*, 4-7.

Sun, F., Xie, G., & Li, S. (2021). An artificial-neural-network based prediction of heat transfer behaviours for in-tube supercritical co2 flow. *Applied Soft Computing Journal*, *102*. doi:10.1016/j.asoc.2021.107110

Swenson, H., Carver, J., & Kakarala, C. (1965). Heat transfer to supercritical water in smooth-bore tubes. *Journal of Heat Transfer, Transactions of the ASME, Series C*, *87*(4), 477-484. doi:10.1115/1.3689139

Tanaka, H., Nishiwaki, N., Hirata, M., & Tsuge, A. (1971). Forced convection heat transfer to fluid near critical point flowing in circular tube. *International Journal of Heat and Mass Transfer*, *14*(6), 739-750. doi:10.1016/0017-9310(71)90104-9

Tanna, V. L. (2006). *Design and analysis of superconducting current feeder system for the international thermonuclear experimental reactor (iter)* (Tech. Rep. No. FZKA 7256). Karlsruhe, Germany: Forschungszentrum Karlsruhe. doi:10.5445/IR/1000005176

Tao, K., Zhu, J., Cheng, Z., & Li, D. (2022). Artificial neural network analysis of the nusselt number and friction factor of hydrocarbon fuel under supercritical pressure. *Propulsion and Power Research*, *11*(3), 325-336. doi:10.1016/j.jppr.2022.08.002

Taylor, M. (1968). *Correlation of local heat-transfer coefficients for single-phase turbulent flow of* *hydrogen in tubes with temperature ratios to 23* (Tech. Rep. No. NASA-TN-D4332). Cleaveland, Ohio, USA: Lewis Research Center, National Aeronautics and Space Administration.

Touba, R., & McFadden, P. (1966). *Combined turbulent convection heat transfer to near critical water* (Tech. Rep.). Lafayette, Indiana, USA: Purdue Research Foundation.

TVO. (2010, December). *Nuclear power plant unit olkiluoto 3* (Tech. Rep.). Eurajoki, Finland.

U.S. DOE, & GIF. (2002, December). *A technology roadmap for Generation IV nuclear energy systems* (Technical Report). Washington, D.C., USA: U.S. DOE Nuclear Energy Research Advisory Committee and the Generation IV International Forum. Retrieved from `https://www.gen-4.org/gif/upload/docs/application/pdf/2013-09/genivroadmap2002.pdf` (Accessed July 2025)

Vasic, A., Beuthe, T., Zahlan, H., Nava-Dominguez, A., & Wang, D. (2023). *State of the art report und heat transfer at supercriticla pressures rev 2* (Tech. Rep. No. 153-507123-REPT-001). Chalk River, Canada: Canadian Nuclear Laboratories, Atomic Energy of Canada Limited.

Vikhref, Y., Barulin, Y., & Konkov, A. (1967). A study of heat transfer in vertical tubes at supercritical pressures. *Thermal Engineering*, *14*(9).

Vit, J., & Sipova, M. (2025). Treatment and evaluation of surface roughness of fuel cladding to mitigate the deteriorated heat transfer in scw-smr concept. In *11th international symposium on scwrs (isscwr-11).* Pisa, Italy. (February 3-7)

von Karman, T. (1930). Mechanische Ähnlichkeit und turbulenz. *Nachrichten von der Gesellschaft der Wissenschaften zu Göttingen, Fachgruppe 1, Mathematik*, *5*, 58-76.

Wang, C., & Li, H. (2014). Evaluation of the heat transfer correlations for supercritical pressure water in vertical tubes. *Heat Transfer Engineering*, *35*(6-8), 685–692. doi:10.1080/01457632.2013.837756

Wang, D., Dai, X., Tian, R., & Shi, L. (2019). Experimental investigation of the heat transfer of supercritical r134a in a horizontal micro-fin tube. *International Journal of Thermal Sciences*, *138*, 536-549. doi:10.1016/j.ijthermalsci.2019.01.013

Wang, D., Tian, R., Zhang, Y., Li, L., & Shi, L. (2019). Experimental comparison of the heat transfer of supercritical r134a in a micro-fin tube and a smooth tube. *International Journal of Heat and Mass Transfer*, *129*, 1194-1205. doi:10.1016/j.ijheatmasstransfer.2018.10.052

Wang, H., Bi, Q., Wang, L., Lv, H., & Leung, L. K. (2014). Experimental investigation of heat transfer from a 2×2 rod bundle to supercritical pressure water. *Nuclear Engineering and Design*, *275*, 205-218. doi:10.1016/j.nucengdes.2014.04.036

Watts, M., & Chou, C. (1982). Mixed convection heat transfer to supercritical pressure. In *Proceedings of the 7th international international heat transfer conference.* Munich, Germany. (September 6-10)

Wen, Z.-X., Wu, J.-L., Cao, X.-W., Cheng, J.-Q., Wang, S.-S., & Li, Q. (2024). Machine learning and prediction study on heat transfer of supercritical co2 in pseudo-critical zone. *Applied Thermal Engineering*, *243*, 122630. doi:10.1016/j.applthermaleng.2024.122630

Winterton, R. (1998). Where did the dittus and boelter equation come from? *International Journal of Heat and Mass Transfer*, *41*(4), 809-810. doi:10.1016/S0017-9310(97)00177-4

Xiao, R., Zhang, P., Chen, L., & Hou, Y. (2023). Machine learning based prediction of heat transfer deterioration of supercritical fluid in upward vertical tubes. *Applied Thermal Engineering*, *228*, 120477. doi:10.1016/j.applthermaleng.2023.120477

Yamagata, K., Nishikawa, K., Hasegawa, S., Fujii, T., & Yoshida, S. (1972). Forced convective heat transfer to supercritical water flowing in tubes. *Interational Journal of Heat and Mass Transfer*, *15*, 2575-2593. doi:10.1016/0017-9310(72)90148-2

Yan, J., Liu, S., Zheng, S., & Tian, H. (2023). Experimental study on heat-transfer performance of supercritical-pressure r134a and predictions based on artificial neural network. *The Journal of Supercritical Fluids*, *192*, 105809. doi:10.1016/j.supflu.2022.105809

Yang, S. (2013). Heat transfer modes in supercritical fluids. In *The 15th international topical meeting on nuclear reactor thermal-hydraulics (nureth-15).* Pisa, Italy. (May 12-17)

Ye, K., Zhang, Y., Yang, L., Zhao, Y., Li, N., & Xie, C. (2019). Modeling convective heat transfer of supercritical carbon dioxide using an artificial neural network. *Applied Thermal Engineering*, *150*, 686-695. doi:10.1016/j.applthermaleng.2018.11.031

Ye, Z., Zendehboudi, A., Hafner, A., & Cao, F. (2022). General heat transfer correlations for supercritical carbon dioxide heated in vertical tubes for upward and downward flows. *International Journal of Refrigeration*, *140*, 57-69. doi:10.1016/j.ijrefrig.2022.05.013

Yu, J., Jia, B., Wu, D., & Wang, D. (2008). Otimization of heat transfer coefficient correlation at supercritical pressure using genetic algorithms. *Heat and Mass Transfer*, *45*, 757-766. doi:10.1007/s00231-008-0475-4

Zahlan, H., Groeneveld, D., & Tavoularis, S. (2015). Measurements of convective heat transfer to vertical upward flows of co2 in circular tubes at near-critical and supercritical pressures. *Nuclear Engineering and Design*, *289*, 92-107. doi:10.1016/j.nucengdes.2015.04.013

Zahlan, H., Tavoularis, S., & Groeneveld, D. (2015). A look-up table for trans-critical heat transfer in water-cooled tubes. *Nuclear Engineering and Design*, *285*, 109-125. doi:10.1016/j.nucengdes.2014.12.027

Zhalan, H., Groeneveld, D., Tavoularis, S., Mokry, S., & I.Pioro. (2011). Assessment of supercritical heat transfer predictions methods. In *The 5th international symposium on supercritical water cooled reactors.* Vancouver, British Columbia, Canada. (March 13-16)

Zhang, L., Zhu, F., & Tang, R. (2009). Corrosion mechanisms of candidate structural materials for supercritical water-cooled reactor. *Frontiers of Energie and Power Engineering in China*, *3*, 233-240. doi:10.1007/s11708-009-0024-y

Zhang, Q., Li, H., Kong, X., Liu, J., & Lei, X. (2018). Special heat transfer characteristics of supercritical co2 flowing in a vertically-upward tube with low mass flux. *Interational Journal of Heat and Mass Transfer*, *122*, 469-482. doi:10.1016/j.ijheatmasstransfer.2018.01.112

Zhang, R., Tong, W., Xu, S., Qiu, Q., & Zhu, X. (2023). Ann model with feature selection to predict turbulent heat transfer characteristics of supercritical fluids: Take co2 and h2o as examples. *International Journal of Thermal Sciences*, *188*. doi:10.1016/j.ijthermalsci.2023.108247

Zhang, S., Gu, H., Cheng, X., & Xiong, Z. (2014). Experimental study on heat transfer of supercritical freon flowing upward in a circular tube. *Nuclear Engineering and Design*, *280*, 305-315. doi:10.1016/j.nucengdes.2014.09.017

Zhao, M., Badea, A., Feuerstein, F., & Cheng, X. (2017). Asessment of experimental data of heat transfer of supercritical water in tubes. In *17th international topical meeting on nuclear reactor thermal hydraulics.* Xi'An, China. (September 3-8)

Zhu, B., Xu, J., Zhang, H., Xie, J., & Li, M. (2020). Effect of non-uniform heating on sco2 heat transfer deterioration. *Applied Thermal Engineering*, *181*.

doi:10.1016/j.applthermaleng.2020.115967

Zhu, J., Zhao, C., Cheng, Z., Lin, D., Tao, Z., & Qiu, L. (2019). Experimental investigation on heat transfer of n-decane in a vertical square tube under supercritical pressure. *International Journal of Heat and Mass Transfer*, *138*, 631-639. doi:10.1016/j.ijheatmasstransfer.2019.04.076

Author's Publications

Wiltschko, F., Otic, I., Cheng, X., (2025). Prediction of heat transfer to supercritical pressure fluid at rough surface, Nuclear Engineering and Design 444(1), doi:https://doi.org/10.1016/j.nucengdes.2025.114394

Song, M., Wiltschko, F., Liu, X, Badea, A. F., Cheng, X., (2025). Development and assessment of the data-informed continuous machine learning approach based on CHF prediction, International Journal of Heat and Mass Transfer 252, doi:10.1016/j.ijheatmasstransfer.2025.127474

Wiltschko, F., Otic, I., Cheng, X. (2025). Experimental investigation of heat transfer to supercritical pressure fluid in tubes with rough inner surface, Journal of Heat and Mass Transfer 147(5), doi:10.1115/1.4067608

Wiltschko, F., Otic, I., Cheng, X. (2025). Prediction of the heat transfer to supercritical pressure fluid at rough surface, *11th International Symposium on Supercritical Water-Cooled Reactors (ISSCWR-11)*. Pisa, Italy, February 3-5.

Wiltschko, F., Sipova, M., Vit, J. and Cheng, X. (2024). Experimental investigation of heat transfer to supercritical pressure R134a in artificially roughened tubes, *31st International Conference on Nuclear Engineering (ICONE-31)*. Prague, Czech Republic, August 4-8

Wiltschko, F., Cheng, X. (2024). Experimental investigation of heat transfer to supercritical pressure R134a in circular tubes with rough surface, *Kerntechnik 2024*. Leipzig, Germany, June 11-13.

Zhou, M., Wiltschko, F. et al., (2022). Large-eddy simulation on thermal-mixing experiment at horizontal T-junction with varied flow temperature, Nuclear Engineering and Design 388, doi:10.1016/j.nucengdes.2021.111644

Wiltschko, F., Qu, W., Xiong, J. (2021). Validation of RANS models and Large Eddy simulation for predicting crossflow induced by mixing vanes in rod bundle, Nuclear Engineering and Technology 53(11), doi:10.1016/j.net.2021.05.034

Wiltschko, F., Otic, I., et al. (2021). One-dimensional investigation of turbulent heat transfer along corroded rod in vertical channels at supercritical pressure conditions, it Proceedings of the European Nuclear Young Generation Forum, ENYGF'21. Tarragona, Spain, September 27-30.

Wiltschko, F., Otic, I., et al. (2021). Numerical analysis of turbulent heat transfer under supercritical pressure conditions, 10th international Symposium on SCWRs (ISSCWR-10). Prague, the Czech Republic, March 15-19.

Appendix

A.1 Nusselt correlations directly considering wall roughness

A.1.1 (J. McCarthy et al., 1968)

$$Nu_b = 0.025 Re_b^{0.8} Pr_b^{0.4} \left(\frac{T_w}{T_b}\right)^{-0.55} \left[1 + 1000 \frac{k_s}{D} \left(log_{10} Re_b - 5.625\right)\right] \tag{A.1.1}$$

A.1.2 (Cook, 1984)

$$Nu_b = \frac{0.4 \left(\frac{c_f}{8}\right) Re_b Pr_b}{1 + \sqrt{\frac{c_f}{8}} \left[5.19 k_s^{0.2} Pr_b^{0.44} - 8.5\right]} \tag{A.1.2}$$

A.1.3 (J. Chen et al., 2022)

$$Nu_b = 0.0107 Re_b^{0.838} \overline{Pr}_b^{0.815} \left(\frac{\bar{c}_p}{c_{p,b}}\right)^{0.18} \left(\frac{\rho_w}{\rho_b}\right)^{0.176} \left(\frac{\mu_w}{\mu_b}\right)^{1.03} \left(\frac{\lambda_w}{\lambda_b}\right)^{-0.455} \left(1 + \frac{S_z}{S_{z0}}\right)^{0.135} \tag{A.1.3}$$

A.2 Nusselt correlations indirectly considering wall roughness

Note: The authors usually suggest equations for the friction factor c_f. Instead, using (Colebrook, 1939) equation (2.70), wall roughness can be considered.

A.2.1 (Petukhov & Kirillov, 1958)

$$Nu_b = \frac{\frac{c_f}{8} Re_b Pr_b}{1.07 + 12.7 \sqrt{c_f/8} \left(Pr_b^{2/3} - 1\right)} \cdot \left(\frac{\mu_w}{\mu_b}\right)^{0.11} \tag{A.2.1}$$

$$c_f = \left[1.82 log_{10}(Re_b) - 1.64\right]^{-2} \tag{A.2.2}$$

A.2.2 (Petukhov et al., 1961)

$$Nu_b = \frac{\frac{c_f}{8} Re_b Pr_b}{1.07 + 12.7 \sqrt{c_f/8} \left(Pr_b^{2/3} - 1\right)} \cdot \left(\frac{\mu_w}{\mu_b}\right)^{-0.11} \cdot \left(\frac{\lambda_w}{\lambda_b}\right)^{0.33} \cdot \left(\frac{\bar{c}_p}{c_{p,b}}\right)^{0.35} \tag{A.2.3}$$

$$c_f = [1.82log_{10}(Re_b) - 1.64]^{-2} \tag{A.2.4}$$

A.2.3 (Kransoshchekov & Protopopov, 1966)

$$Nu_b = \frac{\frac{c_f}{8} Re_b Pr_b}{1.07 + 12.7\sqrt{c_f/8}\left(Pr_b^{2/3} - 1\right)} \cdot \left(\frac{\rho_w}{\rho_b}\right)^{0.3} \cdot \left(\frac{\bar{c}_p}{c_{p,b}}\right)^{n} \tag{A.2.5}$$

$$n = \begin{cases} 0.4 & for\ \frac{T_w}{T_{pc}} \leq 1 \\ n_1 = 0.22 + 0.18\frac{T_w}{T_{pc}} & for\ 1 \leq \frac{T_w}{T_{pc}} \leq 2.5 \\ n_1 + (5n_1 - 2)\left(1 - \frac{T_b}{T_{pc}}\right) & for\ 1 \leq \frac{T_b}{T_{pc}} \leq 1.2 \\ 0.4 & for\ \frac{T_b}{T_{pc}} \geq 1.2 \end{cases} \tag{A.2.6}$$

A.2.4 (Kransoshchekov et al., 1969)

$$Nu_w = \frac{\frac{c_f}{8} Re_w Pr_w}{1.07 + 12.7\sqrt{c_f/8}\left(Pr_w^{2/3} - 1\right)} \cdot \left(\frac{\rho_w}{\rho_b}\right)^{m} \cdot \left(\frac{\bar{c}_p}{c_{p,b}}\right)^{n} \tag{A.2.7}$$

$$c_f = [1.82log_{10}(Re_w) - 1.64]^{-2} \tag{A.2.8}$$

A.2.5 (Grass et al., 1971)

$$Nu_b = \frac{\frac{c_f}{8} Re_b Pr_b}{1.07 + 12.7\sqrt{\frac{c_f}{8}\left(Pr_G^{2/3}\frac{c_{p,b}}{c_{p,G}} - 1\right)}} \tag{A.2.9}$$

$$c_f = [1.82leg_{10}(Re_b) - 1.64]^{-2} \tag{A.2.10}$$

$$Pr_G = \begin{cases} Pr_b & for\ Pr_b < 0.5Pr_w \\ Pr_w & for\ Pr_b > 0.5Pr_w \end{cases} \tag{A.2.11}$$

$$c_{p,G} = \begin{cases} c_{p,b} & for\ Pr_b < 0.5Pr_w \\ c_{p,w} & for\ Pr_b > 0.5Pr_w \end{cases} \tag{A.2.12}$$

A.2.6 (Gnielinski, 1975)

$$Nu_b = \frac{\frac{c_f}{8}(Re_b - 1000)Pr_b}{1 + 12.7\sqrt{\frac{c_f}{8}}\left(Pr_b^{2/3} - 1\right)}\left[1 + \left(\frac{d}{z}\right)^{2/3}\right] \cdot \left(\frac{Pr_b}{Pr_w}\right)^{0.11} \tag{A.2.13}$$

$$c_f = [1.8leg_{10}(Re_b) - 1.5]^{-2} \tag{A.2.14}$$

A.2.7 (Petukhov et al., 1983)

$$Nu_b = \frac{\frac{c_f}{8} Re_b Pr_b}{1 + \frac{900}{Re_b} + \sqrt{c_f/8}\left(\overline{Pr}_b^{2/3} - 1\right)} \tag{A.2.15}$$

$$c_{f0} = [1.82log_{10}(Re_b) - 1.64]^{-2} \tag{A.2.16}$$

$$c_f = c_{f0} \cdot \left(\frac{\rho_w}{\rho_b}\right)^{0.4} \cdot \left(\frac{\mu_w}{\mu_b}\right)^{0.2} \tag{A.2.17}$$

A.2.8 (Kirillov et al., 1990)

$$Nu_b = \frac{\frac{c_f}{8} Re_b \overline{Pr}_b}{1 + \frac{900}{Re_b} + 12.7\sqrt{c_f/8}\left(\overline{Pr}_b^{2/3} - 1\right)} \cdot \left(\frac{\bar{c}_p}{c_{p,b}}\right)^n \cdot \left(\frac{\rho_w}{\rho_b}\right)^{0.4} \cdot \varphi(k^*) \tag{A.2.18}$$

A.2.9 (Razumovskiy et al., 1990)

$$Nu_b = \frac{\left(\frac{c_f}{8}\right) Re_b Pr_b}{1.07 + 12.7\sqrt{\frac{c_f}{8}}\left(Pr_b^{2/3} - 1\right)} \left(\frac{\bar{c}_p}{c_{p,b}}\right)^{0.65} \tag{A.2.19}$$

$$c_f = c_{f,0}\left(\frac{\mu_w}{\mu_b}\frac{\rho_w}{\rho_b}\right)^{0.18} \tag{A.2.20}$$

A.2.10 (V. Kurganov, 1998)

$$Nu_b = \frac{\left(\frac{c_f}{8}\right) Re_b \overline{Pr}_b}{1 + (900/Re_b) + 12.7\sqrt{\frac{c_f}{8}}\left(\overline{Pr}_b^{2/3} - 1\right)} \tag{A.2.21}$$

$$c_f = c_{f,0}\left(\frac{\rho_w}{\rho_b}\right)^{0.4} \tag{A.2.22}$$

A.2.11 (Dang & Hihara, 2004)

$$Nu_b = \frac{\left(\frac{c_{f,film}}{8}\right)(Re_b - 1000)\,Pr_x}{1.07 + 12.7\sqrt{\frac{c_{f,film}}{8}}\left(Pr_x^{2/3} - 1\right)} \tag{A.2.23}$$

$$Pr_x = \begin{cases} \frac{c_{p,b}\mu_b}{k_b} & for\ c_{p,b} \geq \bar{c}_p \\ \frac{\bar{c}_p\mu_b}{k_b} & for\ c_{p,b} < \bar{c}_p\ and\ \frac{\mu_b}{k_b} \geq \frac{\mu_{film}}{k_{film}} \\ \frac{\bar{c}_p\mu_{film}}{k_{film}} & for\ c_{p,b} < \bar{c}_p\ and\ \frac{\mu_b}{k_b} < \frac{\mu_{film}}{k_{film}} \end{cases} \tag{A.2.24}$$

$$Re_{film} = \frac{Gd}{\mu_{film}} \tag{A.2.25}$$

A.3 Nusselt correlations not considering wall roughness

A.3.1 (Sieder & Tate, 1936)

$$Nu_b = 0.027Re_b^{0.8}Pr_b^{1/3}\left(\frac{\mu_w}{\mu_b}\right)^{0.14} \tag{A.3.1}$$

A.3.2 (J. R. McCarthy & Wolf, 1960)

$$Nu_b = 0.025Re_b^{0.8}Pr_b^{0.4}\left(\frac{T_b}{T_w}\right)^{0.55} \tag{A.3.2}$$

A.3.3 (Bishop et al., 1965)

$$Nu_b = 0.0069Re_b^{0.9}\overline{Pr}_b^{0.66}\left(\frac{\rho_w}{\rho_b}\right)^{0.43}\left(1 + 2.4\frac{d}{z}\right) \tag{A.3.3}$$

A.3.4 (Swenson et al., 1965)

$$Nu_w = 0.00459Re_w^{0.923}\overline{Pr}_w^{0.613}\left(\frac{\rho_w}{\rho_b}\right)^{0.231} \tag{A.3.4}$$

A.3.5 (J. Jackson & Fewster, 1975)

$$Nu_b = 0.0183Re_b^{0.82}\overline{Pr}_b^{0.5}\cdot\left(\frac{\rho_w}{\rho_b}\right)^{0.3} \tag{A.3.5}$$

A.3.6 (Liao & Zhao, 2002)

$$Nu_b = 0.354Re_b^{0.8}Pr_b^{0.4}\cdot\left(\frac{\overline{Gr}_b}{Re_b^{2.7}}\right)^{0.157}\cdot\left(\frac{\rho_w}{\rho_b}\right)^{1.297}\cdot\left(\frac{\overline{c}_p}{c_{p,b}}\right)^{0.296} \tag{A.3.6}$$

A.3.7 (Kuang et al., 2008)

$$Nu_b = 0.0239\cdot Re_b^{0.959}\cdot\overline{Pr}_b^{0.833}\cdot\left(\frac{\lambda_w}{\lambda_b}\right)^{0.0863}\cdot\left(\frac{\mu_w}{\mu_b}\right)^{0.832}\cdot\left(\frac{\rho_w}{\rho_b}\right)^{0.31}\cdot\left(Gr_q\right)^{0.014}\cdot\left(q^+\right)^{-0.021} \tag{A.3.7}$$

A.3.8 (Cheng et al., 2009b)

$$Nu = 0.023\cdot Re^{0.8}\cdot Pr^{1/3}\cdot F \tag{A.3.8}$$

$$F = min\left(F_1, F_2\right) \tag{A.3.9}$$

$$F_1 = 0.85 + 0.776\left(\pi_A\cdot 10^3\right)^{2.4} \tag{A.3.10}$$

$$F_2 = \frac{0.48}{\left(\pi_{A,pc} \cdot 10^3\right)^{1.55}} + 1.21 \cdot \left(1 - \frac{\pi_A}{\pi_{A,pc}}\right) \tag{A.3.11}$$

A.3.9 (J. Jackson, 2009)

$$Nu_b = 0.021 Re_b^{0.8} Pr_b^{0.4} \cdot \left(\frac{\rho_w}{\rho_b}\right)^{0.3} \cdot \left(\frac{\overline{c}_p}{c_p}\right)^{n} \tag{A.3.12}$$

$$n = \begin{cases} 0.4 & for\ T_b < T_w < T_{pc} \\ 0.4 + 0.2\left(\frac{T_w}{T_{pc}} - 1\right) & for\ T_b < Tpc < T_w \\ 0.4 + 0.2\left(\frac{T_w}{T_{pc}} - 1\right)\left[1 - 5\left(\frac{T_b}{T_{pc}} - 1\right)\right] & for\ Tpc < T_b < 1.2T_{pc}\ and\ T_b < T_w \\ 0.4 & for\ 1.2T_{pc} < T_b < T_w \end{cases} \tag{A.3.13}$$

A.3.10 (Gupta et al., 2011)

$$Nu_b = 0.0061 \cdot Re_b^{0.904} \cdot \overline{Pr}_b^{0.684} \cdot \left(\frac{\rho_w}{\rho_b}\right)^{0.564} \tag{A.3.14}$$

$$Nu_f = 0.0041 \cdot Re_f^{0.9284} \cdot \overline{Pr}_f^{0.7516} \cdot \left(\frac{\rho_w}{\rho_b}\right)^{0.2585} \cdot \left(\frac{\mu_w}{\mu_b}\right)^{0.3452} \tag{A.3.15}$$

$$Nu_w = 0.033 \cdot Re_w^{0.941} \cdot \overline{Pr}_w^{0.764} \cdot \left(\frac{\rho_w}{\rho_b}\right)^{0.156} \cdot \left(\frac{\mu_w}{\mu_b}\right)^{0.398} \tag{A.3.16}$$

$$Nu_w^* = Nu_w \left[1 + exp\left(-\frac{z}{24d}\right)\right]^{0.3} \tag{A.3.17}$$

A.3.11 (D. E. Kim & Kim, 2011)

$$Nu_b = 2.0514 \cdot Re_b^{0.928} \cdot Pr_b^{0.742} \cdot \left(\frac{\rho_w}{\rho_b}\right)^{1.305} \cdot \left(\frac{\mu_w}{\mu_b}\right)^{-0.669} \cdot \left(\frac{\overline{c}_p}{c_{p,b}}\right)^{0.888} \cdot (q^+)^{0.792} \tag{A.3.18}$$

A.3.12 (Badea et al., 2018)

$$Nu_b = \alpha_1 Re_b^{\alpha_2} Pr_b \alpha_3 Pr_w \alpha_4 \left(\frac{\rho_w}{\rho_b}\right)^{\alpha_5} \left(\frac{\lambda_w}{\lambda_b}\right)^{\alpha_6} \left(\frac{\nu_w}{\nu_b}\right)^{\alpha_7} \left(\frac{c_{p,w}}{c_{p,b}}\right)^{\alpha_8} \left(\frac{\pi_{Ac}}{\pi_{Ac,pc}}\right)^{\alpha_9} \tag{A.3.19}$$

$$\pi_{Ac} = \frac{\dot{q}_w}{G} \cdot \frac{\beta_b}{c_{p,b}} \tag{A.3.20}$$

no DHT:

$$\begin{aligned}
\alpha_1 &= 1.464 \times 10^{-2} \\
\alpha_2 &= 8.695 \times 10^{-1} \\
\alpha_3 &= 4.995 \times 10^{-1} \\
\alpha_4 &= 1.278 \times 10^{-1} \\
\alpha_5 &= 1.243 \times 10^{0} \\
\alpha_6 &= 3.267 \times 10^{-1} \\
\alpha_7 &= 4.329 \times 10^{-2} \\
\alpha_8 &= 1.608 \times 10^{-1} \\
\alpha_9 &= 2.217 \times 10^{-1}
\end{aligned}$$

DHT

$$\begin{aligned}
\alpha_1 &= 5.864 \times 10^{-3} \\
\alpha_2 &= 9.158 \times 10^{-1} \\
\alpha_3 &= -1.189 \times 10^{-1} \\
\alpha_4 &= -9.812 \times 10^{-3} \\
\alpha_5 &= 1.004 \times 10^{0} \\
\alpha_6 &= 2.644 \times 10^{-2} \\
\alpha_7 &= 2.869 \times 10^{0} \\
\alpha_8 &= 5.746 \times 10^{-2} \\
\alpha_9 &= 1.529 \times 10^{0}
\end{aligned}$$

A.3.13 (Cheng et al., 2019)

For given heat flux:

$$Nu = 0.023 \cdot Re^{0.8} \cdot Pr^{1/3} \cdot F_1 \cdot F_2 \tag{A.3.21}$$

$$F_1 = \begin{cases} 0.98 & \pi_{Ac} < 1.75 \cdot 10^{-4} \\ 0.85 + 0.056 \cdot \left(10^4 \cdot \pi_{Ac}\right)^{1.5} & 1.75 \cdot 10^{-4} \leq \pi_{Ac} \leq 3.75 \cdot 10^{-4} \\ \frac{13.1}{4.5+\left(10^4 \cdot \pi_{Ac}\right)^{1.35}} & 3.75 \cdot 10^{-4} < \pi_{Ac} \end{cases} \tag{A.3.22}$$

$$F_2 = \begin{cases} 0.93 \cdot Pr^{0.265} & Pr \leq 2.5 \\ 1.61 \cdot Pr^{-0.333} & Pr > 2.5 \end{cases} \tag{A.3.23}$$

$$\pi_{Ac} = \frac{\dot{q}_w}{G} \cdot \frac{\beta_b}{c_{p,b}} \tag{A.3.24}$$

For given wall temperature:

$$Nu = 0.023 \cdot Re^{0.8} \cdot Pr^{1/3} \cdot F_3 \cdot F_4 \cdot F_5 \tag{A.3.25}$$

$$F_3 = \frac{2.1}{1.4 + \left(\frac{c_{p,b}}{\overline{c_p}}\right)^{0.93}} \tag{A.3.26}$$

$$F_4 = \begin{cases} 1.0 & Pr \leq 6 \\ 0.764 \cdot Pr^{0.167} & Pr > 6 \end{cases} \tag{A.3.27}$$

$$F_5 = \begin{cases} 1.44 \cdot \left(\frac{\rho_b}{\rho_w}\right) - 0.48 & \frac{\rho_b}{\rho_w} \leq 1.3 \\ 1.584 \cdot \left(\frac{\rho_b}{\rho_w}\right)^{-0.49} & \frac{\rho_b}{\rho_w} > 1.3 \end{cases} \tag{A.3.28}$$